Untersuchung von Mercaptocarbenen und deren Eigenschaften mittels Matrixisolation

Investigations Towards Mercaptocarbenes and Their Properties *via* Matrix Isolation

Dissertation zur Erlangung des Doktorgrades

der Naturwissenschaftlichen Fachbereiche

im Fachgebiet Organische Chemie

der Justus-Liebig-Universität Gießen

Vorgelegt von Markus Schauermann aus Reichelsheim

Betreuer: Prof. Dr. Peter R. Schreiner, PhD

Eidesstattliche Erklärung

Ich erkläre: Ich habe die vorgelegte Dissertation selbständig und ohne unerlaubte fremde Hilfe und nur mit den Hilfen angefertigt, die ich in der Dissertation angegeben habe. Alle Textstellen, die wörtlich oder sinngemäß aus veröffentlichten Schriften entnommen sind, und alle Angaben, die auf mündlichen Auskünften beruhen, sind als solche kenntlich gemacht. Bei den von mir durchgeführten und in der Dissertation erwähnten Untersuchungen habe ich die Grundsätze guter wissenschaftlicher Praxis, wie sie in der „Satzung der Justus-Liebig-Universität Gießen zur Sicherung guter wissenschaftlicher Praxis“ niedergelegt sind, eingehalten.

Ort, Datum Markus Schauermann

Dekan: Prof. Dr. Thomas Wilke

Prodekan: Prof. Dr. Klaus Müller-Buschbaum

Studiendekan: Prof. Dr. Reinhard Dammann

Erstgutachter: Prof. Dr. Peter R. Schreiner, PhD

Zweitgutachter: Prof. Dr. Hermann A. Wegner

Zusammenfassung

Carbene und carbenoide Verbindungen wurden bis heute im breiten Kontext in Bezug auf synthetische Anwendungen, Aufklärung (bio)chemisch relevanter Prozesse und das Verständnis von präbiotischer Chemie untersucht. Metal-Carben-Komplexe, wie die Grubbs-, Fischer- und Schrock-Komplexe, sowie *N*-heterozyklische Carbene (NHCs) spielen eine essentielle Rolle für chemische Industrieprozesse. Chemikerinnen und Chemiker entwickelten eine Vielzahl von Anwendungen für NHCs, was insbesondere in Bezug auf metall-freie, nachhaltige Chemie (*sustainable chemistry*) von großer Bedeutung ist. Sie spielen ebenfalls eine wichtige Rolle in biologischen Systemen wie Thiamin (Vitamin B_1), einem Enzym verantwortlich für biokatalytische Reaktionen wie z.B. die Benzoin-Kondensation. Die genannten Anwendungen bedingen Carbene, die eine gewisse Stabilität aufweisen. Sehr reaktive Carbene, wie Methylen oder Hydroxymethylen, konnten erst durch spezielle Techniken nachgewiesen werden. Diese wurden intensiv in Bezug auf präbiotische Chemie als Grundbausteine für Aminosäuren und Kohlenhydrate, welche zum Teil auch im interstellaren Raum nachgewiesen werden konnten, untersucht.

Die Arbeitsgruppe um P. R. Schreiner isolierte erfolgreich verschiedene Hydroxycarbene und untersuchte sie hingehend ihrer Stabilität. Hierbei stellte sich heraus, dass einige unter kryogenen Bedingungen stabil sind, wohin gegen andere Reaktionen zeigen, die nur durch den Tunneleffekt erklärt werden können. Auch wenn es sich bei Hydroxycarbenen um gut untersuchte Spezies handelt, fehlt es an Methoden, ihre Kongenere, Mercaptocarbene, zu generieren und zu isolieren. Für diese gibt es nur wenige Untersuchungen, meist theoretischer Natur. Das Kernthema dieser Arbeit ist die Suche nach geeigneten, neuen Vorläufersubstanzen und deren Synthese, sowie die Isolation und Untersuchung von Mercaptocarbenen.

In der vorliegenden Arbeit beschreibe ich die Untersuchung von Hydroxymercaptomethylen (HO–Ċ–SH), das sich unter kryogenen Bedingungen als stabil in Bezug auf mögliche Tunnelreaktionen erwies. Weiterhin konnte Aminomercaptomethylen (H_2N–Ċ–SH), ausgehend von 2-Amino-2-thioxoessigsäure, photochemisch generiert werden. Das Carben entsteht als CO_2-Komplex, der durch Schweratomtunneln zurück zum Edukt reagiert. Auf der Suche nach einer passenden Vorläufersubstanz für Phenylmercaptomethylene (Ph–Ċ–SH) bemerkte ich die Bildung eines Thiophen-Derivates. Diese einfache Eintopf- Reaktion kann auf verschiedene α-Ketocarbonsäureester angewendet werden.

Abstract

Carbenes and carbenoid species have been extensively studied in a broad context for synthetic applications, insights into (bio)chemical reactions, and understanding interstellar and prebiotic chemistry. Metal carbenoids, such as Grubbs-, Fischer-, and Schrock carbenes, as well as *N*-heterocyclic carbenes (NHC) play a crucial role in industrial synthesis. Furthermore, chemists developed a broad scope of applications for NHCs in the context of sustainable chemistry to avoid metals in synthesis. They also play an important role in biochemistry, e.g., in thiamine (vitamin B_1), a vitamin responsible for catalytic reactions like, e.g., benzoin condensations. More reactive carbenes have been extensively studied as intermediates in prebiotic chemistry as building blocks for the chemical evolution of amino acids and sugars that were partly identified in interstellar media.

Schreiner's group generated various hydroxycarbenes and investigated their tunneling behavior. Although sophisticated methods for the generation of hydroxy and aminocarbenes lead to a good understanding of these systems, it still lacks methods towards congeners of these species, namely mercaptocarbenes. They have been rarely investigated and only few theoretical investigations can be found in the literature. The key topic of this work is the theoretical and experimental investigation of mercaptocarbenes and synthesis of suitable new precursor systems for their generation.

We reported the generation of hydroxymercaptomethylene (HO–C̈–SH) that is remarkably stable under cryogenic conditions at 3 K and that does not show any tunneling reactions. We also reported the photochemical generation of aminomercaptomethylene (H_2N–C̈–SH) in its complex with CO_2 from 2-amino-2-thioxoacetic acid. This complex undergoes backreaction to the starting material by heavy atom tunneling.

On the search for a suitable precursor system for phenylmercaptomethylene (Ph–C̈–SH) we noticed the formation of a thiophene derivative. This simple one-pot reaction starting from substituted α-keto carboxylic acid esters to substituted thiophenes represents a new synthetic approach towards these substituted heterocycles.

Preface

This work presented herein was conducted under supervision of Prof. Dr. Schreiner, PhD in the Institute of Organic Chemistry at the Justus Liebig University Giessen from August 2017 to July 2022.

The introduction gives an overview on the background and the broad context of this work regarding the role of carbenes in prebiotic, biological, and industrial chemistry. This part gives a historical background and examples of modern applications in industry and current research.

In the first and second chapter our peer-reviewed publications are presented with permission of the publishers that also contain the experimental details. The publications as well as their corresponding supporting information can be downloaded from the publishers' websites.

Preliminary results that are not published are presented in the third and fourth chapter of this work. Here I describe the new synthetic approach for substituted thiophenes and NMR-based investigations towards the Breslow intermediate.

I thank all my supervisors, colleagues, family, and friends for their constant support during this work. I am particularly grateful to all of them.

Table of Contents

„Home is behind, the world ahead,

And there are many paths to tread

Through shadows to the edge of night,

Until the stars are all alight.

Then world behind and home ahead,

We'll wander back and home to bed.

Mist and twilight, cloud and shade,

Away shall fade! Away shall fade!“

J.R.R. Tolkien

Für meine Familie

Introduction

1. Motivation and Objectives

The field of physical organic chemistry deals with the detailed understanding of chemical mechanisms and reactivity of compounds in all areas of organic chemistry. A deep understanding of biochemical processes helps to develop synthetic procedures through catalyst design and insight into the mechanism of biochemical reactions facilitates the target-oriented synthesis of chemical agents. Our modern society produces all kinds of pollutants that are partly ubiquitous in the oceans, soils and in different layers of earth's atmosphere. Complex chemical reaction networks in these media lead to their degradation involving the sun's irradiation and differing aqueous conditions giving a whole variety of possible products. These degradation products are often unknown as well as the processes that lead to their formation. Understanding these complex systems is important to comprehend their influence on our world's climate especially when talking about climate active compounds in the atmosphere.

The question how these complex chemical systems and even complex forms of life developed from atoms and simple compounds under the rough conditions on prebiotic earth, is still under debate. Atoms form molecules in interstellar media and can enrich on entities like dust grains, comets, and planets. The understanding of chemical evolution from these simple molecules to the first reproducing cells and ultimately to intelligent life is still in its infancy and many of the required steps are still under rarely known.

All the fields mentioned above require special techniques to be investigated such as millimeter (rotational) spectroscopy, matrix isolation, high level computations and simulations as well as advanced laser techniques. In this work I focused my research on reactive sulfur containing species such as aminomercaptomethylene that showed to be able to activate CO_2 even at 3 K and hydroxymercaptomethylene, the first reported free mercaptocarbene. These reactive species might represent reactive linkers to more complex compounds, that may be involved in prebiotic chemistry, which in general can be built from small molecular entities e.g., H_2O, NH_3, H_2S, CS, CO.

2. Carbenes as Reactive Intermediates

Carbenes are electron deficient carbon species bearing two substituents and two unpaired electrons resulting in an electron sextet in the valence shell of the carbon center. This electron deficiency leads to very high reactivity. Carbenes may exist either in singlet or triplet states, the latter being more stable, for example, in methylene. The singlet state either exists as a closed

shell singlet or as an open shell state. The carbene center is approximately sp^2-hybridized but the bonding angles differ depending on substituents and electronic state.[1] The different electronic states result in different reactivities towards other substrates. In general, carbenes themselves can dimerize forming ethylene derivatives. Singlet carbenes readily react with singlet substrates such as typical organic molecules whereas triplet carbenes have to undergo a spin inversion to react with these molecules.[2] One of the first experiments investigating the reactivity of methylene was published by Meerwein and coworkers in 1942. Methylene was generated photochemically from diazomethane and captured with various substrates.[3] This simplest carbene possesses a triplet ground state but this is not necessary the case for all types of carbenes. The singlet state becomes more stable if π-electron donating substituents such as hydroxy and amino groups are involved. In ring systems such as imidazole this stabilizing effect is even more pronounced. These electronic effects in carbenes were extensively studied by Wanzlick in imidazol-2-ylidenes that tend to dimerize.[4-6] Saturated carbene **1** dimerizes in an irreversible fashion whereas its aromatically stabilized counterpart **5** can be isolated (Fig. 1).[7]

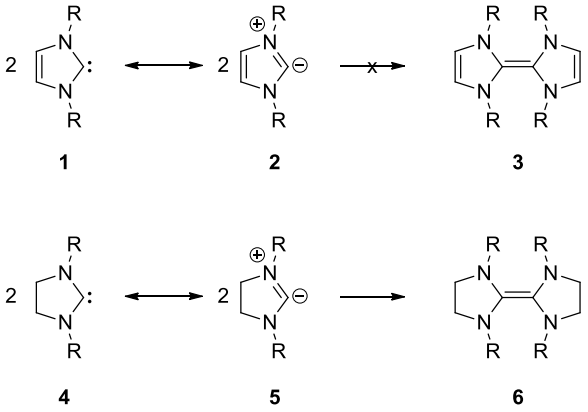

Fig. 1. Dimerization of carbenes **1** and **4**.[7]

Bertrand isolated the first free carbene in 1989.[8] Employing bulky substituents, such as adamantane, hindering dimerization of the carbene, Arduengo managed to isolate the free carbenes **9** and **10** in 1992 (Fig. 2).[9]

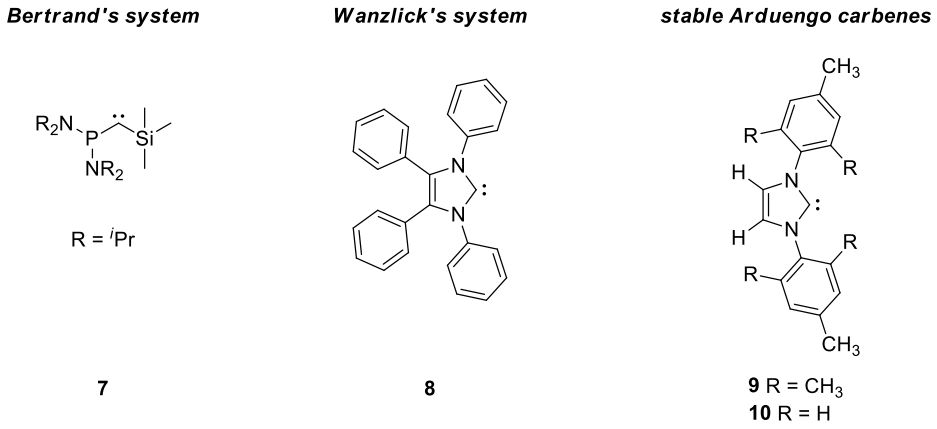

Fig. 2. Bertrand's system **7**, Wanzlick-type carbene **8** and Arduengo-type carbenes (**9**, **10**).[4-6,8,9]

N-heterocyclic carbenes today represent a broad class of compounds used for catalysis as free carbenes or as metal ligands. The resulting metal complexes can be divided in Schrock and Fischer carbene complexes (Fig. 3).[10-13]

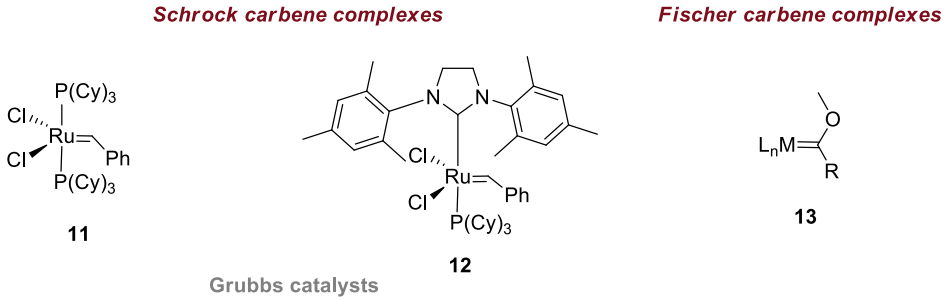

Fig. 3. Carbene-metal complexes like the Grubbs catalysts are used for industrial olefin metathesis. Schrock carbenes feature nucleophilic character whereas Fischer carbenes bearing heteroatoms feature electrophilic character.

In Fischer-type complexes the carbene acts as an electrophile whereas Schrock carbene complexes have nucleophilic character. The free NHCs themselves have shown to have various applications in modern synthetic chemistry. Benzoin-type reactions offered new ways of C–C-coupling reactions by use of various reagents to change the polarity of aldehydes, for example, with thiazolium salts.[14,15] NHCs are also responsible for biologically relevant reactions. Biochemically such transformations can be achieved catalytically, for instance, with thiamine

pyrophosphate (TPP), which is generated from vitamin B_1. TPP is a coenzyme that is active in, e.g., the decarboxylation of pyruvic acid or the transketolase reaction.[16]

The mechanism of TPP-catalyzed reactions was investigated by Breslow in the late 1950s. He suggested the mechanism shown in Figure 4 based on a mechanism reported earlier by Lapworth for the cyanide catalyzed benzoin reaction.[17,18] Basic amino acids deprotonate **14** to form **15**; **15** reacts with an aldehyde to give **16**. The mesomeric structures **17** and **18** represent the "active aldehyde", **18** is known in the literature as the Breslow intermediate.[18] This substrate is able to react with another equivalent of aldehyde to form **19**, which decomposes to the catalyst **15** and the acyloin product **20**.

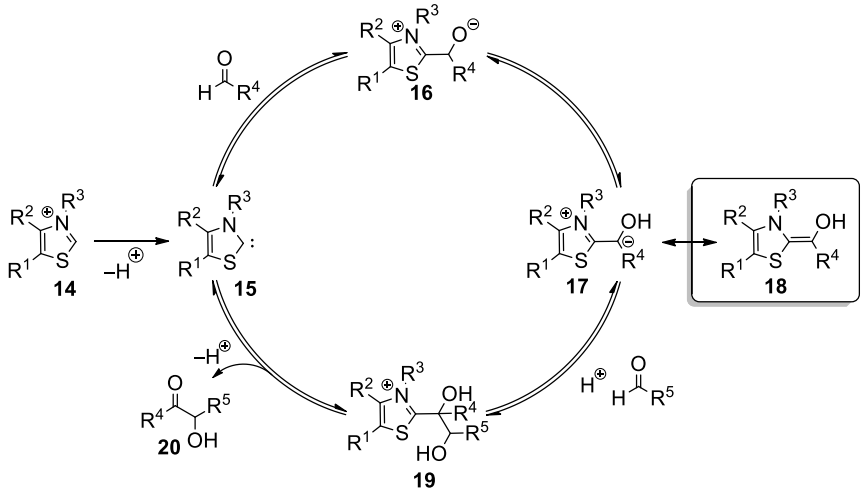

Fig. 4. Postulated mechanism for the thiazolylidene catalyzed Benzoin reaction.[18]

Since Breslow postulated the enaminol form **18** as the key intermediate for this kind of reaction, several attempts to isolate or to spectroscopically identify this intermediate failed. A spectroscopic hint was published by Jordan in his work on brewer's yeast pyruvate carboxylase.[19] Furthermore, Teles used derivatives of thiazole, 1*H*-imidazole and 4*H*-1,2,4-triazole as stable carbene catalysts for benzoin-type reactions and isolated several intermediates that supported Breslow's considerations.[20] In 2012, Rovis isolated triazolylidene derived aza-analogues of the Breslow intermediate and characterized them by X-ray diffraction measurements (XRD).[21] A carbanion enamine could be identified by Tittmann by high resolution XRD in pyruvate oxidase.[22] Important progress was made by Berkessel who characterized the 1,2,4-triazolylidene-derived Breslow intermediate in its keto-form by NMR-spectroscopy.[23] Later Berkessel and coworkers have shown that electron-withdrawing groups should make the enaminol more stable. 2,2-Diamino enols that show a similar reactivity like thiamin-based Breslow intermediates could also be characterized by NMR spectroscopy and

XRD.[24,25] In the past years, Berkessel published detailed work on the keto-enol thermodynamics of Breslow intermediates[26,27] In 2019, Berkessel and coworkers succeeded in identifying a thiazolylidene based Breslow intermediate in NMR studies (Fig. 5).[28]

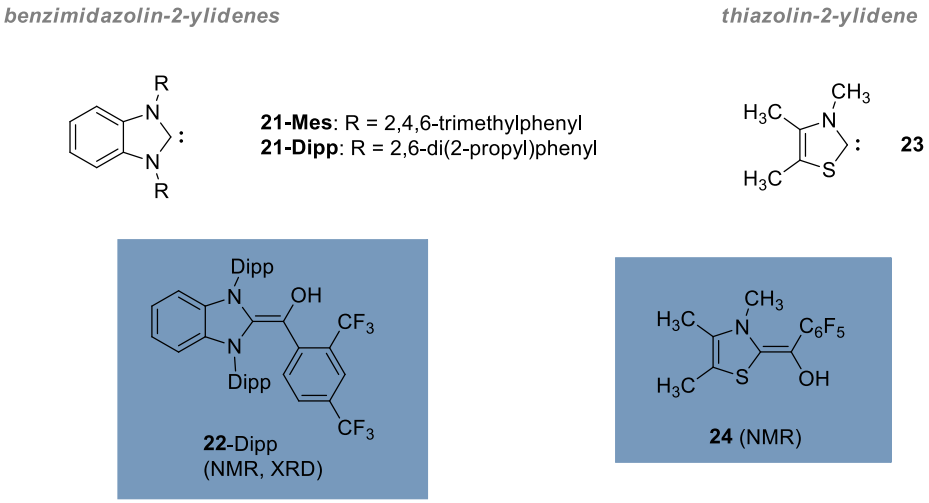

Fig. 5. In 2019, Berkessel successfully characterized systems based on unsaturated/aromatic NHCs by NMR spectroscopy and by XRD.[28]

The systems presented in Figure 5 are stabilized by means of electronic effects and steric hindrance. Smaller carbenes are highly reactive compounds that cannot be studied with "classic" analytical methods. Therefore, matrix isolation technique facilitates the characterization of such compounds under cryogenic conditions.

3. Matrix Isolation Spectroscopy

The isolation of reactive intermediates such as carbenes in solid inert gas matrices under cryogenic conditions allows to record highly resolved IR spectra because translational and rotational degrees of freedom are not thermally accessible. Figure 6 schematically shows the cold head of the matrix isolation apparatus. The sample substance is placed in a sample holder and depending on its vapor pressure eventually needs to be cooled or heated to achieve a suitable dilution in the host gas. The host gas, typically being nitrogen or noble gases, is located in a 2 L glass bulb and its flow can be adjusted by a valve. Typical dilutions of substrate and inert gas are approximately 1:1000.

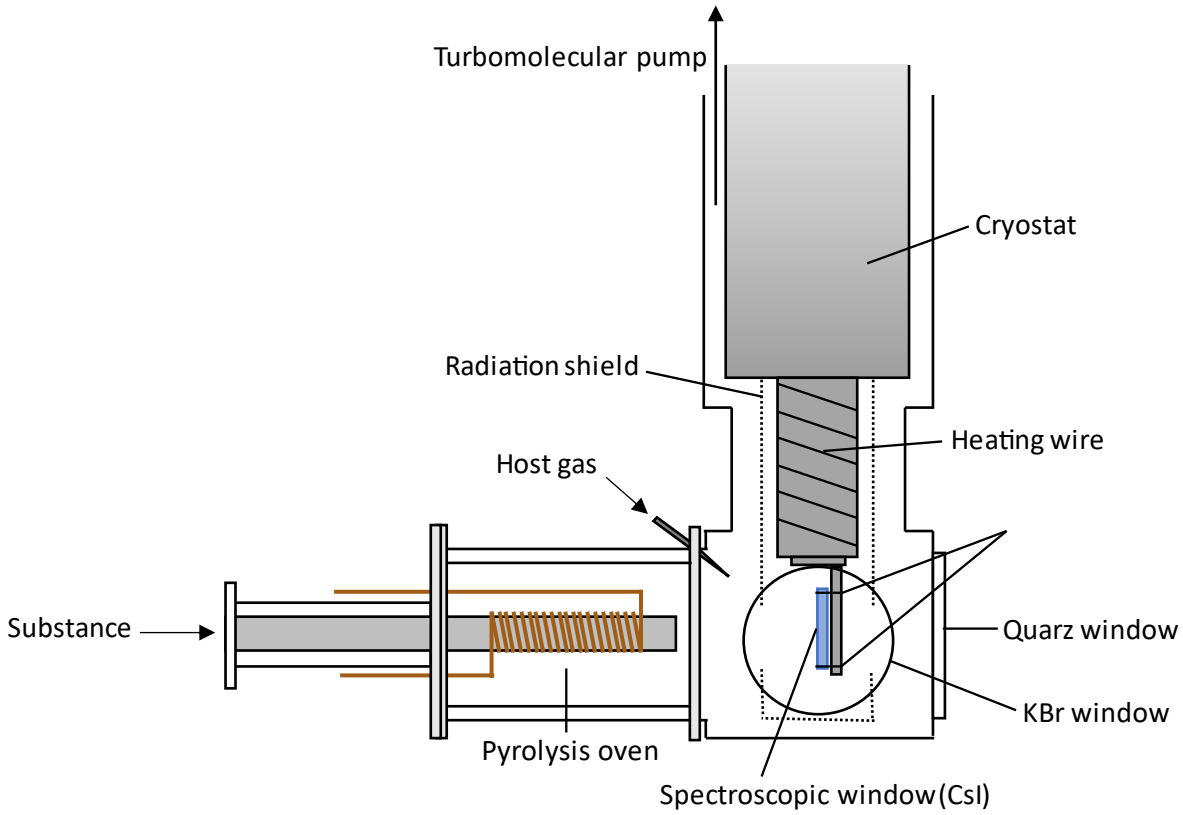

Fig. 6. Schematic representation of the matrix isolation apparatus.

The mixture freezes on a CsI-window that is cooled to 3 K by a Helium cycle cryostat. After deposition, the head is rotated to allow the spectrometer beam to pass the cooling head through the outer KBr- and the CsI-window. To investigate thermal fragments or to generate highly reactive species a pyrolysis oven can be installed. In the oven a quartz tube can be heated up to 1100 °C. The resulting products freeze on the CsI window surrounded by host gas atoms or molecules, the so-called matrix. A more detailed experimental description of this setup is given in the experimental parts of chapter 1 and 2.

Under cryogenic conditions the energetic barriers of typical organic reactions are too high to be overcome. Nevertheless, quantum mechanical tunneling sometimes facilitates reactions even at temperatures near 0 K.

4. Quantum Mechanic Tunneling

The term "quantum mechanical tunneling" (QMT) describes the possibility to find a certain particle with a probability greater than 0 on the other side of an energetic barrier. Therefore, reactions can take place for which the thermal energy is not sufficient, and the activation barrier cannot be surmounted (Fig. 7).

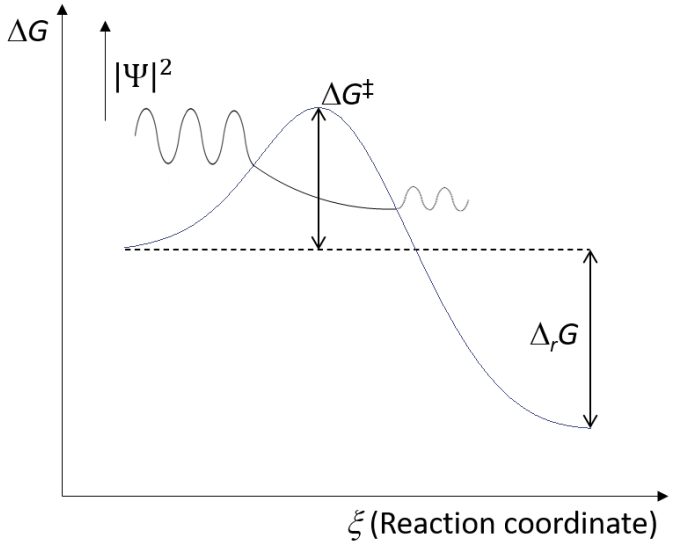

Fig. 7. Reaction profile for an exothermic reaction. On the right side of the barrier the squared wavefunction is greater than 0.

The probability of a particle to cross the barrier by QMT generally depends approximately on the penetration integral Θ below the energetic barrier (1). This approach was developed by Jeffreys, Wentzel, Kramers, and Brillouin in the 1920s. Their findings are concluded in the so called JWKB-approach.[29-32]

$$\Theta = \int_{s_1}^{s_2} \sqrt{2(V(x) - \varepsilon)}\, dx \qquad (1)$$

V(x) describes the energy potential and ε the collision energy of the particle. s_1 and s_2 are the points at both sides of the barrier at the given level of energy. The resulting tunneling probability κ_{JWKB} is given through (2):

$$\kappa_{JWKB} = \frac{1}{1 + \exp(2\Theta)} \qquad (2)$$

When the speed of light *c* is used together with the attempt frequency ω_0 the tunneling half-life is obtained (3):

$$\tau_{JWKB} = \frac{\log(2)}{\omega_0 \cdot c \cdot \kappa_{JWKB}} \tag{3}$$

The barrier for QMT calculations can also be described approximately as a parabolic curve (4).

$$P(E) = \exp\left(\frac{-\pi^2 \cdot w \cdot \sqrt{2 \cdot m \cdot (V_0 - E)}}{h}\right) \tag{4}$$

P(E) depends linearly on the barrier width *w* and on the square root of the barrier height V_0, leading to a stronger impact of the barrier width to the overall tunneling probability.

Transition state theory (TST) developed by Eyring, Evans, and Polanyi in 1935 describes the kinetics of classic thermal reactions.[33-35] TST describes the rate constant *k* depending on Boltzmann's constant k_B, the temperature *T*, Plank's constant *h*, and the equilibrium constant $K^{\ddagger}$ (5).

$$k = \frac{k_B \cdot T}{h} \cdot K^{\ddagger} \tag{5}$$

The equilibrium constant $K^{\ddagger}$ depends on the activation barrier $\Delta G^{\ddagger}$, the temperature, and the gas constant R (6).

$$K^{\ddagger} = \exp\left(-\frac{\Delta G^{\ddagger}}{RT}\right) \tag{6}$$

Not every vibration leads to conversion of the educt to the product. This is included by a probability factor κ also called "transmission coefficient". This leads to more accurate rate constants when including κ (7).

$$k = \kappa \cdot \frac{k_B \cdot T}{h} \cdot K^{\ddagger} \tag{7}$$

QMT is an effect with typically small influence on organic reactions since thermal reactivity dominates these processes at standard or elevated temperatures. Nevertheless, QMT becomes more important when systems are investigated at very low temperatures. At temperatures near 0 K QMT can have a huge influence and even facilitate reactions that are thermally not accessible. Hydroxycarbenes represent a class of compounds that in some cases show QMT and allow to investigate their reactivity under cryogenic conditions.[36]

5. Hydroxycarbenes

Today, hydroxycarbenes are an extensively studied class of carbenes that first was isolated in solid inert gas matrices by Schreiner *et al.* The parent system hydroxymethylene (HO–C̈–H) was generated by thermal extrusion of CO_2 from glyoxylic acid (Fig. 8).[37]

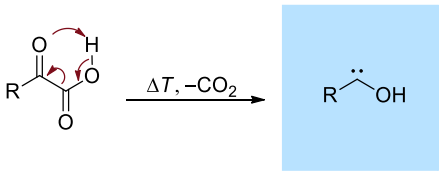

Fig. 8. General procedure for the generation of hydroxycarbenes.[36] Decarboxylation of glyoxylic acid (R=H) yields HO–C̈–H.[37]

At 11 K hydrogen tunneling and the formation of formaldehyde with a half-live of 2 h was observed. After the parent system has been successfully isolated this procedure showed to be applicable for various differently substituted hydroxycarbenes (Fig. 9).[36,38]

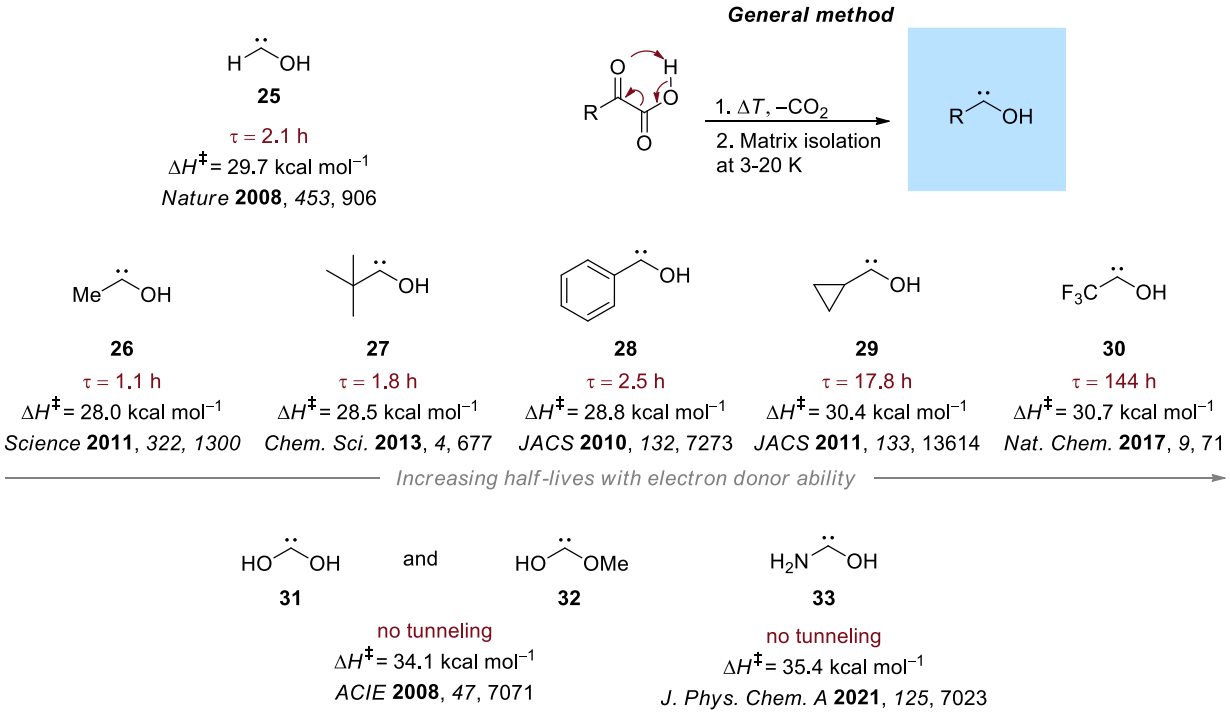

Fig. 9. Substituted α-keto carboxylic acids yield their corresponding hydroxycarbenes upon thermal extrusion of CO_2. The half-life for the H-shift by QMT elongates with the electron-donor ability of the substituents R ($\Delta H^{\ddagger}$ computed at coupled-cluster level of theory with triple-ζ basis set or higher).[36]

The half-lifes of the hydroxycarbenes range from hours to days depending on the electron-donor ability of the substituents. In some cases, no tunneling was observed. For

methylhydroxymethylene the reaction to acetaldehyde (and no reaction to vinyl alcohol **36**) was observed, the latter featuring a lower but broader reaction barrier. This finding represents the first example of a third reaction paradigm: tunneling control of a chemical reaction (Fig. 10).[39]

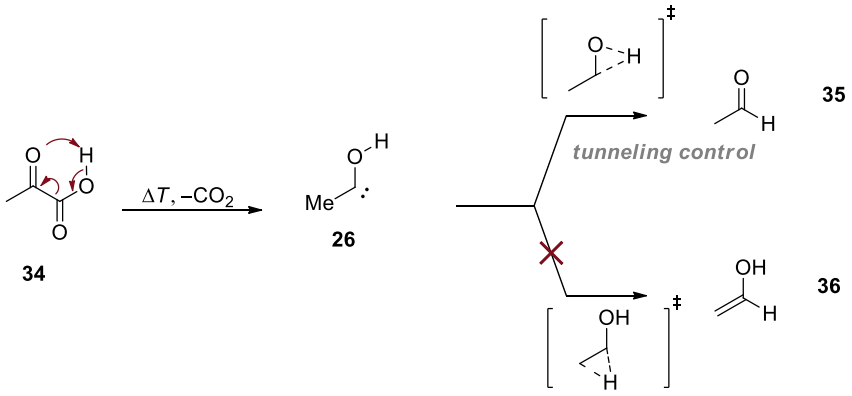

Fig. 10. Tunneling control of the reaction of methylhydroxymethylene to acetaldehyde. The reaction path featuring a higher, but narrower barrier is preferred at cryogenic conditions due to QMT.[39]

Substitution of a radical center with an electron donating- and an electron withdrawing group (EDG, EWG) can significantly stabilize the system. This effect is known as captodative effect (Fig. 11).[40]

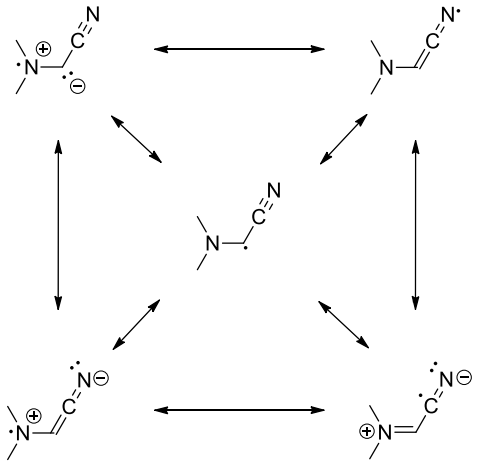

Fig. 11. Captodative effect in a radical substituted by an EWG and an EDG.[40]

For hydroxycarbenes, a captodative effect is also present leading to further stabilization of the carbenes when "push-pull substituents" are attached to the carbene center (Fig. 12).[41-43]

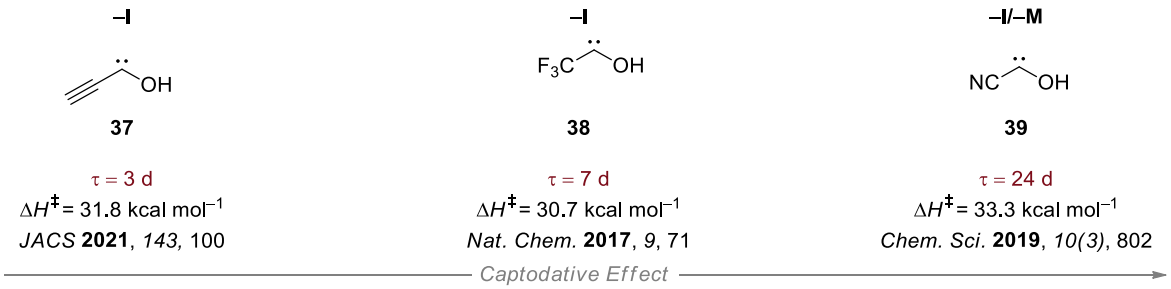

Fig. 12. Captodative effect in hydroxycarbenes ($\Delta H^{\ddagger}$ computed at coupled-cluster level of theory with triple-ζ basis set or higher).[41-43]

In 2018, Schreiner *et al.* succeeded isolating aminomethylene, the parent system of aminocarbenes. In contrast to hydroxycarbenes, no H-tunneling was observed.[44] Figure 13 shows the isodesmic stabilization energies for selected hetero-carbenes. Compared to the parent methylene, the thiol group is least stabilizing while the amino group has the most stabilizing effect. This trend is also true for disubstituted methylene derivatives.[44]

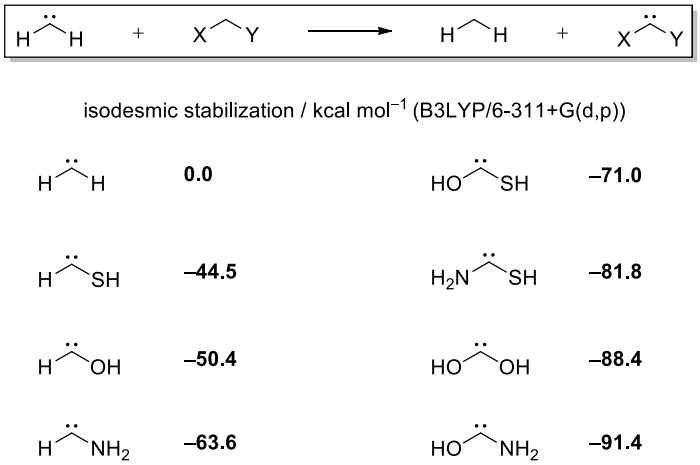

Fig. 13. Isodesmic stabilization energies for selected mono- and disubstituted carbenes.[44]

Although various hydroxycarbenes have been studied, their congeners, mercaptocarbenes, remain elusive species to date and little evidence is found in literature. While most of the carbenes shown in Figure 13 have been isolated and characterized, aminomercaptomethylene and hydroxymercaptomethylene were isolated only very recently by us.[45] On the potential energy surface (PES) of the H_2CSO system all other species were isolated by Schreiner and coworkers in 2010 except hydroxymercaptomethylene.[46] These species might play a role as intermediates in photolytically initiated sulfur transfer reactions. The parent system mercaptomethylene was proposed as an intermediate that formed during molecular cross beam experiments with consecutive mass spectrometry by Kaiser *et al.* in 1998.[47] Its lower energy conformer thioformaldehyde and its isotopologue D_2CS were detected in interstellar media.[48]

Vivekananda *et al*. reported the formation of the dimercaptocarbene radical cation during tandem mass spectrometric experiments.[49] In contrast to hydroxycarbenes, theoretical studies on their congeners, mercapto- and selenocarbenes, suggest that tunneling is too slow in these species to be observable on a reasonable time scale due to enlarged bond lengths and resulting tunneling paths.[50] Concerning a 1,2[H]-shift from the SH group and/or from an amino group we could confirm these findings experimentally (Fig. 14).

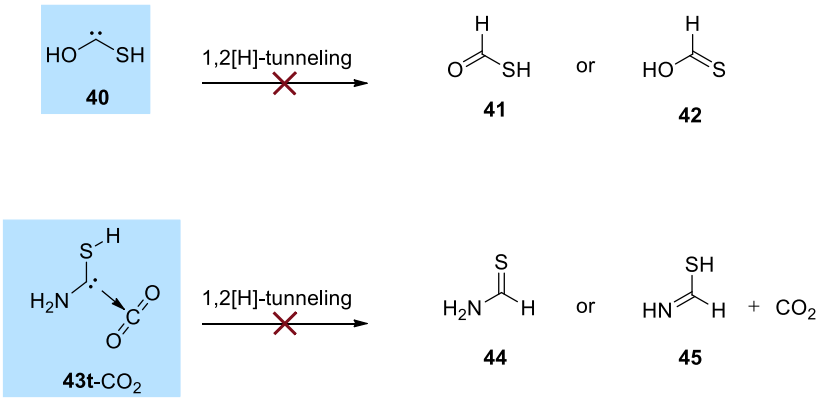

Fig. 14. For hydroxymercaptomethylene and aminomercaptomethylene no 1,2[H]-tunneling reactions were observed.[45,51]

For further details to these systems see chapter 1 and 2. In hydroxycarbenes QMT mostly concerns H atoms but heavier atoms can also undergo QMT. This phenomenon is called “heavy atom tunneling”.

Heavy Atom Tunneling

The term “heavy atom tunneling” refers to tunneling reactions involving elements heavier than hydrogen. Since the tunneling probability is strongly influenced by the particle mass, examples for this phenomenon are rare compared to hydrogen atom tunneling. First examples for reactions of this type have been reported in the 1970s and 1980s.[52,53] Whereas for reactions involving H-tunneling, a kinetic isotope effect (KIE) of greater than 7 is typically found at r.t., heavy atom tunneling KIEs are usually smaller than 1.1.[54]

Tunneling control was observed for heavy atom tunneling reactions in *tert*-butylchlorocarbene by Zuev and Sheridan (Fig. 15).[55,56]

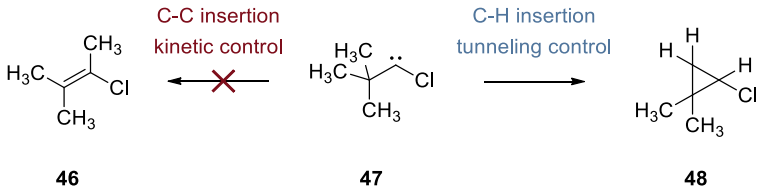

Fig. 15. For *tert*-butylchlorocarbene the reaction to dimethylchlorocyclopropane was observed instead of the 1,2-methyl shift featuring a lower but broader barrier. This is an example for tunneling control involving heavy atom tunneling.[36,54,55]

Starting from the same compound, different tunneling reactions involving heavy atoms can compete with each other. When amino-substituted benzazirine is generated in solid argon under cryogenic conditions, two heavy atom tunneling reactions can be observed leading either to *p*-aminophenylnitrene by nitrogen tunneling or to an amino-substituted keteneimine by carbon tunneling (Fig. 16).[56]

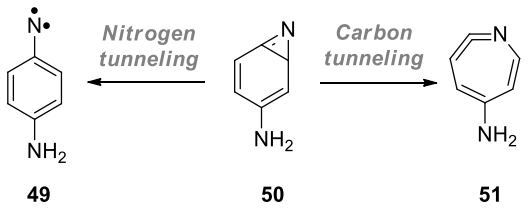

Fig. 16. Competitive heavy atom tunneling in amino-substituted benzazirine.[56]

In our studies we found that heavy atom tunneling can even lead to CO_2 activation at cryogenic conditions starting from a CO_2-complex of aminomercaptomethylene. For details see chapter 3. The knowledge about reactive species such as carbenes as well as QMT as shown above also gives insights into processes that might be present in interstellar media and on prebiotic earth leading to the first building blocks of life.

6. Interstellar and Prebiotic Chemistry

The natural occurring elements of the periodic system form in stars and supernovae and distribute in the cosmos to create nebulae, planets, and other entities in the universe. Under suitable conditions simple molecules form. Up to date, a whole variety of simple molecules was detected in these interstellar media.[57] Just recently, various organic compounds such as organic amines, amino acids, *N*-heterocycles, carboxylic acids and polyaromatic hydrocarbons were detected from the Hayabusa2 spacecraft on the near-Earth asteroid Ryugu.[58] Reactions of small

molecules, i.e., H_2O, CO, CS, and NH_3, abundant in interstellar media, might lead to the formation of essential building blocks for life on interstellar entities such as the prebiotic earth forming amino acids and sugars. These in turn represent essential parts of important macromolecular structures.

Deoxyribonucleic acid (DNA) is an essential building block of life on earth bearing the coded information necessary for reproduction, a key attribute of life. The backbone of the DNA double helix consists of phosphoric acid and ribose, a furanose.[59] Therefore, sugars are crucial building blocks for life. Carbohydrates, such as ribose, can be formally described with the general formular $(CH_2O)_n$, hydrates of carbon. The simplest "carbohydrate" following this description is formaldehyde. It was shown by Butlerov in 1861 that formaldehyde reacts to a variety of higher sugars in basic aqueous solution in the so-called formose reaction.[60] In the 1950s Breslow investigated the mechanism of this reaction. He found an autocatalytic influence of glycolaldehyde **51** through hydrogen bonding to formaldehyde **50** that is formed in the first step of the formose reaction and postulated "active aldehydes" as reactive intermediates for this initial step (Fig. 17).[18] The term "active aldehyde" has been introduced in literature already in the early 1950s.[61]

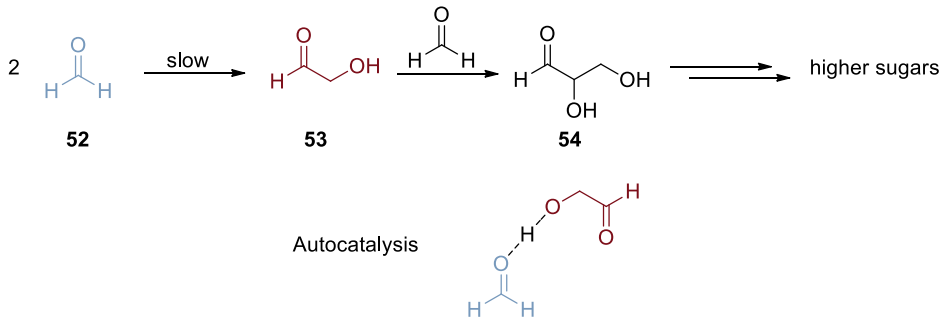

Fig. 17. Formaldehyde slowly forms glycolaldehyde that catalyzes this initial reaction in an autocatalytic process.[18]

Higher products of this reaction such as trioses and tetroses do also catalyze the primary reaction but to a lower extend. Whereas lower monosaccharides have higher activation potentials, higher sugars activate formaldehyde to a lower extend and aldoses generally feature lower activity in the initial reaction.[62] Formaldehyde reacts to glycolaldehyde and trioses but pentoses and hexoses form from C2 and C3 sugars.

However, for the initial reaction two formaldehyde molecules must react to glycolaldehyde. This is not possible without further activation or an Umpolung. Hydroxymethylene represents a high energy conformer of formaldehyde that is formally the adduct of C and H_2O that has

been postulated as "activated formaldehyde" as early as in 1921.[63] Schreiner and coworkers isolated this species and could furthermore show that this carbene indeed reacts with formaldehyde to glycolaldehyde.[37,64] Hydroxymethylene could also be involved in the formation of amino acids *via* a reaction with aminomethylene (Fig. 18).[44,64] This nitrogen analogue of hydroxymethylene can form from activated carbon and ammonia.[65-69]

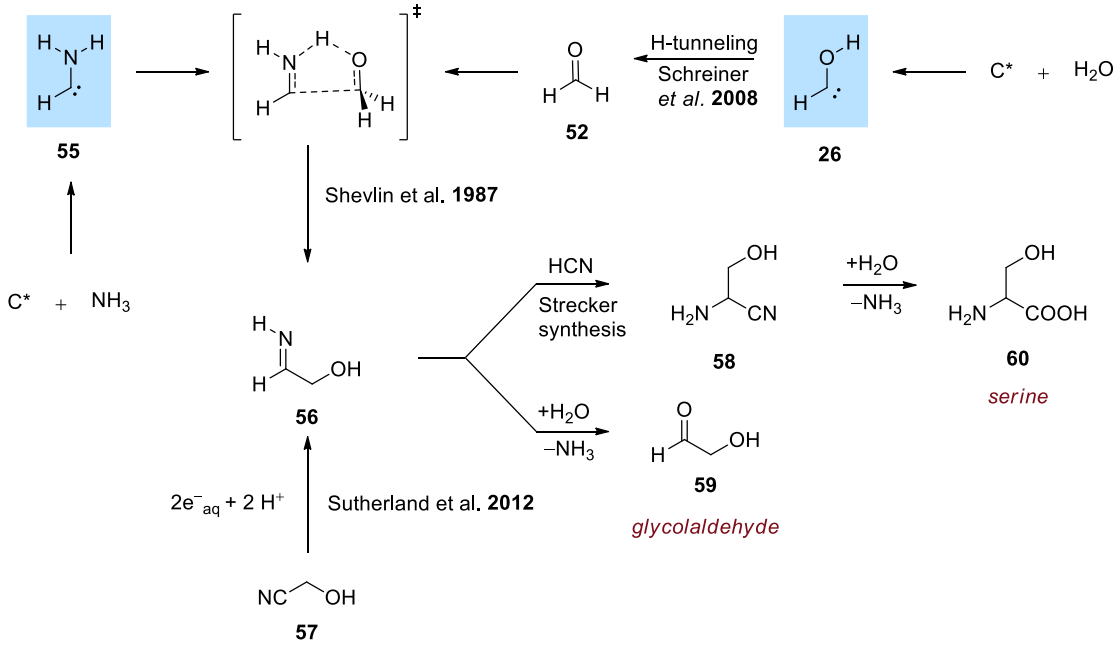

Fig. 18. Aminomethylene and hydroxymethylene might play an important role in (interstellar) prebiotic chemistry leading to amino acids like serine and simple sugars like glycolaldehyde that are essential building blocks of life.[44,64]

In conclusion, these small reactive molecules could in theory yield amino acids and small sugars under prebiotic conditions. Starting from carbon, water, ammonia, and other small and abundant molecules in space these might represent the earliest steps in chemical evolution ultimately leading to life.

7. CO_2 Activation

Making use of abundant CO_2 as a C_1-building block for chemical synthesis is an important goal that features removal of CO_2 from the atmosphere to reduce climate change and leads to sustainable chemistry as well as green fuels. Various activation methods to make use of CO_2 have been developed in the past decades including e.g., *N*-heterocyclic carbenes (NHCs),[70] ionic liquids,[71] Grignard reagents,[72] frustrated Lewis pairs (FLPs),[73] phosphorus betaines,[74] and poly-oxometallates[75] (Fig. 19).

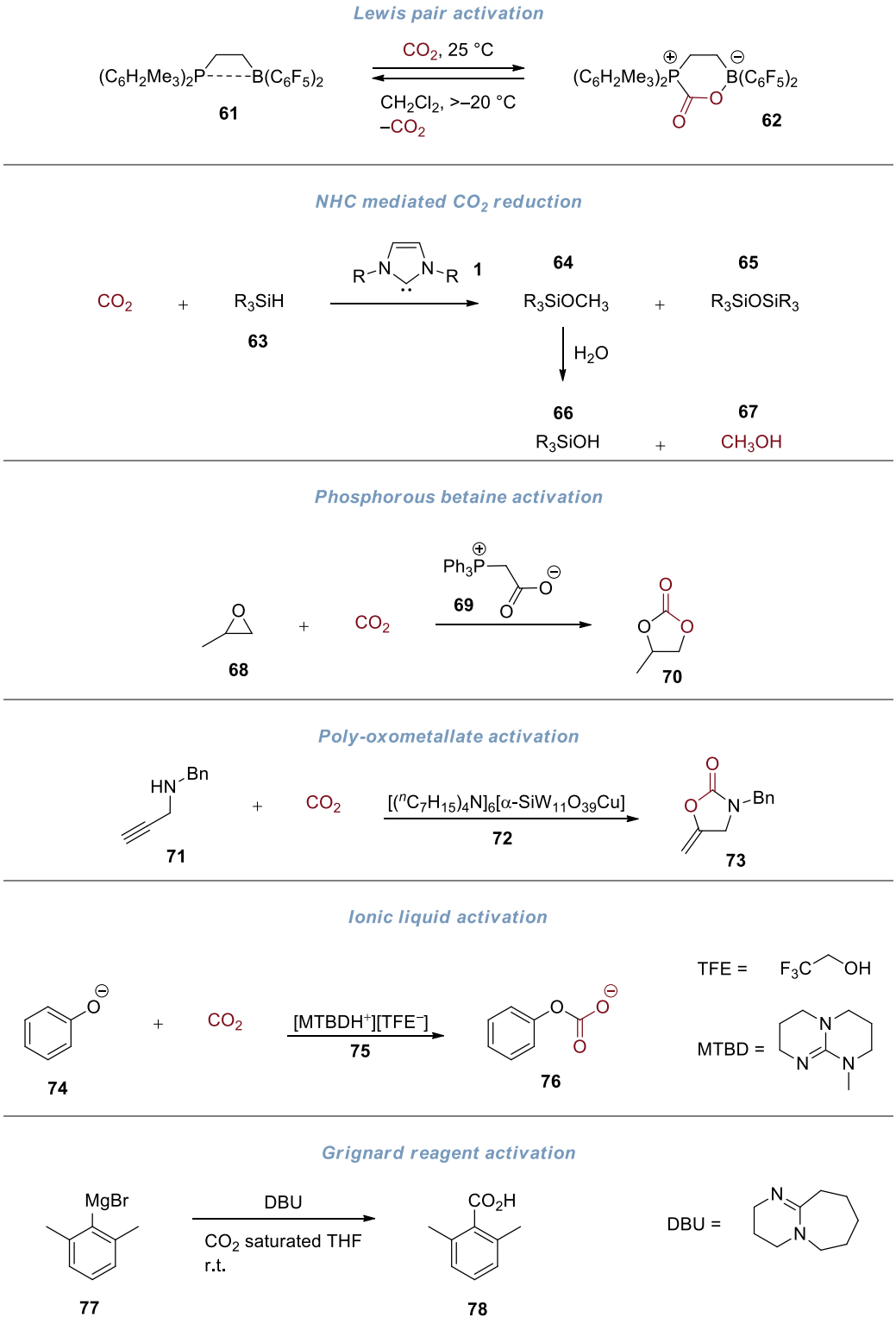

Fig. 19. CO_2 activation employing various reagents or catalysts.[70-75]

NHCs form carboxylates when reacted with CO_2. These remarkably stable compounds can be used for thermal *in situ* NHC generation (Fig. 20).[76]

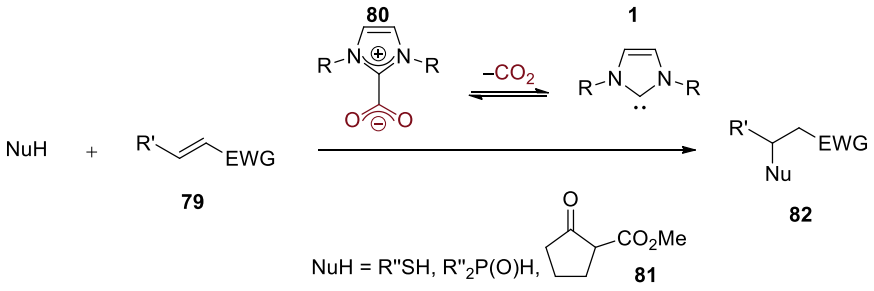

Fig. 20. NHC catalyzed Michael addition using an NHC-carboxylate.[76]

The mechanism of the addition of CO_2 to an NHC is still under debate. Alkorta, Merced Montero-Campillo, and Elguero investigated the thermodynamic stability of various NHC-CO_2 systems regarding the formation of NHC-CO_2 complexes and their corresponding carboxylates. Theoretical investigations suggest the formation of a non-covalent bond NHC-CO_2 complex preceding the formation of the carboxylate. Depending on the nature of the NHC these complexes are even thermodynamically more stable than their corresponding carboxylates (gas-phase computations) (Fig. 21).[77]

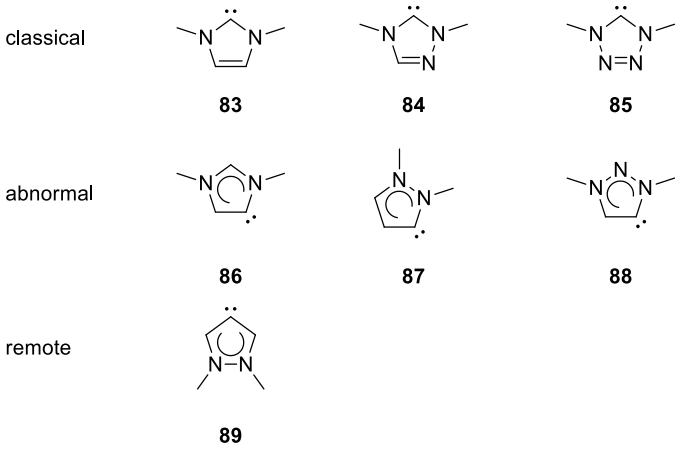

Fig. 21. NHCs investigated by Alkorta, Merced Montero-Campillo, and Elguero.[78]

The number of nitrogen atoms in the NHCs influences their Lewis basicity which strongly impacts the ability of the NHC to bind CO_2. Energy decomposition analyses show that the energy needed to bend the CO_2 molecule increases with the number of nitrogen atoms in the NHC. For **77** the formation of the carboxylate is endothermic by +10 kcal mol^{-1} while the formation of the complex is exothermic by −15 kcal mol^{-1}.[77]

Denning and Falvey theoretically investigated the stability of NHC complexes with CO_2 in different solvents with polarities between 1,4-dioxane and water and found that polar environments favor a shorter, more polar bond between the carbene and CO_2.[78] A detailed understanding on the mechanisms involved in NHC-catalyzed CO_2 activation allows rational

catalyst design to further improve these reactions. In our study on aminomercaptomethylene, representing the smallest centerpiece of the NHC thiazole, we found that it forms a carbene-CO_2 complex under matrix isolation conditions. Heavy atom tunneling allows CO_2 activation through the formation of a covalent bond under cryogenic conditions. Please see chapter 3 for further information.

8. Thiophene Synthesis

Polymers and gels bearing thiophene linkers feature electronic properties that make them valuable components for organic field-effect transistors as alternatives for silicon-based technology.[79,80] Due to their photochemical properties, thiophenes can be used as chemosensors for metals such as aluminum, indium, and mercury,[81] but also for organic compounds such as nucleic acids down to the zeptomolar level.[82] Technical applications need large amounts of building blocks, such as functionalized thiophenes together with a cost efficient synthesis that can compete with the production of their silicon counterparts. Besides electronic applications thiophenes can be used in pharmaceutical compounds[83] and thiophene-diazo compounds can be used as organic dyes.[84] Being anticancer- and antimicrobial agents as well as antioxidative and anticorrosive, thiophenes are a compound class of wide interest and new synthetic routes expand the variety of derivatives accessible for all kinds of applications.[85] While thiophene itself is a by-product of the petrochemical industry, substituted thiophenes can be synthesized through different synthetic strategies.[86] The Gewald reaction yields substituted thiophenes from aldehydes or ketones and α-cyano esters in the presence of sulfur.[87] A modified version starting from cyano acetone gives 2-aminothiophenes.[88] In industry thiophene is produced by reacting CS_2 with butanol in the presence of an oxide catalyst at about 500 °C in ca. 2000 t per year (Fig. 22).[89]

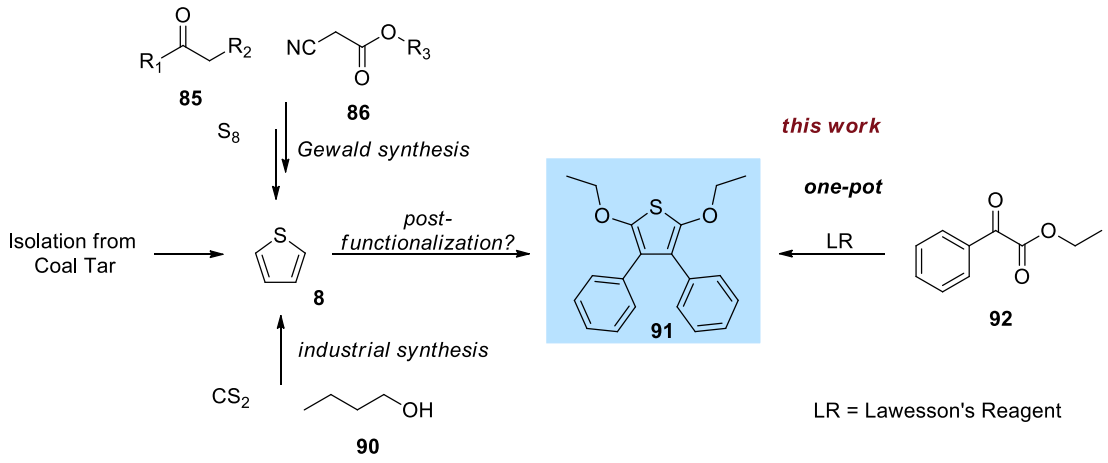

Fig. 22. Previously reported sources for (substituted) thiophenes and our approach.

Depending on the target compound post-functionalization might be more expensive and inefficient compared to one-pot reactions to obtain highly functionalized thiophenes. I herein report such a one-pot reaction to obtain α-ether and β-substituted phenyl substituted thiophenes from readily available α-keto carboxylic acids that makes them suitable for further functionalization, e.g., the generation of polymers and gels that are widely used in electronics.[90]

This type of reactivity is known from the P_4S_{10} mediated condensation of aromatic diketones like **88** (Fig. 23) or benzil that represents a rare example for this reactivity.[91] This reaction proved to be applicable to various substituted ethyl benzoylformate derivatives. Detailed information is given in chapter 4.

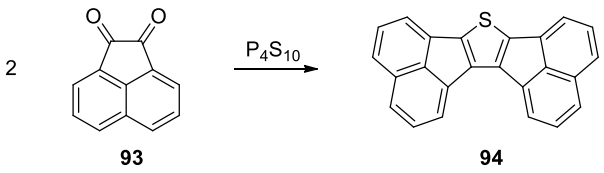

Fig. 23. P_4S_{10} mediated condensation of **88** to **89.**[91]

9. Closing Remarks

We succeeded in the generation and isolation of two new mercapto carbenes, an unknown species to date. Hydroxymercaptomethylene (HO–C̈–SH) showed to be stable under cryogenic conditions whereas aminomercaptomethylene (H_2N–C̈–SH) can activate CO_2 even at 3 K through heavy atom QMT. While HO–C̈–SH can be generated by high vacuum flash pyrolysis, H_2N–C̈–SH is only accessible *via* photochemistry. Thermal decomposition of the starting material yields exclusively thioformamide that itself shows complex photochemistry.[91] Figure 24 illustrates the key systems relevant in this work.

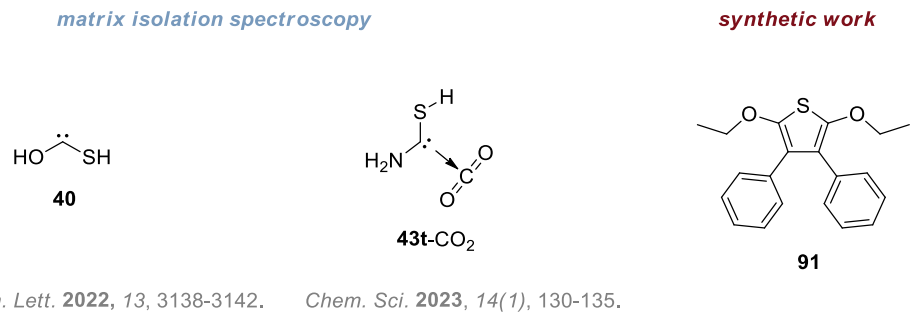

Fig. 24. The key systems investigated herein: HO–C̈–SH,[45] H_2N–C̈–SH,[93] and substituted thiophenes.

Besides the isolation and characterization of two new mercaptocarbenes, we developed a new synthetic pathway to substituted thiophenes that might be suitable for further functionalization and investigations towards their physical properties.

The presented work opens the door for further investigations on mercaptocarbenes and their properties as well as new thiophene based compounds for a broad range of applications.

10. References

[1] N. Bodor, M. J. S. Dewar, J. S. Wasson, *J. Am. Chem. Soc.* **1972**, *94(26)*, 9095.

[2] R. C. Woodworth, P. S. Skell, *J. Am. Chem. Soc.* **1959**, *81(13)*, 3383.

[3] H. Meerwein, H. Rathjen, H. Werner, *Ber. Dtsch. Chem. Ges.* **1942**, *75(12)*, 1610.

[4] H.-J. Schönherr, H.-W. Wanzlick, *Justus Liebigs Ann. Chem.* **1970**, *731(1)*, 176.

[5] H.-J. Schönherr, H.-W. Wanzlick, *Chem. Ber.* **1970**, *103(4)*, 1037.

[6] H.-W. Wanzlick, *Angew. Chem. Int. Ed.* **1962**, *1(2)*, 75.

[7] Y. Liu, P. E. Lindner, D. M. Lemal, *J. Am. Chem. Soc.* **1999**, *121*, 10626.

[8] A. Igau, H. Grutzmacher, A. Baceiredo, G. Bertrand, *J. Am. Chem. Soc.* **1988**, *110*, 6463.

[9] A. J. Arduengo III, H. R. Dias, R. L. Harlow, M. Kline, *J. Am. Chem. Soc.* **1992**, *114(14)*, 5530.

[10] M. Scholl, S. Ding, C. W. Lee, R. H. Grubbs, *Org. Lett.* **1999**, *1(6)*, 953.

[11] P. Schwab, R. H. Grubbs, J. W. Ziller, *J. Am. Chem. Soc.* **1996**, *118(1)*, 100.

[12] P. Schwab, M. B. France, J. W. Ziller, R. H. Grubbs, *Angew. Chem. Int. Ed.* **1995**, *34(18)*, 2039.

[13] E. O. Fischer, *Angew. Chem.* **1974**, *86(18)*, 651.

[14] D. Seebach, *Angew. Chem.* **1979**, *91(4)*, 259.

[15] H. Stetter, G. Dämbkes, *Synthesis* **1980**, *4*, 309.

[16] B. C. P. Jansen, *Vitam. Horm.* **1949**, *7*, 83.

[17] A. Lapworth, *J. Chem. Soc. Trans.* **1903**, *83*, 995.

[18] R. Breslow, *J. Am. Chem. Soc.* **1958**, *80(14)*, 3719.

[19] D. J. Kuo, F. Jordan, *J. Biol. Chem* **1983**, *258(22)*, 13415.

[20] J. H. Teles, J. P. Melder, K. Ebel, R. Schneider, E. Gehrer, W. Harder, S. Brode, D. Enders, K. Breuer, G. Raabe, *Helv. Chim. Acta* **1996**, *79(1)*, 61.

[21] D. A. Dirocco, K. M. Oberg, T. Rovis, *J. Am. Chem. Soc.* **2012**, *134(14)*, 6143.

[22] D. Meyer, P. Neumann, E. Koers, H. Sjuts, S. Lüdtke, G. M. Sheldrick, R. Ficner, K. Tittmann, *PNAS* **2012**, *109(27)*, 10867.

[23] A. Berkessel, S. Elfert, K. Etzenbach-Effers, J. H. Teles, *Angew. Chem. Int. Ed.* **2010**, *49(39)*, 7120.

[24] A. Berkessel, V. R. Yatham, S. Elfert, J. M. Neudörfl, *Angew. Chem. Ind. Ed.* **2013**, *52(42)*, 11158.

[25] A. Berkessel, S. Elfert, V. R. Yatham, J. M. Neudörfl, N. E. Schlörer, J. H. Teles, *Angew. Chem. Int. Ed.* **2012**, *51(49)*, 12370.

[26] M. Paul, P. Sudkaow, A. Wessels, N. E. Schlörer, J. Neudörfl, A. Berkessel, *Angew. Chem. Int. Ed.* **2018**, *57(27)*, 8310.

[27] M. Paul, M. Breugst, J. M. Neudörfl, R. B. Sunoj, A. Berkessel, *J. Am. Chem. Soc.* **2016**, *138(15)*, 5044–5051.

[28] M. Paul, J. M. Neudörfl, A. Berkessel, *Angew. Chem. Int. Ed.* **2019**, *58(31)*, 10596.

[29] H. A. Kramers, *Z. Phys.* **1926**, *39(10)*, 828.

[30] G. Wentzel, *Z. Phys.* **1927**, *43(8)*, 524.

[31] H. Jeffreys, *Proc. London Math. Soc.* **1925**, *2(1)*, 428.

[32] L. Brillouin, *J. Phys. Radium* **1926**, *7(353)*, 79.

[33] M. G. Evans, M. Polanyi, *Trans. Faraday Soc.* **1938**, *34*, 11.

[34] M. G. Evans, M. Polanyi, *Trans. Faraday Soc.* **1935**, *31*, 875.

[35] H. Eyring, *Chem. Rev.* **1935**, *17*, 65.

[36] P. R. Schreiner, *J. Am. Chem. Soc.* **2017**, *139(43)*, 15276.

[37] P. R. Schreiner, H. P. Reisenauer, F. C. Pickard IV, A. C. Simmonett, W. D. Allen, E. Mátyus, A. G. Császár, *Nature* **2008**, *453(7197)*, 906.

[38] D. Gerbig, P. R. Schreiner, Tunneling in the Reactions of Carbenes and Oxacarbenes, John Wiley & Sons, Inc., Hoboken, NJ, **2014**.

[39] P. R. Schreiner, H. P. Reisenauer, D. Ley, D. Gerbig, C. H. Wu, W. D. Allen, *Science* **2011**, *332(6035)*, 1300.

[40] H. G. Viehe, Z. Janousek, R. Merenyi, *Acc. Chem. Res.* **1985**, *18*, 148.

[41] A. K. Eckhardt, F. R. Erb, P. R. Schreiner, *Chem. Sci.* **2019**, *10(3)*, 802.

[42] B. Bernhardt, M. Ruth, A. K. Eckhardt, P. R. Schreiner, *J. Am. Chem. Soc.* **2021**, *143(10)*, 3741.

[43] A. Mardyukov, H. Quanz, P. R. Schreiner, *Nat. Chem.* **2017**, *9(1)*, 71.

[44] A. K. Eckhardt, P. R. Schreiner, *Angew. Chem. Int. Ed.* **2018**, *57(19)*, 5248.

[45] M. Schauermann, P. R. Schreiner, *J. Phys. Chem. Lett.* **2022**, *13*, 3138.

[46] P. R. Schreiner, H. P. Reisenauer, J. Romanski, G. Mloston, *J. Am. Chem. Soc.* **2010**, *132(21)*, 7240.

[47] R. I. Kaiser, C. Ochsenfeld, M. Head-Gordon, Y. T. Lee, *Science* **1998**, *279(5354)*, 1181.

[48] N. Marcelino, J. Cernicharo, E. Roueff, M. Gerin, R. Mauersberger, *Astrophys. J.* **2005**, *620(1)*, 308.

[49] S. Vivekananda, R. Srinivas, M. Manoharan, E. D. Jemmis, *J. Phys. Chem. A* **1999**, *103(26)*, 5123.

[50] J. Sarka, A. G. Császár, P. R. Schreiner, *Collect. Czech. Chem. Commun.* **2011**, *76(6)*, 645.

[51] B. Bernhardt, M. Schauermann, E. Solel, A. K. Eckhardt, P. R. Schreiner, *Chem. Sci* **2023**, *14*, 130.

[52] B. K. Carpenter, *J. Am. Chem. Soc.* **1983**, *105(6)*, 1700.

[53] S. L. Buchwalter, G. L. Gloss, *J. Am. Chem. Soc.* **1979**, *101(16)*, 4688.

[54] C. Castro, W. L. Karney, *Angew. Chem. Int. Ed.* **2020**, *132(22)*, 8431.

[55] P. Zuev, R. S. Sheridan, *J. Am. Chem. Soc.* **1994**, *116(9)*, 4123.

[56] C. M. Nunes, A. K. Eckhardt, I. Reva, R. Fausto, P. R. Schreiner, *J. Am. Chem. Soc.* **2019**, *141(36)*, 14340.

[57] D. E. Woon, Interstellar & Circumstellar Species: A Bibliography (astrochymist.org), **2022**.

[58] H. Naraoka, Y. Takano, J. P. Dworkin, Y. Oba, K. Hamase, A. Furusho, N. O. Ogawa, M. Hashiguchi, K. Fukushima, Y. Tsuda, *et. al*, *Science* **2023**, *379(6634)*, 6634.

[59] J. D. Watson, F. H. C. Crick, *Cold Spring Harb. Symp. Quant. Biol.* **1953**, *18*, 123.

[60] A. M. Butlerov, *Justus Liebigs Ann. Chem.* **1861**, *120*, 295.

[61] E. Racker, The Mechanism of Enzyme Action, The Johns Hopkins Press, Baltimore, MD, **1954**.

[62] T. I. Khomenko, M. M. Sakharov, O. A. Golovina, *Russ. Chem. Rev.* **1980**, *49(6)*, 570.

[63] E. C. C. Baly, I. M. Heilbron, W. F. Barker, *J. Chem. Soc. Trans.* **1921**, *119*, 1025.

[64] A. K. Eckhardt, M. M. Linden, R. C. Wende, B. Bernhardt, P. R. Schreiner, *Nat. Chem.* **2018**, *10(11)*, 1141.

[65] P. B. Shevlin, D. W. McPherson, P. Melius, *J. Am. Chem. Soc.* **1981**, *103*, 7006.

[66] P. B. Shevlin, D. W. McPherson, P. Melius, *J. Am. Chem. Soc.* **1983**, *105*, 488.

[67] D. W. McPherson, M. L. Mckee, P. B. Shevlin, *J. Am. Chem. Soc.* **1983**, *105*, 6493.

[68] D. W. McPherson, K. Rahman, I. Martinez, P. B. Shevlin, *Orig. Life Evol. Biosph.* **1987**, *17*, 275.

[69] P. R. Schreiner, H. P. Reisenauer, *ChemPhysChem* **2006**, *7*, 880.

[70] L. Yang, H. Wang, *ChemSusChem* **2014**, *7(4)*, 962.

[71] C. Wang, H. Luo, D.-E. Jiang, H. Li, S. Dai, *Angew. Chem. Int. Ed.* **2010**, *122(34)*, 6114.

[72] J. M. Valera Lauridsen, S. Y. Cho, H. Y. Bae, J. W. Lee, *Organometallics* **2020**, *39(9)*, 1652.

[73] C. M. Mömming, E. Otten, G. Kehr, R. Fröhlich, S. Grimme, D. W. Stephan, G. Erker, *Angew. Chem. Int. Ed.* **2009**, *48(36)*, 6643.

[74] H. Zhou, G. X. Wang, W. Z. Zhang, X. B. Lu, *ACS Catal.* **2015**, *5(11)*, 6773.

[75] M. Y. Wang, Q. W. Song, R. Ma, J. N. Xie, L. N. He, *Green Chem.* **2015**, *18(1)*, 282.

[76] M. Hans, L. Delaude, J. Rodriguez, Y. Coquerel, *J. Org. Chem.* **2014**, *79(6)*, 2758.

[77] I. Alkorta, M. Merced Montero-Campillo, J. Elguero, *Chem. Eur. J.* **2017**, *23(44)*, 10604.

[78] D. M. Denning, D. E. Falvey, *J. Org. Chem.* **2017**, *82(3)*, 1552.

[79] Y. Liu, X. Zhan, Y. Leu, Macromol. *Chem. Phys.* **2011**, *212(5)*, 428.

[80] F. A. Larik, M. Faisal, A. Saeed, Q. Abbas, M. A. Kazi, N. Abbas, A. A. Thebo, D. M. Khan, P. A. Channar, *J. Mater. Sci. Mater. Electron.* **2018**, *29(21)*, 17975.

[81] R. S. Fernandes, N. S. Shetty, P. Mahesha, S. L. Gaonkar, *J. Fluoresc.* **2022**, *32*, 19.

[82] K. Doré, S. Dubus, H. A. Ho, I. Lévesque, M. Brunette, G. Corbeil, M. Boissinot, G. Boivin, M. G. Bergeron, D. Boudreau, M. Leclerc, *J. Am. Chem. Soc*. **2004**, *126(13)*, 4240.

[83] C. Wu, E. R. Decker, N. Blok, H. Bui, T. J. You, J. Wang, A. R. Bourgoyne, V. Knowles, K. L. Berens, G. W. Holland, T. A. Brock, R. A. F. Dixon, *J. Med. Chem.* **2004**, *47(8)*, 1969.

[84] M. M. Abdou, *Am. J. Chem.* **2013**, *3(5)*, 126.

[85] R. Shah, P. K. Verma, *BMC Chem.* **2019**, *13(54)*, 1.

[86] J. Schatz, in *Sci. Synth.*, **2002**.

[87] K. Gewald, E. Schinke, H. Böttcher, *Chem. Ber.* **1966**, *99(8)*, 2712.

[88] G. A. Eller, W. Holzer, *Molecules* **2006**, *11(5)*, 371.

[89] J. Swanston, Ullmann's Encyclopedia of Industrial Chemistry, Wiley-VCH, Weinheim, **2006**.

[90] G. Barbarella, M. Melucci, G. Sotgiu, *Adv. Mater.* **2005**, *17(13)*, 1581.

[91] O. C. Musgrave, B. J. Morrison, *Phosphorus, Sulfur Silicon Rel. Elem.* **2002**, *177(12)*, 2725.

[92] B. Bernhardt, F. Dressler, A. K. Eckhardt, J. Becker, P. R. Schreiner, *Chem. Eur. J.* **2021**, *27(22)*, 6732.

[93] B. Bernhardt, M. Schauermann, E. Solel, A. K. Eckhardt, P. R. Schreiner, *Chem. Sci.* **2022**, *14*, 130.

Chapter 1: Hydroxy Mercapto Methylene: The Missing H_2CSO Isomer

1.1. Introduction

We report the isolation of hydroxymercaptomethylene (HO–C̈–SH) under cryogenic conditions *via* pyrolysis of 2-ethoxy-2-thioxo-acetic acid. The two most stable carbene rotamers form *via* extrusion of ethylene and CO_2 from this precursor. This donor-stabilized carbene represents a hitherto uncharacterized CH_2SO species and the first spectroscopically characterized free mercaptocarbene. CCSD(T)/cc-pVTZ computations support our findings.

Understanding the chemistry of fundamental small molecules on prebiotic Earth leading to chemical evolution and ultimately to life is still an ongoing endeavor of research.[1] Besides hydrogen, carbon, nitrogen, and oxygen, sulfur is a crucial element in biological chemistry as it is incorporated in, e.g., cysteine that is responsible for the formation of macroscopic structures such as proteins. Besides NO and CO, H_2S is a signaling molecule in the human body and helps regulate cell functions and organs.[2] H_2S is cytoprotective at low concentrations but can also be toxic when reaching supraphysiological levels[2] H_2S, CS, COS, and highly reactive small molecules such as mercaptocarbenes are likely to be relevant (by analogy to their all-oxo species) as building blocks for larger S-containing molecules in prebiotic chemistry. The reaction of H_2S with atomic carbon yields mercaptomethylene that fragments into atomic hydrogen and HCS according to molecular crossed beam experiments by Kaiser *et al*.[3] The authors proposed the fragmentation of HCS to H and CS that further reacts with •SH and •OH radicals to give CS_2 and COS in the atmosphere of Jupiter. Ghadiri, Leman, and Orgel showed COS to mediate amino acid condensation to peptides under prebiotic conditions.[4] Furthermore, thioformate facilitates the condensation of amino acids to peptides in aqueous solution showing the importance of small sulfur containing molecules in prebiotic chemistry.[5] Thioformaldehyde represents the lowest energy species of the H_2CS system and has also been detected in interstellar entities such as dark clouds, hot cores, and comets like Hale-Bopp.[6-8] Its isotopologue D_2CS was detected in the Barnard I cloud.[9] Reactions of simple building blocks like H_2O + CS, H_2 + COS, or H_2S + CO represent direct entry channels for the CH_2OS system that appears rather simple but displays intriguing structural diversity. While stable molecular entities like HC(O)SH, and HC(S)OH come to mind immediately, and are well-known, oxathiirane (**2**), sulfine (**3**), H–C≡S–O–H (**6**) with a formal CS triple bond,[10] and formaldehyde O-sulfide (**7**) have only been prepared relatively recently.[11] Even though hydroxy mercaptomethylene (**1**) looks like another species of this stoichiometry that should be readily accessible (Fig. 1), it has not been reported to date whilst its radical cation could be detected *via* mass spectrometry.[12]

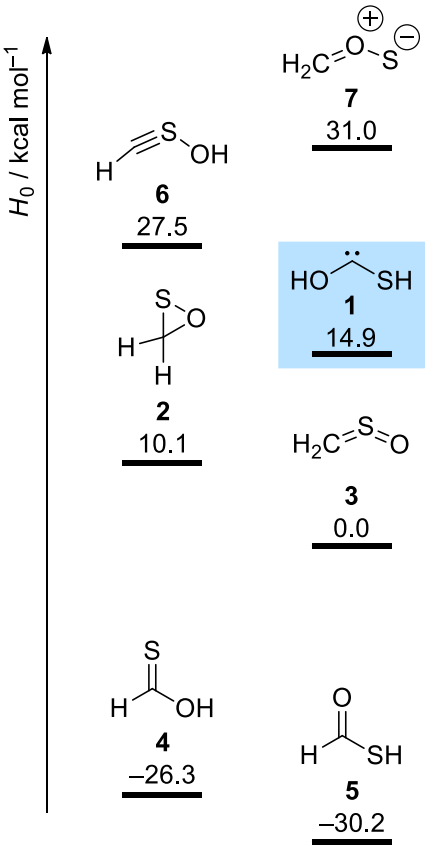

Fig. 1. Molecular structures and relative energies of bound CH_2SO species at CCSD(T)/cc-pVTZ + ZPVE as shown by us earlier.[11]

After hydroxymethylene and many of its derivatives were detected under cryogenic conditions,[13] it was expected that the S and Se congeners can be prepared in an analogous fashion. Computational studies suggest that tunneling, which is common for hydroxycarbenes,[14] is extremely slow in these systems.[15] Although there is spectrometric evidence for the parent **1**,[16,17] it has not been characterized spectroscopically. We showed recently that flash vacuum pyrolysis (FVP) of 1,3-dithietane 1,3-dioxide delivers **2** (Scheme 1), which can be transformed photochemically into several other CH_2SO isomers, except **1**.[11] One of the challenges associated with making small and fundamental molecules is the nature of the precursor, which often presents a (synthetic) conundrum by itself. Thus, while **2** and **6** can be prepared *via* irradiation of **3** at different wavelengths, **1** is not photochemically accessible through any of the other CH_2SO isomers. Hence, another precursor is needed. Here we demonstrate that 2-ethoxy-2-thioxo-acetic acid (**8**) is a suitable precursor for generating **1** thermally through FVP and trapping in a cold matrix (10 K) in an excess of argon.

1.2. Results and Discussion

Our idea was to utilize the ester pyrolysis of **8** to generate the corresponding monothiooxalic acid (**9**) that releases carbene **1** upon decarboxylation (Fig. 2).

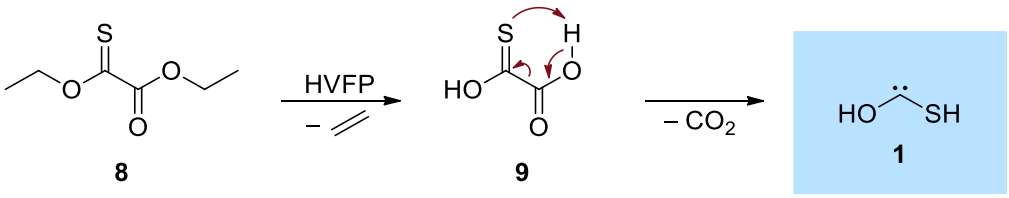

Fig. 2. Ethylene extrusion leads to the formation of intermediate **9**, which further reacts in an allowed 5c-6e rearrangement to carbene **1**.

Under FVP conditions **9** forms in the gas phase and undergoes a 5c-6e thermally allowed CO_2 extrusion to **1**. We identified the CO and OH bond stretching vibration of the isotopologues **1tt/1ct** and **1tt/1ct-*d*$_2$** (t and c indicate *trans* and *cis* stereochemistry for the rotation of the OH and SH moieties) as their strongest absorptions when compared to coupled cluster computations (CCSD(T)/cc-pVTZ, unscaled, Figs. 3 and 4). We excluded the rotamerization of conformers of **9** since no changes in the C=O stretching vibration regions were observed upon irradiation (see SI for further details).

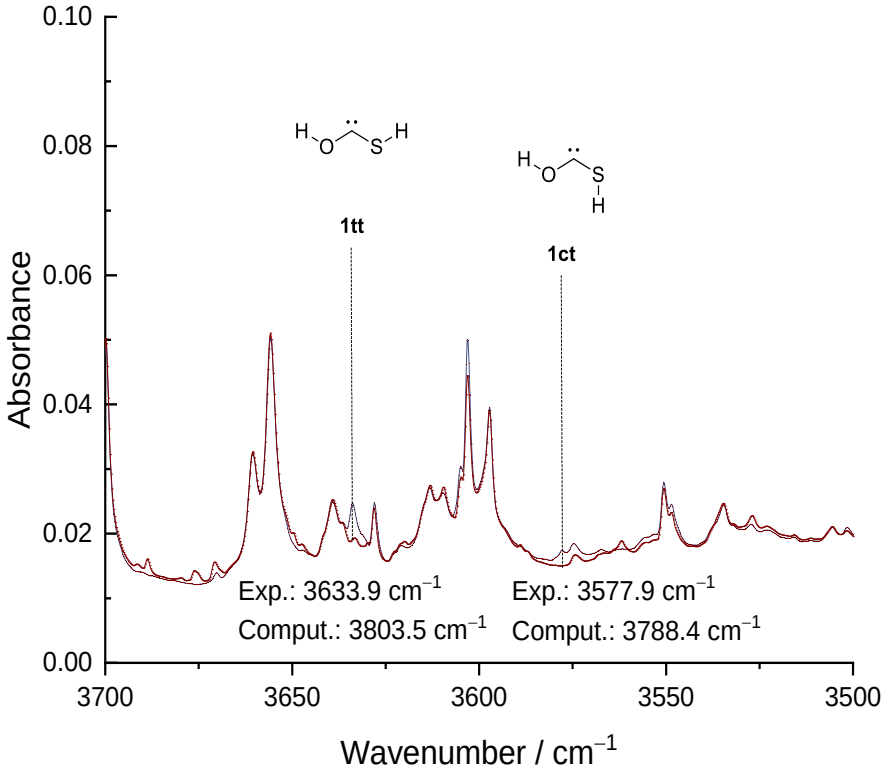

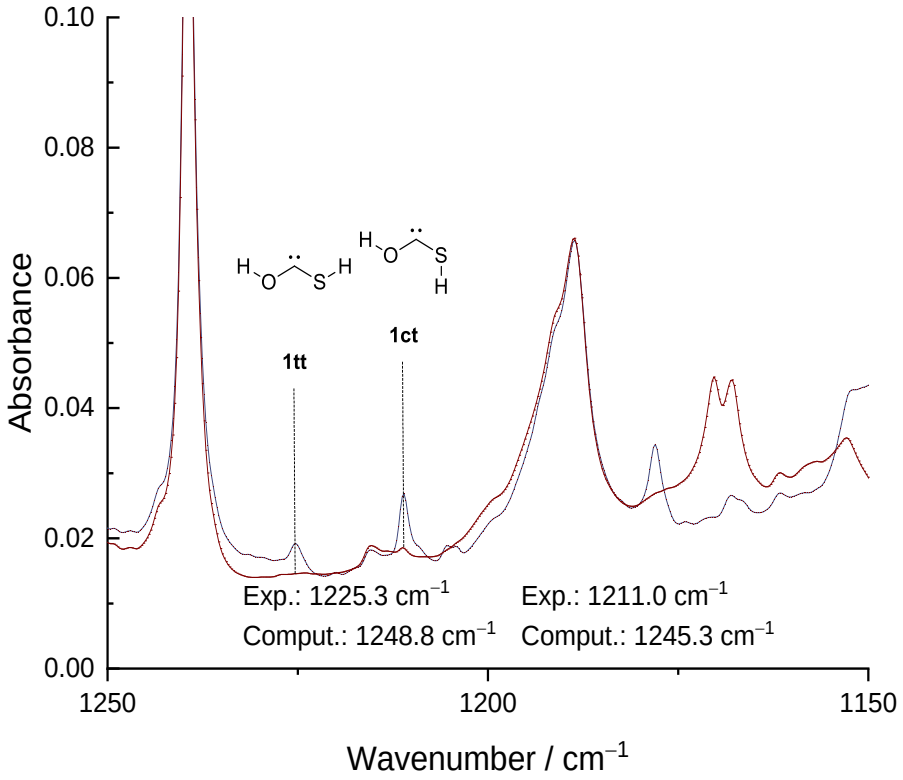

Fig. 3. Comparison of the relevant parts of the matrix isolation infrared spectrum of **8** upon HVFP (blue) and the spectrum recorded after 20 min of UV irradiation (red) (254 nm); for the full spectra see Figure 14. The OH (top) and CO stretching vibrations (bottom) of **1tt** and **1ct** vanish upon irradiation. Computed vibrations at the CCSD(T)/cc-pVTZ level of theory, unscaled.

To ensure the assignments of the IR bands of **1** we synthesized perdeuterated **8** starting from oxalyl chloride and EtOH-d_5. As expected, the characteristic OD bands shift significantly compared to the OH vibrations. Gratifyingly, **1ct-*d*$_2$** and **1tt-*d*$_2$** form upon FVP of **8**-d_{10} in analogous fashion as the protio species (Fig. 4).

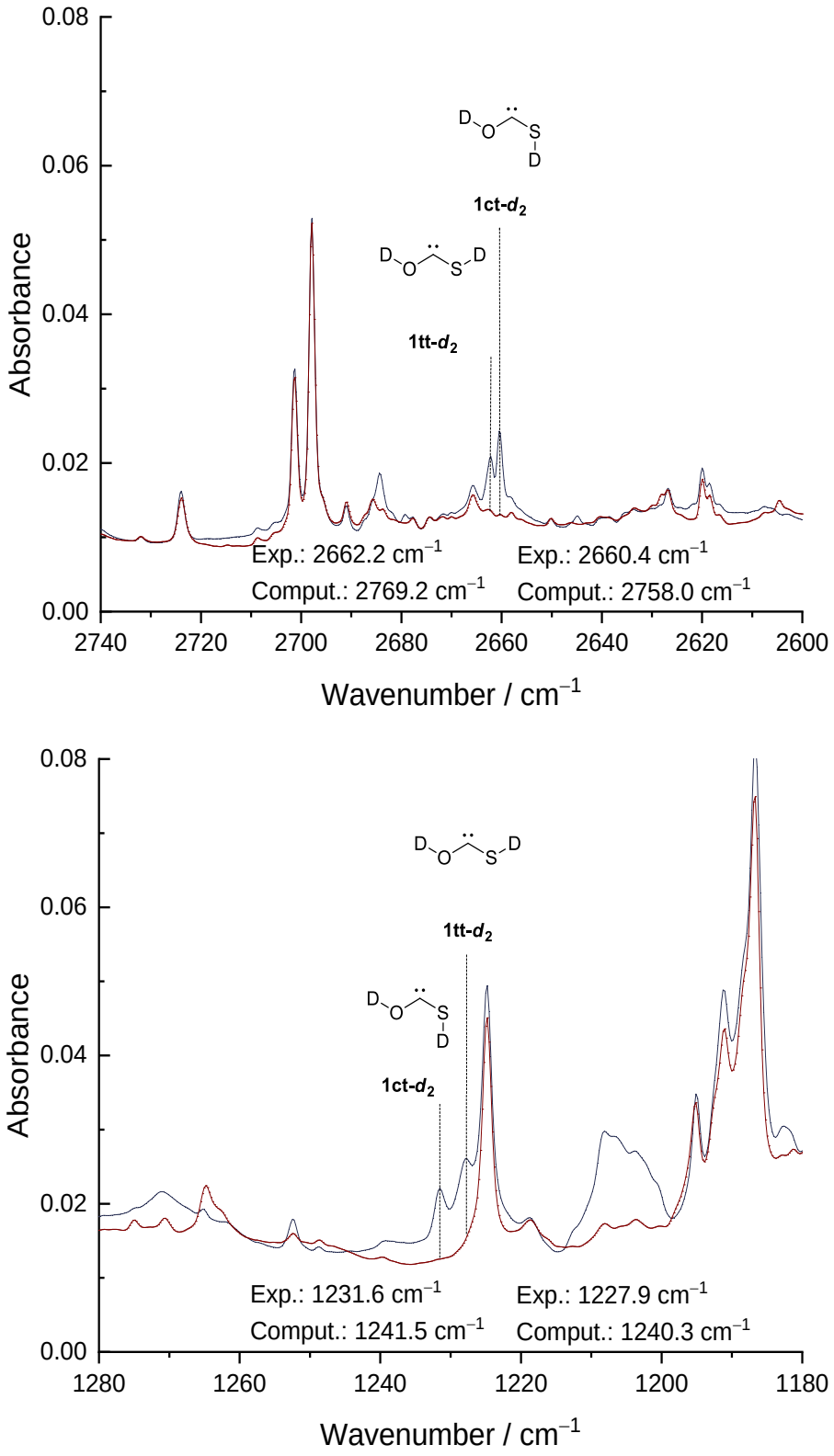

Fig. 4. The matrix isolation infrared spectra of **8** after HVFP (blue) and the spectrum recorded after 20 min of UV irradiation (red) (254nm) show that **1tt-*d*$_2$** and **1ct-*d*$_2$** vanish. A broad band at 1205 cm^{-1} can be assigned to **8-*d*$_{10}$** that also decomposes upon UV irradiation. Computed vibrations at the CCSD(T)/cc-pVTZ level of theory, unscaled.

Irradiation of the matrix leads to a fast 1,2[H]-shift across the CO bonds of **1tt** and **1ct** to give the thioformic acid conformers **E5** and **Z5** (Fig. 5) that are already present after pyrolysis. Consequently, the bands of these species increase in intensity upon irradiation for 8 min due to the carbenes reacting to **E5** and **Z5**. Further irradiation leads to the decomposition of these species to smaller fragments. Without irradiation, the carbene conformers show no intrinsic reactivity. There are no indications of hydrogen tunneling even when warming the system to 35 K for 5 min and re-cooling.

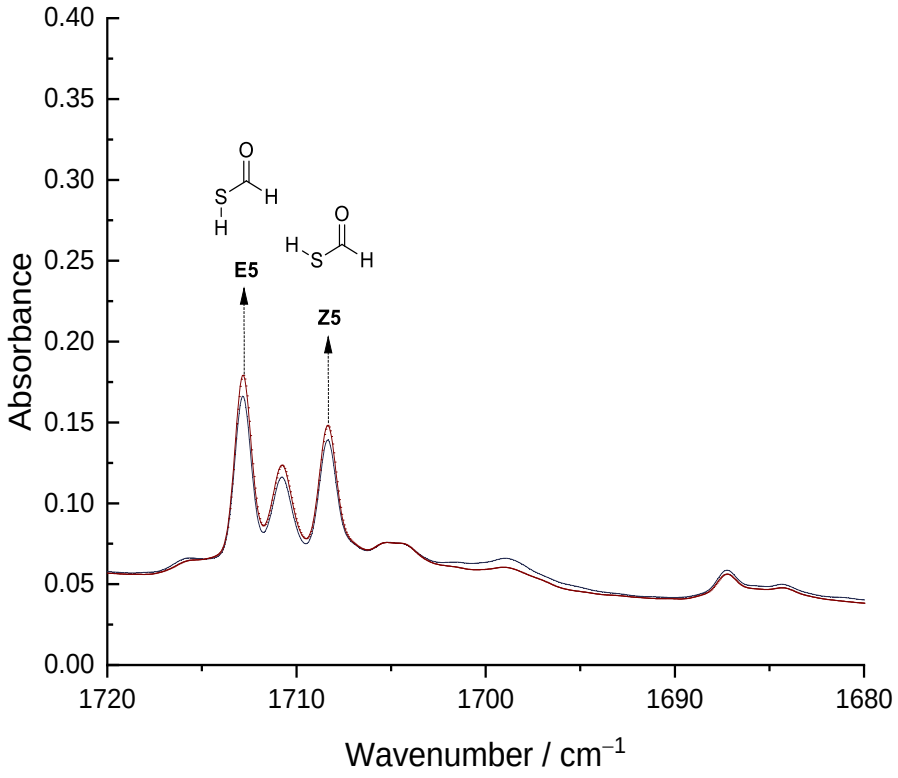

Fig. 5. Formation of the thioformic acid conformers **E5** and **Z5** after pyrolysis of **8** at 900 °C (blue spectrum). The intensities of the bands of **E5** and **Z5** increase upon 254 nm irradiation of the matrix for 8 min (red).

To confirm these findings, we modeled the tunneling kinetics with density functional theory (DFT) computations at the B3LYP/6-311++G(3df,3pd) level of theory utilizing canonical variational transition state theory with small curvature tunneling (CVT/SCT).[17] Figure 6 shows the PES and the interconnection of the observed species (for a detailed PES see experimental part). The computations predict that **1tt** and **1ct** should not show measurable tunneling reactivity as the half-lives are longer than the measurable time scale (see experimental part for details),[15] in agreement with our observation that the spectra did not change at least over the course of several days.

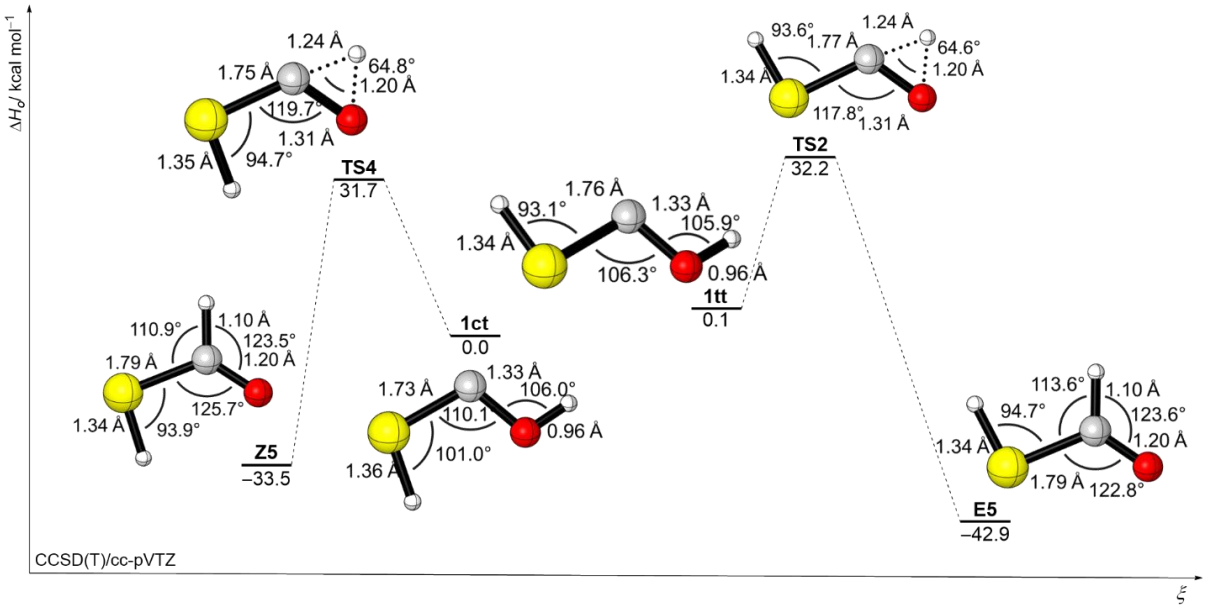

Fig. 6. Structures **1tt** and **1ct** undergoing 1,2-[H] shifts across the CO bond (ΔH_0 at CCSD(T)/cc-pVTZ).

Conformers **1ct** and **1tt** rearrange to **Z5** and **E5**, respectively, *via* a 1,2-[H] shift across their CO bonds. A 1,2-[H] shift along the CS bond of **1tt** would lead to HC(S)OH conformer **E4** that was not observed. The rotamerization of **1tt** to **1ct** is associated with a barrier of 15.3 kcal mol^{-1}. This interconversion does not occur *via* tunneling because the barrier is rather wide. Like its congener dihydroxymethylene, hydroxymercaptomethylene is persistent under cryogenic conditions and no tunneling reactions take place. Carbene **1** has a similar stabilization enthalpy compared to dihydroxymethylene (−71.0 kcal mol^{-1} and −88.4 kcal mol^{-1} (B3LYP/6-311++G(d,p)) according to the homodesmotic equation 1 (X, Y = O and/or S).[18,19]

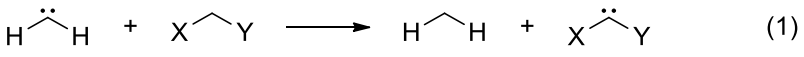

(1)

Similar to dihydroxymethylene, **1** has a singlet ground state; triplet ^{3}**1** is about 37 kcal mol^{-1} higher in energy (vertical, CCSD(T)/cc-pVTZ). The experimentally detected conformers of **1** also are the most stable according to our computations. Their stability can be explained by minimization of their dipole moments that are smallest for the **1tt** and **1ct** conformers (Fig. 7) in the gas phase.

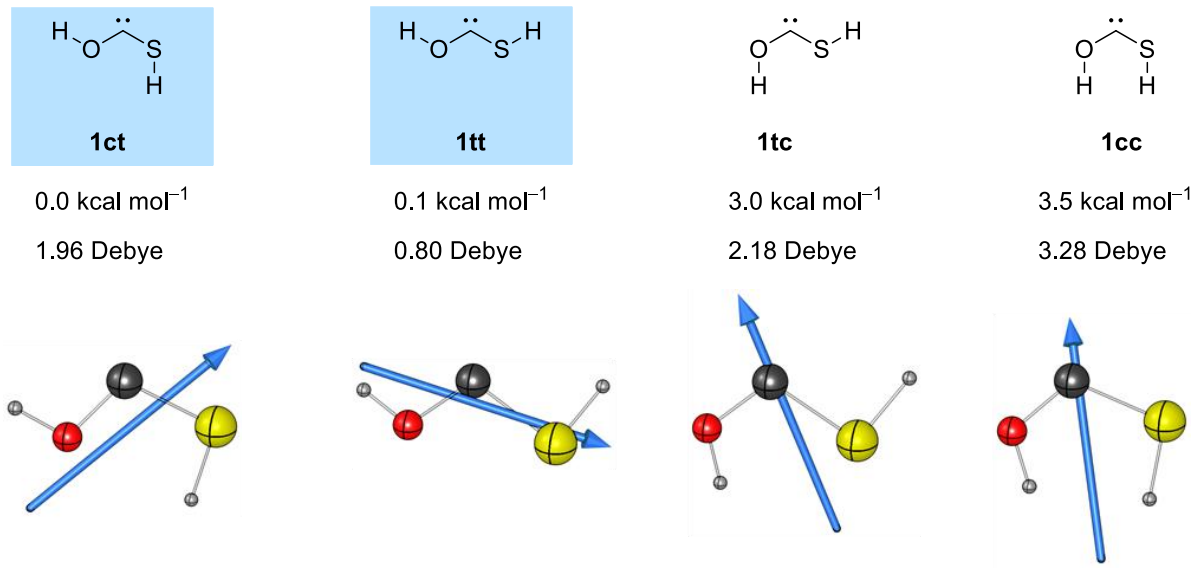

Fig. 7. The most stable conformers **1ct** and **1tt** also possess the lowest dipole moments (CCSD(T)/cc-pVTZ), given as vectors in blue.

Carbenes bear an electron sextet at the carbon center making them formally electron-deficient. This can, however, be overwritten when heteroatoms are attached to the carbene center that donate electrons into the carbene's empty *p*-orbital. The heteroatom π-donation of sulfur is captured in HOMO−1, whereas the π-donation of oxygen is visualized by HOMO−3 (Fig. 8).

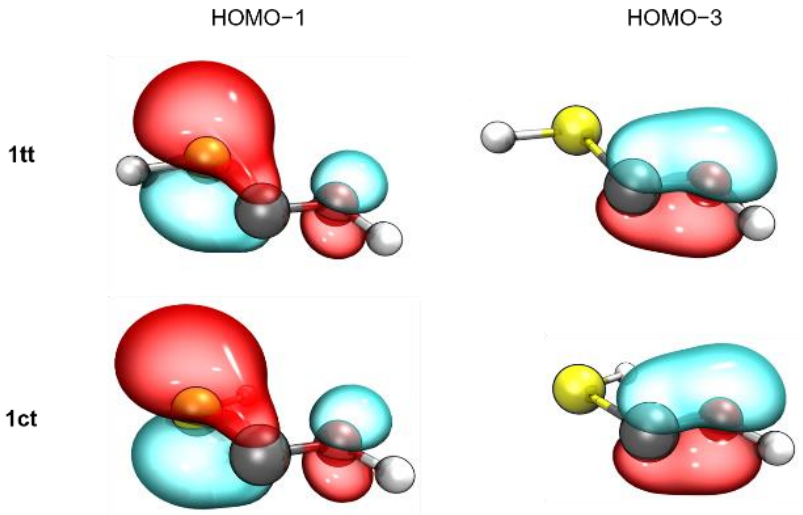

Fig. 8. The HOMO−1 of **1tt** and **1ct** display the π-donation of the sulfur atom to the carbene center whereas HOMO−3 visualizes the π-donation of the oxygen atom (images generated with VMD software).

The orbitals of the carbon atom and the oxygen atom in HOMO−3 are in a closer energetic and geometric proximity resulting in a lower energy of the orbital compared to HOMO−1. Therefore, the oxygen atom contributes more to the overall stabilization of the carbene.

In summary, we report the isolation of the two most stable conformers of hydroxymercaptomethylene (**1**, HO–C̈–SH), the first spectroscopically identified mercaptocarbene and the missing isomer on the PES of the CH_2SO system. Similar to its congener dihydroxymethylene, **1** shows no tunneling reactivity and is persistent at least up to 35 K. As a formal adduct of H_2O and CS, this intermediate might represent a high-energy linker to sulfur containing prebiotic molecules.

1.3. Experimental

Methods

Matrix isolation studies

The matrix isolation experiments were performed using a Sumitomo cryostat system consisting of an F-70 compressor unit and an RDK 408D2 closed-cycle refrigerator cold head. For infrared (IR) measurements polished KBr and BaF_2 windows in the vacuum shroud and a CsI window on the sample holder was used. Silicon diodes attached to the sample holder measured the temperature (deposition at 15 K, measurements at 3 K). During the experiments pure diethylmonothiooxalate (**8**) was kept in a storage bulb in the dark and at −30 to −25 °C. The matrix host gas (Ar, gas purity of 99.999%) was stored in a 2 L glass balloon that was refilled and flushed three times with Ar before the experiments. The typical deposition time of our experiments was 2 h depositing a total amount of ca. 150 mbar of Ar together with **8** on the matrix window. For irradiation a high-pressure mercury lamp (SP200) in conjunction with an MSH 150 monochromator system from LOT-QuantumDesign GmbH was used. The IR spectra were recorded with a Bruker Vertex 70 FTIR spectrometer equipped with a standard KBr or wide-range beam-splitter in a range from 7000 cm^{-1} to 350 cm^{-1} (resolution: 0.7 cm^{-1}). For every measurement 50 scans were recorded. For ultra-violet/visible (UV/Vis) measurements a Jasco V-760 spectrophotometer was used in the range from 190 nm to 800 nm (resolution: 1 nm). A background spectrum of the cold matrix window was recorded prior to deposition. While depositing the matrix was kept in the dark to avoid unwanted photochemistry.

Computations

The computations at the B3LYP[20,21]/6-311++G(3df,3pd)[22,23] level of theory using an ultrafine grid and very tight conversion criteria were performed with Gaussian16 Revision B.01 (full citations of electronic structure codes are given at the end of this document. The computed minimum structures on the PES feature no imaginary frequencies and all transition states possess one imaginary frequency.

CVT/SCT rate constants were computed with POLYRATE 2017[24] at the B3LYP/6-311++G(3df,3pd) level of theory.

For coupled-cluster computations (CCSD(T)[25,26]/cc-pVTZ[27-31]) CFOUR 1.0 was used with the following keywords: ABCDTYPE=AOBASIS, CC_PROG=ECC, SCF_CONV=10, and CC_CONV=7; CONVERGENCE=8 in addition for geometry optimizations; VIB=EXACT for analytical computations of harmonic frequencies; METHOD=TS for transition states.

The images in Figure 6 were generated with VMD software support by the Theoretical and Computational Biophysics group at the Beckman Institute, University of Illinois at Urbana-Champaign.

General analytics

All NMR spectra were recorded with a Bruker Avance III (HD) AV400 (400 MHz) spectrometer and a Bruker Avance III HD AV600 (600 MHz) at 298 K. Chemical shifts (δ) are given in ppm relative to the respective solvent residual peak of $CDCl_3$ (δ = 7.26 and 77.16 ppm). ATR-IR spectra were recorded on a Bruker Alpha spectrometer (4000 – 400 cm^{-1}). High resolution mass spectrometry was performed with a Bruker Impact II (negative mode ESI-MS).

Synthesis of the Starting Materials

Diethylmonothiooxalate (**8**)

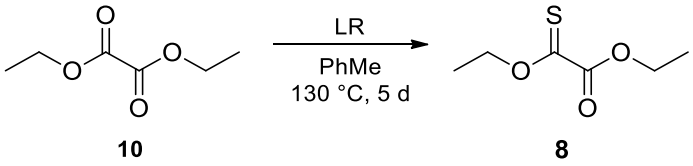

Fig. 9. Synthesis of Diethylmonothiooxalate (**8**).

Diethyl oxalate was obtained from Sigma-Aldrich Chemie GmbH in > 99% purity and was used without further purification. 1.08 g diethyl oxalate (1.0 mL, 6.8 mmol) and 5 g Lawesson's reagent (LR) (12.5 mmol) were dissolved in 50 mL of dry toluene and stirred for 5 days (reflux). The solution was cooled to r.t. and filtered over a silica plug to remove side products formed of LR (pentane/diethylether 20:1). The solvents were removed and the residue was purified *via* column chromatography (pentane/diethylether 20:1, R_f = 0.25). The product was obtained as a yellow liquid in 34% yield.

Yield: 164.4 mg (1.05 mmol, 34%).

^{1}H-NMR (400 MHz, $CDCl_3$): δ = 4.62 (q, J = 7.1 Hz, 2H), 4.33 (q, J = 7.2 Hz, 2H), 1.48 (t, J = 7.1 Hz, 3H), 1.36 (t, J = 7.1 Hz, 3H) ppm.

^{13}C-NMR (101 MHz, $CDCl_3$): δ = 201.4, 159.9, 69.5, 63.2, 14.1, 13.5 ppm.

IR (ATR): ν = 2985.1, 1734.5, 1445.7, 1367.6, 1250.7, 1173.5, 1088.8, 1001.4, 897.4, 813.0, 764.1, 677.9 cm^{-1}.

HRMS (ESI): m/z = 185.0246 $[M+Na]^+$ (calcd. m/z = 185.0243).

Diethyl oxalate-d_{10} (**10-d_{10}**)

1.27 mL EtOH-d_6 (1.0 g, 19.2 mmol, 2 equiv.) was dissolved in 10 mL DCM. 0.85 mL oxalyl chloride (1.2 g, 9.9 mmol, 1 quiv.) was added dropwise at 0 °C over 5 min. The solution was stirred at 0 °C for 1.0 h and at r.t. for another 1.5 h. The solution was washed 2 times with 20 mL $NaHCO_3$ (aqu., 8%) each. The combined aqueous phases were extracted with 20 mL DCM. The combined organic phases were dried over Na_2SO_4. The solvent was removed and the product was obtained as a colorless liquid.

Yield: 1.17g (7.5 mmol, 75%).

^{1}H-NMR (600 MHz, $CDCl_3$): δ = -.

^{13}C-NMR (150.9 MHz, $CDCl_3$): δ = 158.0, 62.5 (p, J = 22.7 Hz), 13.0 (dp, J = 38.8, 19.4 Hz) ppm.

IR (ATR): ν = 2235.7, 1764.4, 1736.3, 1344.5, 1212.1, 1175.4, 1087.0, 1047.4, 966.7, 914.8, 882.5, 733.8, 562.4 cm^{-1}.

HRMS (ESI): m/z = 179.1102 $[M+Na]^+$ (calcd. m/z = 179.1099).

Diethylmonothiooxalate-d_{10} (**8-d_{10}**)

Diethylmonothiooxalate-d_{10} was synthesized starting from diethyl oxalate-d_{10} according to the procedure for **8** starting with 200 mg **10-d_{10}**.

Yield: 88.0 mg (0.51 mmol, 40.0%).

^{1}H-NMR (400 MHz, DMSO-d_6): δ = -.

^{13}C-NMR (101 MHz, DMSO-d_6): δ = 201.5, 160.0, 68.7 (p, J = 22.9 Hz), 62.5 (p, J = 22.7 Hz), 12.7 (ddt, J = 11.6 Hz) ppm.

IR (ATR): ν = 2235.8, 2117.8, 1733.0, 1294.2, 1195.0, 1128.8, 1086.1, 1045.9, 1000.7, 970.2, 876.0, 768.5, 651.3, 589.5 cm^{-1}.

HRMS (ESI): m/z = 195.0870 $[M+Na]^+$ (calcd. m/z = 195.0870).

NMR Spectra

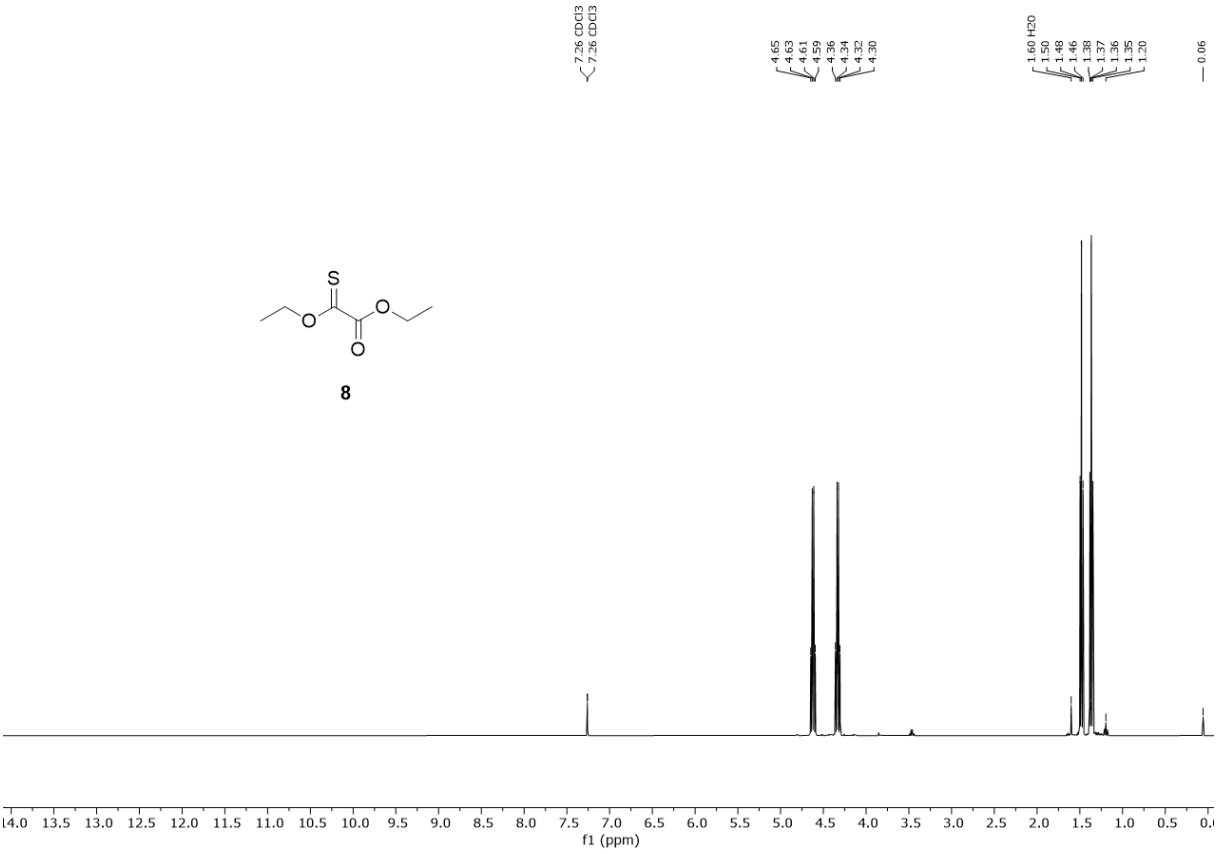

Fig. 10. ^{1}H NMR (400 MHz, $CDCl_3$) of diethylmonothiooxalate (**8**).

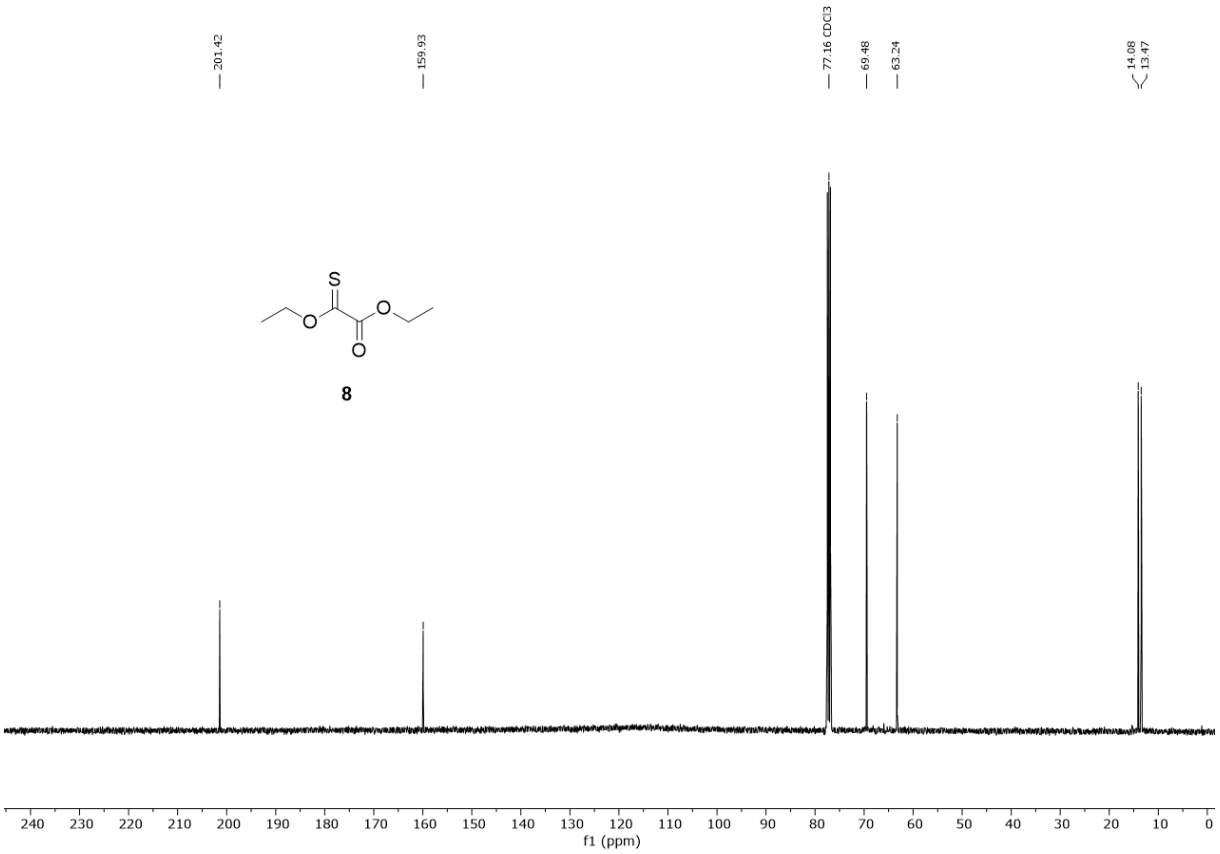

Fig. 11. $^{13}C\{^{1}H\}$ NMR (101 MHz, $CDCl_3$) of diethylmonothiooxalate (**1**).

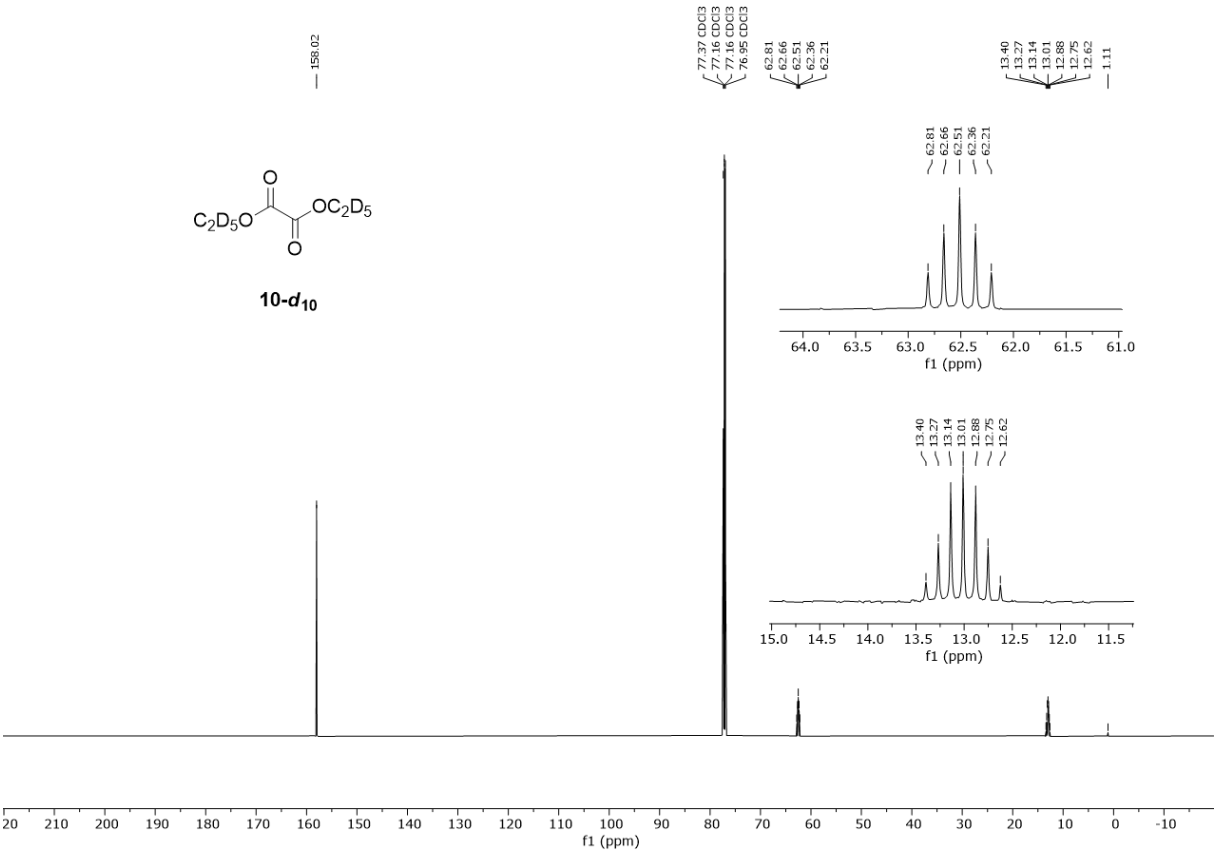

Fig. 12. $^{13}C\{^{1}H\}$ NMR (101 MHz, $CDCl_3$) of diethyl oxalate-d_{10} (**10-*d*$_{10}$**). (Splitting visualizes full deuteration).

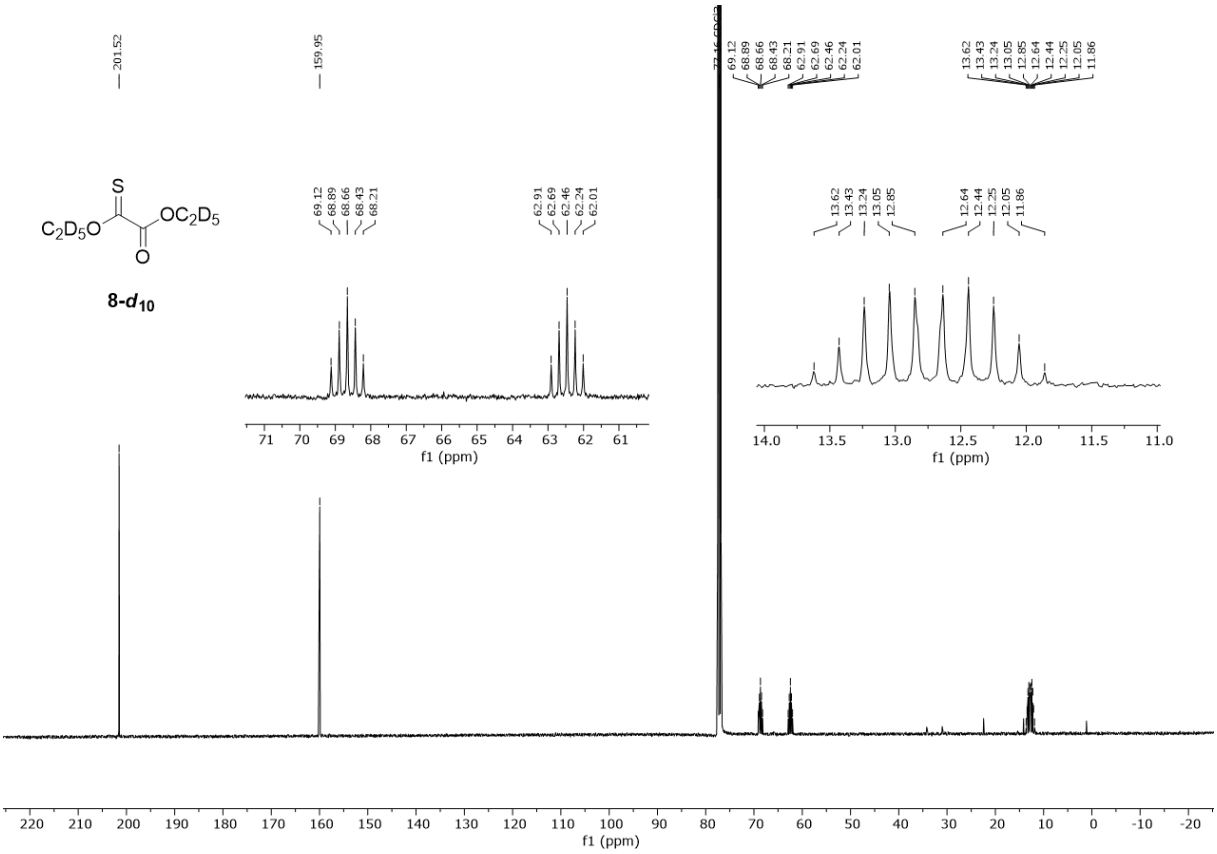

Fig. 13. $^{13}C\{^1H\}$ NMR (101 MHz, $CDCl_3$) of diethylmonothiooxalate-d_{10} (**8-*d*$_{10}$**). (Splitting visualizes full deuteration).

Matrix Isolation UV/VIS Spectrum

We need high pyrolysis temperatures to observe the described spectra and most of the precursor decomposed to CO_2, CO, and COS. The absorption of the fragments is therefore very low and not visible in the UV region (Fig. 14).

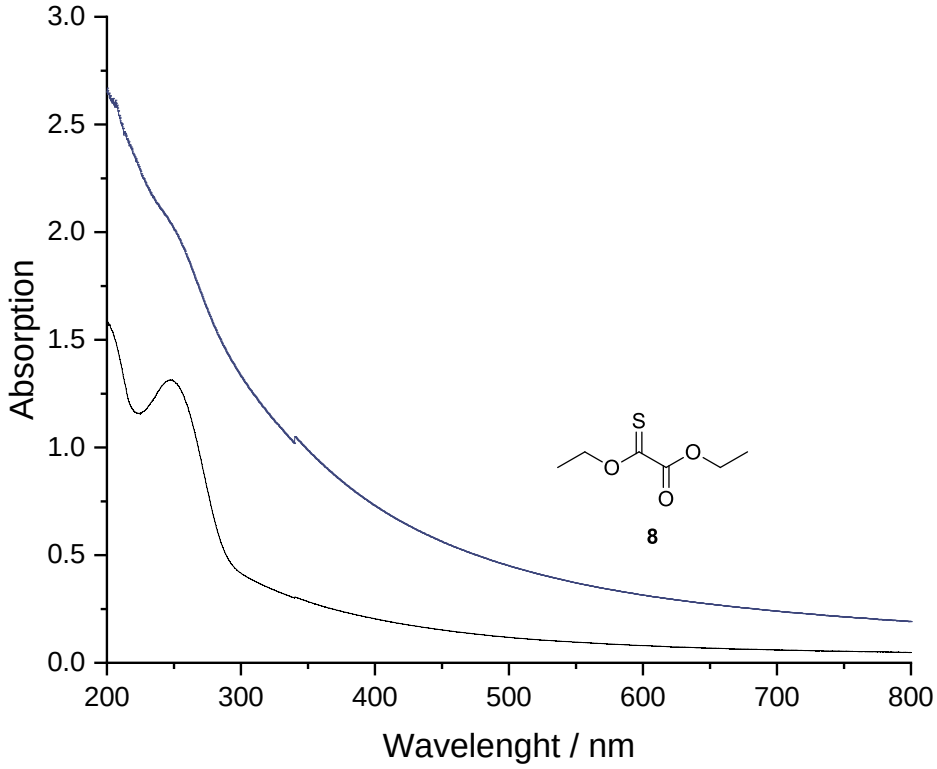

Fig. 14. The black trace shows the reference UV spectrum of **8** in solid Ar at 3 K and the blue trace the UV spectrum of the pyrolysis mixture. At around 340 nm a small bulge arises due to the lamp exchange.

Matrix Isolation IR Spectra

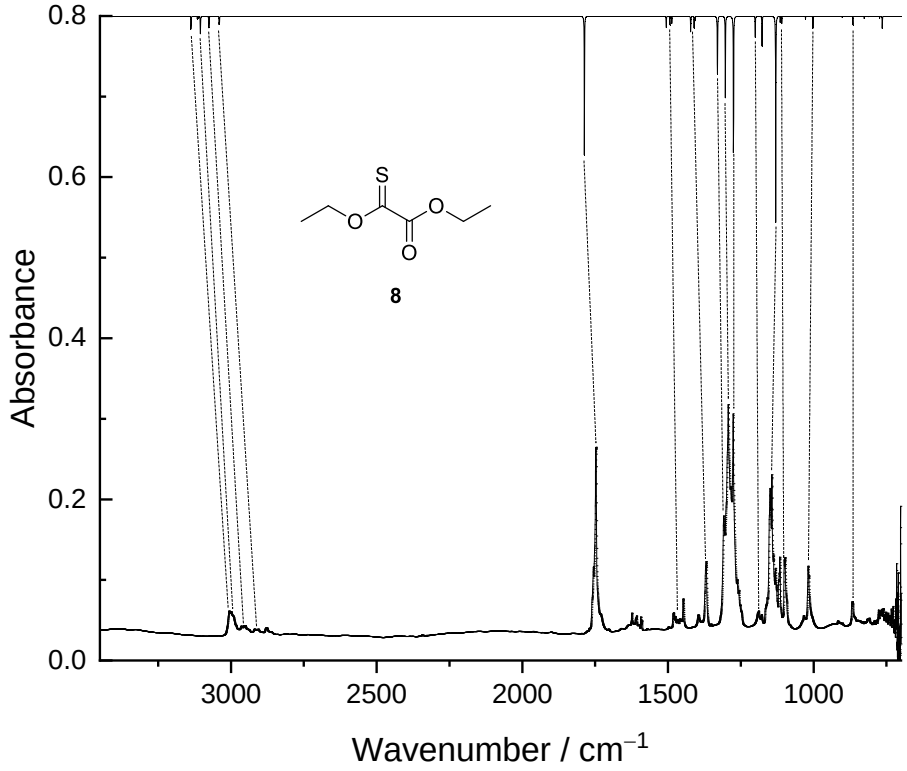

Fig. 15. Computed spectrum of **8** at the B3LYP/6-311++G(3df,3pd) level of theory compared to the IR spectrum of matrix isolated **8** in solid argon at 3 K.

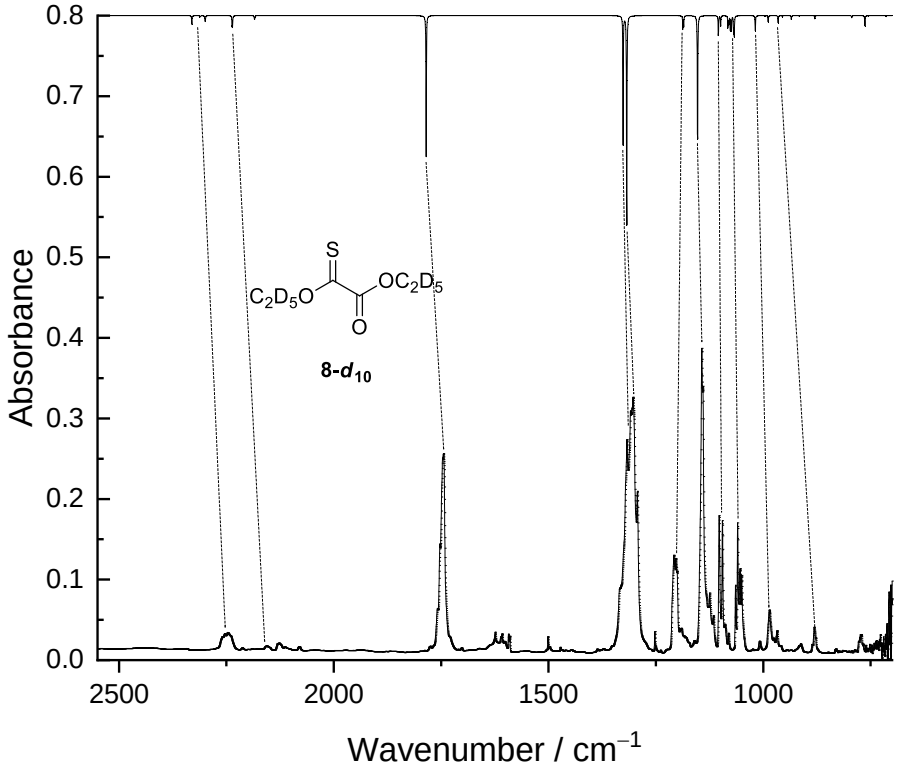

Fig. 16. Computed spectrum of **8-*d*$_{10}$** at the B3LYP/6-311++G(3df,3pd) level of theory compared to the IR spectrum of matrix isolated **8-*d*$_{10}$** in solid argon at 3 K.

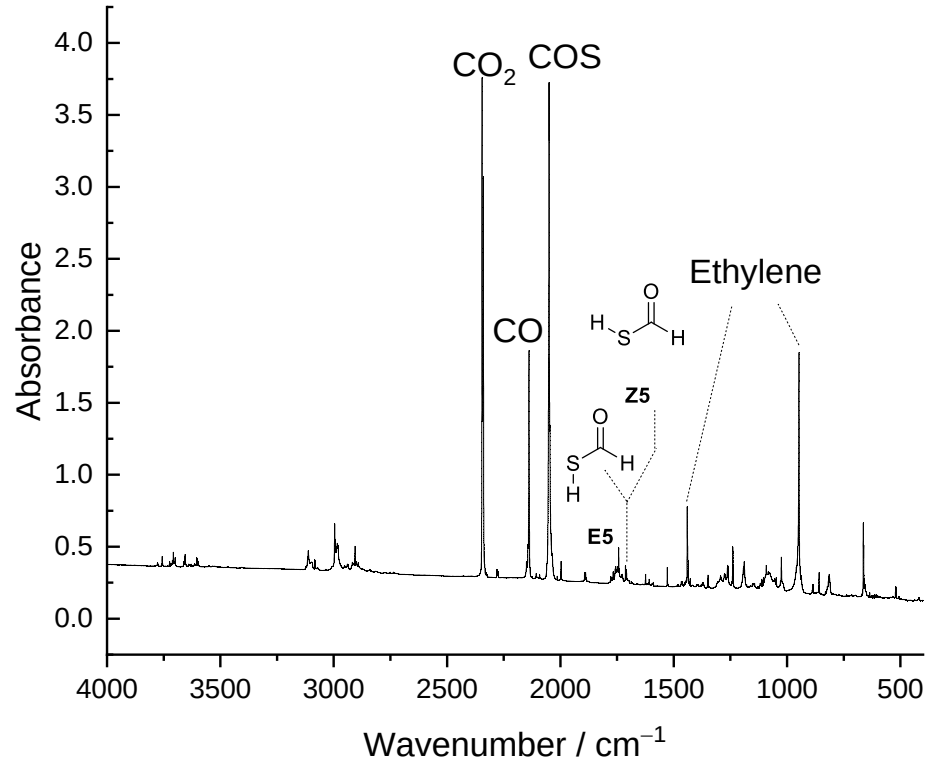

Fig. 17. Matrix isolated fragments of **8** upon HVFP at 900 °C.

We observed several new bands in the carbonyl region upon pyrolysis of **8** (Figure 15). These bands can be assigned to conformers of **9** and **8'** that are hardly distinguishable.

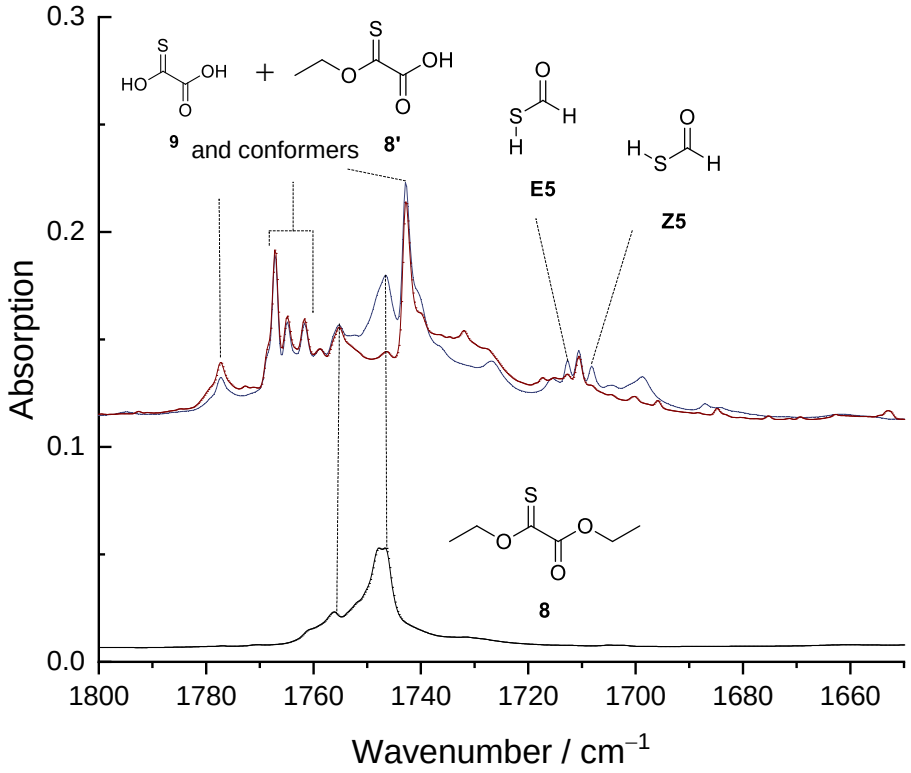

Fig. 18. IR-spectra of the pyrolysis of **8** before (blue) and after irradiation (red) for 20 min with 254 nm compared to the reference spectrum of **8**.

While bands **E5** and **Z5** appear when the matrix is irradiated for 8 min, prolonged irradiation leads to the decomposition of these compounds. The precursor itself decomposes upon irradiation. No distinct photochemistry of the conformers of **8'** and **9** upon irradiation can be found probably due to fast interconversion of the conformers. The compounds oxathiirane **2**, the $H_2O \cdot CS$ complex, **7**, **6**, and **3** have not been observed. We observed tiny amounts of **Z4**.

IR Spectroscopic Data

Table 1. Comparison of experimental vibrational frequencies of **1ct** isolated in an argon matrix at 15 K and computed vibrational frequencies at the CCSD(T)/cc-pVTZ level of theory (unscaled).

Assignment	Sym.	$\tilde{\nu}_{harm.}$ / cm^{-1}	$I_{rel.}$ / km mol^{-1}	$\tilde{\nu}_{exp.}$ / cm^{-1}	$I_{rel.}$
δ(COS)	*a'*	419.1	3.1	n.o.	n.o.
τ(SH)	*a''*	532.8	14.7	n.o.	n.o.
ν(CS)	*a'*	693.6	44.5	n.o.	n.o.
τ(OH)	*a''*	701.8	97.6	n.o.	n.o.
δ(CSH)	*a'*	899.3	97.3	n.o.	n.o.
ν(CO)	*a'*	1245.3	226.1	1211.0	w
δ(COH)	*a'*	1331.4	39.9	n.o.	n.o.
ν(SH)	*a'*	2581.3	15.4	n.o.	n.o.
ν(OH)	*a'*	3788.4	153.3	3577.9	w

rel. experimental intensities (vw = very weak, w = weak, m = middle, s = strong, vs = very strong); n.o. = not observed; o.o.r. = out of range.

Table 2. Comparison of experimental vibrational frequencies of **1ct-*d*$_2$** isolated in an argon matrix at 15 K and computed vibrational frequencies at the CCSD(T)/cc-pVTZ level of theory (unscaled).

Assignment	Sym.	$\tilde{\nu}_{harm.}$ / cm^{-1}	$I_{rel.}$ / km mol^{-1}	$\tilde{\nu}_{exp.}$ / cm^{-1}	$I_{rel.}$
δ(COS)	*a'*	373.0	2.0	n.o.	n.o.
τ(D)	*a''*	419.1	7.0	n.o.	n.o.
τ(OD)	*a''*	519.3	49.3	n.o.	n.o.
ν(CS)	*a'*	639.8	9.6	n.o.	n.o.
δ(CSD)	*a'*	725.7	101.9	n.o.	n.o.
δ(COD)	*a'*	1041.3	19.8	n.o.	n.o.
ν(CO)	*a'*	1241.5	230.0	1227.9	w
ν(SD)	*a'*	1853.4	7.8	n.o.	n.o.
ν(OD)	*a'*	2758.0	89.0	2660.4	w

rel. experimental intensities (vw = very weak, w = weak, m = middle, s = strong, vs = very strong); n.o. = not observed; o.o.r. = out of range.

Table 3. Comparison of experimental vibrational frequencies of **1tt** isolated in an argon matrix at 15 K and computed vibrational frequencies at the CCSD(T)/cc-pVTZ level of theory (unscaled).

Assignment	Sym.	$\tilde{\nu}_{harm.}$ / cm^{-1}	$I_{rel.}$ / km mol^{-1}	$\tilde{\nu}_{exp.}$ / cm^{-1}	$I_{rel.}$
δ(COS)	*a'*	411.9	7.0	n.o.	n.o.
τ(SH)	*a''*	485.3	3.0	n.o.	n.o.
τ(OH)	*a''*	702.2	104.7	n.o.	n.o.
ν(CS)	*a'*	739.4	98.5	n.o.	n.o.
δ(CSH)	*a'*	940.2	78.4	n.o.	n.o.

ν(CO)	*a'*	1248.8	245.0	1225.3	w
δ(COH)	*a'*	1332.1	44.4	n.o.	n.o.
ν(SH)	*a'*	2725.7	0.5	n.o.	n.o.
ν(OH)	*a'*	3803.5	170.1	3633.9	w

rel. experimental intensities (vw = very weak, w = weak, m = middle, s = strong, vs = very strong); n.o. = not observed; o.o.r. = out of range.

Table 4. Comparison of experimental vibrational frequencies of **1tt-*d*$_2$** isolated in an argon matrix at 15 K and computed vibrational frequencies at the CCSD(T)/cc-pVTZ level of theory (unscaled).

Assignment	Sym.	$\tilde{\nu}_{harm.}$ / cm^{-1}	$I_{rel.}$ / km mol^{-1}	$\tilde{\nu}_{exp.}$ / cm^{-1}	$I_{rel.}$
τ(SD)	*a''*	373.0	1.9	n.o.	n.o.
δ(COS)	*a'*	392.1	6.0	n.o.	n.o.
τ(OD)	*a''*	517.5	55.2	n.o.	n.o.
ν(CS)	*a'*	671.1	22.0	n.o.	n.o.
δ(CSD)	*a'*	725.8	110.7	n.o.	n.o.
δ(COD)	*a'*	1046.2	26.0	n.o.	n.o.
ν(CO)	*a'*	1240.3	257.9	1231.6	w
ν(SD)	*a'*	1957.4	0.2	n.o.	n.o.
ν(OD)	*a'*	2769.2	96.9	2662.2	w

rel. experimental intensities (vw = very weak, w = weak, m = middle, s = strong, vs = very strong); n.o. = not observed; o.o.r. = out of range.

Table 5 compares the experimental isotope shift to the computed shifts. The close proximity of a second H atom that is exchanged for D at the SH position might lead to a greater discrepancy between experiment and literature.

Table 5. Experimental isotope shift of the OH/OD stretching band compared to the computational shifts.

	$\Delta\upsilon$(OH/OD)$_{\mathbf{1tt}}$	$\Delta\upsilon$(OH/OD)$_{\mathbf{1ct}}$
experimental	971.7	917.5
computed	1034.3	1030.4

Computed Potential Energy Surface

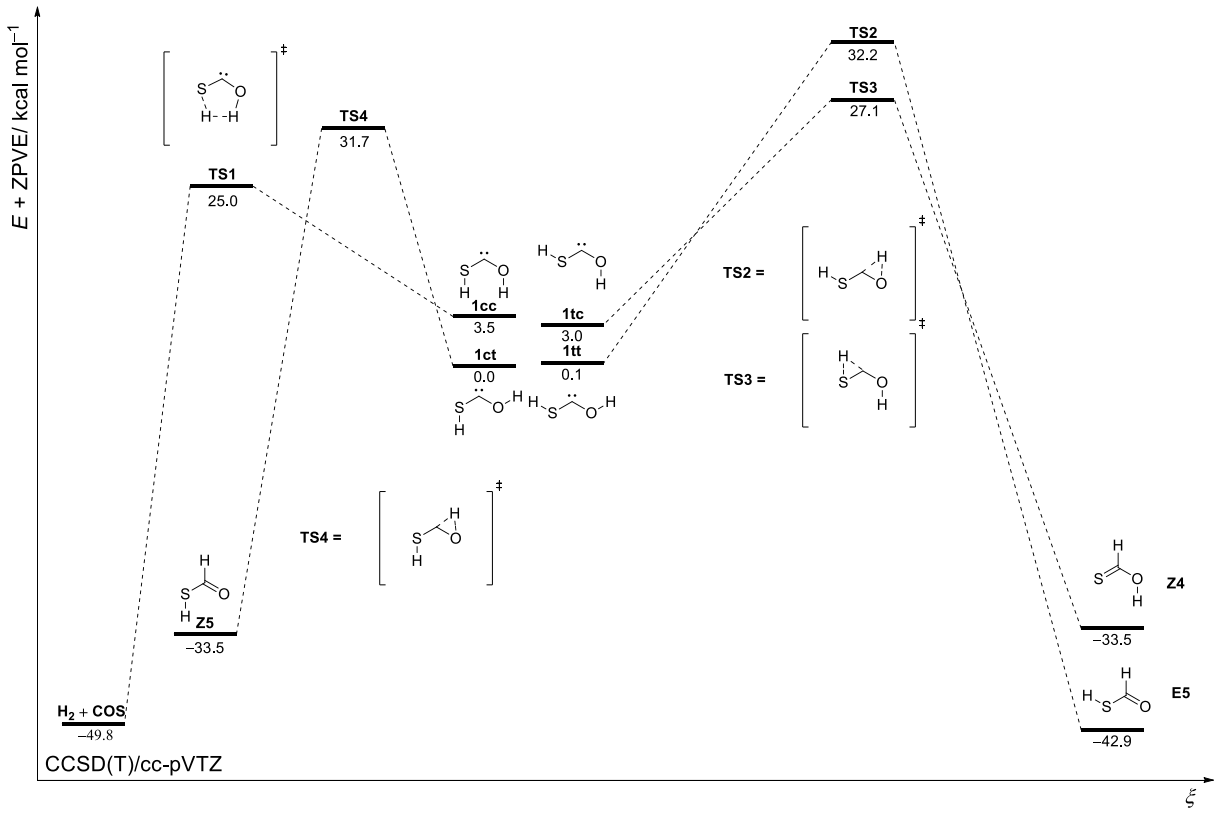

Fig. 19. PES of **1** at the CCSD(T)/cc-pVTZ level of theory.

Table 6. Energies of small fragments of the H_2CSO system on the CCSD(T)/cc-pVTZ level of theory compared to **1ct**.

Fragments	Energy / kcal mol^{-1}
$COS + H_2$	−5.0
$H_2O + CS$	−49.2
$H_2S + CO$	−49.8

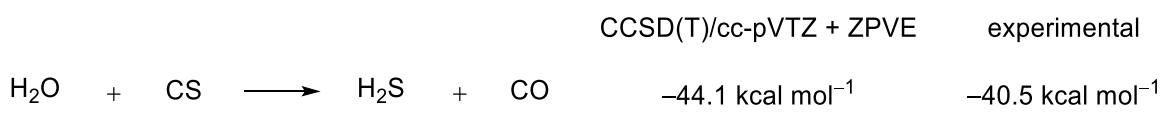

Fig. 20. Isodesmic Reaction energy compared to $\Delta_f H^\circ_{gas}$ taken from the NIST database.[32]

Wiberg Bond Indices

The natural resonance theory (NRT) analysis and the Wiberg bond indices were computed with NBO7 at the B3LYP/6311++G(3df,3pd) level of theory based on geometries at the CCSD(T)/cc-pVTZ level of theory.

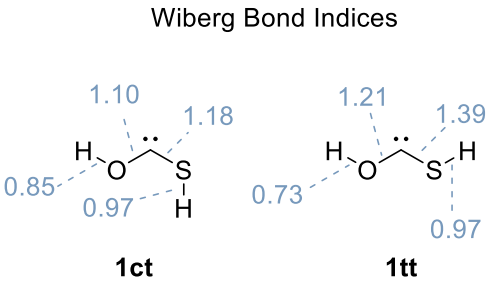

The natural resonance theory (NRT) analysis of **1ct** and **1tt** is depicted in Figure 21.

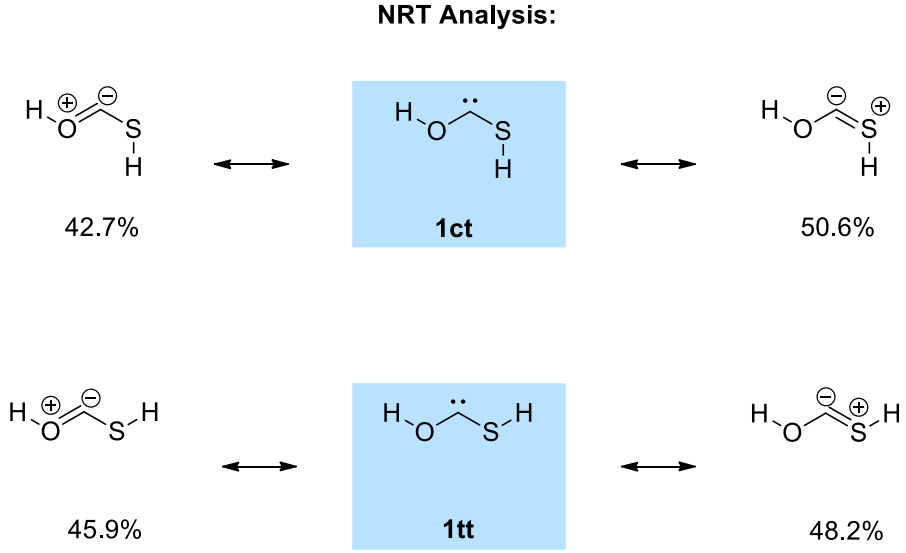

Fig. 21. NRT analysis of **1ct** and **1tt** at the B3LYP/6-311++G(3df,3pd) level of theory with structures optimized at the CCSD(T)/cc-pVTZ level of theory.

In both conformers we found a similar weight of the two resonance structures with the CS double bound structure being more important. This further indicates a stronger stabilization of the carbene due to sulfur compared to oxygen. The carbene structure is typically not found in such analysis. Since both ylidic structures are nearly equally important for both systems, the structure is best described as a carbene.

PES of **1tt**

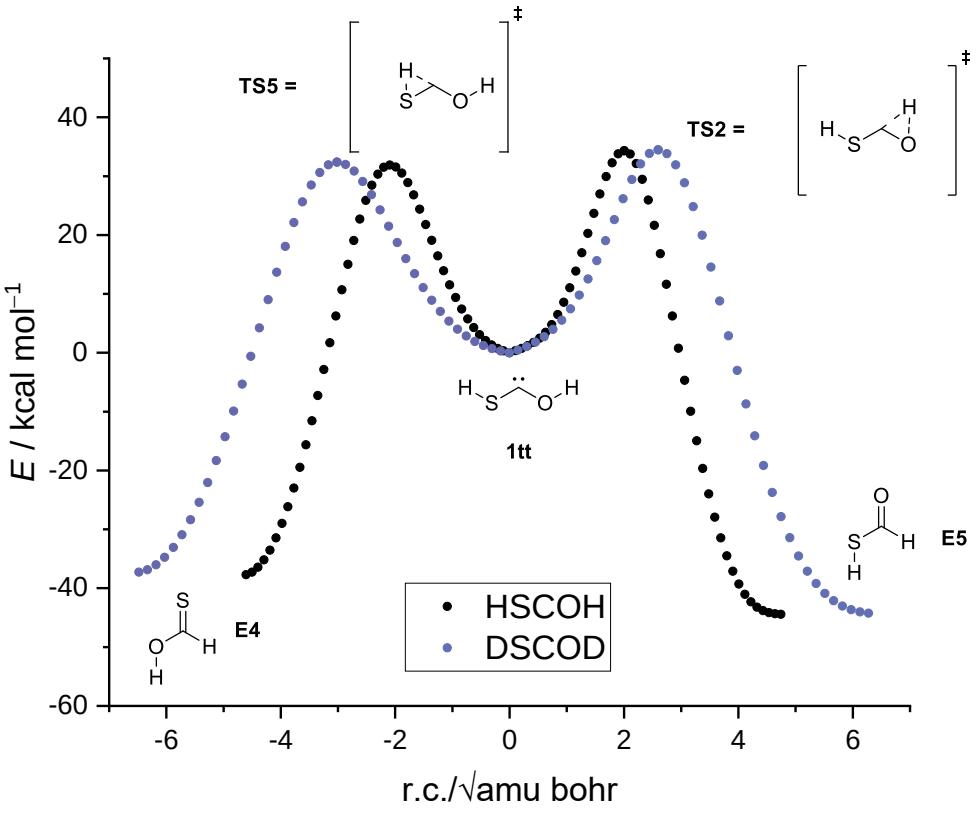

Fig. 22. IRC curves for possible reaction pathways of **1tt** and **1tt-*d*$_2$** computed at the B3LYP/6 311++G(3df,3pd) level of theory.

Tunneling Computations with POLYRATE

Table 7. Computed rate constants in s^{-1} of the reaction of **1tt** to **E4** at the B3LYP/6-311++G(3df,3pd) level of theory.

T / K	TST	CVT	CVT/ZCT	CVT/SCT
4.00	0.00×10^{0}	0.00×10^{0}	0.00×10^{0}	0.00×10^{0}
5.00	0.00×10^{0}	0.00×10^{0}	0.00×10^{0}	0.00×10^{0}
6.00	0.00×10^{0}	0.00×10^{0}	0.00×10^{0}	0.00×10^{0}
8.00	0.00×10^{0}	0.00×10^{0}	0.00×10^{0}	0.00×10^{0}
10.00	0.00×10^{0}	0.00×10^{0}	0.00×10^{0}	0.00×10^{0}
20.00	5.19×10^{-143}	4.79×10^{-143}	2.39×10^{-143}	2.39×10^{-143}
28.00	6.78×10^{-99}	6.41×10^{-99}	3.20×10^{-99}	3.20×10^{-99}
40.00	9.19×10^{-66}	8.84×10^{-66}	4.42×10^{-66}	4.42×10^{-66}
50.00	2.82×10^{-50}	2.73×10^{-50}	1.37×10^{-50}	1.37×10^{-50}
75.00	1.40×10^{-29}	1.37×10^{-29}	6.89×10^{-30}	6.88×10^{-30}
77.36	2.56×10^{-28}	2.51×10^{-28}	1.26×10^{-28}	1.26×10^{-28}
100.00	3.40×10^{-19}	3.34×10^{-19}	1.69×10^{-19}	1.69×10^{-19}
125.00	6.11×10^{-13}	6.03×10^{-13}	3.06×10^{-13}	3.05×10^{-13}
150.00	9.37×10^{-9}	9.27×10^{-9}	4.72×10^{-9}	4.70×10^{-9}
175.00	9.39×10^{-6}	9.31×10^{-6}	4.75×10^{-6}	4.74×10^{-6}
194.70	6.31×10^{-4}	6.26×10^{-4}	3.21×10^{-4}	3.19×10^{-4}
200.00	1.70×10^{-3}	1.69×10^{-3}	8.66×10^{-4}	8.62×10^{-4}
225.00	9.84×10^{-2}	9.77×10^{-2}	5.03×10^{-2}	5.01×10^{-2}
250.00	2.55×10^{0}	2.54×10^{0}	1.31×10^{0}	1.30×10^{0}
273.15	3.07×10^{1}	3.06×10^{1}	1.58×10^{1}	1.58×10^{1}
275.00	3.68×10^{1}	3.66×10^{1}	1.90×10^{1}	1.89×10^{1}
298.15	2.94×10^{2}	2.93×10^{2}	1.52×10^{2}	1.51×10^{2}
300.00	3.43×10^{2}	3.41×10^{2}	1.77×10^{2}	1.76×10^{2}
325.00	2.27×10^{3}	2.26×10^{3}	1.18×10^{3}	1.17×10^{3}
350.00	1.15×10^{4}	1.15×10^{4}	6.02×10^{3}	5.97×10^{3}
373.15	4.27×10^{4}	4.25×10^{4}	2.24×10^{4}	2.23×10^{4}
375.00	4.71×10^{4}	4.69×10^{4}	2.47×10^{4}	2.46×10^{4}
400.00	1.62×10^{5}	1.61×10^{5}	8.55×10^{4}	8.48×10^{4}

Table 8. Computed rate constants in s^{-1} of the reaction of **1tt** to **E5** at the B3LYP/6-311++G(3df,3pd) level of theory.

T / K	TST	CVT	CVT/ZCT	CVT/SCT
4.00	0.00×10^{0}	0.00×10^{0}	0.00×10^{0}	0.00×10^{0}
5.00	0.00×10^{0}	0.00×10^{0}	0.00×10^{0}	0.00×10^{0}
6.00	0.00×10^{0}	0.00×10^{0}	0.00×10^{0}	0.00×10^{0}
8.00	0.00×10^{0}	0.00×10^{0}	0.00×10^{0}	0.00×10^{0}
10.00	0.00×10^{0}	0.00×10^{0}	0.00×10^{0}	0.00×10^{0}
20.00	1.11×10^{-271}	1.09×10^{-271}	5.45×10^{-272}	5.45×10^{-272}
28.00	8.46×10^{-191}	8.35×10^{-191}	4.18×10^{-191}	4.18×10^{-191}
40.00	4.31×10^{-130}	4.27×10^{-130}	2.14×10^{-130}	2.14×10^{-130}
50.00	9.74×10^{-102}	9.66×10^{-102}	4.86×10^{-102}	4.85×10^{-102}
75.00	6.88×10^{-64}	6.84×10^{-64}	3.45×10^{-64}	3.45×10^{-64}

77.36	1.39×10^{-61}	1.39×10^{-61}	7.01×10^{-62}	7.00×10^{-62}
100.00	6.22×10^{-45}	6.20×10^{-45}	3.14×10^{-45}	3.13×10^{-45}
125.00	1.53×10^{-33}	1.53×10^{-33}	7.77×10^{-34}	7.76×10^{-34}
150.00	6.21×10^{-26}	6.19×10^{-26}	3.16×10^{-26}	3.15×10^{-26}
175.00	1.72×10^{-20}	1.72×10^{-20}	8.81×10^{-21}	8.79×10^{-21}
194.70	3.52×10^{-17}	3.51×10^{-17}	1.81×10^{-17}	1.80×10^{-17}
200.00	2.12×10^{-16}	2.12×10^{-16}	1.09×10^{-16}	1.09×10^{-16}
225.00	3.26×10^{-13}	3.26×10^{-13}	1.68×10^{-13}	1.68×10^{-13}
250.00	1.17×10^{-10}	1.17×10^{-10}	6.07×10^{-11}	6.05×10^{-11}
273.15	1.05×10^{-8}	1.05×10^{-8}	5.46×10^{-9}	5.44×10^{-9}
275.00	1.45×10^{-8}	1.45×10^{-8}	7.58×10^{-9}	7.55×10^{-9}
298.15	6.19×10^{-7}	6.18×10^{-7}	3.24×10^{-7}	3.23×10^{-7}
300.00	8.15×10^{-7}	8.14×10^{-7}	4.27×10^{-7}	4.25×10^{-7}
325.00	2.47×10^{-5}	2.47×10^{-5}	1.30×10^{-5}	1.29×10^{-5}
350.00	4.62×10^{-4}	4.62×10^{-4}	2.45×10^{-4}	2.43×10^{-4}
373.15	4.93×10^{-3}	4.92×10^{-3}	2.62×10^{-3}	2.61×10^{-4}
375.00	5.88×10^{-3}	5.87×10^{-3}	3.13×10^{-3}	3.11×10^{-4}
400.00	5.46×10^{-2}	5.45×10^{-2}	2.92×10^{-2}	2.90×10^{-2}

Table 9. Computed rate constants in s^{-1} of the reaction of **1ct** to **Z5** at the B3LYP/6-311++G(3df,3pd) level of theory.

T / K	TST	CVT	CVT/ZCT	CVT/SCT
4.00	0.00×10^{0}	0.00×10^{0}	0.00×10^{0}	0.00×10^{0}
5.00	0.00×10^{0}	0.00×10^{0}	0.00×10^{0}	0.00×10^{0}
6.00	0.00×10^{0}	0.00×10^{0}	0.00×10^{0}	0.00×10^{0}
8.00	0.00×10^{0}	0.00×10^{0}	0.00×10^{0}	0.00×10^{0}
10.00	0.00×10^{0}	0.00×10^{0}	0.00×10^{0}	0.00×10^{0}
20.00	4.03×10^{-192}	4.02×10^{-192}	2.02×10^{-192}	2.01×10^{-192}
28.00	5.62×10^{-134}	5.61×10^{-134}	2.82×10^{-134}	2.82×10^{-134}
40.00	2.53×10^{-90}	2.53×10^{-90}	1.27×10^{-90}	1.27×10^{-90}
50.00	6.30×10^{-70}	6.29×10^{-70}	3.17×10^{-70}	3.16×10^{-70}
75.00	1.09×10^{-42}	1.08×10^{-42}	5.48×10^{-43}	5.47×10^{-43}
77.36	4.97×10^{-41}	4.97×10^{-41}	2.51×10^{-41}	2.51×10^{-41}
100.00	4.82×10^{-29}	4.82×10^{-29}	2.44×10^{-29}	2.44×10^{-29}
125.00	7.72×10^{-21}	7.71×10^{-21}	3.92×10^{-21}	3.92×10^{-21}
150.00	2.33×10^{-15}	2.33×10^{-15}	1.19×10^{-15}	1.19×10^{-15}
175.00	1.94×10^{-11}	1.94×10^{-11}	9.96×10^{-12}	9.95×10^{-12}
194.70	4.72×10^{-9}	4.72×10^{-9}	2.43×10^{-9}	2.42×10^{-9}
200.00	1.72×10^{-8}	1.72×10^{-8}	8.86×10^{-9}	8.85×10^{-9}
225.00	3.41×10^{-6}	3.41×10^{-6}	1.77×10^{-6}	1.76×10^{-6}
250.00	2.37×10^{-4}	2.37×10^{-4}	1.23×10^{-4}	1.23×10^{-4}
273.15	6.07×10^{-3}	6.07×10^{-3}	3.17×10^{-3}	3.16×10^{-3}
275.00	7.68×10^{-3}	7.68×10^{-3}	4.01×10^{-3}	4.00×10^{-3}
298.15	1.15×10^{-1}	1.15×10^{-1}	6.03×10^{-2}	6.01×10^{-2}
300.00	1.40×10^{-1}	1.40×10^{-1}	7.35×10^{-2}	7.33×10^{-2}
325.00	1.64×10^{0}	1.64×10^{0}	8.66×10^{-1}	8.64×10^{-1}
350.00	1.36×10^{1}	1.36×10^{1}	7.22×10^{0}	7.19×10^{0}
373.15	7.51×10^{1}	7.51×10^{1}	4.00×10^{1}	3.99×10^{1}
375.00	8.54×10^{1}	8.54×10^{1}	4.55×10^{1}	4.53×10^{1}

400.00	4.27×10^2	4.27×10^2	2.29×10^2	2.28×10^2

Cartesian Coordinates of Computed Structures

In this section the electronic and zero-point vibrational energies (ZPVEs) are provided for each structure. For transition states, the imaginary frequency is given additionally; all other structures display only real frequencies. For the full coordinates please see the published supporting information:

https://pubs.acs.org/doi/abs/10.1021/acs.jpclett.2c00344

Table 10. Electronic and zero-point vibrational energies (ZPVEs) at the CCSD(T)/cc-pVTZ level of theory.

Structure	**E / au**	**ZPVE / kcal mol^{-1}**	**ν_i /i cm^{-1}**
1ct	−512.020313713959695	17.4308	
1tt	−512.020655956711153	17.7110	
1tc	−512.015188195778933	17.2288	
1cc	−512.014010186277460	16.9471	
^{3}1	−511.959531554498085	16.1418	
E4	−512.079567495039555	19.6616	
Z5	−512.090025648339633	17.5282	
E5	−512.088387776539321	17.4536	
TS1	−511.973553562476070	13.1141	1836.7767
TS2	−511.963259392573946	13.8158	2084.1781
TS3	−511.966798818802033	14.4457	1740.4392
TS4	−511.963819056292891	13.7017	2062.9640
TS_1tt_to_1ct	−511.994688938890761	16.6131	503.1489
COS	−510.918785451803160	5.7182	
H_2	−1.172336686948533	6.3035	

Full Citations for Electronic Structure Codes

Gaussian 16

Gaussian 16, Revision A.03; Frisch, M. J.; Trucks, G. W.; Schlegel, H. B.; Scuseria, G. E.; Robb, M. A.; Cheeseman, J. R.; Scalmani, G.; Barone, V.; Petersson, G. A.; Nakatsuji, H.; Li, X.; Caricato, M.; Marenich, A. V.; Bloino, J.; Janesko, B. G.; Gomperts, R.; Mennucci, B.; Hratchian, H. P.; Ortiz, J. V.; Izmaylov, A. F.; Sonnenberg, J. L.; Williams-Young, D.; Ding, F.; Lipparini, F.; Egidi, F.; Goings, J.; Peng, B.; Petrone, A.; Henderson, T.; Ranasinghe, D.; Zakrzewski, V. G.; Gao, J.; Rega, N.; Zheng, G.; Liang, W.; Hada, M.; Ehara, M.; Toyota, K.; Fukuda, R.; Hasegawa, J.; Ishida, M.; Nakajima, T.; Honda, Y.; Kitao, O.; Nakai, H.; Vreven, T.; Throssell, K.; Montgomery, J. A., Jr.; Peralta, J. E.; Ogliaro, F.; Bearpark, M. J.; Heyd, J. J.; Brothers, E. N.; Kudin, K. N.; Staroverov, V. N.; Keith, T. A.; Kobayashi, R.; Normand, J.; Raghavachari, K.; Rendell, A. P.; Burant, J. C.; Iyengar, S. S.; Tomasi, J.; Cossi, M.; Millam, J. M.; Klene, M.; Adamo, C.; Cammi, R.; Ochterski, J. W.; Martin, R. L.; Morokuma, K.; Farkas, O.; Foresman, J. B.; Fox, D. J., Gaussian Inc., Wallingford CT **2016**.

Cfour

Coupled-Cluster techniques for Computational Chemistry, a quantum-chemical program package by Stanton, J.F.; Gauss, J.; Harding, M.E.; Szalay, P.G. with contributions from Auer, A.A.; Bartlett, R.J.; Benedikt, U.; Berger, C.; Bernholdt, D.E.; Bomble, Y.J.; Christiansen, O.; Heckert, M.; Heun, O.; Huber, C.; Jagau, T.-C.; Jonsson, D.; Jusélius, J.; Klein, K.; Lauderdale, W.J.; Matthews, D.A.; Metzroth, T.; O'Neill, D.P.; Price, D.R.; Prochnow, E.; Ruud, K.; Schiffmann, F.; Stopkowicz, S.; Tajti, A.; Vázquez, J.; Wang, F.; Watts, J.D. and the integral packages MOLECULE (Almlöf, J. and Taylor, P.R.), PROPS (Taylor, P.R.), ABACUS (Helgaker, T.; Jensen, H.J. Aa.; Jørgensen, P. and Olsen, J.), and ECP routines by Mitin, A. V. and van Wüllen, C. For the current version, see; CFOUR, **2010**.

Polyrate 2017-C

POLYRATE 2017-C; Zheng, J.; Bao, J. L.; Meana-Pañeda, R.; Zhang, S.; Lynch, B. J.; Corchado, J. C.; Chuang, Y.-Y.; Fast, P. L.; Hu, W.-P.; Liu, Y.-P.; Lynch, G. C.; Nguyen, K. A.; Jackels, C. F.; Ramos, A. F.; Ellingson, B. A.; Melissas, V. S.; Vill, J.; Rossi, I.; Coitio, E. L.; Pu, J.; Albu, T. V.; Steckler, R.; Garrett, B. C.; Isaacson, A. D.; Truhlar, D. G., **2017**.

CYLview

CYLview, 1.0b; Legault, C. Y., Université de Sherbrooke, **2009** (http://www.cylview.org).

NBO7

Glendening, E. D.; Badenhoop, J, K.; Reed, A. E.; Carpenter, J. E.; Bohmann, J. A.; Morales, C. M.; Karafiloglou, P.; Landis, C. R.; Weinhold, F. NBO 7.0, **2018**, Theoretical Chemistry Institute, University of Wisconsin, Madison.

1.4. References

[1] R. M. Lemmon, *Chem. Rev.* **1969**, *70*, 95.

[2] B. L. Predmore, D. J. Lefer, G. Gojon, *Antioxid. Redox Sign.* **2012**, *17(1)*, 119.

[3] R. Kaiser, C. Ochsenfeld, M. Head-Gordon, Y. Lee, *Science* **1998**, *279(5354)*, 1181.

[4] L. Leman, L. Orgel, M. R. Ghadiri, *Science* **2004**, *306(5694)*, 283.

[5] R. Lohrmann, L. Orgel, *Science* **1968**, *161(3836)*, 64.

[6] L. M. Woodney, M. F. A'Hearn, J. McMullin, N. Samarasinha, *Earth Moon Planets* **1997**, *78(1-3)*, 69.

[7] D. Despois, *Earth Moon Planets 1997*, *79(1)*, 103.

[8] Y. Minh, W. M. Irvine, M. Brewer, *Astron. Astrophys.* **1991**, *244*, 181.

[9] N. Marcelino, J. Cernicharo, E. Roueff, M. Gerin, R. Mauersberger, *Astrophys. J.* **2005**, *620(1)*, 308.

[10] P. R. Schreiner, H. P. Reisenauer, J. Romanski, G. A. Mloston, *Angew. Chem. Int. Ed.* **2009**, *121*, 8277.

[11] P. R. Schreiner, H. P. Reisenauer, J. Romanski, G. A. Mloston, *J. Am. Chem. Soc.* **2010**, *132*, 7240.

[12] D. Lahem, R. Flammang, M. T. Nguyen, *Chem. Phys. Lett.* **1997**, *270(1-2)*, 93.

[13] P. R. Schreiner, *Trends Chem.* **2020**, *2(11)*, 980.

[14] P. R. Schreiner, *J. Am. Chem. Soc.* **2017**, *139*, 15276.

[15] J. Sarka, A. G. Császár, P. R. Schreiner, *Collect. Czech. Chem. Commun.* **2011**, *76(6)*, 645.

[16] S. Doddipatla, C. He, R. I. Kaiser, Y. Luo, R. Sun, G. R. Galimova, A. M. Mebel, T. J. Millar, *PNAS* **2020**, *117(37)*, 22712.

[17] E. E. Gard, M. J. Kleeman, D. S. Gross, L. S. Hughes, J. O. Allen, B. D. Morrical, D. P. Fergenson, T. Dienes, M. E. Gälli, R. Johnson, *Science* **1998**, *279(5354)*, 1184.

[18] P. R. Schreiner, H. P. Reisenauer, *Angew. Chem. Int. Ed.* **2008**, *120(37)*, 7179.

[19] A. K. Eckhardt, P. R. Schreiner, *Angew. Chem. Int. Ed.* **2018**, *57(19)*, 5248.

[20] D. Becke, *J. Chem. Phys.* **1988**, *88*, 1053.

[21] C. Lee, W. Yang, R. G. Parr, *Phys. Rev. B* **1988**, *37*, 785.

[22] A. D. McLean, G. S. Chandler, *J. Chem. Phys.* **1980**, *72*, 5639.

[23] R. Krishnan, J. S. Binkley, R. Seeger, J. A. Pople, *J. Chem. Phys.* **1980**, *72*, 650.

[24] J. Zheng, J. L. Bao, R. Meana-Pañeda, S. Zhang, B. J. Lynch, J. C. Corchado, Y.-Y. Chuang, P. L. Fast, W.-P. Hu, Y.-P. Liu, G. C. Lynch, K. A. Nguyen, C. F. Jackels, A. F. Ramos, B. A. Ellingson, V. S. Melissas, J. Villà, I. Rossi, E. L. Coitiño, J. Pu, T. V. Albu, A. Ratkiewicz, R. Steckler, B. C. Garrett, A. D. Isaacson, D. G. Truhlar, Polyrate-version 2017-C, University of Minnesota, Minneapolis, MN, **2017**.

[25] G. D. Purvis III, R. J. Bartlett, *J. Chem. Phys.* **1982**, *76*, 1910.

[26] K. Raghavachari, G. W. Trucks, J. A. Pople, M. Head-Gordon, *Chem. Phys. Lett.* **1989**, *157*, 479.

[27] D. E. Woon, T. H. Dunning Jr., *J. Chem. Phys.* **1995**, *103*, 4572.

[28] T. H. Dunning Jr., *J. Chem. Phys.* **1989**, *90*, 1007.

[29] K. A. Peterson, D. E. Woon, T. H. Dunning Jr., *J. Chem. Phys.* **1994**, *100*, 7410.

[31] R. A. Kendall, T. H. Dunning Jr., R. J. Harrison, *J. Chem. Phys.* **1992**, *96*, 6796.

[32] D. D. Wagman, J. D. Cox, V. A. Medvedev, CODATA Key Values for Thermodynamics, Hemisphere Publishing Corp., New York, **1984**.

Chapter 2: Reversible CO_2 Activation *via* Heavy-Atom Quantum Tunneling

Reprinted with permission from B. Bernhardt, M. Schauermann, E. Solel, A. K. Eckhardt, P. R. Schreiner, *Chem. Sci.* **2023**, *14(1)*, 130–135.

2.1. Introduction

The search for methods to bind CO_2 and use it synthetically as a C1-building block under mild conditions is an ongoing endeavour of great urgency. The formation of heterocyclic carbene-carbon dioxide adducts occurs rapidly when the carbene is generated in solution in the presence of CO_2. Here we demonstrate the reversible formation of a complex of the hitherto unreported aminomercaptocarbene ($H_2N–\ddot{C}–SH$) with CO_2 isolated in solid argon by photolysis of 2-amino-2-thioxoacetic acid. Remarkably, the complex disappears in the dark as deduced by time-dependent matrix infrared measurements, and equilibrates back to the covalently bound starting material. This thermodynamically excluded process below 8 K is made possible through heavy-atom quantum mechanical tunnelling, as also evident from density functional theory and ab initio computations at the CCSD(T)/cc-pVTZ level of theory. Our results provide insight into CO_2 activation using a carbene and emphasize the role of quantum mechanical tunnelling in organic processes, even involving heavy atoms.

Incorporating CO_2 in industrial synthesis for basic chemicals, drugs, or fuels is a key goal in sustainable chemistry[1,2] and much effort has been made to develop CO_2 activating systems: Besides frustrated Lewis pairs[3], ionic liquids[4], superbases[5], poly-oxometallates[6], and phosphorus ylides[7], *N*-heterocyclic carbenes (NHCs) can be used to activate CO_2[8,9]. Such carbenes form carboxylates that can be further used for synthetic applications, *e.g.*, for carbene catalyzed carba-, sulfa-, and phospha-Michael additions[10] or as catalysts for other carbene-promoted CO_2 fixation reactions[11-16], *e.g.*, as organic carbonates[17]. Azolium carboxylates are remarkably stable[18], because intramolecular neutralization even through transfer of the R^3-group does not occur (Fig. 1)[19]. The zwitterionic structure, however, also implies that charge separation has to occur in the attack of the carbene on the highly unreactive carbon of CO_2. NHC-carboxylates can be used as carbene-precursors when CO_2 is thermally extruded *in situ*. Some decarboxylation reactions can be achieved photochemically, *e.g.*, acetic acid extrudes CO_2 when irradiated with UV light.[20] Photodecarboxylation has also been used for synthetic applications.[21] The photolysis of thiazol-2-carboxylic acid and imidazole-2-carboxylic acid results in the formation of carbene-CO_2 complexes, but the reverse reaction has not been reported.[22,23] For various C(sp^3) carboxylates $^{13}CO_2$ exchange in solution was reported recently and carbon nucleophiles and enolates were postulated as intermediates.[24] Our results suggest the presence of carbene-CO_2 complexes in such reactions.

Here we present the preparation and reaction of a novel carbene, namely aminomercaptomethylene (**1**, $H_2N–\ddot{C}–SH$) in its complex with CO_2 (**1**-CO_2) that reacts back to

2-amino-2-thioxoacetic acid (**2**) under cryogenic conditions (Fig. 1). The concomitant transfer of a proton onto the CO_2 moiety leads to a neutral system instead of a zwitterion as in case of the azolium carboxylates, and this process is associated with a very low barrier. Additionally, we demonstrate that the association reaction is accelerated through heavy-atom quantum mechanical tunneling (QMT) that opens new possibilities for affecting the reactions of CO_2 with carbenes or other nucleophiles. In this context we demonstrate the first evidence for **1**, the parent structure of nature's thiazol-2-ylidene active site in, *e.g.*, thiamine (vitamin B1) and pyruvate decarboxylase[25], in its complex with CO_2. Coincidently, **1**-CO_2 resembles a rare example of a spectroscopically characterized member of the family of mercaptocarbenes (R–C̈–SH) of which hydroxymercaptomethylene was the first spectroscopically identified member.[26] Spectrometric evidence has been reported for parent mercaptomethylene.[27,28]

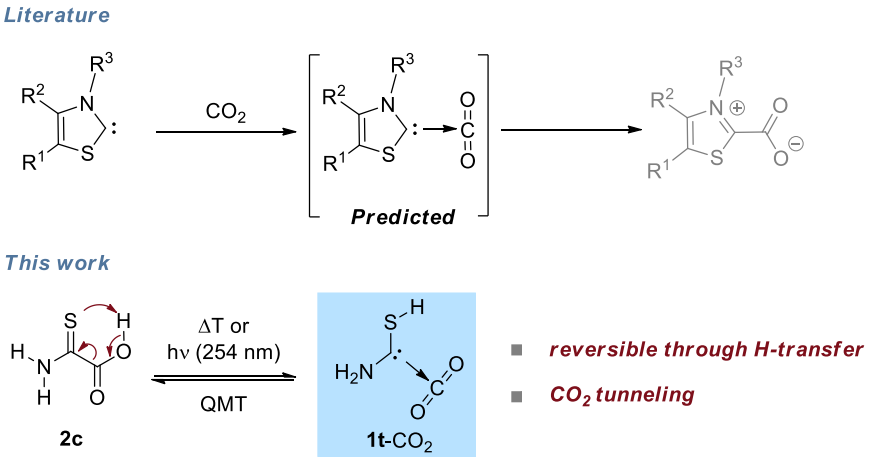

Fig. 1. In solution NHCs add to CO_2 to form carboxylate zwitterions. In this study the model system **2c** photodecarboxylates to give **1t**-CO_2. This *ene*-type reaction is reversible under cryogenic conditions and dominated by QMT below 8 K indicating non-covalent bound complexes as intermediates of the carboxylate formation.

Under cryogenic conditions the contribution of QMT to the overall reaction rate is larger compared to ambient conditions and sometimes completely determines the qualitative outcome of a reaction.[29-31] While proton tunneling is a rather common feature, heavy-atom QMT is encountered less frequently.[32-35] However, sometimes even larger groups are transferred as in the case of trifluoroacetyl nitrene, which reacts to trifluoromethyl isocyanate by transferring the CF_3-group in a formal [1,2]-shift *via* QMT.[36]

High-vacuum flash pyrolysis (HVFP) of α-keto carboxylic acids gives rise to the corresponding hydroxycarbenes that have been investigated *via* matrix isolation spectroscopy.[31,37-43] Besides their intriguing QMT behavior, some hydroxycarbenes add to carbonyls in nearly barrierless

carbonyl-ene reactions.[44] The reaction **1t**-CO_2 → **2c** (Fig. 1) resembles another example of this reaction type. In analogy to these studies, we used **2** as the precursor for the generation of **1** complexed with CO_2.

2.2. Results and Discussion

We synthesized **2** *via* saponification of commercially available ethyl thiooxamate (see the experimental part for details). After deposition of **2** on a CsI window at 3 K together with a large excess of Ar, we exclusively observe its most stable *anti-(E)*-conformer **2c** (Fig. 2). The *anti-(Z)*-conformer **2t** is 4.3 kcal mol^{-1} higher in energy (CCSD(T)/cc-pVTZ) and, hence, not populated at 3 K. To isolate free aminomercaptomethylene **1** we performed multiple HVFP experiments exposing **2** to pyrolysis temperatures ranging from 300 up to 1150 °C. However, we could not detect even traces of **1** and only observed CO_2 and thioformamide together with small amounts of its thiolimine tautomer[45] as the pyrolysis products. This result is not completely unexpected as the corresponding carbonyl species (here a thioamide) has been the main pyrolysis product in all our previous studies on the matrix isolation of hydroxycarbenes, which followed similar strategies.[29] Furthermore, the computed Gibbs free potential energy hypersurface (PES) of the pyrolysis explains the absence of **1** in such experiments (*cf.* Supplementary Materials). Fortunately, we were able to isolate the desired carbene **1** complexed with CO_2 photochemically as outlined in the following.

Upon UV irradiation there are several conceivable reaction paths of **2c**. Photoinduced rotamerizations of carboxylic acids[46-50] and isomerizations of thioamides to thiolimines[51-62] are well known under cryogenic conditions. As **2c** contains both of these functionalities, many photoproducts can be envisaged, *e.g.*, the higher lying conformer **2t** and 16 conformationally distinct thiolimines, which are 11.4 to 34.4 kcal mol^{-1} higher in energy than **2c** (B3LYP/6-311++G(3df,3pd), see the Supplementary Materials for an energetic ranking and experimental data of the rotamerization and tautomerization of **2**). Furthermore, we observed the formation of a complex of *trans*-**1** and CO_2 (**1t**-CO_2) evidenced by a characteristic matrix infrared (IR) band with maxima at 2336.1, 2333.2, and 2330.4 cm^{-1} in good agreement with the computed antisymmetric CO_2 stretching vibration at 2356.7 cm^{-1} (B3LYP/6-311++G(3df,3pd), anharmonic) in the complex. Weaker bands at 3444.9 (computed: 3404.6), 1634.8 (1633.0), and 641.8 (625.3) cm^{-1} can be assigned to **1t**-CO_2 as well. These bands reach their maximum intensity after 4 min of irradiation at 254 nm (Fig. 2). The assignment is further supported by comparing experimental and computed shifts of perdeuterated **1t**-CO_2-d_3 (Supplementary Materials).

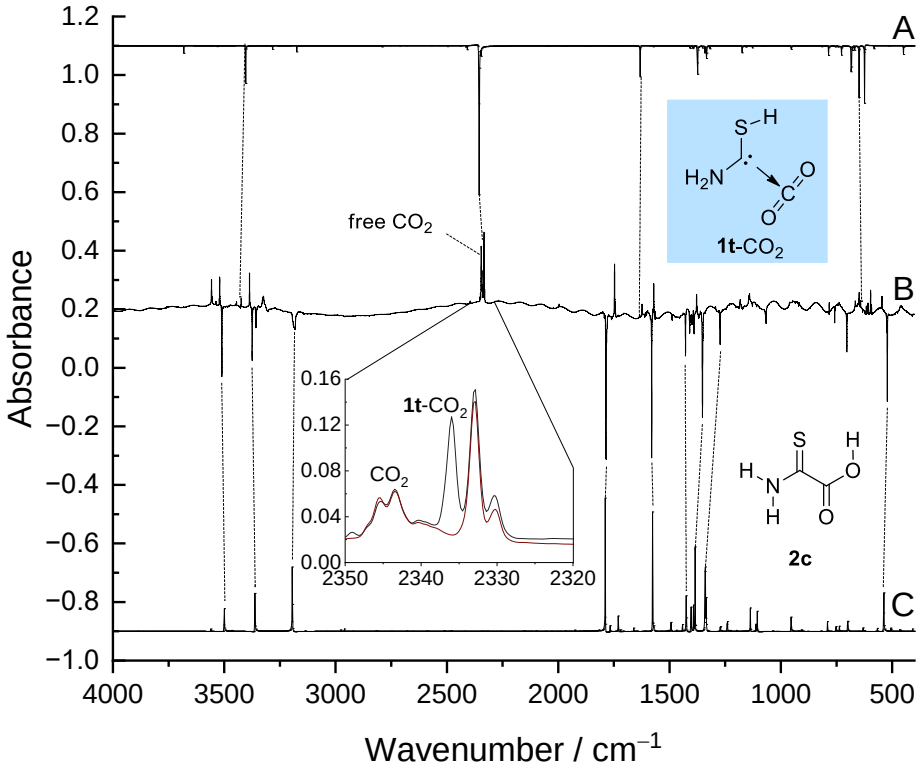

Fig. 2. Experimental matrix-IR difference spectrum (B) of spectra measured before and after 4 min of irradiation at 254 nm compared with the anharmonic spectrum of **1t**-CO_2 (A) and **2c** (C) computed at the B3LYP/6-311++G(3df,3pd) level of theory (anharmonic). Increasing bands not assigned here are discussed in the Supplementary Materials. Inset: Spectra recorded before (black) and after (red) keeping the matrix in the dark for 70 h.

Much to our surprise, once generated, **1t**-CO_2 converts back to **2c** in the dark. The half-life ($t_{1/2}$) of this process depends on the matrix site[63] and can be derived by monitoring the time-dependent band profile of the antisymmetric CO_2 stretching vibration of **1t**-CO_2. The decay of the maximum at 2336.1 cm^{-1} yields $t_{1/2}$ = 26 min (3 K) while the maximum at 2333.2 cm^{-1} yields $t_{1/2}$ = 3.8 d (20 K, no reaction at 3 K). The third maximum (2330.4 cm^{-1}) cannot be reliably evaluated due to its small intensity and long half-life. Distinct matrix sites presumably lead to different distances between the two fragments in **1t**-CO_2, which result in different half-lives. The first value is in excellent agreement with CVT/SCT//B3LYP/6-311+G(d,p) computations yielding $t_{1/2}$ = 55 min at 3 K for the **1t**-CO_2 → **2c** reaction while the second value agrees well with CVT/SCT//B3LYP/6-311++G(3df,3pd) computations ($t_{1/2}$ = 7.6 d). The C–C distance in **1t**-CO_2 is 2.971 Å at the first and 3.005 Å at the latter level of theory. For details on the kinetic analyses see the Supplementary Materials.

Even though the computed barrier of 4.2 kcal mol^{-1} (CCSD(T)/cc-pVTZ) is low, the **1t**-CO_2 → **2c** reaction cannot occur thermally at 3 K, and only QMT explains the experimental

observation. To ensure that there is no activation by the spectrometer's light source we repeated the experiment measuring every 5 min while the matrix was not exposed to the spectrometer globar beam between measurements. We also prepared perdeuterated **1t**-CO_2-d_3 whose half-life extends to $t_{1/2}$ = 36 min (3 K) in the first and $t_{1/2}$ = 5.1 d (20 K) in the second matrix site (see the Supplementary Materials for details). This is in good agreement with CVT/SCT//B3LYP/6-311++G(3df,3pd) computations ($t_{1/2}$ = 259 min at 3 K, second matrix site: 7.6 d at 20 K). This effect is small (KIE = 1.4 at 3 K, computed: 4.7 at 3 K) owing to the minute movements of the H/D atoms in the QMT process (*vide infra*). Additionally, we performed kinetic measurements at temperatures between 3 K and 12 K to solidify the QMT mechanism of the reaction **1t**-CO_2 (2336.1 cm^{-1}) → **2c** (Fig. 3). Note that at 20 K we could not detect **1t**-CO_2 in this matrix site presumably due to its very fast reaction ($t_{1/2}$ < 1 min). The logarithmic rate *vs.* inverse temperature plots (Arrhenius plots) of theory and experiment in Fig. 3 agree well with the regions of Arrhenius and non-Arrhenius behavior, underlining our QMT hypothesis. We conclude that at temperatures below 8 K QMT dominates this reaction entirely. Above 20 K the rate grows exponentially since the barrier of 4.2 kcal mol^{-1} (CCSD(T)/cc-pVTZ) can be overcome thermally. This system allows for measuring of the kinetics up to temperatures that are in the transition range between the QMT-dominated and the thermally-dominated regions.

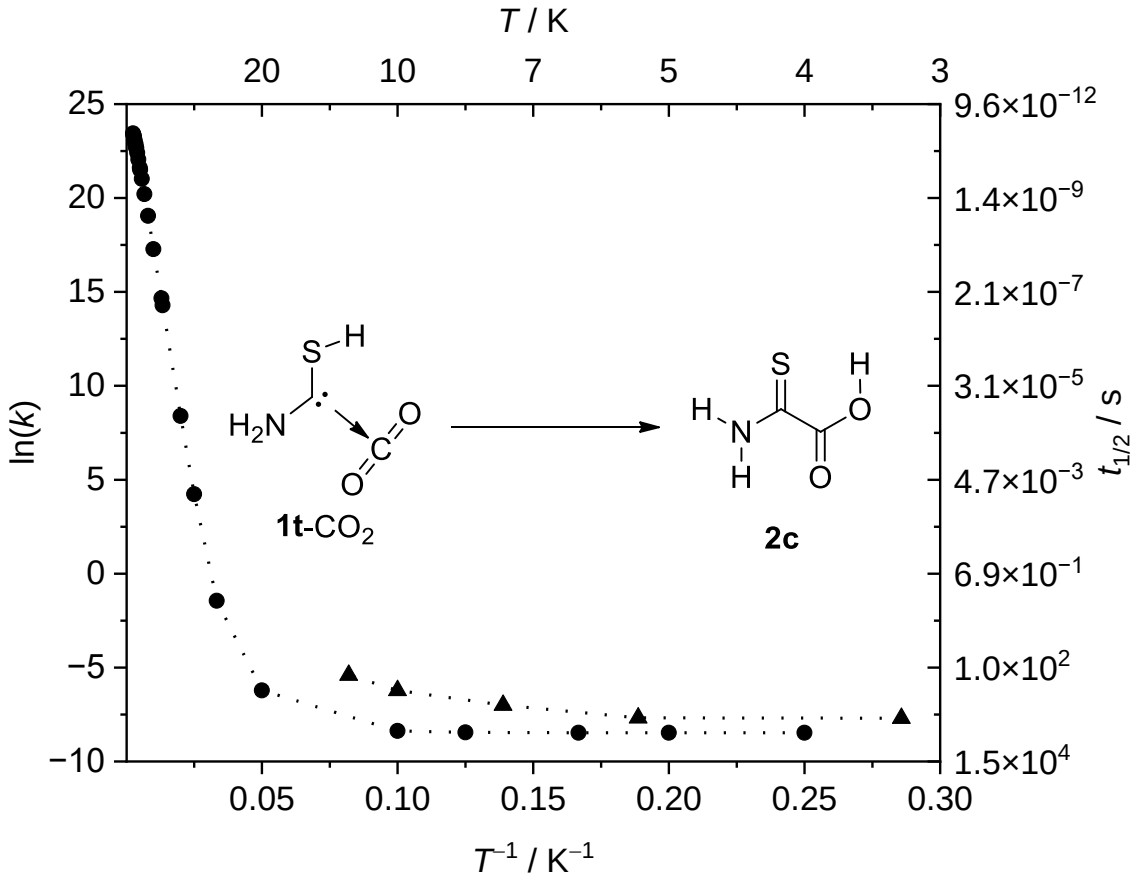

Fig. 3. Arrhenius plot of the experimental rate constants (k) of the reaction of **1t**-CO_2 (2336.1 cm^{-1}) to **2c** at different temperatures (T; triangles) compared to computed rates (CVT/SCT//B3LYP/6-311+G(d,p); circles). Above 20 K the classic thermal reactivity dominates this reaction (linear curve). Below 8 K (constant values) this reaction can only occur *via* QMT.

Our result can be rationalized comparing the geometry of **1t**-CO_2 with that of **TS_CO2** (point B; Fig. 4). In **TS_CO2** the S–H bond does not elongate; the distance the hydrogen atom moves is the result of the H–S–C angle decreasing. Instead, the main movement in **TS_CO2** is the two carbon atoms approaching each other by about 0.7 Å. Two hydrogen bonds form between the thiol- and the amino-group facilitating the bonding and activation of CO_2. Upon C–C-bond formation the curve flattens and reaches point C (Fig. 4B) corresponding to a zwitterionic structure similar to the carboxylate products in reactions of NHCs with CO_2 (*cf.* Fig. 1). However, point C is not a minimum on the PES (υ_i = 164.5 cm^{-1}, B3LYP/6-311++G(3df,3pd)) and a hydrogen shift immediately occurs yielding an uncharged species. The potential of this hydrogen transfer is steep and this step does not contribute to the observable kinetics of the reaction. Hence, the measured kinetics (Fig. 3) are due to the two fragments **1** and CO_2 approaching each other and not the subsequent hydrogen transfer. Therefore, below 8 K the reaction mechanism can be best described as heavy-atom QMT.

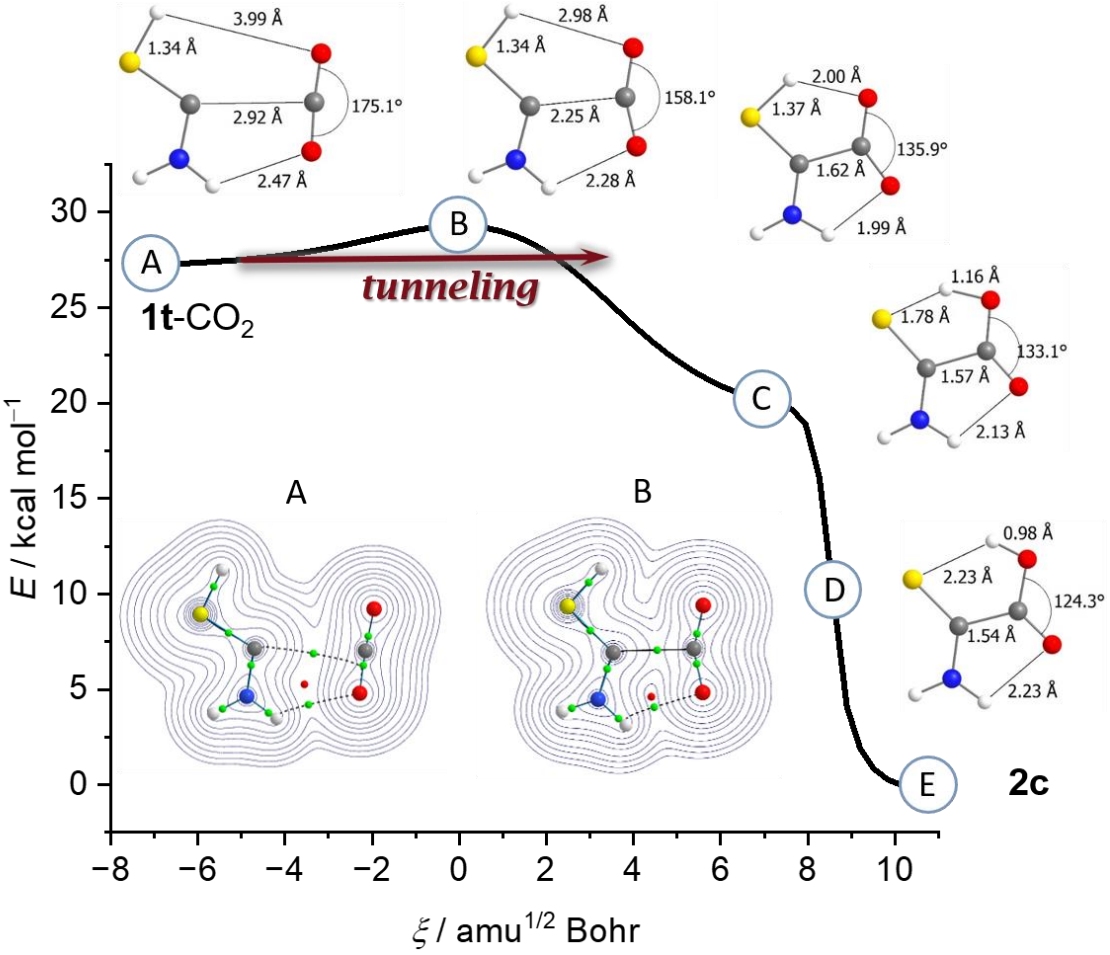

Fig. 4. Potential Energy Hypersurface. Bond critical points (green) and a ring critical point (red) in **1t**-CO_2 indicate bonding interactions between the carbon atoms and between oxygen and the amino group. This is also visualized by the Laplacian. When reaching the transition state B the RCP shifts towards the N-H-O hydrogen bond showing this bond to be particular important for the activation of CO_2. Along the PES of the reaction **1t**-CO_2 → **2c** the zwitterion is located on a flat shoulder (snapshot C), which is, however, not a minimum. Once the C–C-bond is formed the hydrogen shift occurs without further activation. The IRC curve was computed at the B3LYP/6-311++G(3df,3pd) level of theory.

Carbene **1** possesses a singlet ground state and the vertical (adiabatic) singlet/triplet energy gap amounts to 110.3 (41.4) kcal mol^{-1} at the CCSD(T)/cc-pVTZ level of theory. In **1t**-CO_2 these values are 61.8 (57.2) kcal mol^{-1} (B3LYP/6-311++G(3df,3pd). Complex **1t**-CO_2 is stabilized by 4.2 kcal mol^{-1} (CCSD(T)/cc-pVTZ) compared to the free fragments. Bond critical point analysis (Fig. 4B) of **1t**-CO_2 suggests hydrogen bonding interactions (green) between the amino group and CO_2 as well as an onset of interactions between the carbon atoms, even at a distance of nearly 3 Å. This leads to a circular arrangement of bonding interactions indicated by a ring

critical point (red). The attractive interaction can be interpreted by electron donation from the carbene lone pair to the π^*-CO_2 orbital (Fig. 4A).

Complexes of carbenes with CO_2 might represent transient intermediates in carbene mediated CO_2 activation in general. We theoretically found complexes of aminomethylene[64], dihydroxymethylene[38], and aminohydroxymethylene[65] with CO_2 to be minimum structures on their PES. The carbonyl-ene reactions of aminomethylene and dihydroxymethylene are barrierless while the CO_2 addition of aminohydroxymethylene is associated with an activation barrier of 3.9 kcal mol^{-1} (CCSD(T)/cc-pVTZ). However, these complexes have not been observed experimentally since the mentioned carbenes have been generated under HVFP conditions in the gas phase, when entropy precludes their formation.

As noted above, a CO_2 complex of thiazolylidene has been spectroscopically identified earlier, but the back reaction, *i.e.*, CO_2 activation has not been reported. We reproduced these results and also found no evidence for reverse reaction to take place even upon annealing the matrix to 32 K. Note that in thiazolylidene the proton has to be transferred from the NH group (and not from the SH moiety as in **1t**-CO_2). This possibility is in principle also given in **1t**-CO_2 *via* **TS15** (Fig. 5).

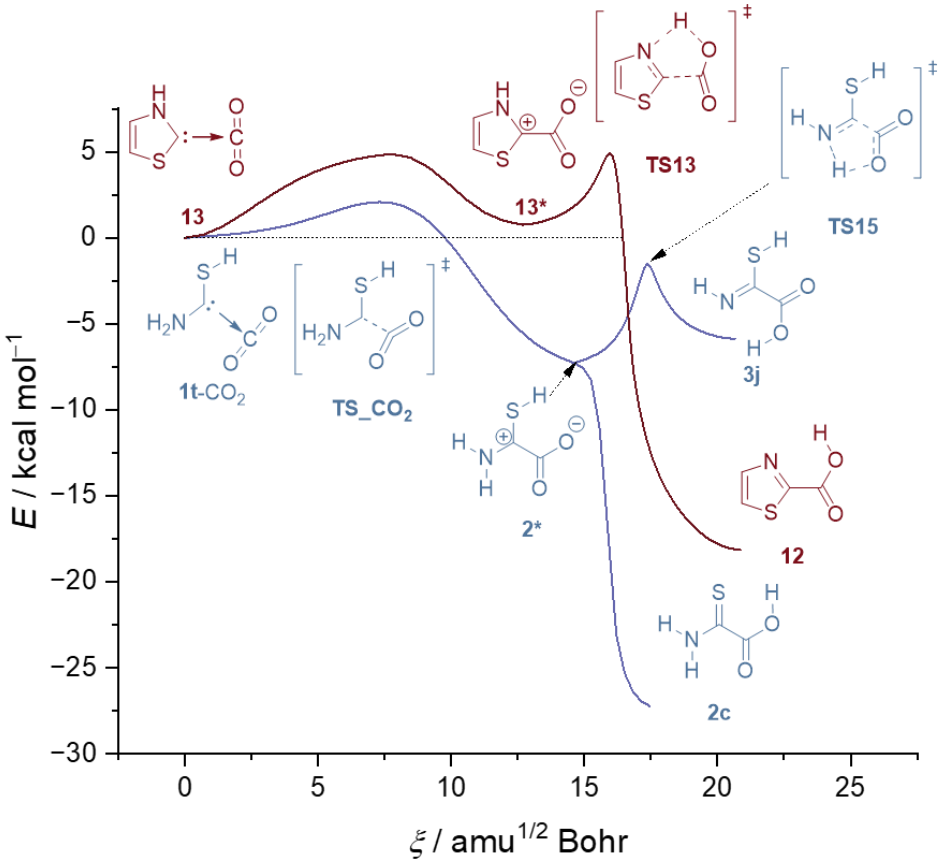

Fig. 5. IRC curves of the H transfer in **1t**-CO_2 from the SH group and the NH_2 group (blue) compared to the reaction profile of **13** (red). All profiles were computed at the B3LYP/6-311++G(3df,3pd) level of theory.

While the H-transfer from SH is barrierless (Fig. 5, blue), in both cases transfers from NH feature a second barrier after the formation of the zwitterion (**2*** and **13***). In the case of thiazolylidene the formation of the zwitterion itself is even endothermic. This leads to a large barrier integral and QMT cannot take place. Accordingly, only for the reaction of **1t**-CO_2 to **2c** tunneling was observed. While NHCs readily react with CO_2 in solution to form stable carboxylates, this is not possible in the gas phase or in inert gas matrices due to the charge separation. In **1t**-CO_2 the thiol group facilitates the formation of a covalent bond by avoiding charge separation through an H shift.

We isolated a complex of aminomercaptomethylene with CO_2 in solid argon by photolysis of 2-amino-2-thioxoacetic acid. The carbene itself is a rare example of spectroscopically examined aminocarbenes as well as mercaptocarbenes. Once generated, the complex reacts back to the precursor in a heavy-atom quantum tunneling process at 3 K. At slightly higher temperatures thermal activation contributes to the overall reaction rate.

2.3. Experimental

Methods

Matrix Isolation Studies

All matrix isolation experiments were performed with a Sumitomo cryostat system consisting of an F-70 compressor unit and an RDK 408D2 closed-cycle refrigerator cold head. For the infrared (IR) measurements polished KBr windows in the vacuum shroud and a CsI window on the sample holder were used. Silicon diodes attached to the sample holder measured the temperature (deposition at 15 K, measurements at 3 K if not stated otherwise). During the experiments, pure 2-amino-2-thioxoacetic acid (**2**) was kept in a storage bulb in the dark and at room temperature (r.t.). The matrix host gas (Ar, gas purity of 99.999%) was stored in a 2 L glass balloon that was refilled and flushed three times with Ar before every experiment. The typical deposition time of our experiments was 1 h in which a total amount of ca. 60 mbar of Ar together with **2** were deposited on both sides of the matrix window. For irradiation a high-pressure mercury lamp (SP200) in conjunction with an MSH 150 monochromator system from LOT-QuantumDesign GmbH was used. The IR spectra were recorded with a Bruker Vertex 70 FTIR spectrometer equipped with a standard KBr or wide-range beam-splitter in a

range from 7000 cm^{-1} to 350 cm^{-1} (resolution: 0.7 cm^{-1}). For every measurement 50 scans were performed. For ultraviolet/visible (UV/Vis) measurements a Jasco V-760 spectrophotometer was used in the range from 190 nm to 800 nm (resolution: 1 nm). Prior to deposition a background spectrum of the cold matrix window was recorded. During deposition the matrix was kept in the dark to avoid unwanted photochemistry.

Computations

All computations at the B3LYP[66,67]/6-311++G(3df,3pd)[68,69] and the MP2[70,71]/def2-QZVPP[72,73] levels of theory using an ultrafine grid and very tight geometry conversion criteria were performed with Gaussian16 Revision B.01 (full citations of electronic structure codes are given at the end of this document). Anharmonic frequencies at the B3LYP/6-311++G(3df,3pd) level of theory were computed using the Freq=Anharmonic keyword. The computed minima on the PES feature no imaginary frequencies while all transition states possess one such frequency. UV/Vis spectra were computed at the TD-B3LYP/6-311++G(3df,3pd) level of theory. Bond and ring critical points were computed using the output=wfn keyword at the B3LYP/6-311+G(3df,3pd) level of theory and visualized with AIMAII studio.

CVT/SCT rate constants were computed with POLYRATE 2017 at B3LYP/6-311+G(d,p).

Natural bond orbitals (NBO), natural resonance theory (NRT), and Wiberg bond indices were computed with NBO7 at the B3LYP/6-311++G(3df,3pd) level of theory based on geometries at the same level.

For coupled-cluster computations (CCSD(T)[74,75]/cc-pVTZ[76-79]) CFOUR 1.0 was used with the following keywords: ABCDTYPE=AOBASIS, CC_PROG=ECC, SCF_CONV=8, and CC_CONV=10; CONVERGENCE=8 in addition for geometry optimizations; VIB=EXACT for analytical computations of harmonic frequencies; METHOD=TS for transition states.

Bond and ring critical points and the Laplacian have been visualized using the AIMAll software package[80] with Bader's quantum theory of atoms in molecules (QTAIM)[81].

Synthesis of the Starting Materials

2-Amino-2-Thioxoacetic Acid (**2**)

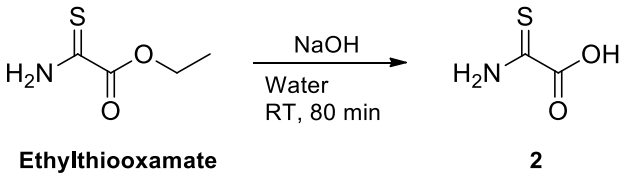

Fig. 6. Synthesis of 2-amino-2-thioxoacetic acid (**2**).

Ethylthiooxamate was obtained from TCI Europe N. V. in > 98% purity and was used without further purification. 0.30 g (2.25 mmol) ethylthiooxamate was dissolved in 20 mL aqueous NaOH (2.8 mol L^{-1}) and stirred for 80 min at r.t. The solution was cooled to 0 °C and concentrated aqueous HCl (12 mol L^{-1}) was added until pH = 3-4 was reached. The solution was extracted four times with 80 mL ethyl acetate in total. The solvent was removed and **2** was obtained as a yellow solid. If necessary, the product was purified by sublimation.

Yield: 74 mg (0.70 mmol, 31%).

^{1}H NMR (400 MHz, DMSO-d_6): δ = 10.2 (s, 1H (NH)), 9.84 (s, 1H (NH)), not visible (broad s, 1H (OH)) ppm.

^{13}C{^{1}H} NMR (101 MHz, DMSO-d_6): δ = 192.4, 164.1 ppm.

IR (ATR): ν = 3406.5, 3289.6, 2722.7, 2410.6, 1720.4, 1593.4, 1444.4, 1406.6, 1240.5, 1183.9, 919.6, 846.5, 752.0, 692.4, 636.6, 589.3, 469.6 cm^{-1}.

HRMS (ESI): *m/z* = 103.9811 $[M-H]^+$ (calcd. *m/z* = 103.9812).

All-Deutero-2-Amino-2-Thioxoacetic Acid (**2**-d_3**)**

176 mg **2** was dissolved in 20 mL D_2O (99.9%) purchased from Deutero GmbH. After 14 days the solvent was removed and the product was obtained as a yellow solid. If necessary, the product was purified by sublimation.

Yield: 181 mg (0.68 mmol, quant.).

^{1}H NMR (400 MHz, DMSO-d_6): δ = 10.2 (s, 1H (NH)), 9.87 (s, 1H (NH)) (visible through exchange with water in the solvent), not visible (broad s, 1H (OH)) ppm.

^{13}C{^{1}H} NMR (101 MHz, DMSO-d_6): δ = 192.1, 163.9 ppm.

IR (ATR): ν = 2902.9, 2559.8, 2408.5, 2091.6, 1971.5, 1705.4, 1478.2, 1322.4, 1226.4, 1158.7, 1013.1, 774.2, 692.9, 616.1, 537.7, 467.6 cm^{-1}.

HRMS (ESI): *m/z* = 105.9934 $[M\text{-}D]^+$ (calcd. *m/z* = 105.9937).

High resolution mass spectrometry was performed with a Bruker MicrOTOF (negative mode ESI-MS).

CO_2-Exchange Experiments in Solution

Inert Conditions

In a glove box 50 mg K-**2** were dispersed in 8 ml of dry DMF in a Fischer-Porter tube. The tube was degassed three times and filled with 1 atm of $^{13}CO_2$. The solution was stirred for 20 h at 70 °C. The solvent was removed *via* distillation (50 °C at 30 mbar).

Standard Conditions

50 mg **K-2** were dispersed in 8 ml of DMF in a Fischer-Porter tube. The tube was degassed three times and filled with 1 atm of $^{13}CO_2$. The solution was stirred for 20 h at 70 °C. The solvent was removed *via* distillation (50 °C at 30 mbar).

NMR Spectra

All NMR spectra were recorded with a Bruker AV400 spectrometer at 298 K. The chemical shifts (δ) are given in ppm relative to the respective solvent residual peak of DMSO-d_6 (δ = 2.50 and 39.5 ppm). ATR-IR spectra were recorded on a Bruker Alpha spectrometer (4000 – 400 cm^{-1}).

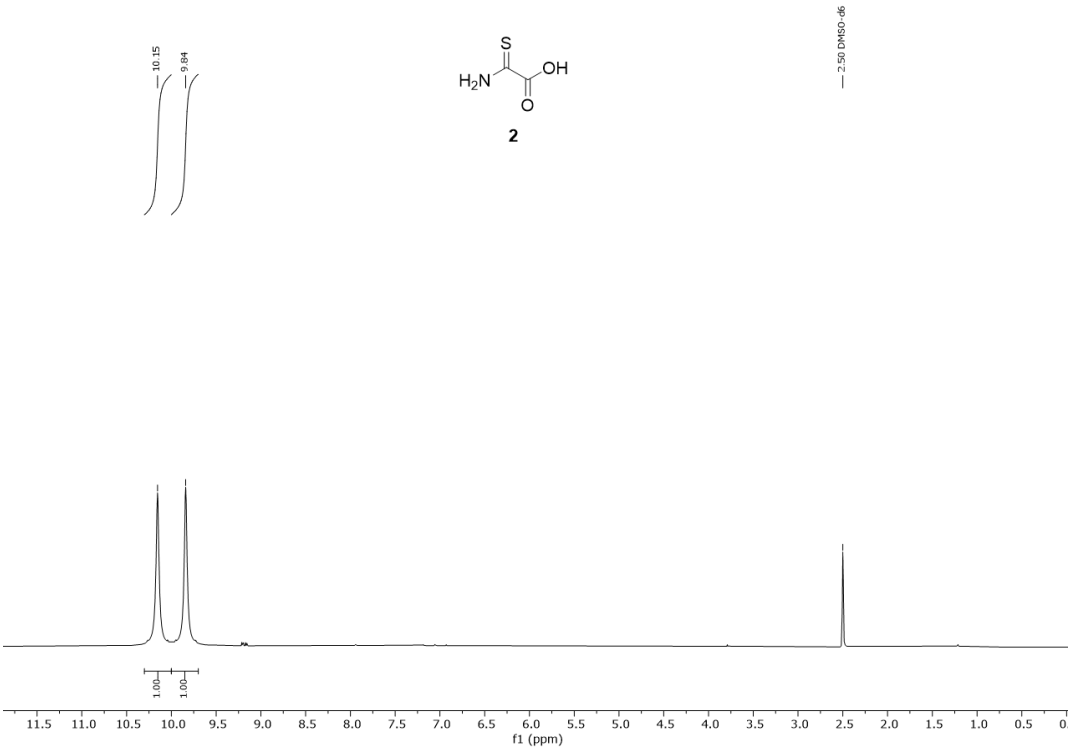

Fig. 7. ^{1}H NMR (400 MHz, DMSO-d_6) of 2-amino-2-thioxoacetic acid (**2**).

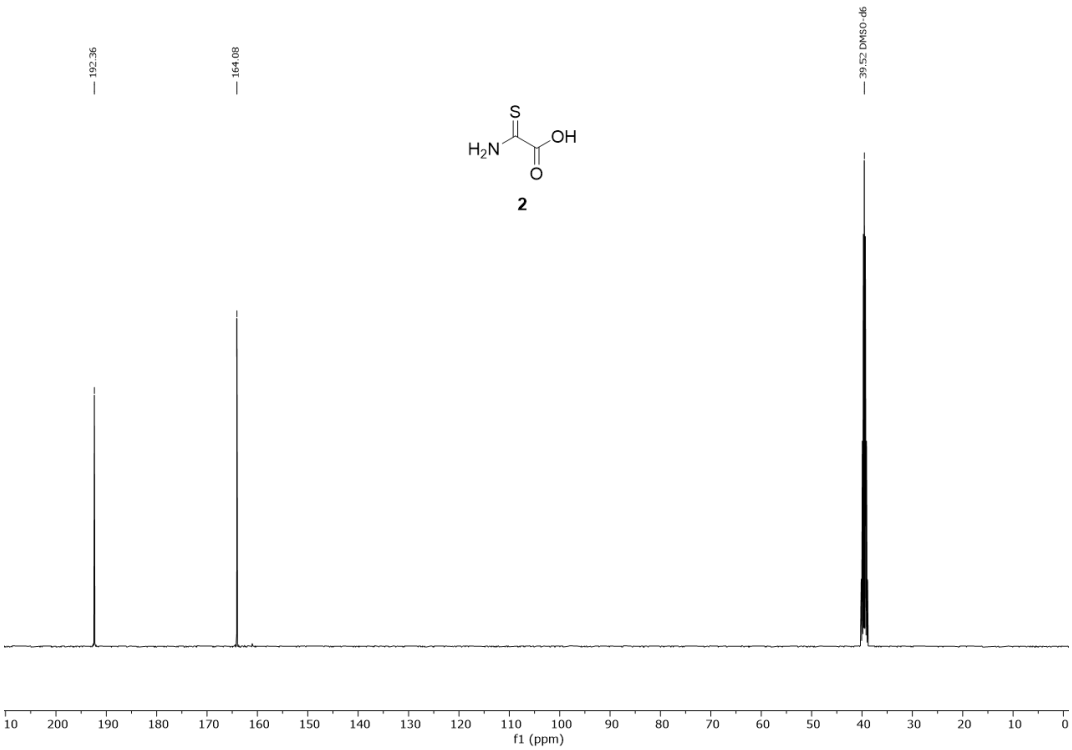

Fig. 8. $^{13}C\{^{1}H\}$ NMR (101 MHz, DMSO-d_6) of 2-amino-2-thioxoacetic acid (**2**).

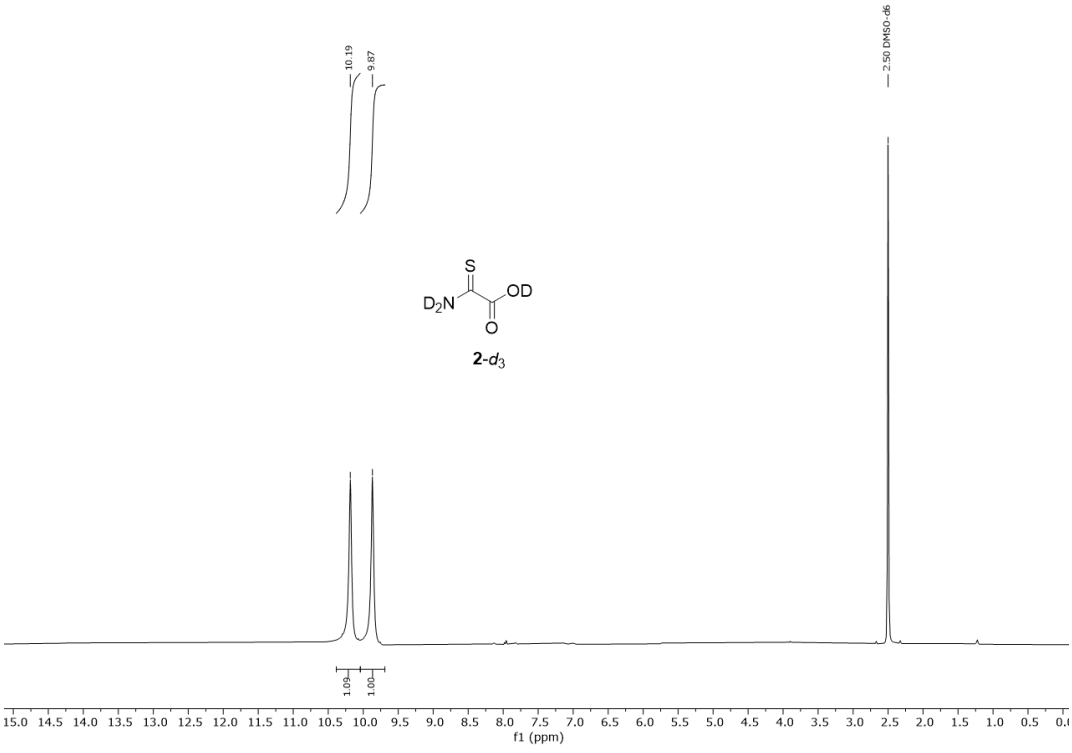

Fig. 9. ^{1}H NMR (400 MHz, DMSO-d_6) of 2-amino-2-ahioxoacetic acid-d_3 (**2**-d_3) (visible through exchange with water in the solvent).

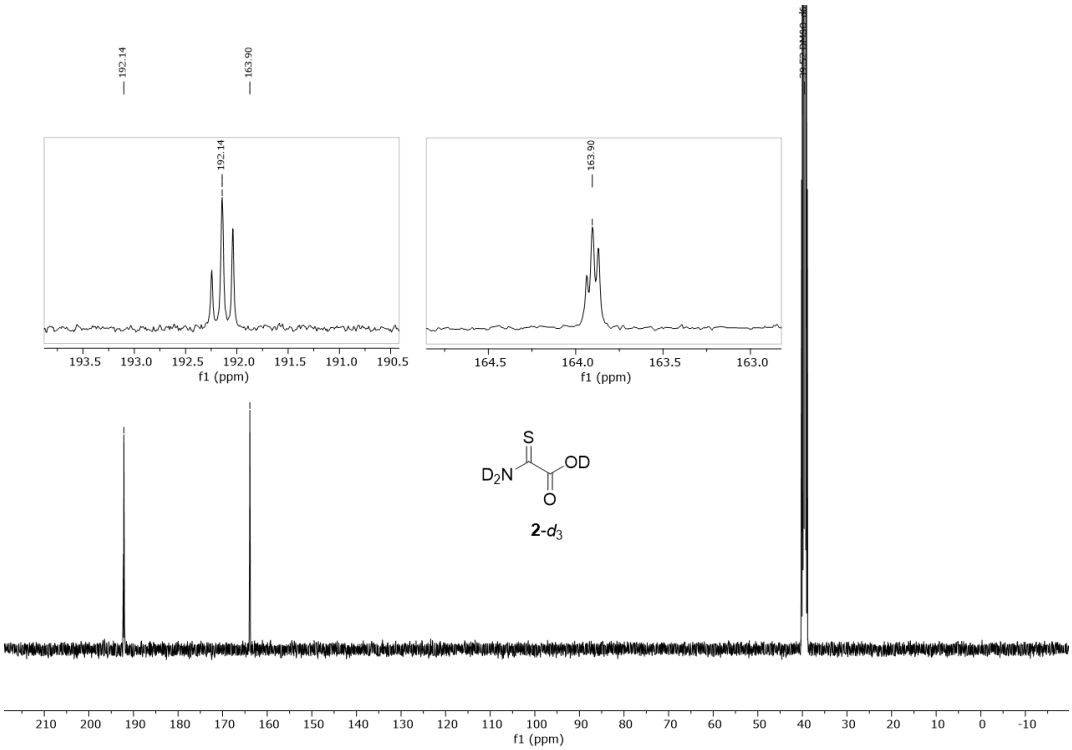

Fig. 10. $^{13}C\{^{1}H\}$ NMR (101 MHz, DMSO-d_6) of 2-amino-2-thioxoacetic acid-d_3 (**2**-d_3) (splitting visualizes complete deuteration).

$^{13}CO_2$-exchange experiment

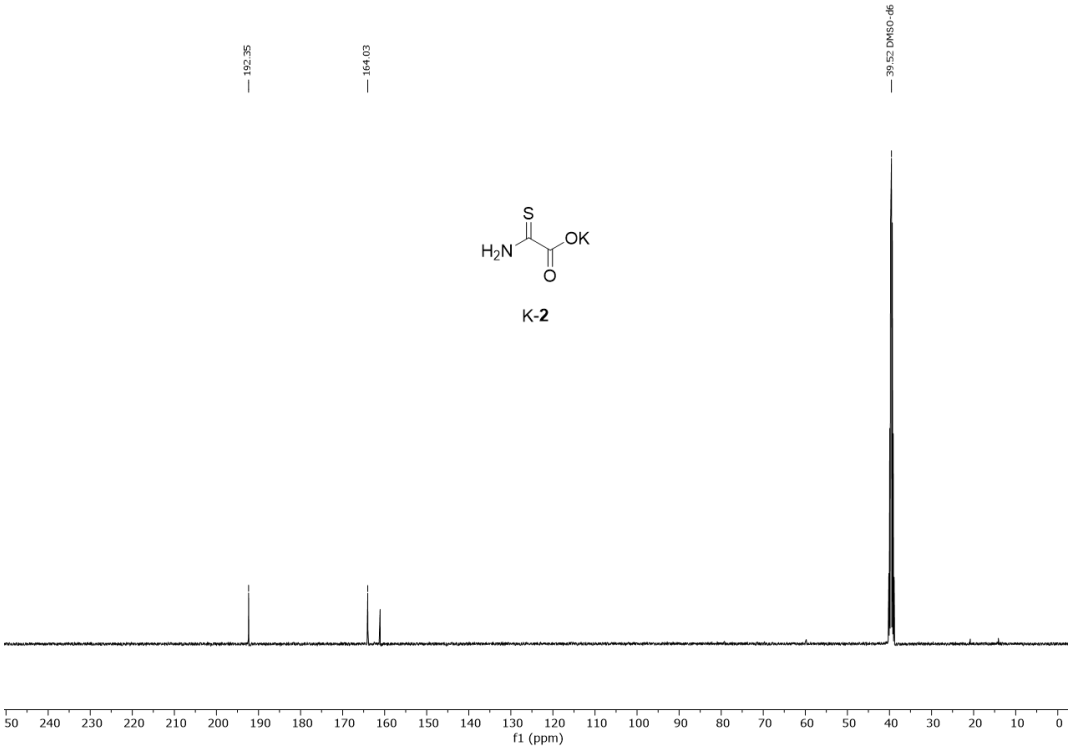

Fig. 11. $^{13}C\{^1H\}$ NMR (101 MHz, DMSO-d_6) of 2-amino-2-thioxoacetic acid potassium salt (K-**2**).

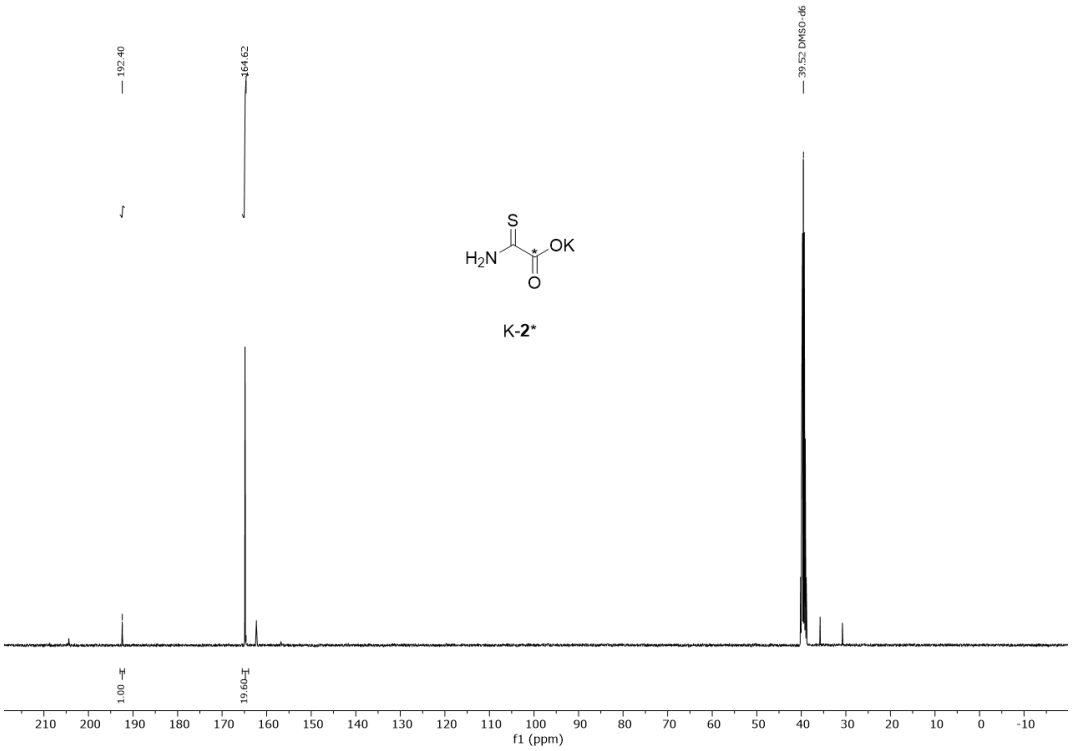

Fig. 12. $^{13}C\{^1H\}$ NMR (101 MHz, DMSO-d_6) of ^{13}C-labelled 2-amino-2-thioxoacetic acid potassium salt (K-**2***).

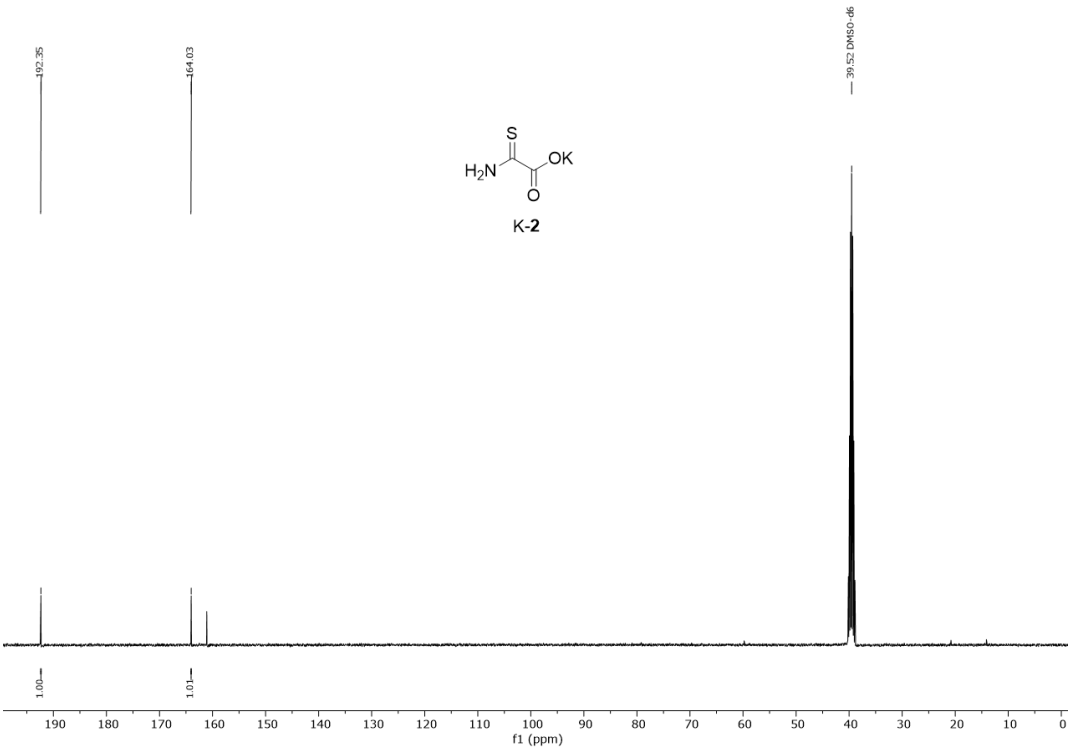

Fig. 13: ^{13}C NMR (101 MHz, DMSO-d_6) of potassium-2-amino-2-thioxoacetic acetate (K-**2**) with DMF.

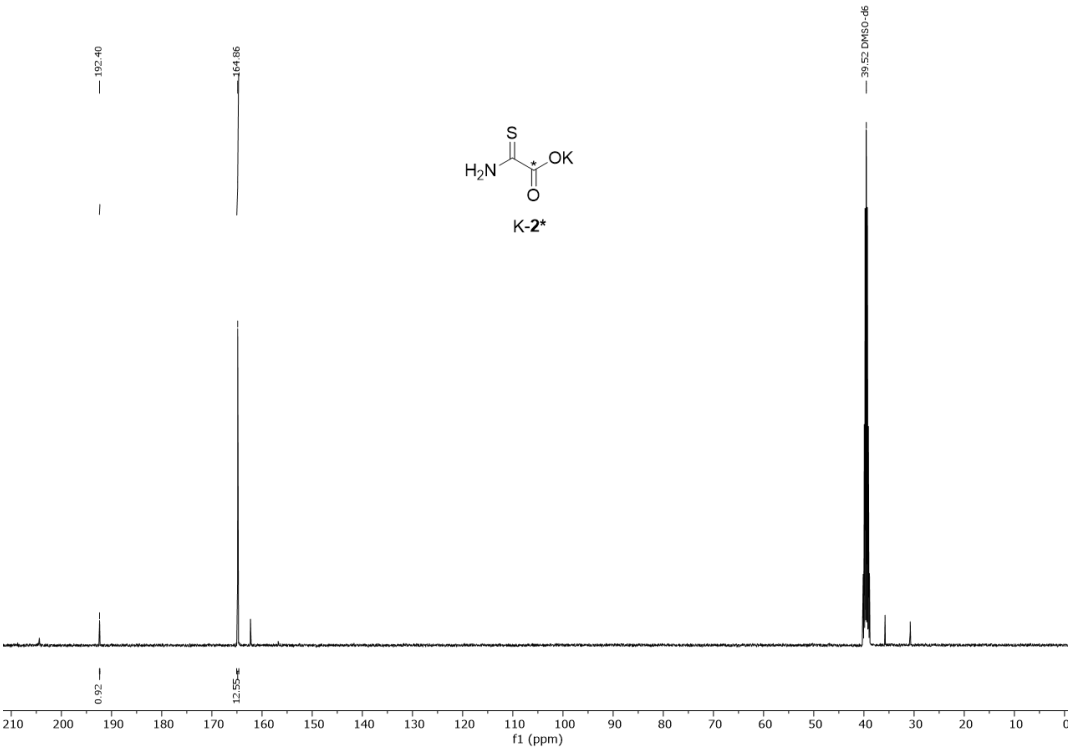

Fig. 14: ^{13}C NMR (101 MHz, DMSO-d_6) of C-labelled potassium-2-amino-2-thioxoacetic acetate (K-**2***) with DMF (12,7% enrichment of ^{13}C).

Matrix IR Spectra

2-Amino-2-Thioxoacetic Acid

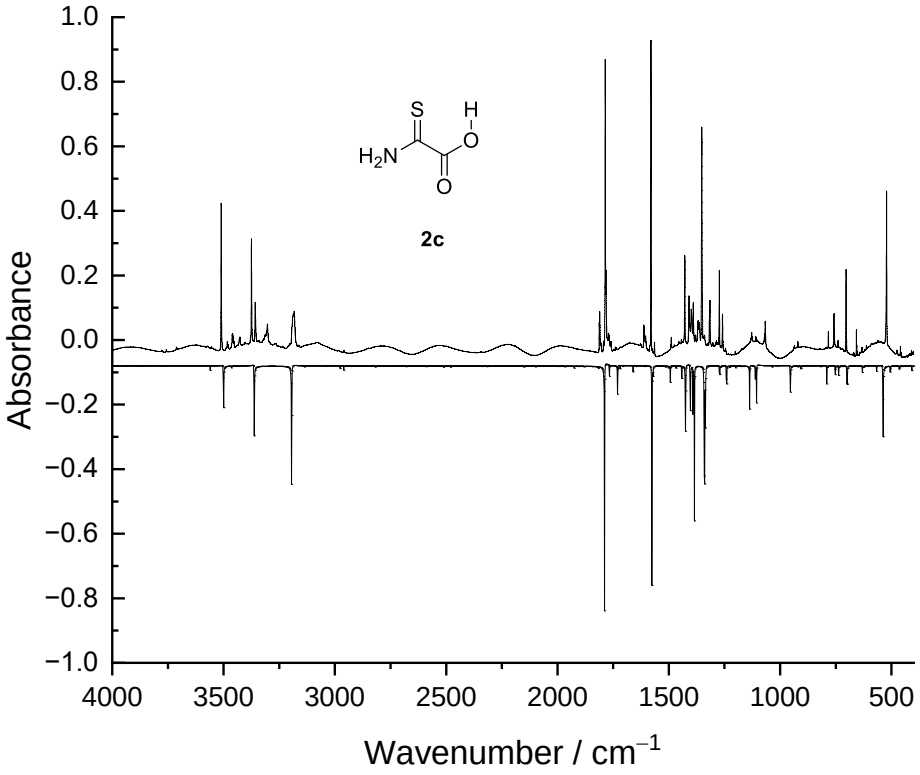

Fig. 15. Experimental spectrum of 2-amino-2-thioxoacetic acid recorded at 3 K in an Ar matrix (upper trace) compared to the computed anharmonic spectrum at the B3LYP/6-311++G(3df,3pd) level of theory (most stable conformer **2c**, lower trace).

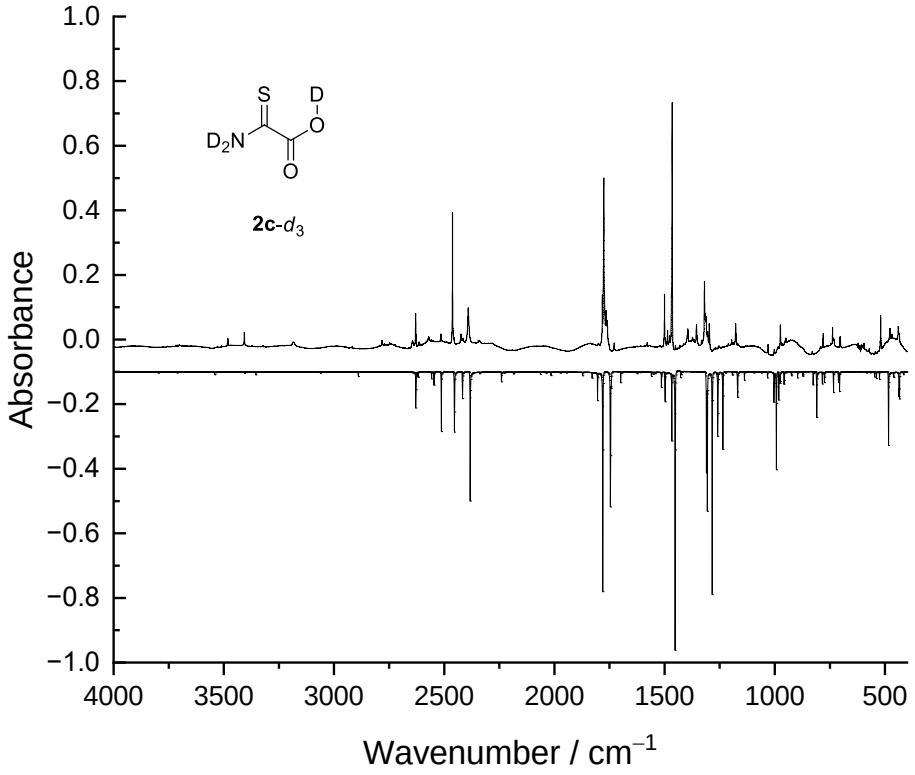

Fig 16. Experimental spectrum of trideuterated 2-amino-2-thioxoacetic acid recorded at 3 K in an Ar matrix (upper trace) compared to the computed anharmonic spectrum at the B3LYP/6-311++G(3df,3pd) level of theory (most stable conformer **2c**-d_3, lower trace).

Pyrolysis of 2-Amino-2-Thioxoacetic Acid (**2**)

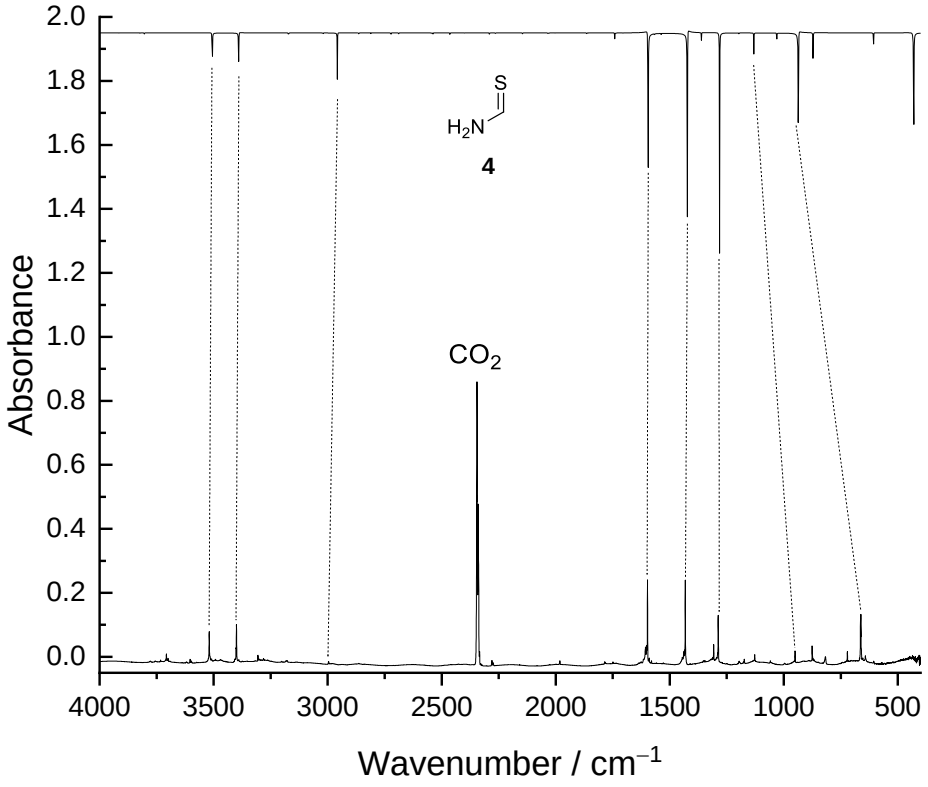

Fig. 17. Under HVFP conditions **2** decomposes to CO_2 and thioformamide[45] (**4**; computed anharmonic spectrum at the B3LYP/6-311++G(3df,3pd) level of theory). Changing the pyrolysis temperature from 300 °C to 1150 °C increases the degree of decomposition. Aminomercaptomethylene (**1**) could not be detected in any HVFP experiment.

Photolysis of 2-Amino-2-Thioxoacetic Acid (**2**)

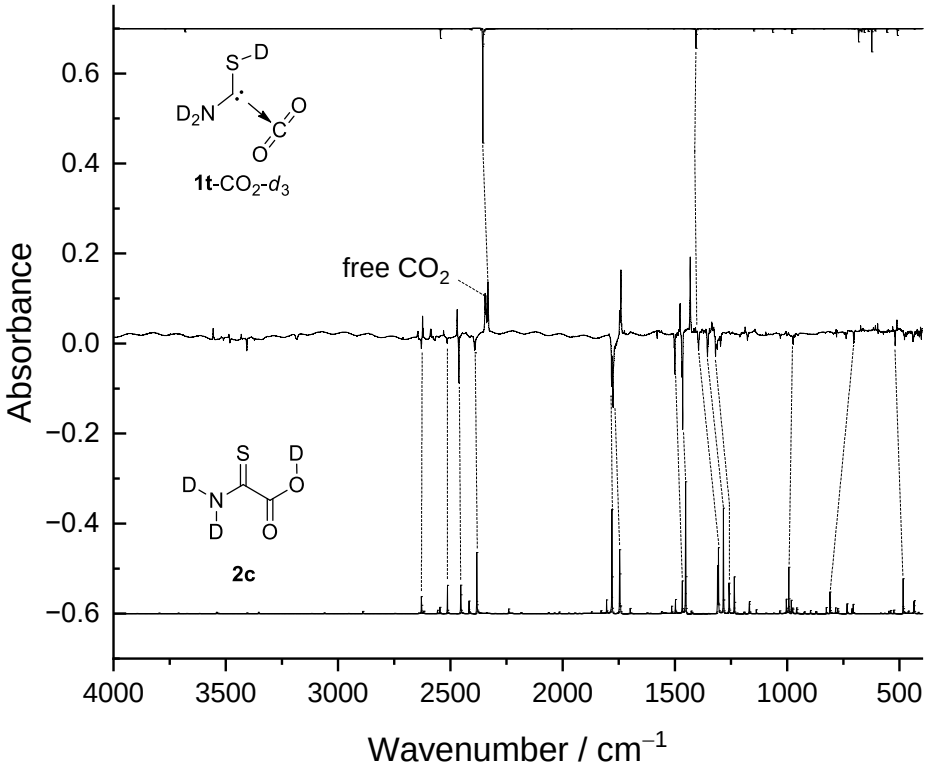

Fig. 18. Irradiation of perdeuterated **2c**-d_3 at 254 nm for 4 min generates **1t**-CO_2-d_3. The corresponding difference spectrum between 1 min and 4 min of irradiation is compared to the computed spectra of **1t**-CO_2-d_3 computed at the B3LYP/6-311++G(3df,3pd) level of theory. The corresponding spectra for the undeuterated isotopologue are depicted in the main text.

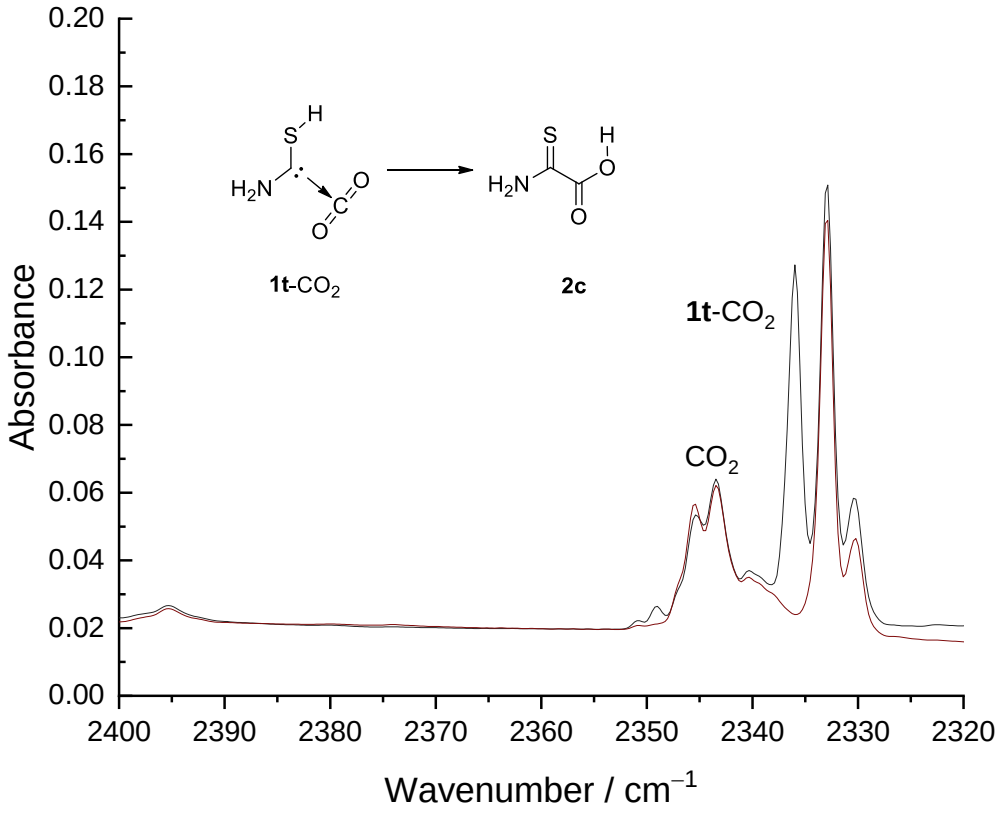

Fig. 19. To exclude activation induced by the IR spectrometer the matrix was kept for 70 h in the dark and **1t**-CO_2 still vanishes.

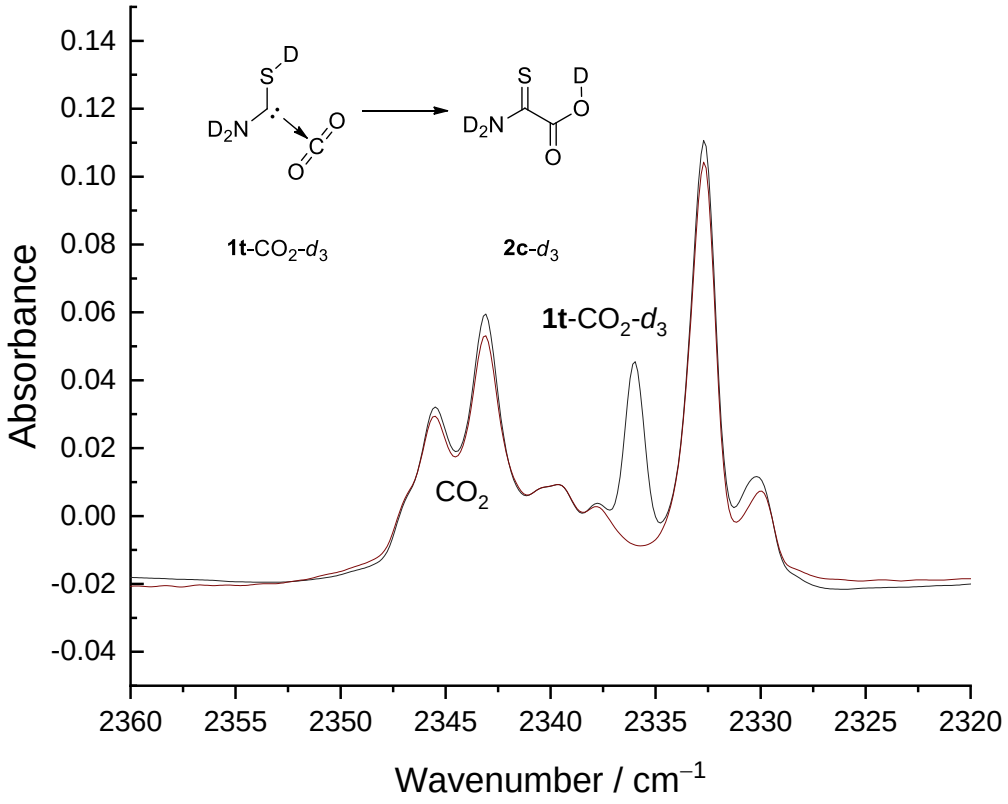

Fig. 20. To exclude activation induced by the IR spectrometer the matrix was kept in the dark for 67 h and **1t**-CO_2-d_3 still vanishes.

Further irradiation decomposes both complexes but to a different extent (Fig. 21). The black trace shows the spectrum of the starting material. After 1 min of irradiation (254 nm) **1t**-CO_2 starts to form and nearly no free CO_2 has evolved. The spectrum measured after irradiation for additional 3 min (red trace) shows strong absorptions of CO_2 and the complex bands further ensue. After another 10 min of irradiation the CO_2 bands ensue but the complex's bands start to decrease.

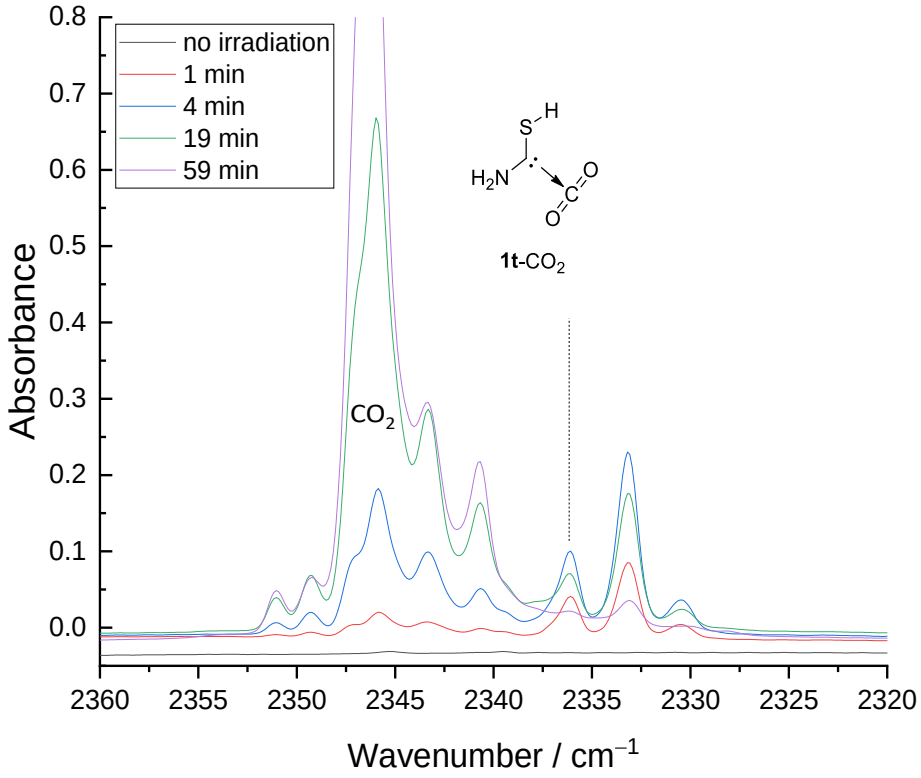

Fig. 21. Optimal irradiation time. The black spectrum was measured after deposition of precursor **2**. When the matrix is irradiated at 254 nm for 1 min (red spectrum) **1t**-CO_2 starts to form. Upon further irradiation for 3 min the bands of the complex ensue and free CO_2 starts to form (blue spectrum). Further irradiation for 15 min leads to decomposition of **1t**-CO_2.

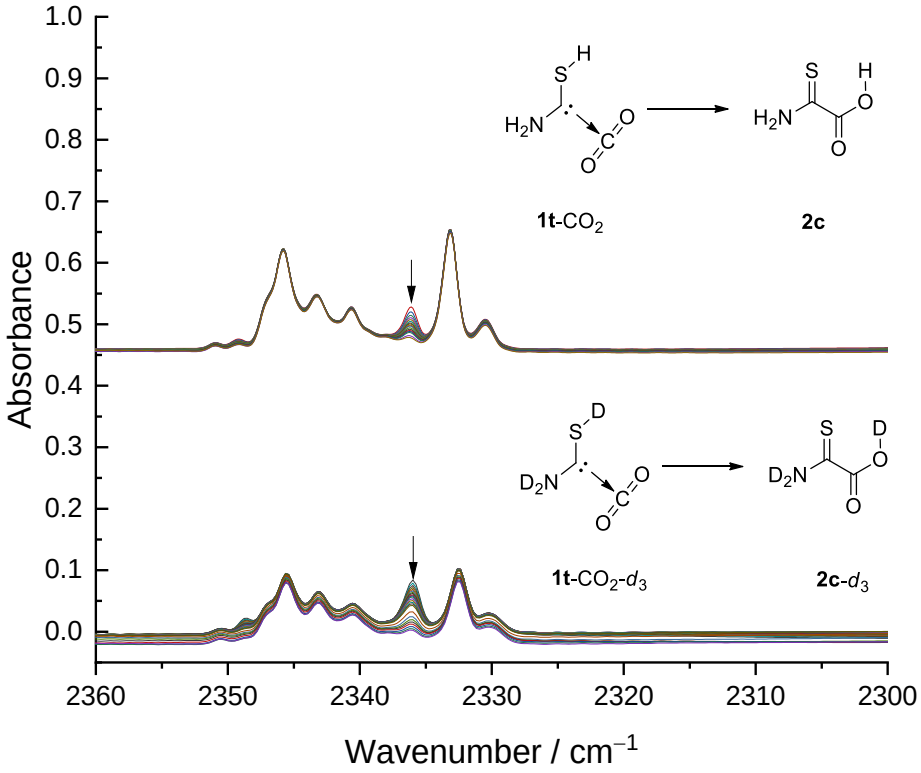

Fig. 22. Both **1t**-CO_2 and its perdeuterated isotopologue **1t**-CO_2-d_3 react back to the starting material **2** with half-lives of 31 min and 90 min, respectively.

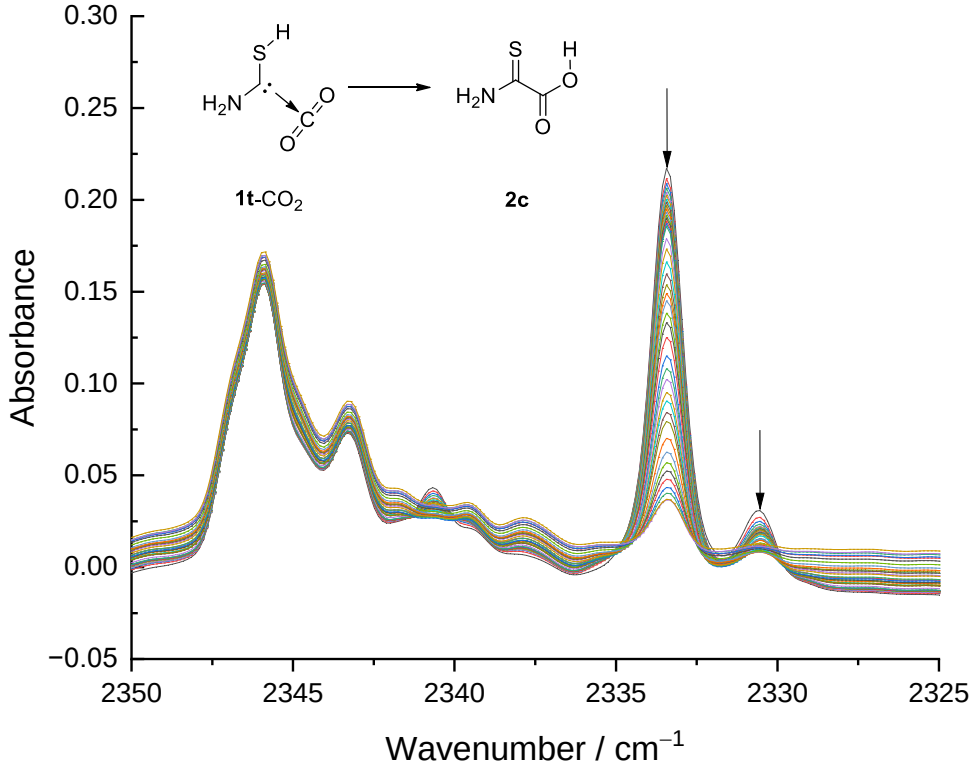

Fig. 23. Two other matrix sites of **1t**-CO_2 lead to slower kinetics at 20 K (left arrow: 95 h, right arrow 16 h).

Rotamerization of 2-Amino-2-Thioxoacetic Acid (**2**)

Upon irradiation of an Ar matrix containing **2c** at 254 nm for 1 min **2c** rotamerizes to **2t**. When keeping the resulting matrix in the dark **2t** vanishes with a half-life of 1.5 h (CVT/SCT//B3LYP/6-311+G(d,p): 1.3 h at 10 K). Repeating the same experiment with perdeuterated **2**, we do not observe this spontaneous reverse reaction. This clearly hints towards a QMT reaction from **2t** to **2c**, which is associated with an activation barrier of 9.9 kcal mol^{-1} at the CCSD(T)/cc-pVTZ level of theory.

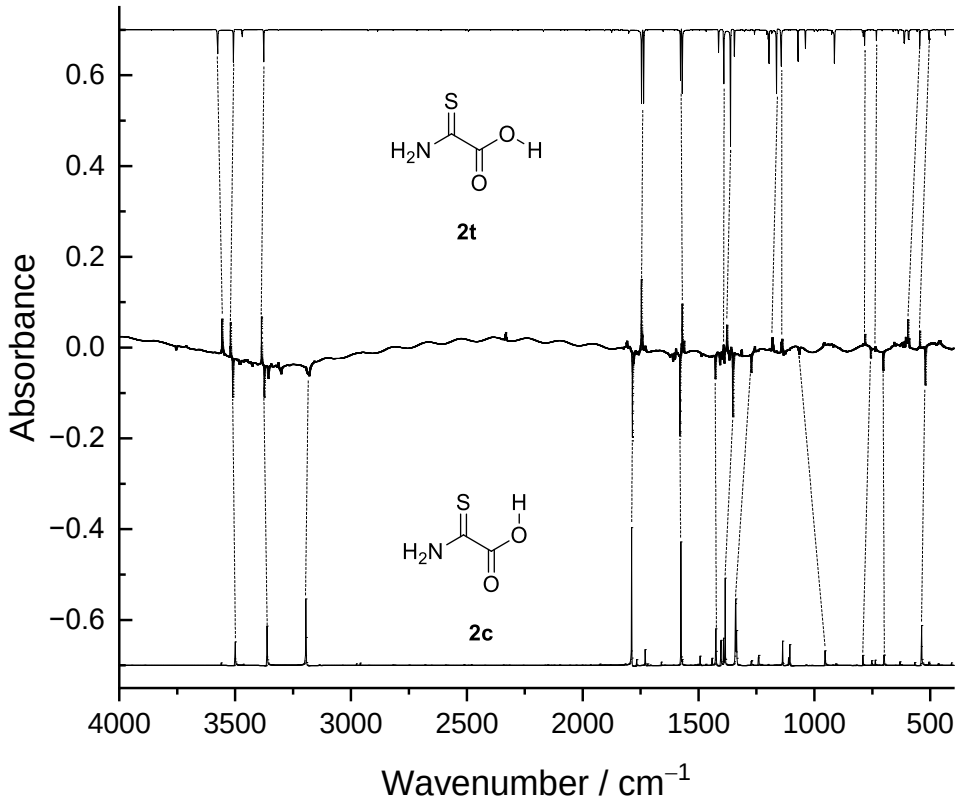

Fig. 24. Experimental difference spectrum compared to the computed anharmonic spectra of **2c** and **2t** at the B3LYP/6-311++G(3df,3pd) level of theory. Upon irradiation at 254 nm for 1 min **2c** rotamerizes to **2t**.

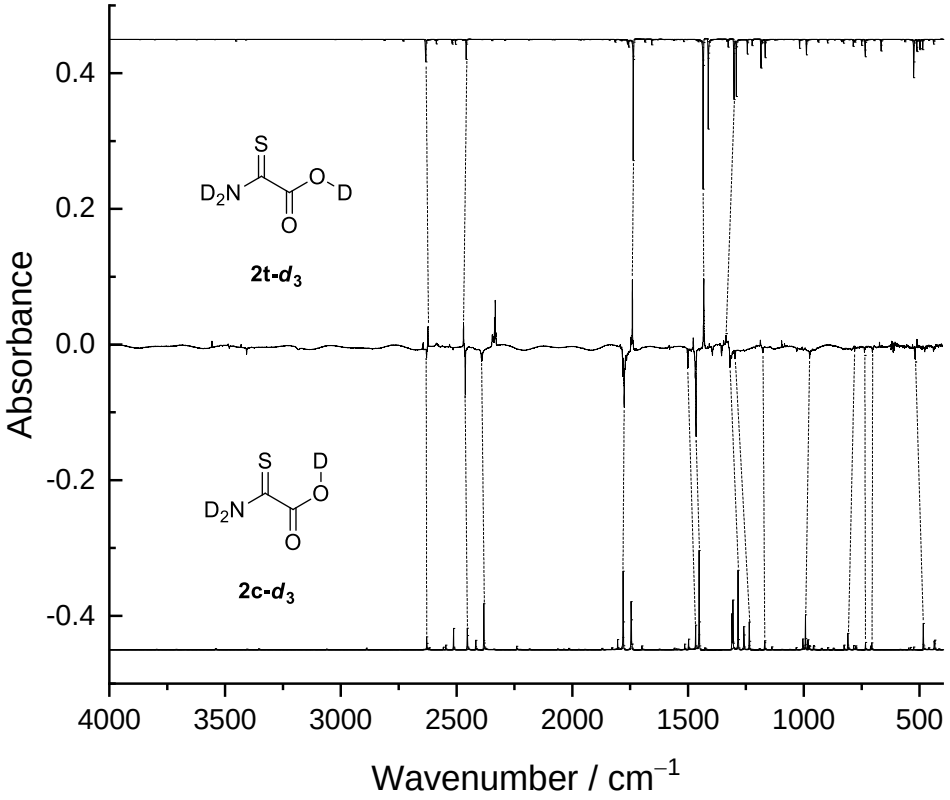

Fig. 25. Experimental difference spectrum compared to the computed anharmonic spectra of **2c**-d_3 and **2t**-d_3 at the B3LYP/6-311++G(3df,3pd) level of theory. Upon irradiation at 254 nm for 1 min **2t**-d_3 rotamerizes to **2c**-d_3.

Isomerization of 2-Amino-2-Thioxoacetic Acid (**2**)

Thiolimine tautomers form under UV-irradiation from the corresponding thioamides[51,53]. Both **2c** and **2t** can undergo isomerization to 16 conceivable conformers of the corresponding thiolimine (**3**) *via* 1,3*[H]*-shifts and consecutive rotamerizations. After 4 min of irradiation, we observed two new bands in the CO-stretching region, which we assign to two thiolimine conformers that are formed in one elementary step from **2c** and **2t**, respectively. These two species (**3a** and **3b**) vanish with half-lives of 1.8 h and 2.3 h. When investigating the perdeuterated starting material, the corresponding bands do not vanish implicating that these 1,3*[H]*-shifts are also QMT reactions. Only two such cases of 1,3*[H]*-shifts *via* QMT are reported for thioamides[51,60,62]. Interconversions of thiolimine conformers *via* SH rotational QMT have been reported recently[45,53] and might contribute to the overall decrease of the thiolimine concentration over time.

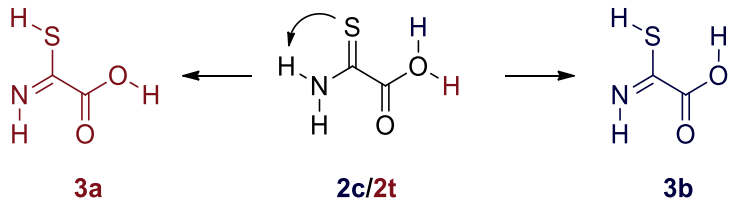

Fig. 26. Thiolimines **3a** and **3b** are the only of 16 conceivable conformers of **3** that can form in one elemental step from **2c** and **2t** without further rotamerizations.

Fig. 27 shows the carbonyl region of the IR spectrum, in which **3a** and **3b** show the highest band intensities. **3a** and **3b** react back to the starting material when keeping the matrix in the dark.

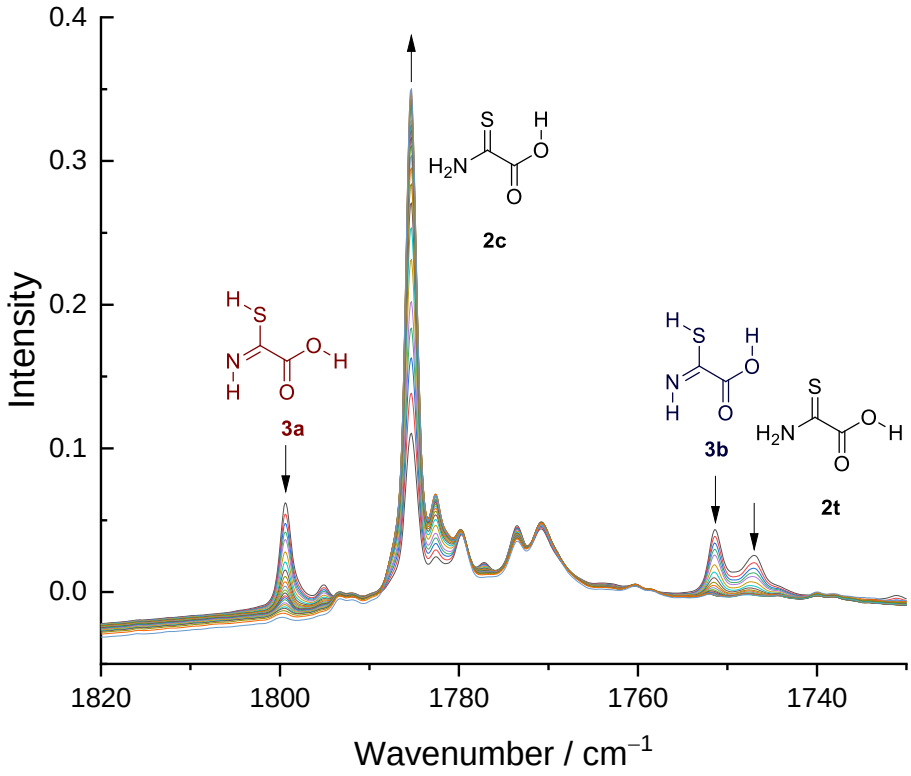

Fig. 27. A 1,3[H] shift leads to various thiolimine conformers of the precursor. We assign those bands tentatively to **3a** and **3b**. They vanish over time and reform the precursor **2c**. In the perdeuterated case, the corresponding bands remain unchanged.

Thiazolylidene-CO_2 Complex (**13**)

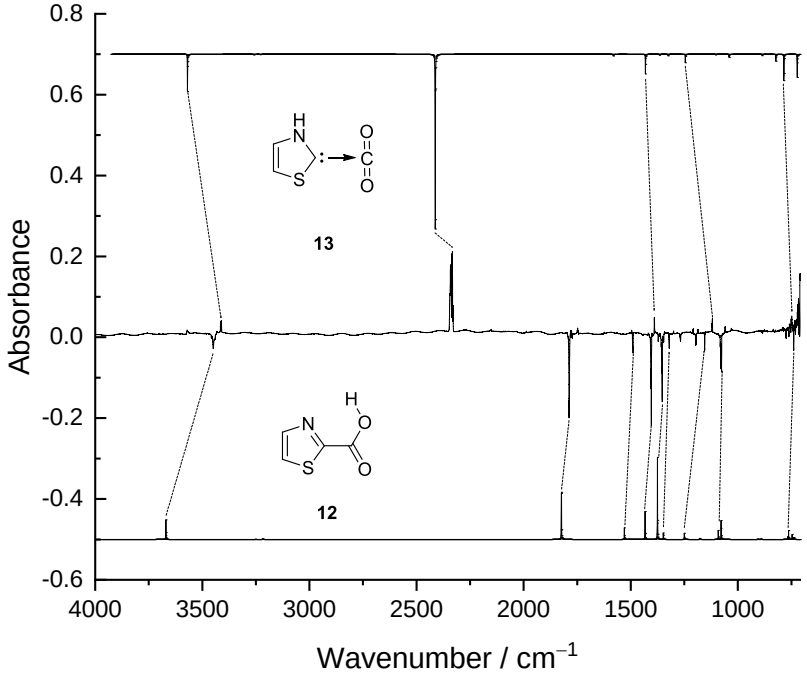

Fig. 28. Top: Computed spectrum of **13** at the B3LYP/6-311++G(3df,3pd) level of theory. Bottom: Computed spectrum of **12** at the B3LYP/6-311++G(3df,3pd) level of theory. Middle: Difference spectrum before and after irradiation of the matrix with 254 nm for 10 min. All observed bands agree with reported reference data.[23]

IR Spectroscopic Data

Table 1. Comparison of experimental vibrational frequencies **1t**-CO_2 isolated in an argon matrix at 3 K and computed vibrational frequencies at the B3LYP/6-311++G(3df,3pd) level of theory (unscaled).

Assignment[a]	Sym.	$\tilde{\nu}_{anharm.}$ / cm^{-1}	$I_{rel.}$ / km mol^{-1}	$\tilde{\nu}_{harm.}$ / cm^{-1}	$I_{rel.}$ / km mol^{-1}	$\tilde{\nu}_{exp.}$ / cm^{-1}	$I_{rel.}$[b]
δ(CCO)	*a'*	52.2	2.6	47.0	3.5	o.o.r.	o.o.r.
τ(CC)	*a''*	57.9	2.7	51.4	1.7	o.o.r.	o.o.r.
ω(CC)	*a''*	86.3	1.5	101.6	8.6	o.o.r.	o.o.r.
δ(CCN)	*a'*	116.7	7.8	102.1	0.5	o.o.r.	o.o.r.
δ(CCO)	*a'*	139.5	0.5	147.3	0.4	o.o.r.	o.o.r.
δ(NCS)	*a'*	398.4	12.3	399.9	12.5	n.o.	n.o.
τ(CS)	*a''*	451.7	22.4	431.6	26.7	n.o.	n.o.
$\delta(CO_2)$	*a'*	625.3	114.9	628.5	122.0	641.8	w
$\omega(CO_2)$	*a''*	650.4	94.4	674.9	1.5	n.o.	n.o.
$\omega(NH_2)$	*a''*	670.8	15.1	683.6	148.7	n.o.	n.o.
υ(CS)	*a'*	684.2	34.9	705.5	32.9	n.o.	n.o.
τ(CN)	*a''*	728.3	24.4	733.6	2.6	n.o.	n.o.
δ(CSH)	*a'*	955.7	13.2	970.8	14.1	n.o.	n.o.
δ(CNH)	*a'*	1176.2	18.0	1204.5	16.4	n.o.	n.o.
$\upsilon_s(CO_2)$	*a'*	1380.7	1.2	1366.1	1.6	n.o.	n.o.
υ(CN)	*a'*	1395.7	10.9	1405.9	98.0	n.o.	n.o.
$\delta(NH_2)$	*a'*	1633.0	58.2	1664.5	77.7	1634.8	w
$\upsilon_{as}(CO_2)$	*a'*	2356.7	516.4	2404.6	562.2	2336.1, 2333.2, 2330.4	s
υ(SH)	*a'*	2570.8	0.5	2685.1	0.8	n.o.	n.o.
$\upsilon_s(NH_2)$	*a'*	3175.1	11.4	3404.2	8.8	n.o.	n.o.
$\upsilon_{as}(NH_2)$	*a'*	3404.6	67.4	3586.6	86.1	3444.9	w

a: assignments (ν = stretching, δ = bending, ω = wagging, τ = twisting, ρ = rocking; s = symmetric, as = antisymmetric).

b: rel. experimental intensities (vw = very weak, w = weak, m = middle, s = strong, vs = very strong); n.o. = not observed; o.o.r. = out of range.

Table 2. Comparison of experimental vibrational frequencies of **1t**-CO_2-d_3 isolated in an argon matrix at 3 K and computed vibrational frequencies at the B3LYP/6-311++G(3df,3pd) level of theory (unscaled).

Assignment[a]	Sym.	$\tilde{\nu}_{anharm.}$ / cm^{-1}	$I_{rel.}$ / km mol^{-1}	$\tilde{\nu}_{harm.}$ / cm^{-1}	$I_{rel.}$ / km mol^{-1}	$\tilde{\nu}_{exp.}$ / cm^{-1}	$I_{rel.}$[b]
δ(CCO)	*a'*	51.4	2.7	45.9	3.3	o.o.r.	o.o.r.
τ(CC)	*a''*	54.4	2.7	49.1	1.4	o.o.r.	o.o.r.
ω(CC)	*a''*	84.0	1.0	93.2	5.8	o.o.r.	o.o.r.
δ(CCN)	*a'*	104.2	4.4	97.7	0.4	o.o.r.	o.o.r.
δ(CCO)	*a'*	137.4	0.4	145.8	0.3	o.o.r.	o.o.r.
τ(CS)	*a''*	326.1	18.0	317.7	20.4	o.o.r.	o.o.r.
δ(NCS)	*a'*	356.7	10.2	358.2	10.1	n.o.	n.o.
ω(ND_2)	*a''*	510.2	39.0	522.0	45.7	530.2	w
ω(NCS)	*a''*	557.6	17.4	569.7	12.6	n.o.	n.o.
δ(CO_2)	*a'*	624.3	102.2	628.2	119.1	615.9	w
υ(CS)	*a''*	670.6	11.2	671.2	33.1	n.o.	n.o.
ω(CO_2)	*a'*	671.8	15.1	676.0	27.3	n.o.	n.o.
δ(CSD)	*a'*	702.9	3.8	713.6	2.5	n.o.	n.o.
δ(CND)	*a'*	967.6	8.4	987.2	14.4	n.o.	n.o.
δ(ND_2)	*a'*	1150.8	15.7	1168.5	17.9	n.o.	n.o.
υ_s(CO_2)	*a'*	1386.8	2.7	1366.4	3.4	n.o.	n.o.
υ(CN)	*a'*	1406.9	112.9	1438.7	130.5	1408.3	w
υ(SD)	*a'*	1869.7	0.2	1929.0	0.2	n.o.	n.o.
υ_{as}(CO_2)	*a'*	2356.3	529.6	2404.2	564.2	2336.0, 2332.6, 2330.2	s
υ_s(ND_2)	*a'*	2365.3	8.2	2464.6	10.0	n.o.	n.o.
υ_{as}(ND_2)	*a'*	2544.9	42.1	2645.3	50.0	2577.9	w

a: assignments (ν = stretching, δ = bending, ω = wagging, τ = twisting, ρ = rocking; s = symmetric, as = antisymmetric).

b: rel. experimental intensities (vw = very weak, w = weak, m = middle, s = strong, vs = very strong); n.o. = not observed; o.o.r. = out of range.

Table 3. Computed vibrational frequencies of **1c**-CO_2 at the B3LYP/6-311++G(3df,3pd) level of theory (unscaled). We did not observe **1c**-CO_2 experimentally.

Assignment[a]	Sym.	$\tilde{\nu}_{anharm.}$ / cm^{-1}	$I_{rel.}$ / km mol^{-1}	$\tilde{\nu}_{harm.}$ / cm^{-1}	$I_{rel.}$ / km mol^{-1}	$\tilde{\nu}_{exp.}$ / cm^{-1}	$I_{rel.}$[b]
δ(CCO)	*a'*	38.4	7.4	46.2	4.9	o.o.r.	o.o.r.
τ(CC)	*a''*	45.8	4.9	49.0	4.5	o.o.r.	o.o.r.
ω(CC)	*a''*	47.2	24.4	103.1	29.9	o.o.r.	o.o.r.
δ(CCN)	*a'*	85.6	1.4	103.6	2.2	o.o.r.	o.o.r.
δ(CCO)	*a'*	124.5	0.4	135.2	0.2	o.o.r.	o.o.r.
δ(NCS)	*a'*	391.1	6.9	396.6	6.1	n.o.	n.o.
τ(CS)	*a''*	481.5	0.0	524.6	0.0	n.o.	n.o.
$\delta(CO_2)$	*a'*	625.6	102.2	637.8	110.0	n.o.	n.o.
$\omega(NH_2)$	*a''*	636.0	101.5	669.1	76.2	n.o.	n.o.
$\omega(CO_2)$	*a''*	675.9	36.2	677.8	76.7	n.o.	n.o.
υ(CS)	*a'*	689.4	21.5	709.2	21.1	n.o.	n.o.
τ(CN)	*a''*	724.4	10.5	729.2	2.8	n.o.	n.o.
δ(CSH)	*a'*	906.9	38.9	941.6	40.3	n.o.	n.o.
δ(CNH)	*a'*	1158.9	8.7	1189.0	8.7	n.o.	n.o.
$\upsilon_s(CO_2)$	*a'*	1389.6	1.8	1368.7	1.3	n.o.	n.o.
υ(CN)	*a'*	1418.8	42.5	1427.9	94.0	n.o.	n.o.
$\delta(NH_2)$	*a'*	1625.7	64.7	1656.1	83.9	n.o.	n.o.
$\upsilon_{as}(CO_2)$	*a'*	2271.7	549.7	2408.3	567.8	n.o.	n.o.
υ(SH)	*a'*	2361.2	115.5	2413.2	122.2	n.o.	n.o.
$\upsilon_s(NH_2)$	*a'*	3156.9	19.3	3383.9	19.6	n.o.	n.o.
$\upsilon_{as}(NH_2)$	*a'*	3409.5	58.5	3582.2	77.2	n.o.	n.o.

a: assignments (ν = stretching, δ = bending, ω = wagging, τ = twisting, ρ = rocking; s = symmetric, as = antisymmetric).

b: rel. experimental intensities (vw = very weak, w = weak, m = middle, s = strong, vs = very strong); n.o. = not observed; o.o.r. = out of range.

Table 4. Computed vibrational frequencies of **1c**-CO_2-d_3 at the B3LYP/6-311++G(3df,3pd) level of theory (unscaled). We did not observe **1c**-CO_2-d_3 experimentally.

Assignment[a]	Sym.	$\tilde{\nu}_{anharm.}$ / cm^{-1}	$I_{rel.}$ / km mol^{-1}	$\tilde{\nu}_{harm.}$ / cm^{-1}	$I_{rel.}$ / km mol^{-1}	$\tilde{\nu}_{exp.}$ / cm^{-1}	$I_{rel.}$[b]
δ(CCO)	*a'*	7.7	3.5	45.7	4.7	o.o.r.	o.o.r.
τ(CC)	*a''*	47.0	4.8	47.4	4.2	o.o.r.	o.o.r.
ω(CC)	*a''*	83.7	1.2	89.7	19.7	o.o.r.	o.o.r.
δ(CCN)	*a'*	87.8	3.2	98.5	1.7	o.o.r.	o.o.r.
δ(CCO)	*a'*	127.0	0.2	134.7	0.2	o.o.r.	o.o.r.
δ(NCS)	*a'*	334.7	4.9	339.7	4.5	o.o.r.	o.o.r.
τ(CS)	*a''*	374.2	2.1	395.7	2.4	n.o.	n.o.
ω(ND_2)	*a''*	499.9	44.7	516.5	46.9	n.o.	n.o.
ω(NCS)	*a''*	552.3	12.1	565.3	11.5	n.o.	n.o.
δ(CO_2)	*a'*	634.7	100.6	636.9	108.7	n.o.	n.o.
ω(CO_2)	*a''*	673.7	27.3	676.8	27.9	n.o.	n.o.
υ(CS)	*a'*	663.8	3.4	685.7	5.6	n.o.	n.o.
δ(CSD)	*a'*	689.7	33.1	707.1	32.5	n.o.	n.o.
δ(CND)	*a'*	952.2	18.6	970.8	15.8	n.o.	n.o.
δ(ND_2)	*a'*	1154.2	19.5	1171.0	21.6	n.o.	n.o.
υ_s(CO_2)	*a'*	1390.8	3.5	1368.8	2.1	n.o.	n.o.
υ(CN)	*a'*	1428.4	102.2	1458.3	118.2	n.o.	n.o.
υ(SD)	*a'*	1662.6	57.8	1733.5	57.8	n.o.	n.o.
υ_{as}(CO_2)	*a'*	2360.6	546.6	2408.0	576.5	n.o.	n.o.
υ_s(ND_2)	*a'*	2339.9	10.0	2450.1	18.9	n.o.	n.o.
υ_{as}(ND_2)	*a'*	2542.4	34.9	2641.1	43.0	n.o.	n.o.

a: assignments (ν = stretching, δ = bending, ω = wagging, τ = twisting, ρ = rocking; s = symmetric, as = antisymmetric).

b: rel. experimental intensities (vw = very weak, w = weak, m = middle, s = strong, vs = very strong); n.o. = not observed; o.o.r. = out of range.

Table 5. Comparison of experimental vibrational frequencies of **2c** isolated in an argon matrix at 3 K and computed vibrational frequencies at the B3LYP/6-311++G(3df,3pd) level of theory (unscaled).

Assignment[a]	Sym.	$\tilde{\nu}_{anharm.}$ / cm^{-1}	$I_{rel.}$ / km mol^{-1}	$\tilde{\nu}_{harm.}$ / cm^{-1}	$I_{rel.}$ / km mol^{-1}	$\tilde{\nu}_{exp.}$ / cm^{-1}	$I_{rel.}$[b]
τ(CC)	*a''*	92.9	8.3	93.8	7.6	o.o.r.	o.o.r.
δ(CC)	*a'*	267.9	31.3	273.6	29.9	o.o.r.	o.o.r.
δ(CN)	*a'*	360.9	3.5	368.7	3.9	n.o.	n.o.
ω(CCN)	*a''*	410.5	4.7	416.4	8.4	n.o.	n.o.
δ(CCN)	*a'*	466.4	7.1	479.4	8.0	n.o.	n.o.
ω(NH_2)	*a''*	539.5	145.7	531.2	157.3	521.9	s
δ(CCO)	*a'*	559.7	0.3	565.5	0.5	n.o.	n.o.
τ(CN)	*a''*	631.8	8.8	663.1	6.7	n.o.	n.o.
τ(CO)	*a''*	701.1	51.6	737.1	63.8	703.9	m
υ(CC)	*a'*	754.2	17.2	765.3	21.3	758.3	w
ω(CCO)	*a''*	792.2	18.0	799.7	6.1	n.o.	n.o.

Assignment[a]	Sym.	$\tilde{\nu}_{anharm.}$ / cm^{-1}	$I_{rel.}$ / km mol^{-1}	$\tilde{\nu}_{harm.}$ / cm^{-1}	$I_{rel.}$ / km mol^{-1}	$\tilde{\nu}_{exp.}$ / cm^{-1}	$I_{rel.}$[b]
δ(CNH)	*a'*	908.6	7.4	931.5	3.4	n.o.	n.o.
υ(CO)	*a'*	1166.1	0.5	1217.5	4.6	1066.7	w
δ(CNH)	*a'*	1273.7	22.7	1281.4	25.2	1273.2	m
δ(COH)	*a'*	1341.6	319.6	1397.6	446.1	1352.2	s
υ(CN)	*a'*	1405.6	71.1	1443.3	129.6	1428.4	m
δ(NH_2)	*a'*	1577.4	208.2	1615.8	259.2	1580.1	vs
υ(C=O)	*a'*	1790.0	251.7	1821.4	284.3	1758.6	vs
υ(OH)	*a'*	3195.3	231.4	3455.5	217.5	3357.8	w
υ_s(NH_2)	*a'*	3363.6	95.7	3533.4	122.2	3374.9	m
υ_{as}(NH_2)	*a'*	3501.3	70.8	3684.5	83.0	3510.7	m

a: assignments (ν = stretching, δ = bending, ω = wagging, τ = twisting, ρ = rocking; s = symmetric, as = antisymmetric).

b: rel. experimental intensities (vw = very weak, w = weak, m = middle, s = strong, vs = very strong); n.o. = not observed; o.o.r. = out of range.

Table 6. Comparison of experimental vibrational frequencies of **2c**-d_3 isolated in an argon matrix at 3 K and computed vibrational frequencies at the B3LYP/6-311++G(3df,3pd) level of theory (unscaled).

Assignment[a]	Sym.	$\tilde{\nu}_{anharm.}$ / cm^{-1}	$I_{rel.}$ / km mol^{-1}	$\tilde{\nu}_{harm.}$ / cm^{-1}	$I_{rel.}$ / km mol^{-1}	$\tilde{\nu}_{exp.}$ / cm^{-1}	$I_{rel.}$[b]
τ(CC)	*a''*	91.3	7.8	91.5	7.5	o.o.r.	o.o.r.
δ(CC)	*a'*	257.5	30.4	263.0	29.8	o.o.r.	o.o.r.
δ(CN)	*a'*	327.2	1.2	333.0	1.3	o.o.r.	o.o.r.
ω(ND_2)	*a''*	352.4	25.3	352.8	32.1	n.o.	n.o.
ω(CND)	*a''*	437.5	27.7	455.8	53.3	439.8	s
δ(CCO)	*a'*	462.2	6.9	464.2	8.7	469.0	s
ω(CND)	*a''*	485.3	59.2	491.2	14.5	477.8	s
δ(CCO)	*a''*	526.0	0.3	532.1	0.8	519.7	s
τ(CO)	*a'*	526.4	4.7	539.9	22.8	n.o.	n.o.
υ(CC)	*a'*	734.8	14.7	743.3	22.6	738.3	s
ω(CCO)	*a''*	785.4	8.1	795.8	11.0	780.2	s
δ(CND)	*a'*	779.2	0.2	798.4	0.2	n.o.	n.o.
δ(COD)	*a'*	958.8	16.3	1004.1	52.8	974.7	s
δ(ND_2)	*a'*	1095.5	1.2	1116.8	2.7	n.o.	n.o.
υ(CS)	*a'*	1169.7	35.3	1196.7	39.0	1177.4	s
υ(CO)	*a'*	1284.8	151.8	1315.0	245.9	1319.0	s
υ(CN)	*a'*	1452.8	250.0	1491.5	324.8	1465.5	s
υ(C=O)	*a'*	1781.0	214.6	1811.2	307.7	1775.9	s
υ(OD)	*a'*	2383.2	102.7	2515.0	113.2	2391.1	w
υ_s(ND_2)	*a'*	2454.7	25.0	2552.8	101.3	2462.3	m
υ_{as}(ND_2)	*a'*	2629.2	40.1	2728.9	47.2	2629.5	w

a: assignments (ν = stretching, δ = bending, ω = wagging, τ = twisting, ρ = rocking; s = symmetric, as = antisymmetric).

b: rel. experimental intensities (vw = very weak, w = weak, m = middle, s = strong, vs = very strong); n.o. = not observed; o.o.r. = out of range.

Table 7. Comparison of experimental vibrational frequencies of **2t** isolated in an argon matrix at 3 K and computed vibrational frequencies at the B3LYP/6-311++G(3df,3pd) level of theory (unscaled).

Assignment[a]	Sym.	$\tilde{\nu}_{\mathrm{anharm.}}$ / cm^{-1}	$I_{\mathrm{rel.}}$ / km mol^{-1}	$\tilde{\nu}_{\mathrm{harm.}}$ / cm^{-1}	$I_{\mathrm{rel.}}$ / km mol^{-1}	$\tilde{\nu}_{\mathrm{exp.}}$ / cm^{-1}	$I_{\mathrm{rel.}}$[b]
τ(CC)	*a''*	53.0	5.3	51.1	4.1	o.o.r.	o.o.r.
δ(CCO)	*a'*	243.2	6.5	244.9	6.4	o.o.r.	o.o.r.
δ(CCN)	*a'*	380.2	6.2	383.9	6.1	n.o.	n.o.
ω(CCN)	*a''*	386.4	89.4	393.0	66.4	n.o.	n.o.
ω(NH_2)	*a''*	479.5	1.5	465.8	89.3	n.o.	n.o.
δ(CCO)	*a'*	507.9	34.6	475.1	2.3	n.o.	n.o.
δ(CCO)	*a'*	547.4	37.1	553.4	40.3	546.1	w
τ(CO)	*a''*	595.1	49.8	627.6	106.4	597.0	m
τ(CN)	*a''*	614.0	63.4	638.9	2.2	602.6	vw
υ(CC)	*a'*	733.6	23.7	746.5	26.1	738.7	w
ω(CCO)	*a''*	791.6	21.5	800.6	33.6	782.9	w
δ(CNH)	*a'*	922.3	10.0	944.4	7.9	947.7	vw
δ(COH)	*a'*	1145.3	156.0	1187.8	246.8	1183.0	m
δ(CNH)	*a'*	1259.7	6.8	1270.6	14.3	n.o.	n.o.
υ(CS)	*a'*	1347.0	47.9	1396.2	77.9	1361.9	w
υ(CN)	*a'*	1363.6	200.2	1405.5	176.5	1378.5	m
δ(NH_2)	*a'*	1572.3	144.6	1607.0	268.2	1571.3	s
υ(C=O)	*a'*	1747.0	202.6	1777.3	272.6	1747.1	s
υ_s(NH_2)	*a'*	3377.8	54.4	3550.1	96.2	3386.5	m
υ_{as}(NH_2)	*a'*	3507.8	61.9	3695.9	73.8	3520.7	m
υ(OH)	*a'*	3577.0	85.5	3754.9	99.9	3557.1	m

a: assignments (ν = stretching, δ = bending, ω = wagging, τ = twisting, ρ = rocking; s = symmetric, as = antisymmetric).

b: rel. experimental intensities (vw = very weak, w = weak, m = middle, s = strong, vs = very strong); n.o. = not observed; o.o.r. = out of range.

Table 8. Comparison of experimental vibrational frequencies of **2t**-d_3 isolated in an argon matrix at 3 K and computed vibrational frequencies at the B3LYP/6-311++G(3df,3pd) level of theory (unscaled).

Assignment[a]	Sym.	$\tilde{\nu}_{\text{anharm.}}$ / cm^{-1}	$I_{\text{rel.}}$ / km mol^{-1}	$\tilde{\nu}_{\text{harm.}}$ / cm^{-1}	$I_{\text{rel.}}$ / km mol^{-1}	$\tilde{\nu}_{\text{exp.}}$ / cm^{-1}	$I_{\text{rel.}}$[b]
τ(CC)	*a''*	51.6	4.6	50.4	4.0	o.o.r.	o.o.r.
δ(CCO)	*a'*	236.2	6.2	238.1	6.2	o.o.r.	o.o.r.
ω(ND_2)	*a''*	327.5	71.5	314.6	78.8	o.o.r.	o.o.r.
δ(CCN)	*a'*	343.7	3.7	346.6	3.7	o.o.r.	o.o.r.
ω(CCN)	*a''*	387.8	0.7	388.2	2.6	n.o.	n.o.
τ(CN)	*a''*	440.9	8.2	456.7	10.3	n.o.	n.o.
δ(CCO)	*a'*	461.7	2.1	464.6	2.3	n.o.	n.o.
τ(CO)	*a''*	499.1	41.2	517.6	54.6	511.3	w
δ(CCO)	*a'*	513.1	42.9	519.0	47.0	517.0	vw
υ(CC)	*a'*	666.7	20.9	679.7	19.7	673.2	vw
ω(CCO)	*a''*	787.0	14.5	796.9	18.3	n.o.	n.o.
δ(CND)	*a'*	787.6	4.4	798.3	6.8	n.o.	n.o.
δ(COD)	*a'*	990.1	39.1	1017.8	57.1	1006.4	vw
δ(ND_2)	*a'*	1088.8	0.7	1111.1	0.3	n.o.	n.o.
υ(CS)	*a'*	1168.3	40.0	1200.1	61.8	1187.9	w
υ(CO)	*a'*	1303.1	142.8	1334.3	199.9	1327.5	w
υ(CN)	*a'*	1413.9	206.5	1454.8	330.1	1432.6	s
υ(C=O)	*a'*	1737.5	255.2	1768.3	294.7	1740.7	s
υ_s(ND_2)	*a'*	2458.8	47.0	2563.3	81.3	2470.1	m
υ(OD)	*a'*	2633.5	41.8	2731.3	59.1	2623.9	m
υ_{as}(ND_2)	*a'*	2635.3	46.8	2738.4	44.3	2644.6	w

a: assignments (ν = stretching, δ = bending, ω = wagging, τ = twisting, ρ = rocking; s = symmetric, as = antisymmetric).

b: rel. experimental intensities (vw = very weak, w = weak, m = middle, s = strong, vs = very strong); n.o. = not observed; o.o.r. = out of range.

Matrix UV/Vis Spectra

UV/Vis spectra recorded after deposition of **2** (black spectrum in Fig. 30) show an absorption at 293.6 nm, which we assign to **2c** (compd. 276.1 nm with $f = 0.1343$ at B3LYP/6-311++G(3df,3pd)). After 4 min of irradiation at 254 nm the intensity of this absorption decreases. For **2t** we computed the absorbance maximum at 295.4 nm ($f = 0.1304$), which is in accord with a shift to higher wavelengths of the absorption in the experiment (red spectrum). Within 19 h **2c** reforms (the maximum shifts left), but does not reach its initial concentration (blue spectrum).

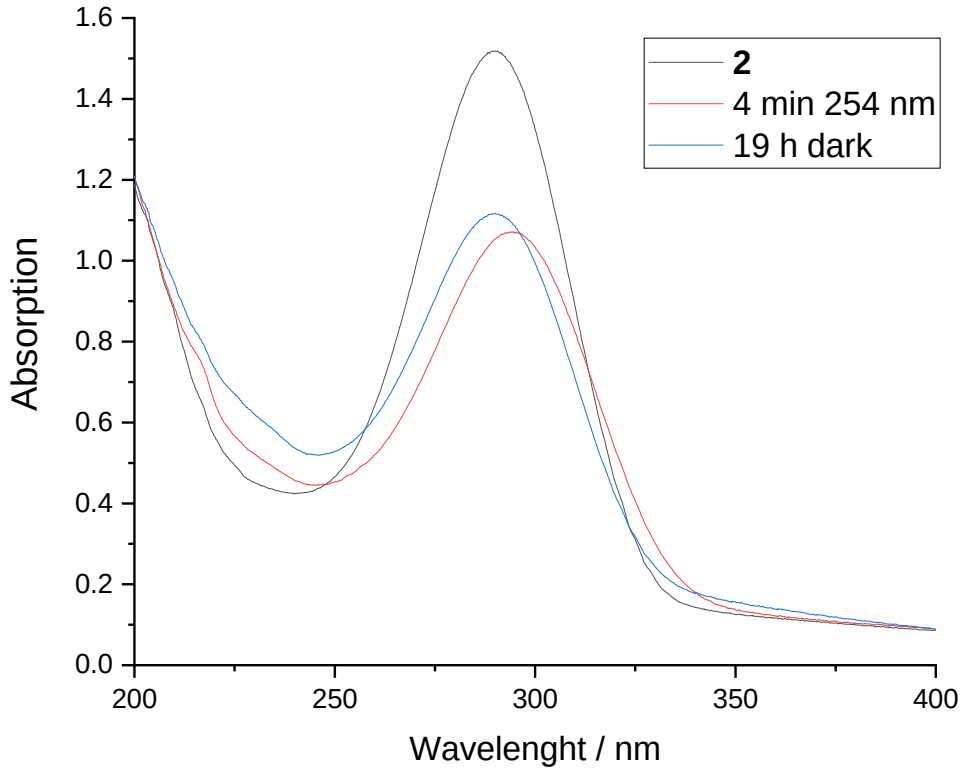

Fig. 29. Experimental matrix UV/Vis spectra. Black: After deposition. Red: After irradiation at 254 nm for 4 min. Blue: After keeping the matrix 19 h in the dark. The baseline of the blue spectrum is shifted to facilitate visual comparison.

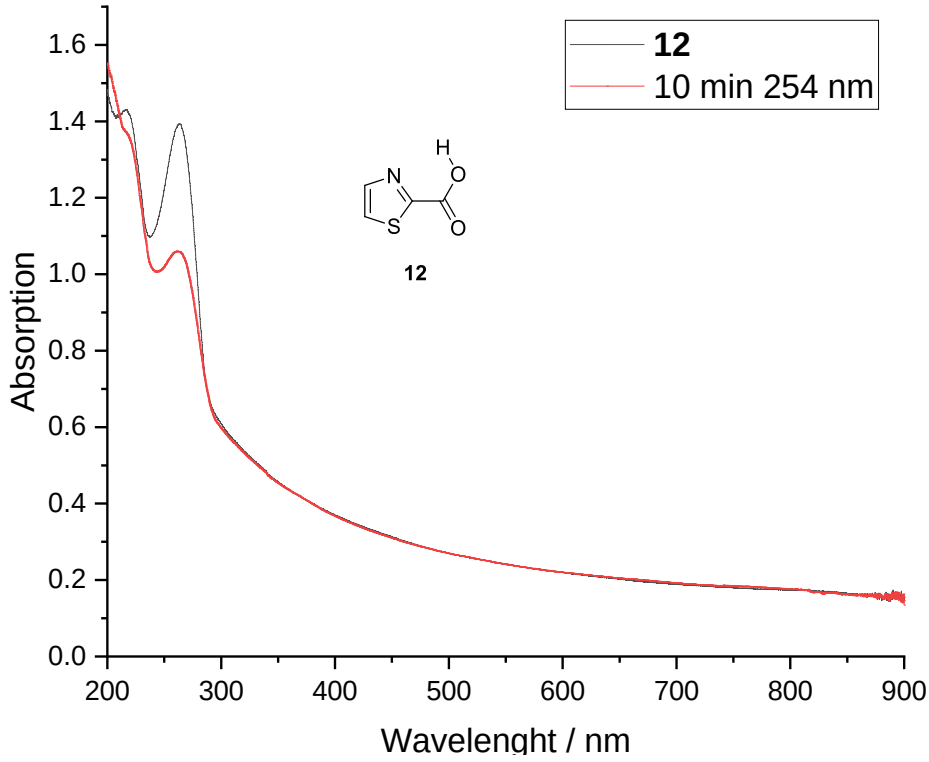

Fig. 30. Experimental matrix UV/Vis spectra of **12**. Black: After deposition. Red: After irradiation at 254 nm for 10 min. The baseline of the red spectrum is shifted to facilitate visual comparison.

Kinetic Analyses

Kinetic Measurements

To evaluate the kinetics of the reactions **1t**-CO_2 → **2c** and **2t** → **2c** we measured the time evolution of the corresponding matrix IR bands at different temperatures. The decay of the integral below the strongest band was measured and plotted to calculate *k* through exponential fitting. The band decay was evaluated *via* integration using a Python script (available at: https://github.com/prs-group/Spectra_Analyzer). The bands at 2336.1 and 2333.2 cm^{-1} (distinct matrix sites displaying different kinetics) were used for the evaluation of the decay of **1t**-CO_2. The third band at 2330.4 cm^{-1} cannot be reliably evaluated due to its small intensity and long half-life.

We performed temperature dependent measurements of the band at 2336.1 cm^{-1}. The results are displayed in Table 9.

Table 9. Experimental rate constants measured at different temperatures. The band at 2336.1 cm^{-1} was used for the evaluation of the decay of **1t**-CO_2. The values of the first reaction

are plotted in an Arrhenius plot in the main text. The values of the second reaction are plotted in Fig. 31.

Reaction	Temperature / K	Experimental k / s^{-1}	Experimental $t_{1/2}$ / h
1t-CO_2 → **2c**	3.5	4.53 x 10^{-4}	0.43
	5.3	4.64 x 10^{-4}	0.41
	7.2	9.10 x 10^{-4}	0.21
	10.0	2.00 x 10^{-3}	0.10
	12.2	4.51 x 10^{-3}	0.04
2t → **2c**	3.5	1.74 x 10^{-4}	1.11
	5.3	1.71 x 10^{-4}	1.13
	7.2	1.75 x 10^{-4}	1.10
	10.0	1.83 x 10^{-4}	1.05
	12.2	1.84 x 10^{-4}	1.05

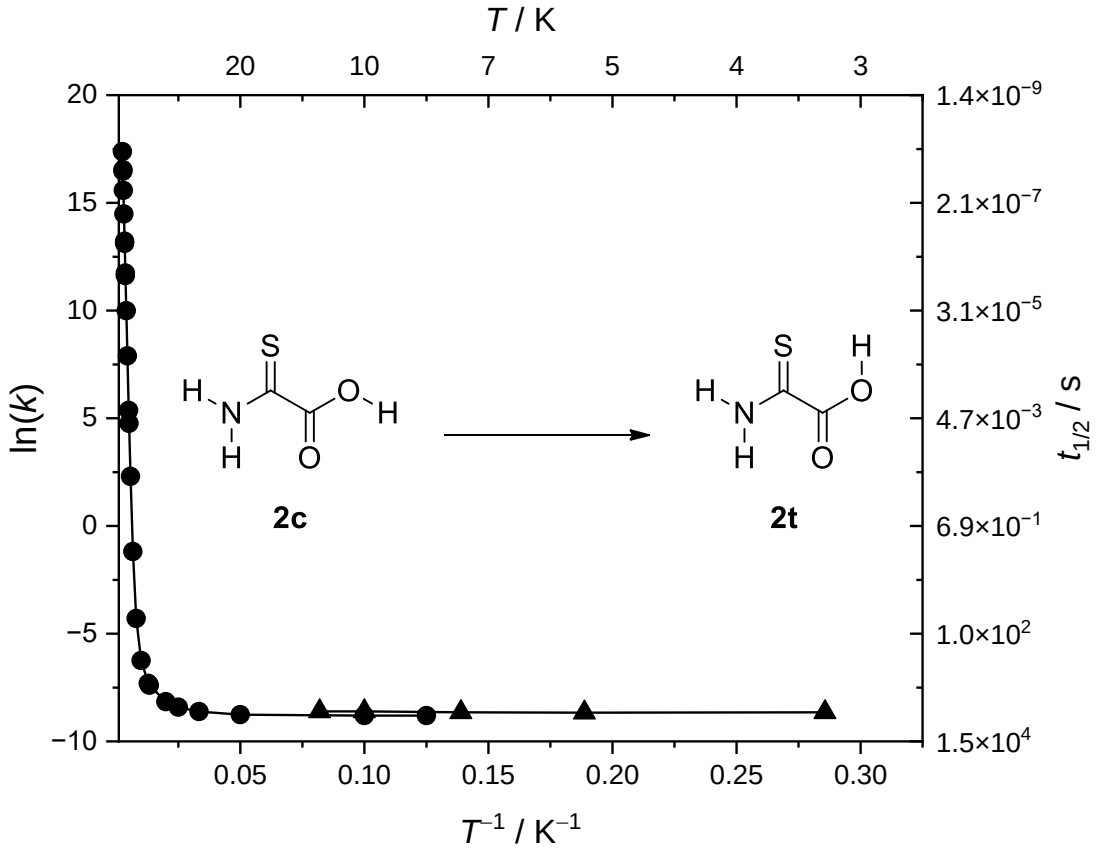

Fig. 31. Arrhenius plot of the **2t** → **2c** reaction. Below 20 K the rotamerization is only feasible *via* QMT since this reaction is associated with a barrier of 9.9 kcal mol^{-1} at the CCSD(T)/cc-pVTZ level of theory (circles: computed rates; triangles: experimental rates).

Figure 33 shows an example of the evaluation of the decay of **1t**-CO_2 (2336.1 cm^{-1}) at 3 K. A biexponential model is used for the fit function. A monoexponential function does not yield a good fit due to the presence of several matrix sites. To obtain *k*, t1 and t2 were scaled with A1 and A2 and the average of the resulting values was further used.

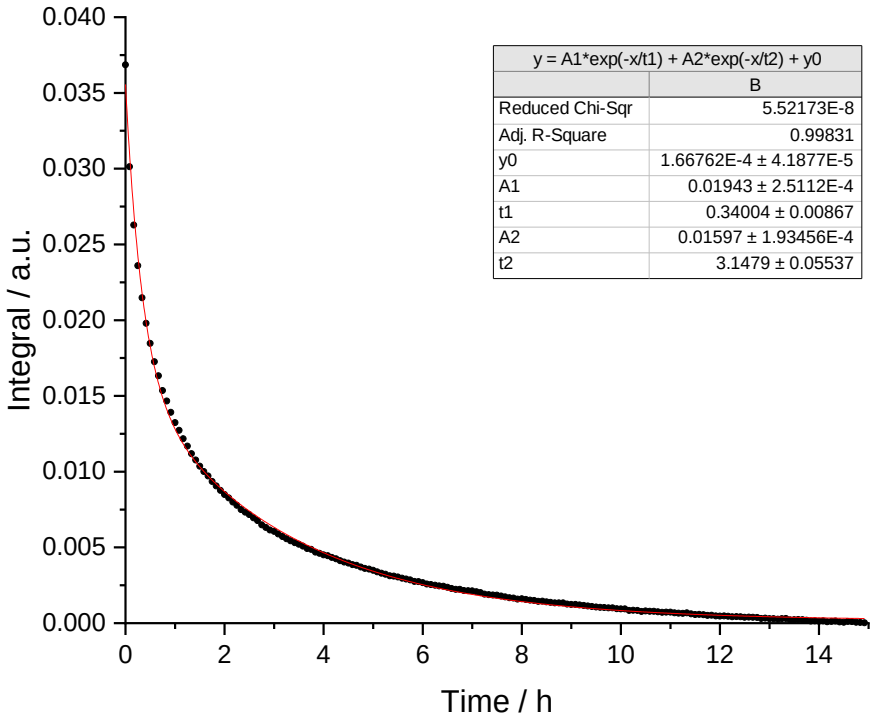

Fig. 32. Decay of the integral of the 2336.1 cm−1 IR band of **1t**-CO2 over time. Black: Measured values. Red: Biexponential fit function.

Figures 33 to 34 show the evaluation of the 2333.2 cm^{-1} band of **1t**-CO_2 compared to bands of **2c**. The resulting QMT half-life of the reaction at this matrix site amounts to ca. 90 h.

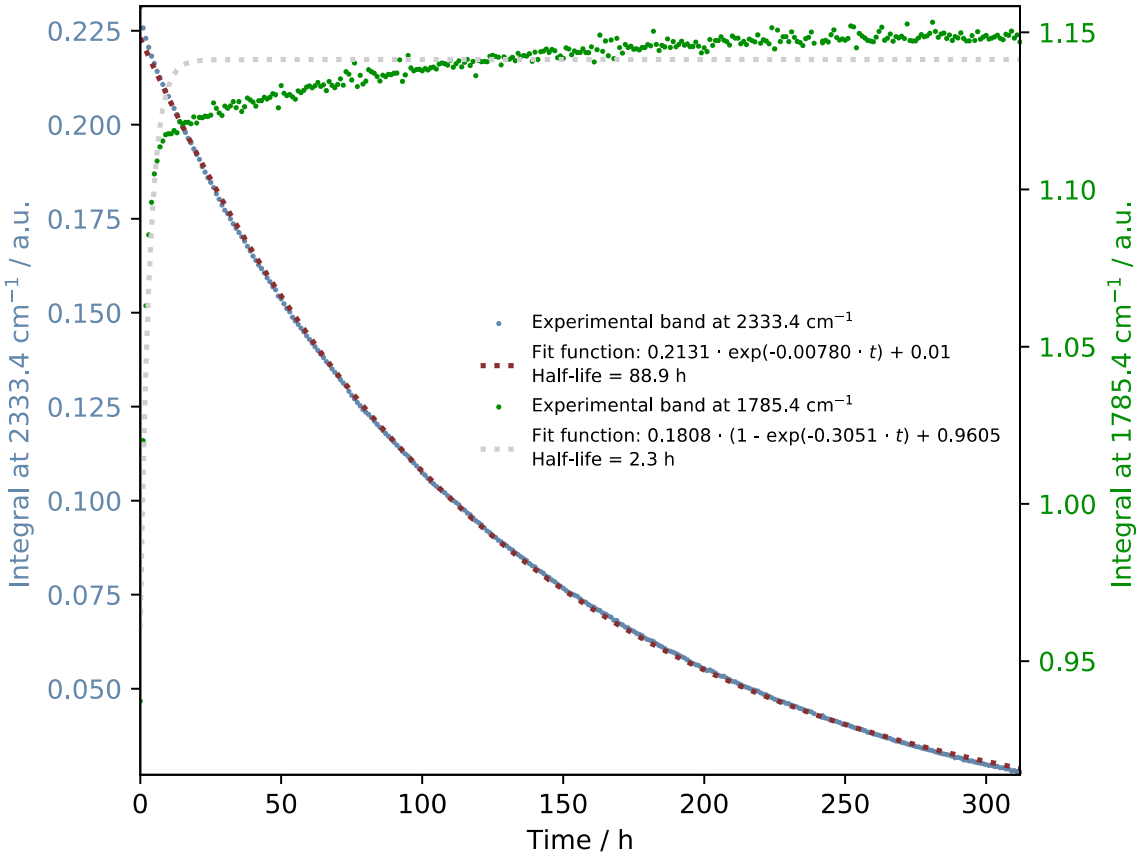

Fig. 33. Evaluation of the **1t**-CO_2 → **2c** reaction. The kinetics of **2c** are dominated by the reaction from **1t**-CO_2 at the above-mentioned matrix site at 2336.1 cm^{-1} and from further side products present after photolysis (*vide supra*).

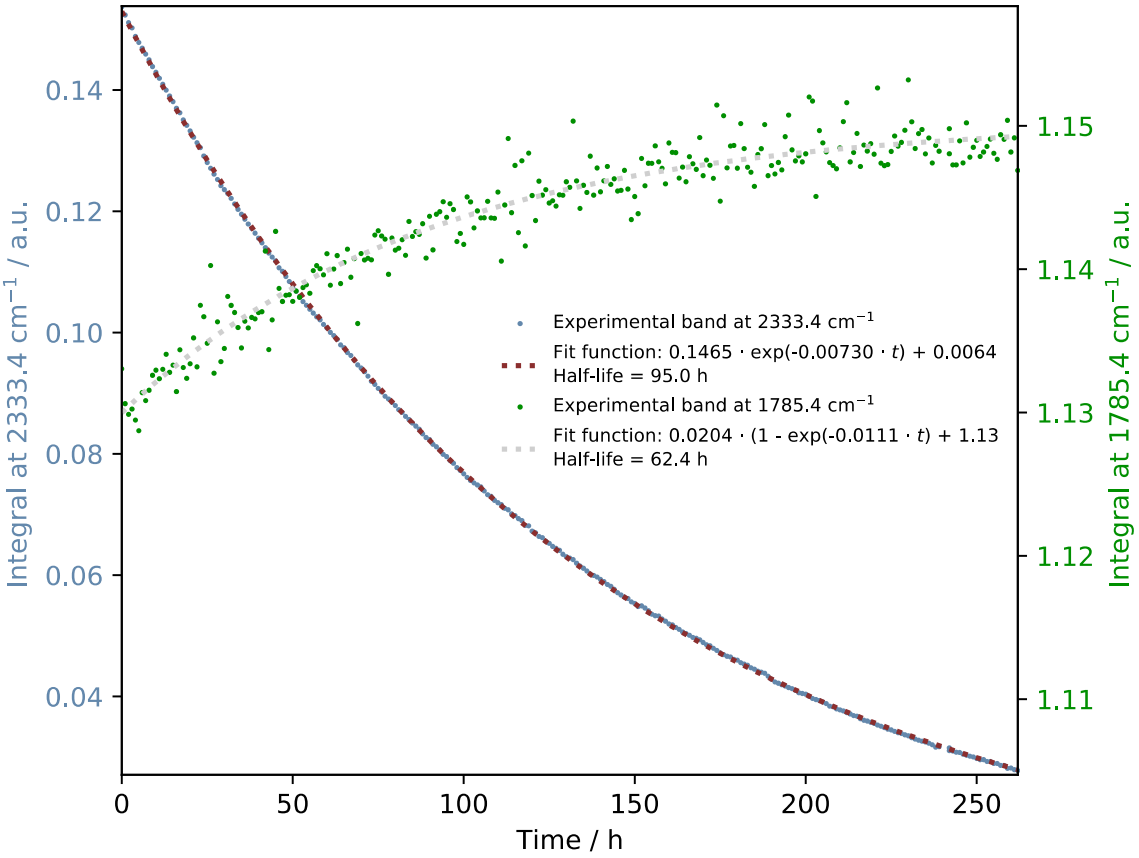

Fig. 34. Evaluation of the **1t**-CO_2 → **2c** (1785.4 cm^{-1}) reaction considering only the points recorded after 50 h when **1t**-CO_2 (2333.2 cm^{-1}) → **2c** is the dominant reaction (*cf.* Fig. 33).

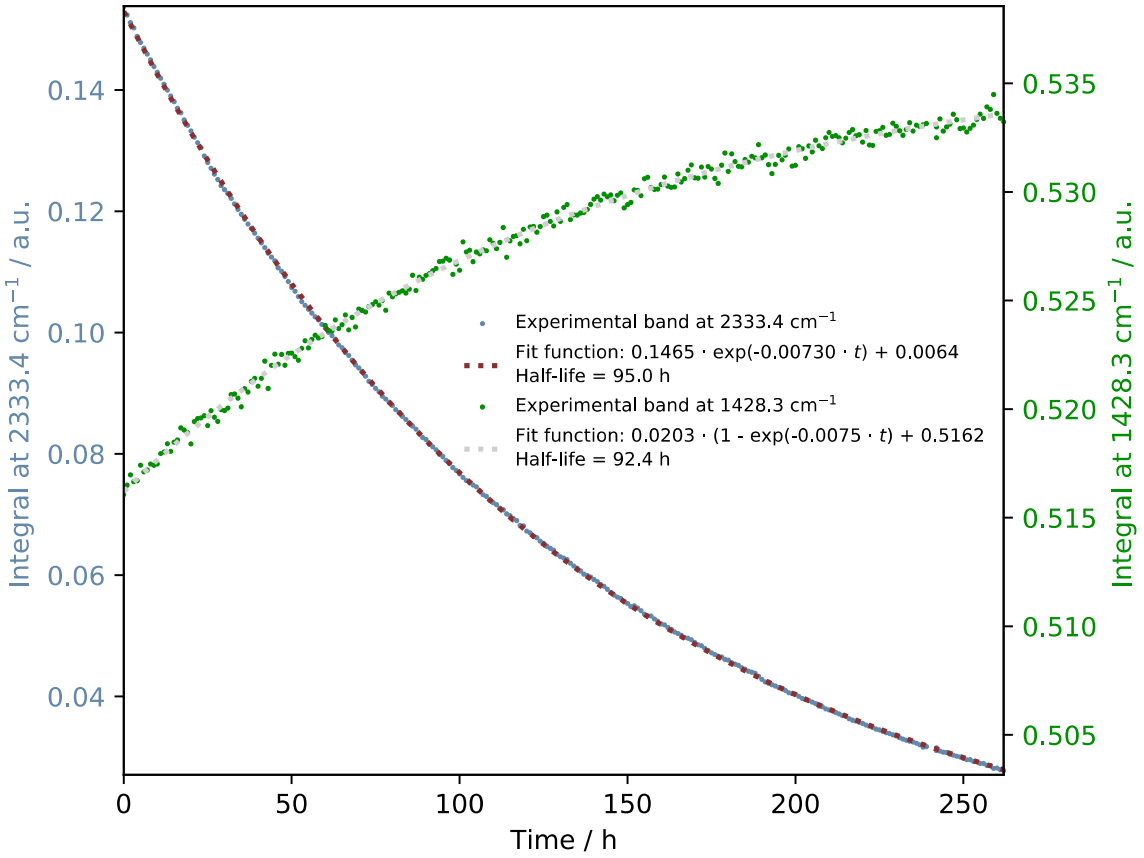

Fig. 35. Evaluation of the **1t**-CO_2 → **2c** (1428.3 cm^{-1}) reaction considering only the points recorded after 50 h when **1t**-CO_2 (2333.2 cm^{-1}) → **2c** is the dominant reaction (*cf.* Fig. 33).

We note that another way to assign the 2333.2 cm^{-1} band would be the *cis*-complex **1c**-CO_2 (computed: 2271.7 cm^{-1}). This band disappears with a long half-life (ca. 90 h) and the hindered rotation of the CS bond to give **1t**-CO_2 is associated with a barrier of 10.7 kcal mol^{-1} (CCSD(T)/cc-pVTZ + ZPVE). The overall **1c**-CO_2 → **1t**-CO_2 → **2c** reaction would represent a domino QMT process, for which only one other example has been reported[50]. However, the experimental half-life is not in accordance at all with the computed half-life of the **1c**-CO_2 → **1t**-CO_2 reaction (CVT/SCT//B3LYP/6-311+G(d,p): 5.23 x 10^{10} years at 10 K). Furthermore, the corresponding band also vanishes in the perdeuterated case providing another hint that these bands can indeed be assigned to different matrix sites of **1t**-CO_2 instead of **1c**-CO_2. Similar behavior has already been observed for other matrix-isolated compounds[50].

Kinetic Computations

Table 10. Computed rate constants at the CVT/SCT//B3LYP/6-311+G(d,p) level of theory. The values of the first reaction are plotted in an Arrhenius plot in the main text. The values of the second reaction are plotted in Fig. 26.

Reaction	Temperature / K	Computed k / s^{-1}	Computed $t_{1/2}$ / h
1t-CO_2 → **2c**	4.0	2.09 x 10^{-4}	0.92
	5.0	2.09 x 10^{-4}	0.92
	6.0	2.10 x10^{-4}	0.92
	8.0	2.13 x 10^{-4}	0.90
	10.0	2.31 x 10^{-4}	0.83
2t → 2c	4.0	N.A.	N.A.
	5.0	N.A.	N.A
	6.0	N.A.	N.A
	8.0	1.50 x 10^{-4}	1.28
	10.0	1.50 x10^{-4}	1.28

The computed rates of the reaction of **1t**-CO_2 to **2c** vary over several orders of magnitude depending on the basis set used in the computations (Table 11). This is expected to be a result of significant changes in the CC distance between **1** and CO_2 for the different basis sets (Table 12). The shortening of the CC distance for smaller basis sets matches our expectations when considering the basis set superposition error (BSSE)[82]. Thinking of the matrix cage, in which the complex forms, the complex might not reach its minimum gas-phase structure due to the restricted cage space (Fig. S31). In addition, different $t_{1/2}$ were measured at different matrix-sites, suggesting different geometries that result in markedly different tunneling rates. The changes in geometries caused by different basis sets can simulate the restrictions enforced by the matrix. B3LYP/6-311+G(d,p) simulates $t_{1/2}$ of the 2336.1 cm^{-1} matrix-site very accurately presumably because the computed CC distance is smaller than, *e.g.*, compared to the B3LYP/6-311++G(3df,3pd) minimum, whose resulting computed $t_{1/2}$ fits well with the 2333.2 cm^{-1} site (Table 11 and Fig. 36).

Table 11. Comparison of the computed half-lives of **1t**-CO_2 → **2c** at different levels of theory with experimental half-lives at different matrix-sites.

Level of Theory	$\Delta E^{\ddagger}$ **/ kcal mol^{-1}**	***k* / h^{-1}**	$t_{1/2}$ **(comp.)**	$t_{1/2}$ **(exp.)**
B3LYP/6-311++G(3df,3pd)	2.15	1.06 x 10^{-6}	7.6 d	3.8 d (2333.2 cm^{-1})
B3LYP/6-311+G(d,p)	1.85	2.09 x 10^{-4}	0.92 h	0.4 h (2336.1 cm^{-1})

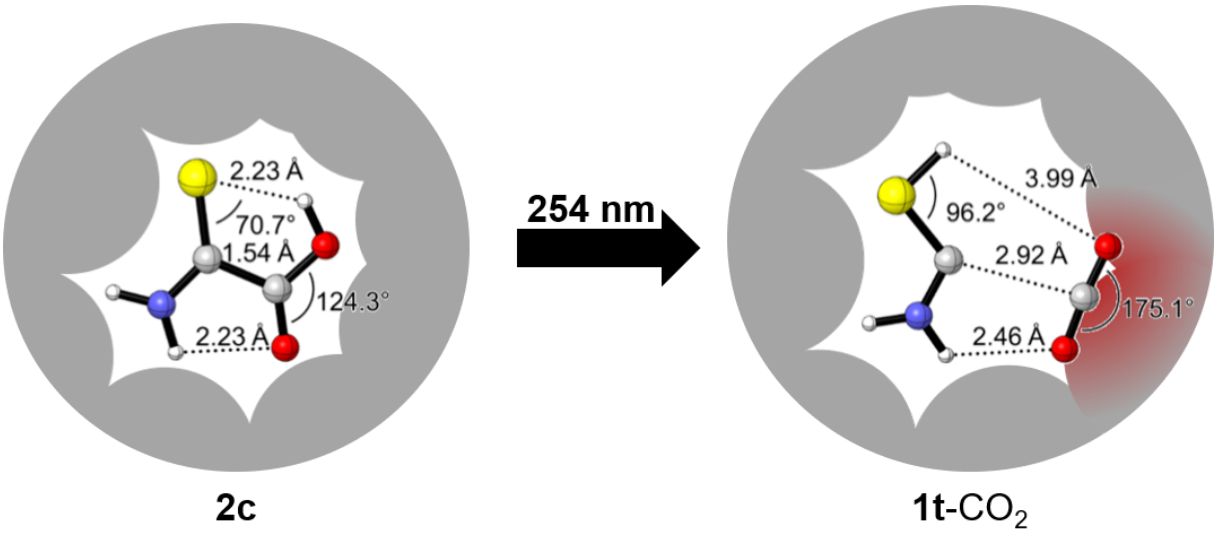

Fig. 36. The Ar matrix cage inhibits the system from reaching the minimum gas-phase geometry of **1t**-CO_2 after photolysis. Geometries were optimized at B3LYP/6-311++G(3df,3pd). The radius of the Ar atoms was approximated to 1.9 Å (Van-der-Waals-radius).[83]

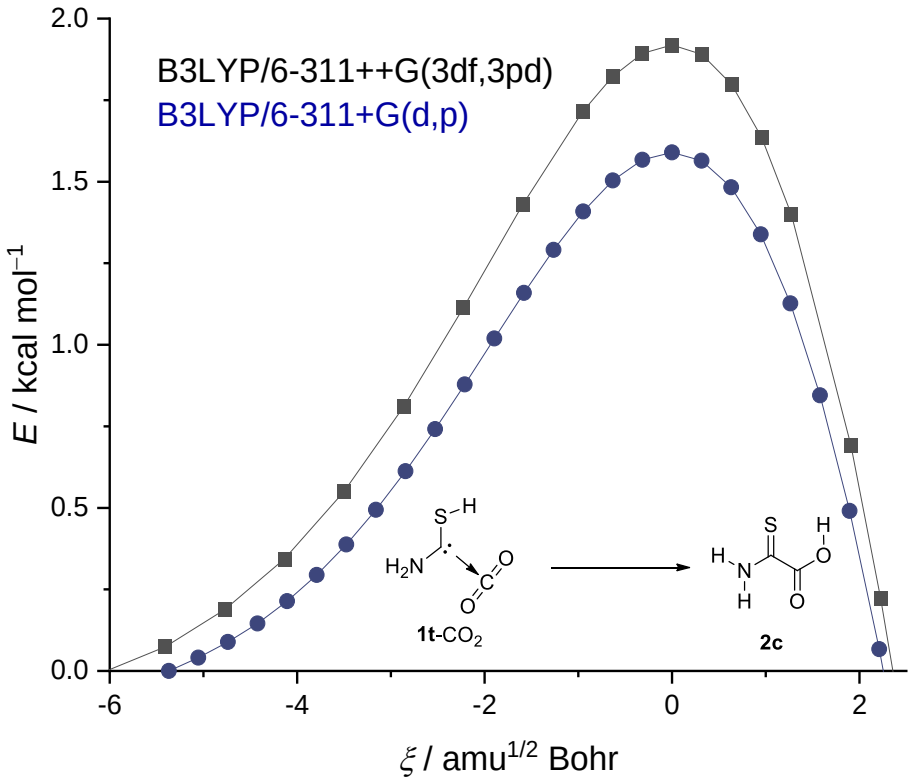

Fig. 37. 1t-CO_2 → **2c** IRC curves at two different levels of theory (only energy values above 0 kcal mol^{-1} are shown). The smaller basis set mimics the surrounding of the complex in the 2336.1 cm^{-1} matrix cage better, while the larger basis set fits $t_{1/2}$ of the 2333.2 cm^{-1} site. The different barrier widths and heights result from different C–C distances in **1t**-CO_2 (Table 12).

We conclude that a smaller C–C bond distance indeed better represents the minimum structure in the 2336.1 cm^{-1} matrix-site than gas phase minimum structures obtained at higher levels of theory. As expected, the rotamerization of **2t** to **2c** was rather insensitive to changes in the basis set, because of the smaller influence on geometries of covalent bonds on the reaction rate. As this reaction does not exhibit noncovalently bound fragments, we also expect a smaller effect of the matrix cage on the geometries compared to the reaction from **1t**-CO_2 to **2c** (Table 12).

Table 12. Comparison of the influence of the level of theory on the C–C bond distance of **2c** and **1t**-CO_2.

Level of Theory	C–C distance **2c** / Å	C–C distance **1t**-CO_2 / Å
B3LYP/6-311++G(3df,3pd)	1.540	3.005
B3LYP-D3BJ/6-311++G(3df,3pd)	1.538	2.851
B3LYP/6-311+G(d,p)	1.543	2.971
B3LYP/6-31+G(d,p)	1.543	2.942
CCSD(T)/cc-pVTZ	1.539	2.963

NBO and QTAIM Analysis.

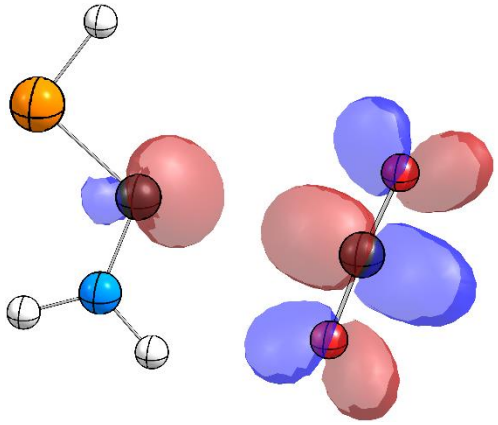

Fig. 38. Electron donation from the carbene lone pair to the π*-CO_2 orbital results in an attractive interaction between **1t** and CO_2.

Table 13. Selected parameters obtained from a QTAIM analysis of **1t**-CO_2 at the B3LYP/6-311++G(3df,3pd) level of theory.

Entry	Type	Atoms	ρ / eÅ^{-3}	$-\nabla^2\rho$ / eÅ^{-5}	G(r) / ρ (r)	H(r) / eÅ^{-3}
1	BCP1	C1 - O7	0.011169	+0.033811	+0.007124	−0.001328
2	BCP2	C1 - N3	0.345661	−0.902908	+0.329806	+0.555533
3	BCP3	N3 - H5	0.343694	−1.714455	+0.060493	+0.489107
4	BCP4	H4 - O7	0.009954	+0.039526	+0.008254	−0.001628
5	BCP5	N3 - H4	0.353381	−1.919840	+0.056557	+0.536517
6	BCP6	C1 - S6	0.212440	−0.405396	+0.069516	+0.170865
7	BCP7	C2 - O7	0.467088	−0.085893	+0.858614	+0.880088
8	BCP8	C2 - O8	0.474101	−0.005124	+0.898183	+0.899464
9	BCP9	S6 - H9	0.225051	−0.705425	+0.051033	+0.227389
10	RCP1	C1 - N3 - H4 - O7	0.008225	+0.035906	+0.007624	−0.001352

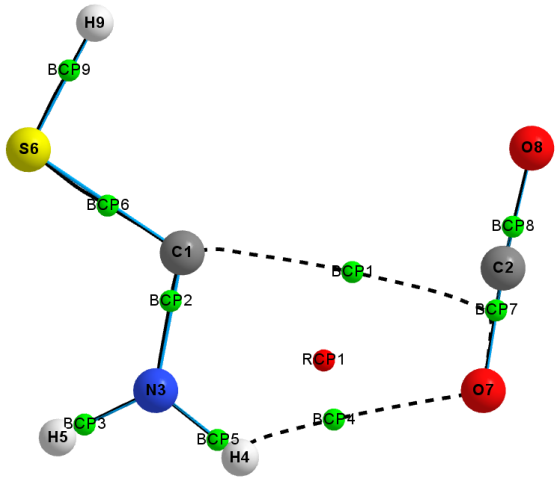

Fig. 39. BCP1 and BCP4 represent attractive interactions compared to hydrogen bonds in different systems showing resonance-assisted hydrogen bonds.[84]

Table 14. Selected parameters obtained from a QTAIM analysis of **TS: 1t**-CO_2 → **2c** at the B3LYP/6-311++G(3df,3pd) level of theory.

Entry	Type	Atoms	ρ / eÅ^{-3}	$-\nabla^2\rho$ / eÅ^{-5}	G(r) / ρ (r)	H(r) / eÅ^{-3}
1	BCP1	C1 - C7	0.015865	+0.065980	+0.014056	-0.002439
2	BCP2	C1 - N2	0.065154	+0.052796	+0.028036	+0.014837
3	BCP3	N2 - H5	0.224839	-0.704291	+0.047381	+0.223454
4	BCP4	C1 - S3	0.348184	-1.943924	+0.053775	+0.539757
5	BCP5	N2 - H4	0.347666	-1.812744	+0.058621	+0.511807
6	BCP6	S3 - H6	0.213184	-0.414497	+0.072635	+0.176260
7	BCP7	H4 - O8	0.352877	-0.946339	+0.333683	+0.570268
8	BCP8	C7 - O8	0.442635	-0.334663	+0.737026	+0.820692
9	BCP9	C7 - O9	0.450880	-0.264327	+0.777743	+0.843825
10	RCP1	C1 – N2 - H4 – O8 – C7	0.015317	+0.078707	+0.016603	-0.003073

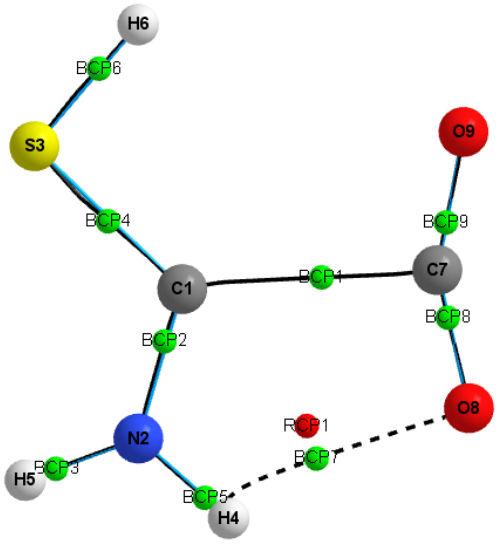

Fig. 40. BCPs and RCP of **TS: 1t-**CO_2 → **2c.**

Computed Potential Energy Surfaces.

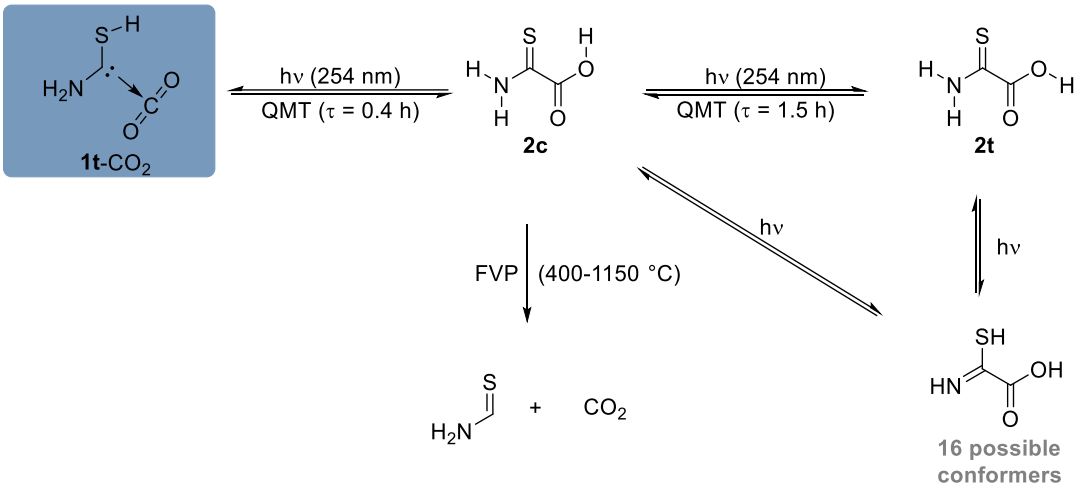

Fig. 41. Reaction network of **2**.

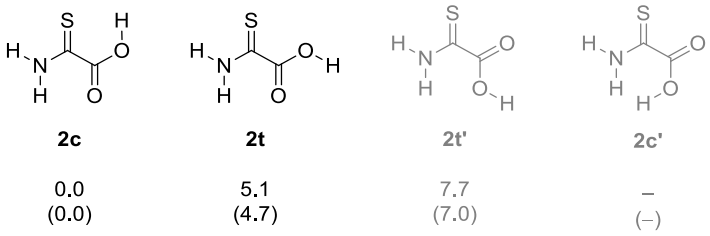

Fig. 42. There are three C_s symmetric conformers of 2-amino-2-thioxoacetic acid (**2**). Among them, **2c** is the most stable one. Conceivable conformer **2c'** could not be located as a local minimum structure even when its geometry was not restricted to the C_s point group. Energies including ZPVEs are given in kcal mol^{-1} at the B3LYP/6-311++G(3df,3pd) (MP2/def2-QZVPP, in brackets) level of theory.

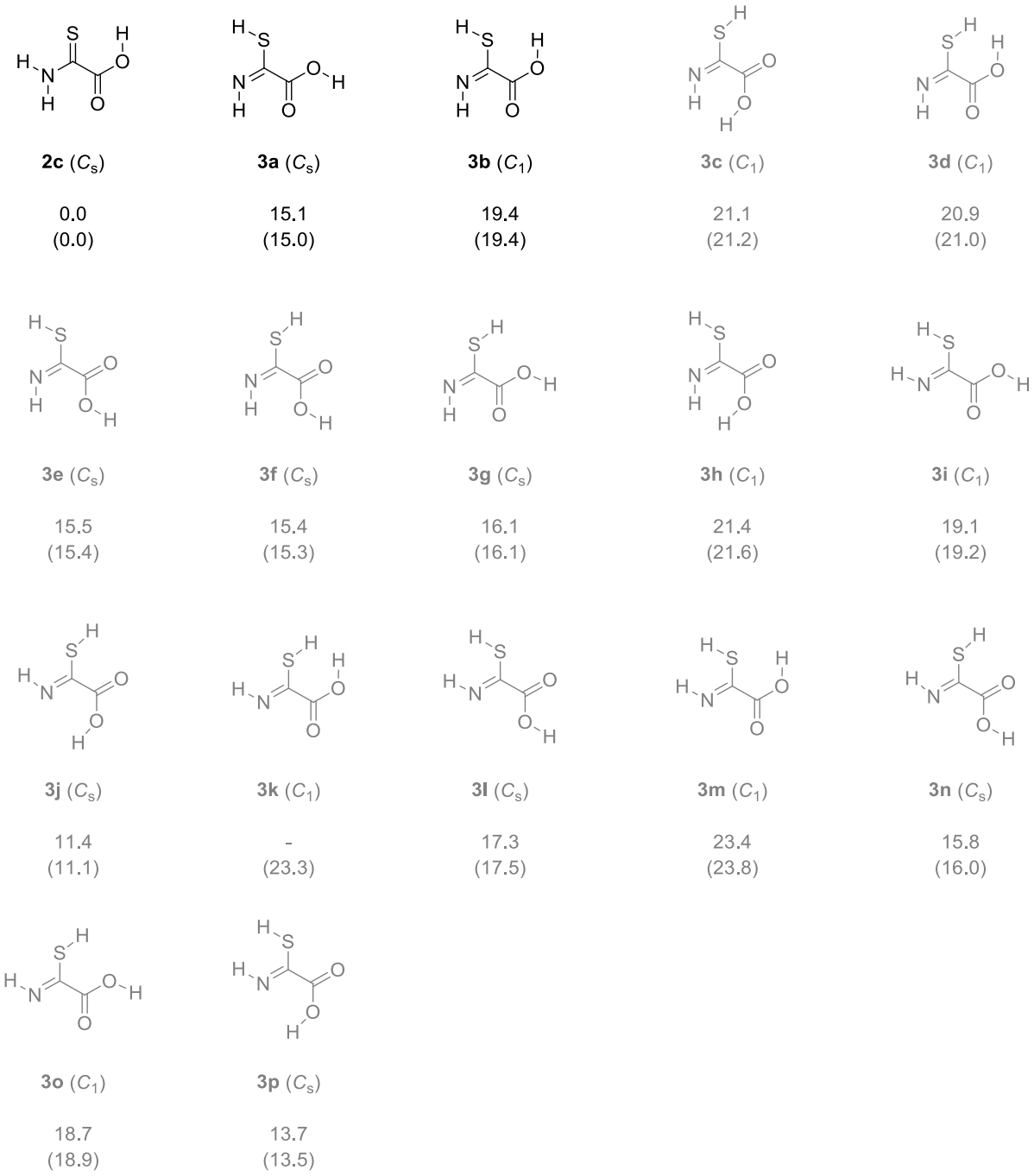

Fig. 43. There are 16 conformers of the thiolimine tautomer of **2**. Energies including ZPVEs are given in kcal mol^{-1} with respect to **2c** at the B3LYP/6-311++G(3df,3pd) (MP2/def2-QZVPP, in brackets) level of theory. For C_1 symmetric conformers, the corresponding C_s geometries represent transition states of the respective rotamerization, which are associated with barriers <1 kcal mol^{-1}. **3k** could not be localized as a stationary point at the B3LYP/6-311++G(3df,3pd) level of theory.

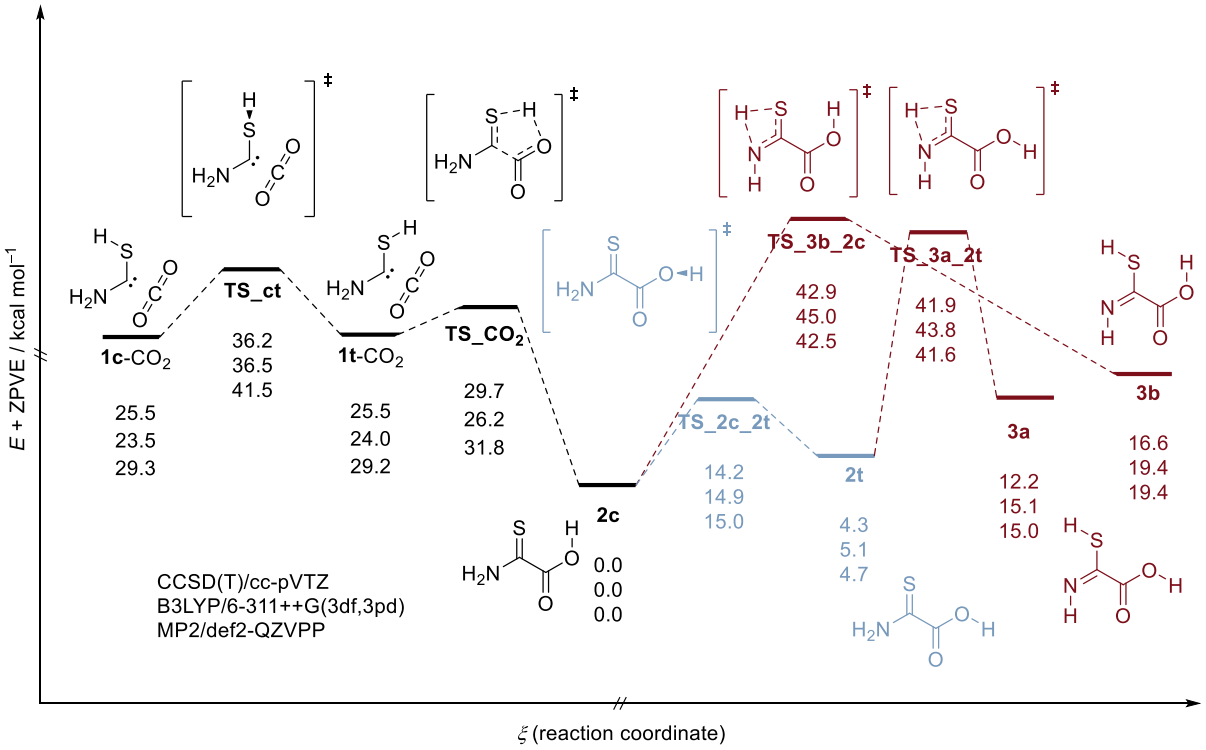

Fig. 44. PES of experimentally observed species. Black: Photodecarboxylation. Blue: Rotamerization. Red: Isomerization.

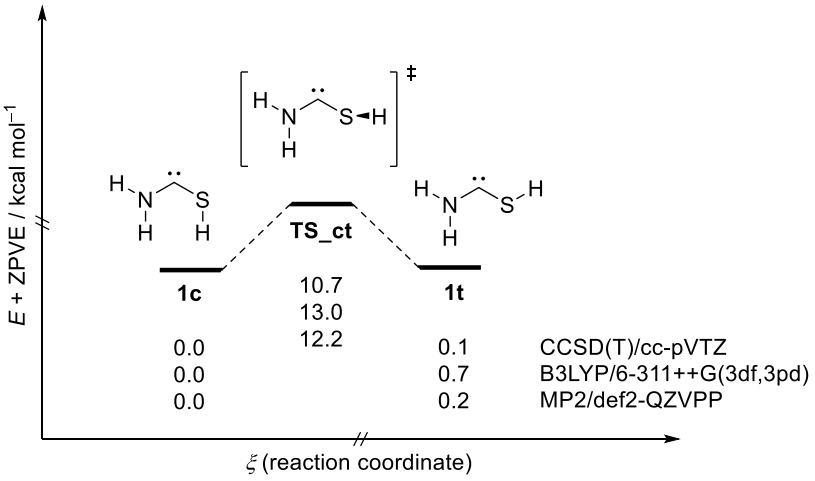

Fig. 45. PES of the rotamerization of free aminomercaptomethylene **1**.

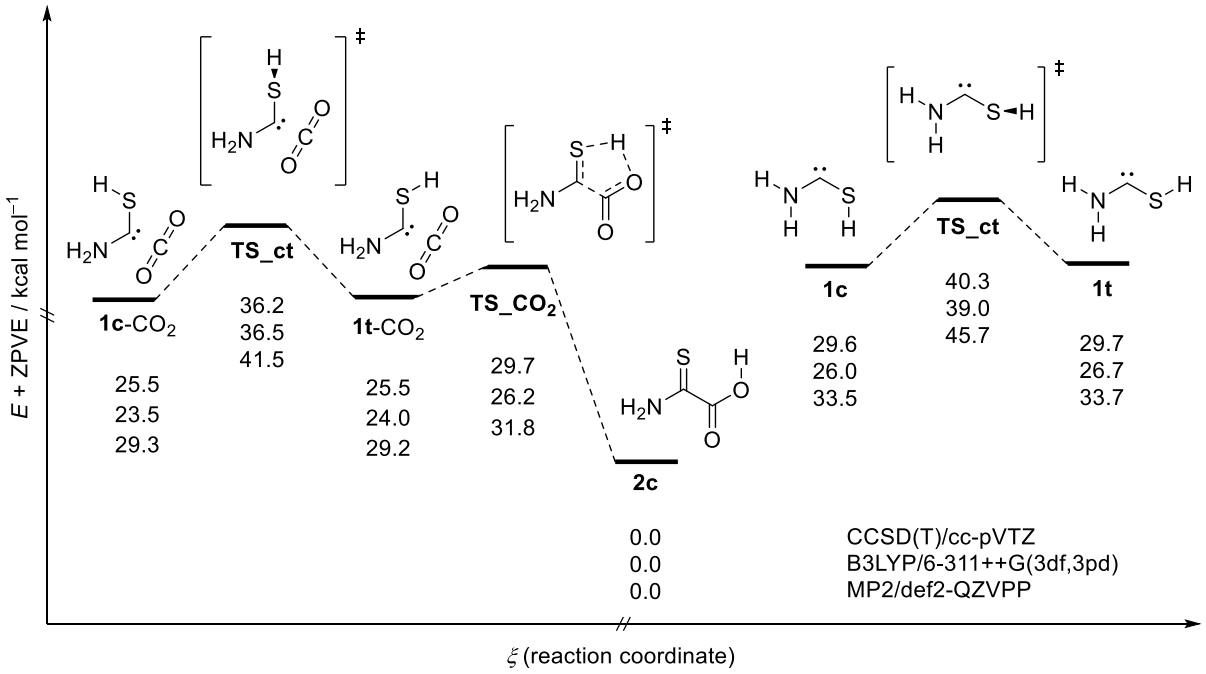

Fig. 46. Comparison of the PESs of **1**-CO_2 (left) and free **1** (right). The energetics of the right PES were obtained by adding the energy of CO_2 computed at the respective level of theory. The complex is stabilized by ca. 4 kcal mol^{-1} compared to free **1**.

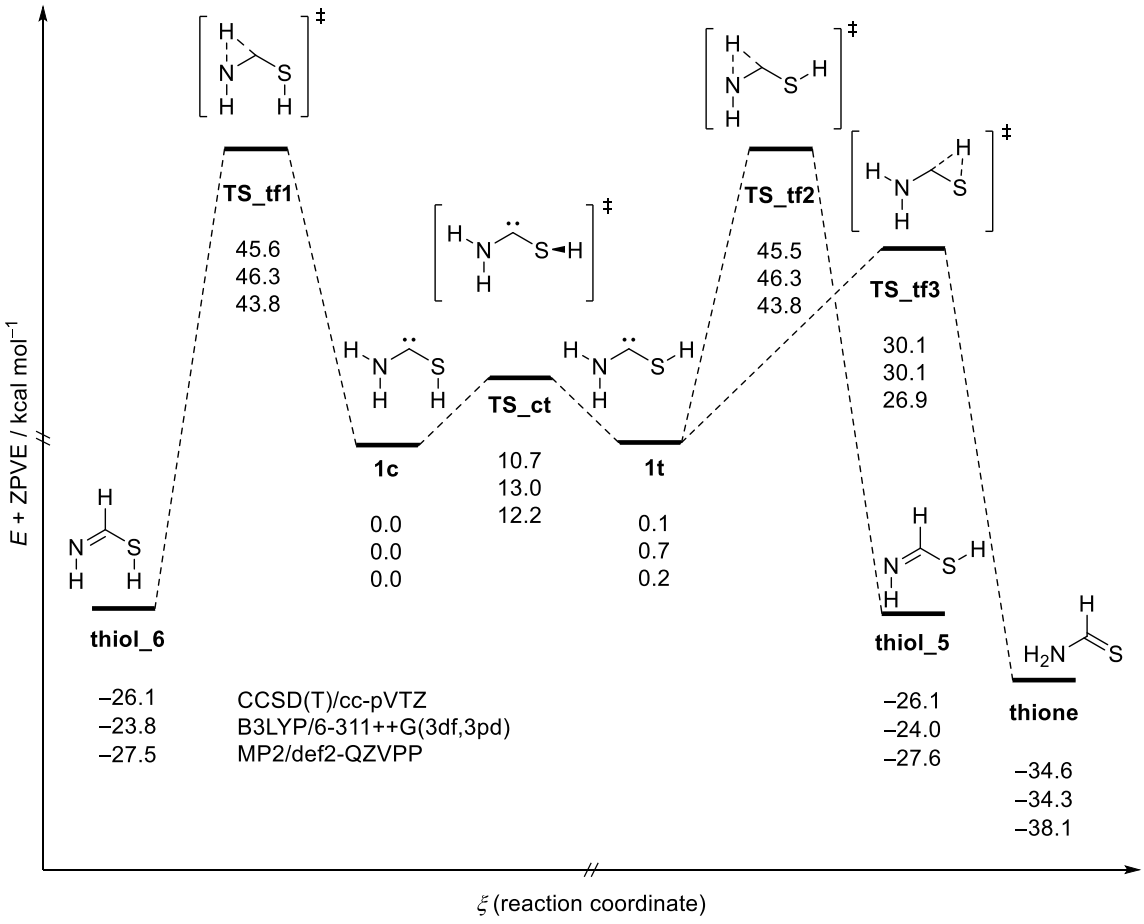

Fig. 47. Connection between free aminomercaptocarbene **1** and thioformamide. Note that **TS_tf3** is planar (C_s) at B3LYP/6-311++G(3df,3pd) and at MP2/def2-QZVPP while it bears C_1 symmetry at CCSD(T)/cc-pVTZ.

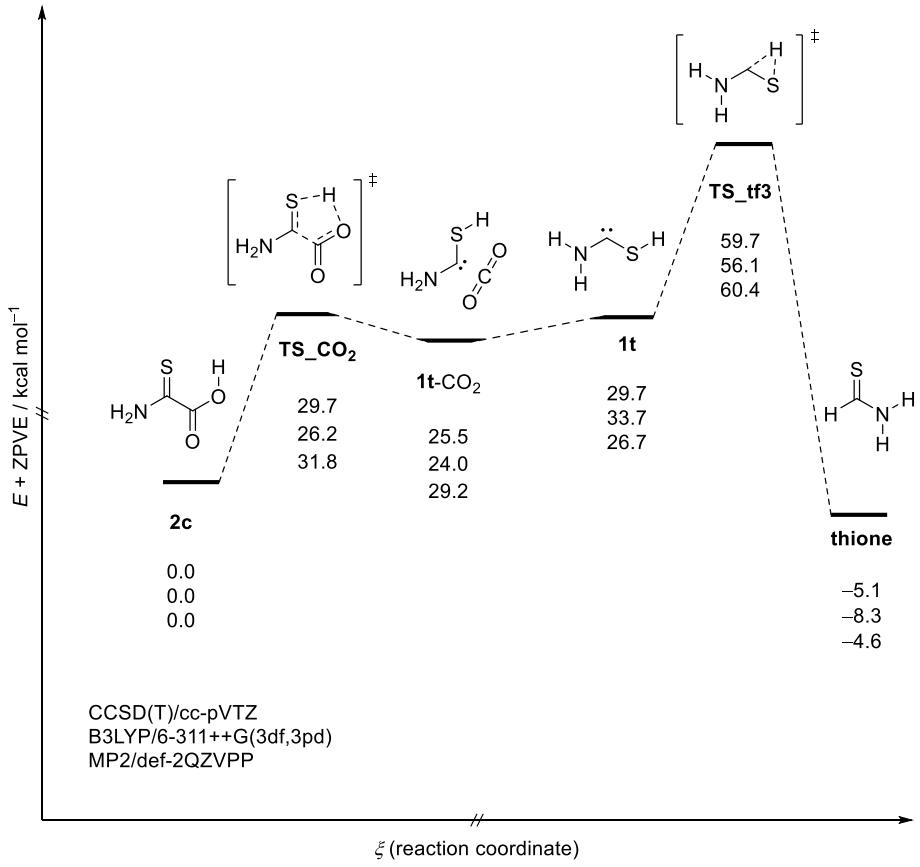

Fig. 48. PES of the pyrolysis of **2c** *via* **1t**-CO_2 and **1t** to yield thioformamide (**thione**) at 0 K. Note that **TS_tf3** is planar (C_s) at B3LYP/6-311++G(3df,3pd) and at MP2/def2-QZVPP while it bears C_1 symmetry at CCSD(T)/cc-pVTZ. Some energies were corrected for CO_2 loss. CO_2 was computed at the respective level of theory.

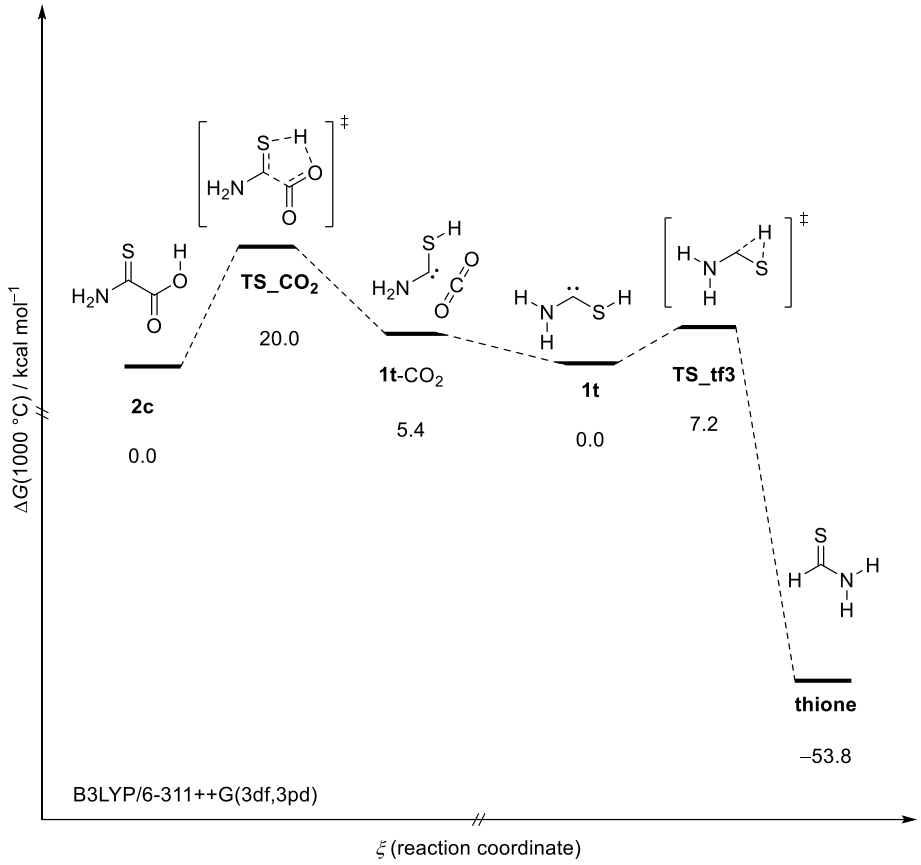

Fig. 49. PES of the pyrolysis of **2c** *via* **1t**-CO_2 and **1t** to yield thioformamide (**thione**) at 1273.15 K (1000 °C). Some energies were corrected for CO_2 loss. CO_2 was computed at the same level of theory. The low activation barrier (**TS_tf3**) is presumably the reason for the absence of **1** in our pyrolysis experiments. For analogue PESs of related systems see below.

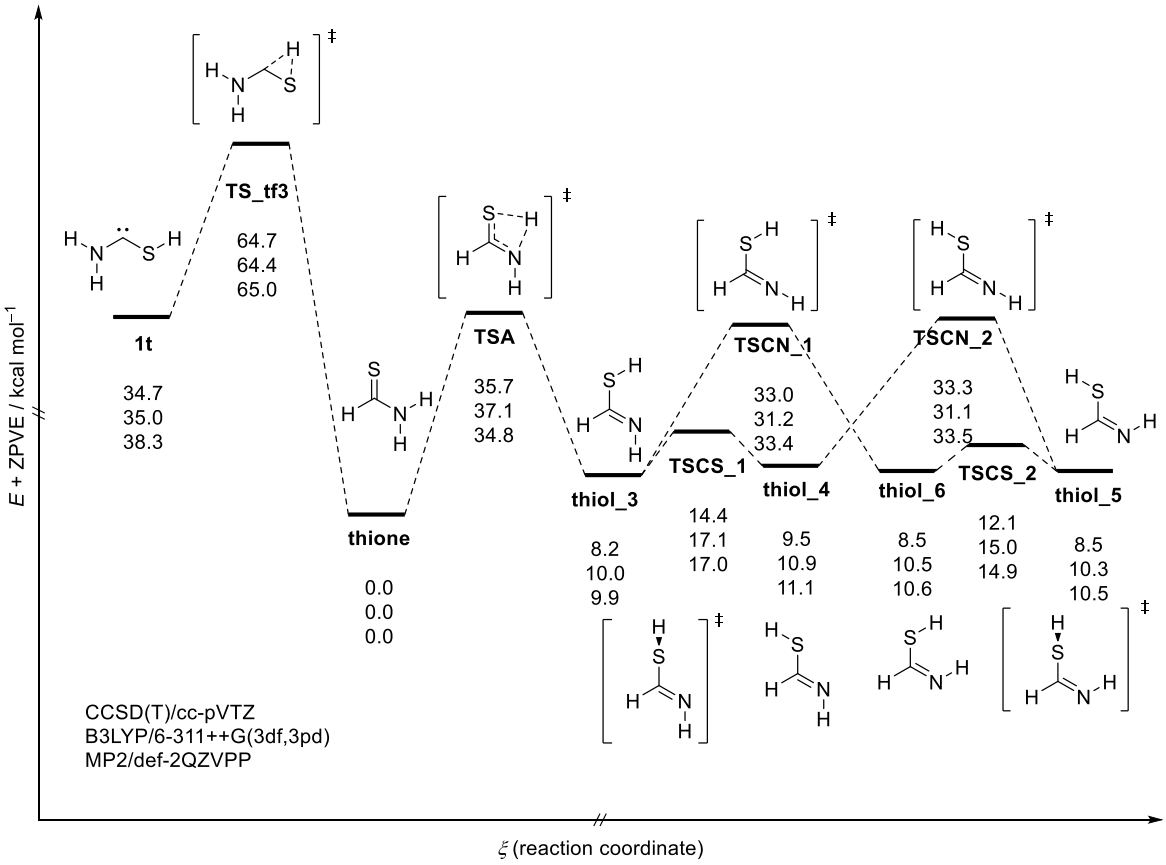

Fig. 50. PES of thioformamide and connection to **1**. Note that **TS_tf3** is planar (C_s) at B3LYP/6-311++G(3df,3pd) and at MP2/def2-QZVPP while it bears C_1 symmetry at CCSD(T)/cc-pVTZ.

Other Carbene-CO_2 Complexes

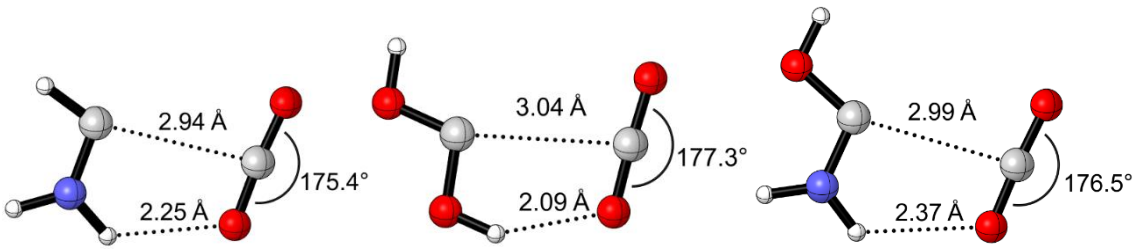

Fig. 51. Minimum geometries of aminomethylene-CO_2, dihydroxymethylene-CO_2, and aminohydroxymethylene-CO_2 complexes at the CCSD(T)/cc-pVTZ level of theory.

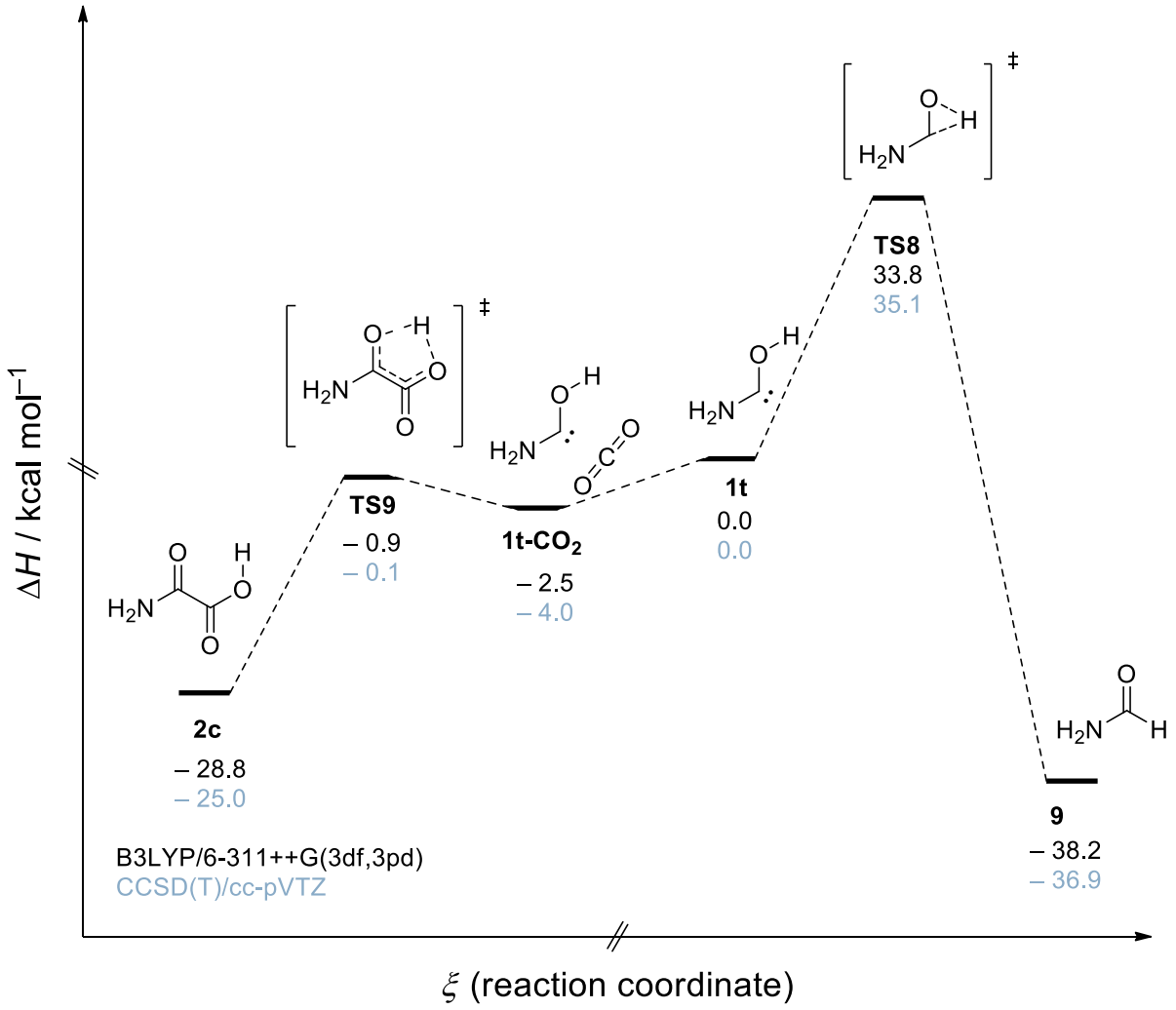

Fig. 52. PES around aminohydroxymethylene.[65] Some energies were corrected for CO_2 loss. CO_2 was computed at the same level of theory.

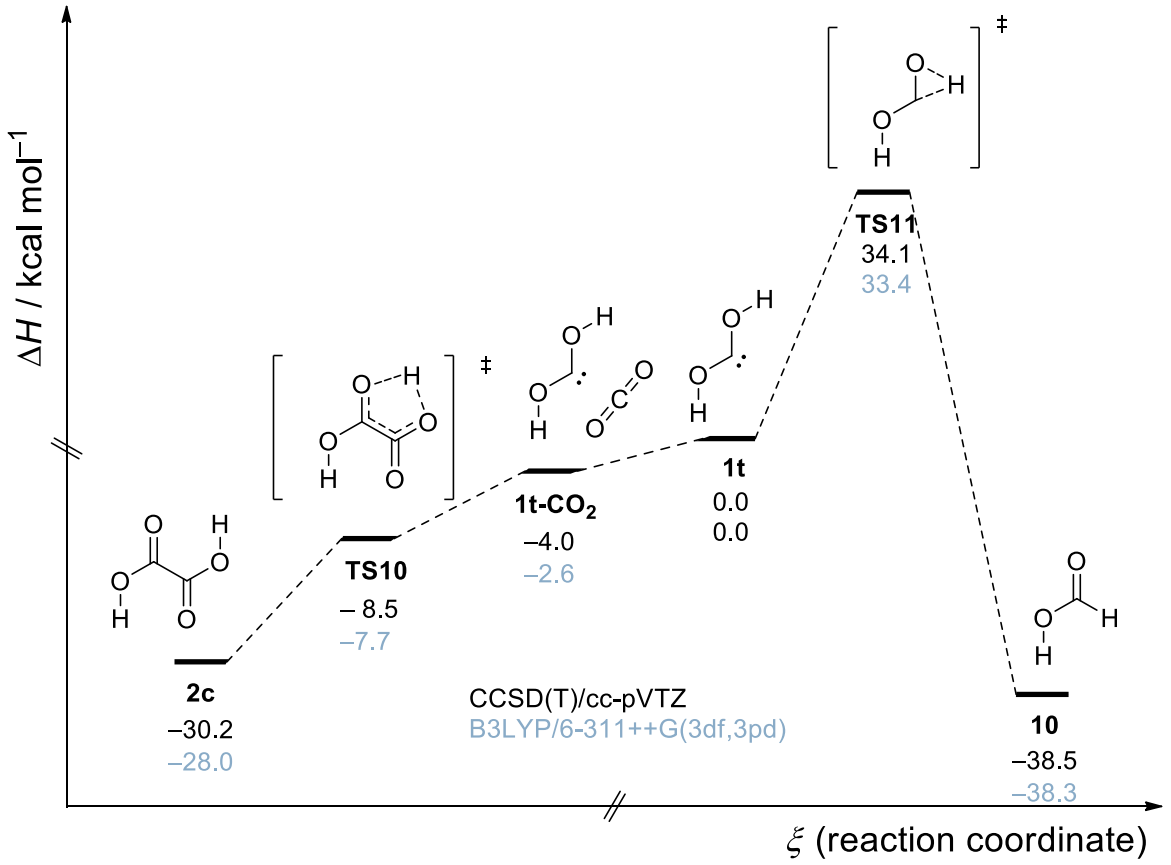

Fig. 53. PES around dihydroxycarbene.[85] Some energies were corrected for CO_2 loss. CO_2 was computed at the same level of theory (ZPVE was not considered, the reaction is pseudo-barrierless).

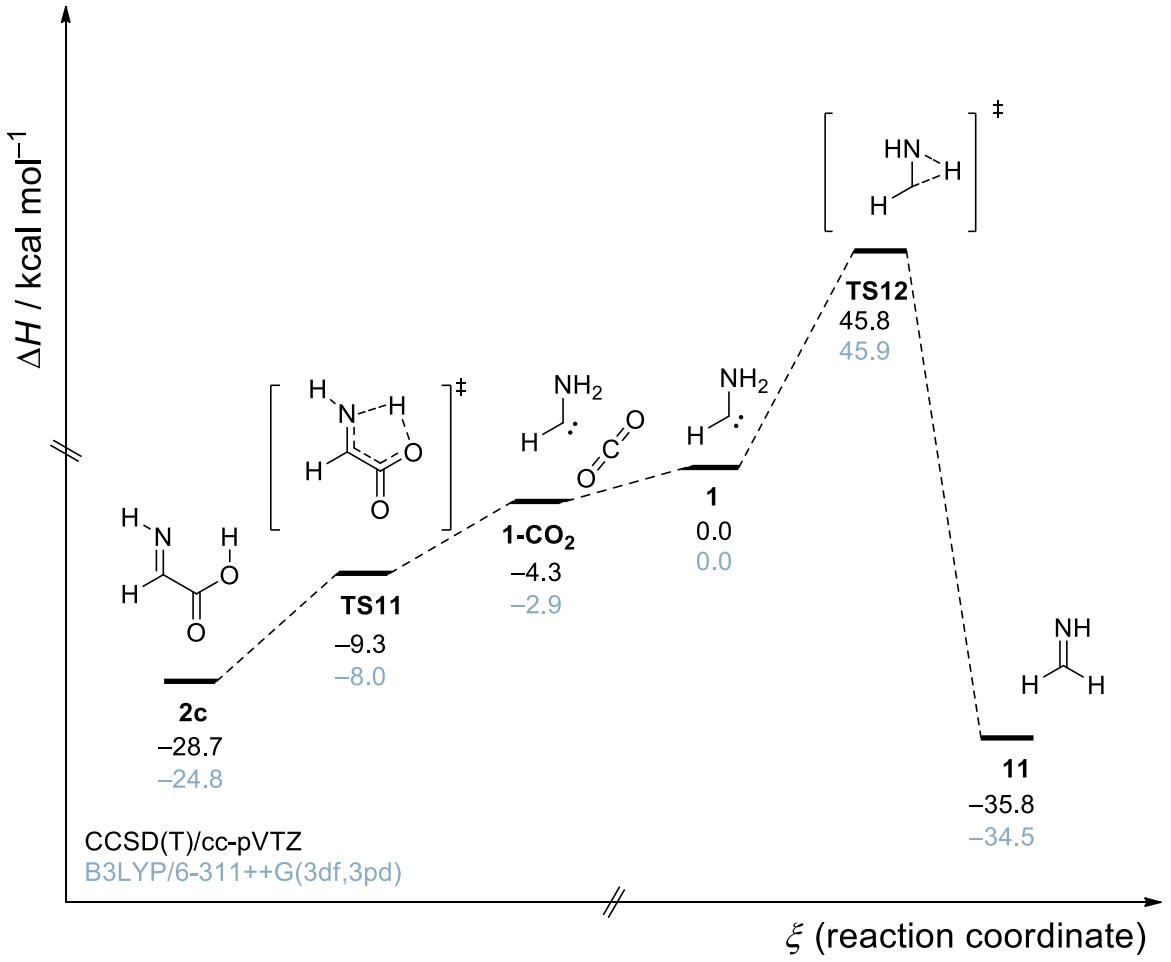

Fig. 54. PES around aminomethylene.[64] Some energies were corrected for CO_2 loss. CO_2 was computed at the same level of theory (ZPVE was not considered, the reaction is pseudo-barrierless).

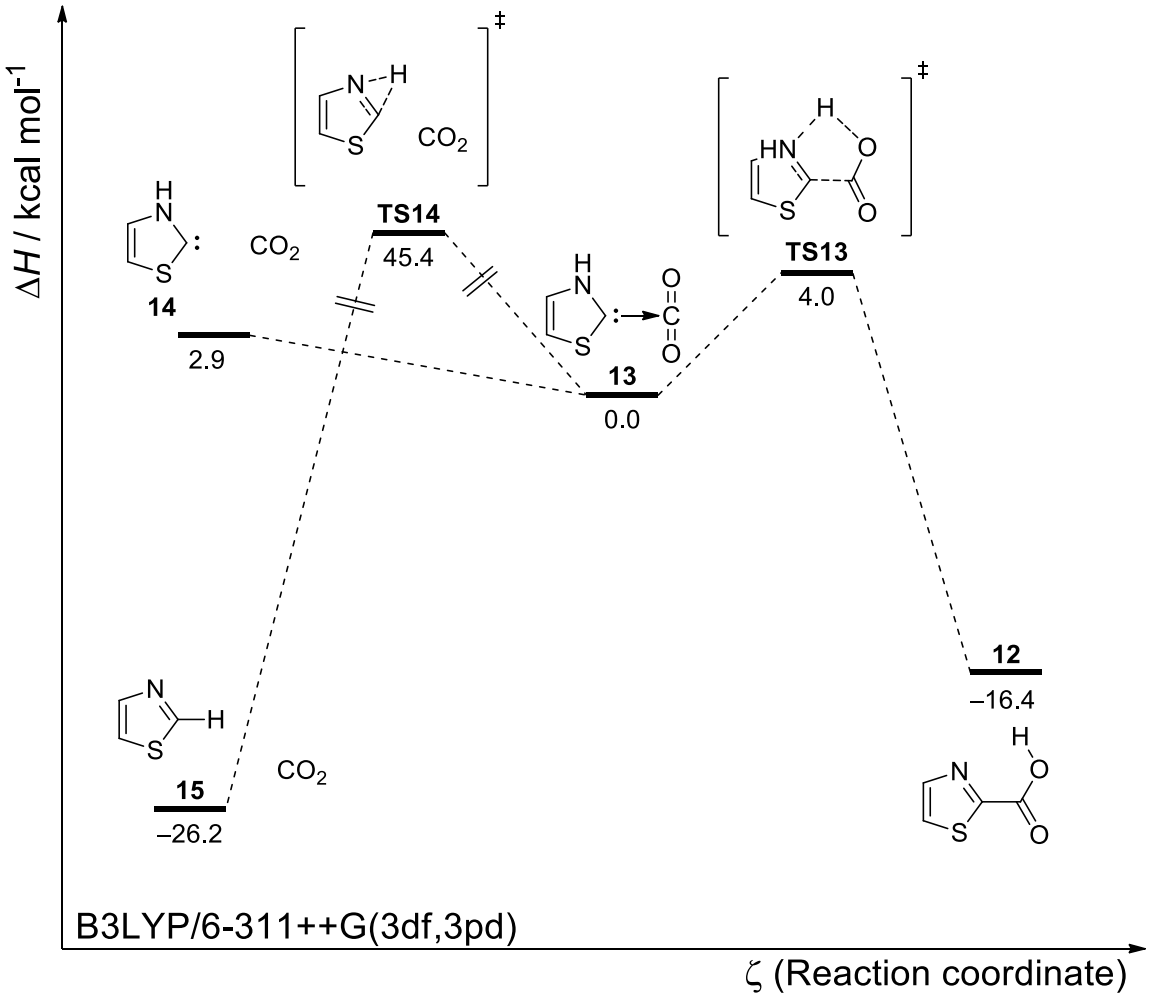

Fig. 55: PES of **13** at the B3LYP/6-311++G(3df,3pd) level of theory.

Tunneling Computations

Table 15. Overview of CVT/SCT tunneling half-lives at the B3LYP/6-311+G(d,p) level of theory. The symmetry number accounts for the degeneracy of the reaction path.

Reaction	Symmetry Number	Tunneling Half-Life
1t-CO_2 → **2c**	1	0.92 h (4 K)
1t-CO_2-d_3 → **2c**-d_3	1	4.32 h (4 K)
1t-$^{13}CO_2$ → **2c**-^{13}C	1	1.55 h (4 K)
3a → **2t**	1	433 a (30 K)
3b → **2c**	1	1.61 a (20 K)
2t → **2c**	2	1.28 h (8 K)
1t-CO_2 → **1c**-CO_2	2	7.55 x 10^{10} a (10 K)
1c-CO_2 → **1t**-CO_2	2	5.23 x 10^{10} a (10 K)
1c → **thiol_6**	2	1.00 x 10^{10} a (35 K)
1t → **thiol_5**	2	9.05 x 10^{9} a (35 K)
1t → **thione**	1	2.63 a (25 K)

Table 16. Computed rate constants in s^{-1} of the reaction **1t**-CO_2 → **2c** at the B3LYP/6-311+G(d,p) level of theory.

T / K	TST	CVT	CVT/ZCT	CVT/SCT
4.00	4.48×10^{-94}	6.08×10^{-95}	7.58×10^{-5}	2.09×10^{-4}
5.00	3.78×10^{-73}	7.64×10^{-74}	7.58×10^{-5}	2.09×10^{-4}
6.00	3.49×10^{-59}	9.19×10^{-60}	7.59×10^{-5}	2.10×10^{-4}
8.00	1.06×10^{-41}	3.89×10^{-42}	7.80×10^{-5}	2.13×10^{-4}
10.00	3.44×10^{-31}	1.54×10^{-31}	8.78×10^{-5}	2.31×10^{-4}
20.00	4.41×10^{-10}	2.92×10^{-10}	1.23×10^{-3}	1.99×10^{-3}
30.00	5.15×10^{-3}	3.88×10^{-3}	2.07×10^{-1}	2.36×10^{-1}
40.00	1.76×10^{1}	1.40×10^{1}	6.71×10^{1}	6.87×10^{1}
50.00	2.29×10^{3}	1.88×10^{3}	4.39×10^{3}	4.43×10^{3}
75.00	1.42×10^{6}	1.20×10^{6}	1.61×10^{6}	1.61×10^{6}
77.36	2.09×10^{6}	1.77×10^{6}	2.31×10^{6}	2.32×10^{6}
100.00	3.33×10^{7}	2.82×10^{7}	3.19×10^{7}	3.20×10^{7}
125.00	2.14×10^{8}	1.79×10^{8}	1.88×10^{8}	1.88×10^{8}
150.00	7.22×10^{8}	5.94×10^{8}	5.98×10^{8}	5.98×10^{8}
175.00	1.70×10^{9}	1.38×10^{9}	1.34×10^{9}	1.34×10^{9}
194.70	2.84×10^{9}	2.26×10^{9}	2.17×10^{9}	2.17×10^{9}
200.00	3.21×10^{9}	2.54×10^{9}	2.42×10^{9}	2.42×10^{9}
225.00	5.23×10^{9}	4.06×10^{9}	3.78×10^{9}	3.78×10^{9}
250.00	7.70×10^{9}	5.85×10^{9}	5.35×10^{9}	5.35×10^{9}
273.15	1.03×10^{10}	7.69×10^{9}	6.91×10^{9}	6.91×10^{9}
275.00	1.05×10^{10}	7.84×10^{9}	7.03×10^{9}	7.03×10^{9}
298.15	1.34×10^{10}	9.79×10^{9}	8.64×10^{9}	8.64×10^{9}
300.00	1.37×10^{10}	9.95×10^{9}	8.76×10^{9}	8.77×10^{9}
325.00	1.70×10^{10}	1.21×10^{10}	1.05×10^{10}	1.05×10^{10}
350.00	2.05×10^{10}	1.43×10^{10}	1.21×10^{10}	1.22×10^{10}
373.15	2.38×10^{10}	1.62×10^{10}	1.36×10^{10}	1.36×10^{10}
375.00	2.41×10^{10}	1.64×10^{10}	1.37×10^{10}	1.37×10^{10}
400.00	2.77×10^{10}	1.84×10^{10}	1.52×10^{10}	1.52×10^{10}

Table 17. Computed rate constants in s^{-1} of the reaction **1t**-CO_2-d_3 → **2c**-d_3 at the B3LYP/6-311+G(d,p) level of theory.

T / K	TST	CVT	CVT/ZCT	CVT/SCT
4.00	4.73×10^{-94}	7.56×10^{-95}	2.50×10^{-5}	4.64×10^{-5}
5.00	3.95×10^{-73}	9.09×10^{-74}	2.50×10^{-5}	4.64×10^{-5}
6.00	3.62×10^{-59}	1.06×10^{-59}	2.51×10^{-5}	4.65×10^{-5}
8.00	1.09×10^{-41}	4.34×10^{-42}	2.60×10^{-5}	4.84×10^{-5}
10.00	3.52×10^{-31}	1.68×10^{-31}	3.01×10^{-5}	5.67×10^{-5}
20.00	4.44×10^{-10}	3.04×10^{-10}	6.08×10^{-4}	9.91×10^{-4}
30.00	5.12×10^{-3}	3.94×10^{-3}	1.59×10^{-1}	1.81×10^{-1}
40.00	1.74×10^{1}	1.41×10^{1}	6.78×10^{1}	6.94×10^{1}
50.00	2.24×10^{3}	1.86×10^{3}	4.91×10^{3}	4.96×10^{3}
75.00	1.37×10^{6}	1.17×10^{6}	1.88×10^{6}	1.89×10^{6}
77.36	2.02×10^{6}	1.72×10^{6}	2.71×10^{6}	2.72×10^{6}
100.00	3.21×10^{7}	2.72×10^{7}	3.67×10^{7}	3.68×10^{7}
125.00	2.05×10^{8}	1.72×10^{8}	2.11×10^{8}	2.11×10^{8}
150.00	6.91×10^{8}	5.71×10^{8}	6.58×10^{8}	6.58×10^{8}
175.00	1.63×10^{9}	1.32×10^{9}	1.45×10^{9}	1.45×10^{9}
194.70	2.72×10^{9}	2.17×10^{9}	2.32×10^{9}	2.32×10^{9}
200.00	3.07×10^{9}	2.44×10^{9}	2.59×10^{9}	2.59×10^{9}
225.00	5.01×10^{9}	3.90×10^{9}	4.00×10^{9}	4.00×10^{9}
250.00	7.39×10^{9}	5.62×10^{9}	5.61×10^{9}	5.61×10^{9}
273.15	9.92×10^{9}	7.39×10^{9}	7.20×10^{9}	7.20×10^{9}
275.00	1.01×10^{10}	7.54×10^{9}	7.32×10^{9}	7.33×10^{9}
298.15	1.29×10^{10}	9.42×10^{9}	8.95×10^{9}	8.95×10^{9}
300.00	1.32×10^{10}	9.58×10^{9}	9.08×10^{9}	9.08×10^{9}
325.00	1.64×10^{10}	1.17×10^{10}	1.08×10^{10}	1.08×10^{10}
350.00	1.98×10^{10}	1.38×10^{10}	1.25×10^{10}	1.25×10^{10}
373.15	2.30×10^{10}	1.57×10^{10}	1.40×10^{10}	1.40×10^{10}
375.00	2.32×10^{10}	1.58×10^{10}	1.41×10^{10}	1.41×10^{10}
400.00	2.68×10^{10}	1.78×10^{10}	1.55×10^{10}	1.55×10^{10}

Table 18. Computed rate constants in s^{-1} of the reaction **1t**-$^{13}CO_2$ → **2c**-$^{13}CO_2$ at the B3LYP/6-311+G(d,p) level of theory.

T / K	TST	CVT	CVT/ZCT	CVT/SCT
4.00	7.74×10^{-95}	1.01×10^{-95}	3.60×10^{-5}	1.24×10^{-4}
5.00	9.28×10^{-74}	1.82×10^{-74}	3.60×10^{-5}	1.24×10^{-4}
6.00	1.08×10^{-59}	2.78×10^{-60}	3.61×10^{-5}	1.24×10^{-4}
8.00	4.41×10^{-42}	1.59×10^{-42}	3.71×10^{-5}	1.26×10^{-4}
10.00	1.70×10^{-31}	7.50×10^{-32}	4.19×10^{-5}	1.34×10^{-4}
20.00	3.10×10^{-10}	2.04×10^{-10}	6.48×10^{-4}	1.01×10^{-3}
30.00	4.06×10^{-3}	3.04×10^{-3}	1.36×10^{-1}	1.52×10^{-1}
40.00	1.47×10^{1}	1.17×10^{1}	5.02×10^{1}	5.14×10^{1}
50.00	1.98×10^{3}	1.62×10^{3}	3.46×10^{3}	3.49×10^{3}
75.00	1.29×10^{6}	1.08×10^{6}	1.36×10^{6}	1.36×10^{6}
77.36	1.90×10^{6}	1.60×10^{6}	1.96×10^{6}	1.97×10^{6}
100.00	3.09×10^{7}	2.60×10^{7}	2.80×10^{7}	2.81×10^{7}
125.00	2.00×10^{8}	1.67×10^{8}	1.69×10^{8}	1.69×10^{8}
150.00	6.83×10^{8}	5.62×10^{8}	5.48×10^{8}	5.48×10^{8}
175.00	1.62×10^{9}	1.31×10^{9}	1.24×10^{9}	1.24×10^{9}
194.70	2.72×10^{9}	2.16×10^{9}	2.02×10^{9}	2.02×10^{9}
200.00	3.07×10^{9}	2.43×10^{9}	2.26×10^{9}	2.26×10^{9}
225.00	5.02×10^{9}	3.90×10^{9}	3.56×10^{9}	3.56×10^{9}
250.00	7.42×10^{9}	5.64×10^{9}	5.06×10^{9}	5.06×10^{9}
273.15	9.97×10^{9}	7.42×10^{9}	6.56×10^{9}	6.56×10^{9}
275.00	1.02×10^{10}	7.57×10^{9}	6.68×10^{9}	6.68×10^{9}
298.15	1.30×10^{10}	9.46×10^{9}	8.23×10^{9}	8.23×10^{9}
300.00	1.32×10^{10}	9.62×10^{9}	8.35×10^{9}	8.35×10^{9}
325.00	1.65×10^{10}	1.17×10^{10}	1.00×10^{10}	1.00×10^{10}
350.00	1.99×10^{10}	1.38×10^{10}	1.16×10^{10}	1.16×10^{10}

Table 19. Computed rate constants in s^{-1} of the reaction **3a** → **2t** at the B3LYP/6-311+G(d,p) level of theory.

T / K	TST	CVT	CVT/ZCT	CVT/SCT
4.00	0.00	0.00	NaN	NaN
5.00	0.00	0.00	NaN	NaN
6.00	0.00	0.00	NaN	NaN
8.00	0.00	0.00	NaN	NaN
10.00	0.00	0.00	NaN	NaN
20.00	0.00	0.00	NaN	NaN
30.00	3.12×10^{-195}	3.12×10^{-195}	1.14×10^{-14}	7.32×10^{-11}
40.00	1.71×10^{-143}	1.71×10^{-143}	1.69×10^{-14}	9.45×10^{-11}
50.00	2.00×10^{-112}	2.00×10^{-112}	2.78×10^{-14}	1.26×10^{-10}
75.00	6.02×10^{-71}	6.02×10^{-71}	1.35×10^{-13}	2.79×10^{-10}
77.36	2.03×10^{-68}	2.03×10^{-68}	1.60×10^{-13}	3.03×10^{-10}
100.00	3.62×10^{-50}	3.61×10^{-50}	8.64×10^{-13}	6.89×10^{-10}
125.00	1.11×10^{-37}	1.11×10^{-37}	6.22×10^{-12}	1.92×10^{-9}
150.00	2.41×10^{-29}	2.40×10^{-29}	4.78×10^{-11}	6.07×10^{-9}
175.00	2.20×10^{-23}	2.19×10^{-23}	3.80×10^{-10}	2.13×10^{-8}
194.70	9.18×10^{-20}	9.15×10^{-20}	1.97×10^{-9}	6.10×10^{-8}
200.00	6.54×10^{-19}	6.52×10^{-19}	3.07×10^{-9}	8.18×10^{-8}
225.00	1.98×10^{-15}	1.98×10^{-15}	2.50×10^{-8}	3.45×10^{-7}
250.00	1.22×10^{-12}	1.21×10^{-12}	2.04×10^{-7}	1.59×10^{-6}
273.15	1.63×10^{-10}	1.62×10^{-10}	1.43×10^{-6}	6.98×10^{-6}
275.00	2.33×10^{-10}	2.31×10^{-10}	1.67×10^{-6}	7.88×10^{-6}
298.15	1.38×10^{-8}	1.37×10^{-8}	1.17×10^{-5}	3.66×10^{-6}
300.00	1.86×10^{-8}	1.84×10^{-8}	1.36×10^{-5}	4.15×10^{-5}
325.00	7.56×10^{-7}	7.51×10^{-7}	1.09×10^{-5}	2.31×10^{-4}
350.00	1.82×10^{-5}	1.80×10^{-5}	8.41×10^{-4}	1.35×10^{-3}
373.15	2.36×10^{-4}	2.34×10^{-4}	5.17×10^{-3}	7.02×10^{-3}
375.00	2.86×10^{-4}	2.83×10^{-4}	5.96×10^{-3}	7.99×10^{-3}
400.00	3.19×10^{-3}	3.16×10^{-3}	3.76×10^{-2}	4.52×10^{-2}

Table 20. Computed rate constants in s^{-1} of the reaction **3b** → **2c** at the B3LYP/6-311+G(d,p) level of theory.

T / K	TST	CVT	CVT/ZCT	CVT/SCT
4.00	0.00	0.00	NaN	NaN
5.00	0.00	0.00	NaN	NaN
6.00	0.00	0.00	NaN	NaN
8.00	0.00	0.00	NaN	NaN
10.00	0.00	0.00	NaN	NaN
20.00	7.48×10^{-265}	7.42×10^{-265}	1.13×10^{-11}	1.97×10^{-8}
30.00	1.08×10^{-172}	1.08×10^{-172}	2.90×10^{-11}	3.12×10^{-8}
40.00	1.47×10^{-126}	1.47×10^{-126}	7.05×10^{-11}	5.37×10^{-8}
50.00	7.53×10^{-99}	7.52×10^{-99}	1.48×10^{-10}	8.88×10^{-8}
75.00	7.53×10^{-62}	7.53×10^{-62}	6.72×10^{-10}	2.51×10^{-7}
77.36	1.36×10^{-59}	1.36×10^{-59}	7.65×10^{-10}	2.74×10^{-7}
100.00	2.59×10^{-43}	2.59×10^{-43}	2.60×10^{-9}	5.98×10^{-7}
125.00	3.56×10^{-32}	3.56×10^{-32}	1.04×10^{-8}	1.37×10^{-6}
150.00	9.68×10^{-25}	9.67×10^{-25}	4.57×10^{-8}	3.22×10^{-6}
175.00	2.00×10^{-19}	1.99×10^{-19}	2.23×10^{-8}	8.15×10^{-6}
194.70	3.38×10^{-16}	3.37×10^{-16}	8.24×10^{-7}	1.82×10^{-5}
200.00	1.94×10^{-15}	1.94×10^{-15}	1.18×10^{-6}	2.28×10^{-5}
225.00	2.47×10^{-12}	2.46×10^{-12}	6.67×10^{-6}	7.23×10^{-5}
250.00	7.51×10^{-10}	7.50×10^{-10}	3.98×10^{-5}	2.59×10^{-4}
273.15	5.90×10^{-8}	5.89×10^{-8}	2.16×10^{-4}	9.32×10^{-4}
275.00	8.11×10^{-8}	8.08×10^{-8}	2.48×10^{-4}	1.04×10^{-4}
298.15	3.07×10^{-6}	3.06×10^{-6}	1.39×10^{-3}	4.04×10^{-3}
300.00	4.01×10^{-6}	4.00×10^{-6}	1.59×10^{-3}	4.52×10^{-3}
325.00	1.09×10^{-4}	1.09×10^{-4}	1.02×10^{-2}	2.11×10^{-2}
350.00	1.85×10^{-3}	1.84×10^{-3}	6.34×10^{-2}	1.03×10^{-2}
373.15	1.82×10^{-2}	1.81×10^{-2}	3.21×10^{-1}	4.45×10^{-1}
375.00	2.16×10^{-2}	2.15×10^{-2}	3.64×10^{-1}	5.00×10^{-1}
400.00	1.85×10^{-1}	1.84×10^{-1}	1.87×10^{0}	2.32×10^{0}

Table 21. Computed rate constants in s^{-1} of the reaction **2t** → **2c** at the B3LYP/6-311+G(d,p) level of theory.

T / K	TST	CVT	CVT/ZCT	CVT/SCT
4.00	0.00	0.00	NaN	NaN
5.00	0.00	0.00	NaN	NaN
6.00	0.00	0.00	NaN	NaN
8.00	5.19×10^{-261}	5.19×10^{-261}	1.89×10^{-6}	1.50×10^{-4}
10.00	1.30×10^{-206}	1.30×10^{-206}	1.89×10^{-6}	1.50×10^{-4}
20.00	1.04×10^{-97}	1.04×10^{-97}	2.00×10^{-6}	1.57×10^{-4}
30.00	2.43×10^{-61}	2.43×10^{-61}	2.33×10^{-6}	1.81×10^{-4}
40.00	4.03×10^{-43}	4.03×10^{-43}	2.92×10^{-6}	2.23×10^{-4}
50.00	3.61×10^{-32}	3.61×10^{-32}	3.87×10^{-6}	2.86×10^{-4}
75.00	1.61×10^{-17}	1.61×10^{-17}	1.02×10^{-5}	6.16×10^{-4}
77.36	1.26×10^{-16}	1.26×10^{-16}	1.15×10^{-5}	6.71×10^{-4}
100.00	3.70×10^{-10}	3.70×10^{-10}	5.45×10^{-5}	1.94×10^{-3}
125.00	1.02×10^{-5}	1.02×10^{-5}	1.32×10^{-3}	1.36×10^{-2}
150.00	9.56×10^{-3}	9.56×10^{-3}	1.07×10^{-1}	3.04×10^{-1}
175.00	1.30×10^{0}	1.30×10^{0}	5.95×10^{0}	9.98×10^{0}
194.70	2.59×10^{1}	2.59×10^{1}	8.24×10^{1}	1.17×10^{2}
200.00	5.25×10^{1}	5.25×10^{1}	1.55×10^{2}	2.13×10^{2}
225.00	9.44×10^{2}	9.44×10^{2}	2.15×10^{3}	2.68×10^{3}
250.00	9.60×10^{3}	9.60×10^{3}	1.85×10^{4}	2.18×10^{4}
273.15	5.66×10^{4}	5.66×10^{4}	9.75×10^{5}	1.11×10^{5}
275.00	6.44×10^{4}	6.44×10^{4}	1.10×10^{5}	1.25×10^{5}
298.15	2.84×10^{5}	2.84×10^{5}	4.47×10^{5}	4.97×10^{5}
300.00	3.16×10^{5}	3.16×10^{5}	4.96×10^{5}	5.50×10^{5}
325.00	1.22×10^{6}	1.22×10^{6}	1.79×10^{6}	1.95×10^{6}
350.00	3.89×10^{6}	3.89×10^{6}	5.43×10^{6}	5.83×10^{6}
373.15	9.95×10^{6}	9.95×10^{6}	1.33×10^{7}	1.42×10^{7}
375.00	1.07×10^{7}	1.07×10^{7}	1.43×10^{7}	1.52×10^{7}
400.00	2.58×10^{7}	2.58×10^{7}	3.34×10^{7}	3.53×10^{7}

Table 22. Computed rate constants in s^{-1} of the reaction **1t**-CO_2 → **1c**-CO_2 at the B3LYP/6-311+G(d,p) level of theory.

T / K	TST	CVT	CVT/ZCT	CVT/SCT
4.00	0.00	0.00	NaN	NaN
5.00	0.00	0.00	NaN	NaN
6.00	0.00	0.00	NaN	NaN
8.00	0.00	0.00	NaN	NaN
10.00	2.64×10^{-257}	2.62×10^{-257}	8.40×10^{-22}	4.20×10^{-19}
20.00	6.86×10^{-123}	6.84×10^{-123}	8.77×10^{-22}	4.39×10^{-19}
30.00	5.26×10^{-78}	5.25×10^{-78}	9.67×10^{-22}	4.83×10^{-19}
40.00	1.60×10^{-55}	1.60×10^{-55}	1.13×10^{-21}	5.54×10^{-19}
50.00	5.23×10^{-42}	5.22×10^{-42}	1.57×10^{-21}	6.95×10^{-19}
75.00	6.17×10^{-24}	6.17×10^{-24}	2.57×10^{-19}	1.73×10^{-17}
77.36	7.83×10^{-23}	7.82×10^{-23}	6.63×10^{-19}	3.37×10^{-17}
100.00	7.35×10^{-15}	7.34×10^{-15}	7.97×10^{-14}	2.46×10^{-13}
125.00	2.15×10^{-9}	2.15×10^{-9}	5.82×10^{-9}	8.76×10^{-9}
150.00	9.78×10^{-6}	9.77×10^{-6}	1.61×10^{-5}	2.02×10^{-15}
175.00	4.08×10^{-3}	4.07×10^{-3}	5.30×10^{-3}	6.12×10^{-13}
194.70	1.60×10^{-1}	1.60×10^{-1}	1.88×10^{-1}	2.09×10^{-11}
200.00	3.80×10^{-1}	3.80×10^{-1}	4.38×10^{-1}	4.83×10^{-1}
225.00	1.31×10^{1}	1.31×10^{1}	1.40×10^{1}	1.50×10^{1}
250.00	2.22×10^{2}	2.22×10^{2}	2.28×10^{2}	2.41×10^{2}
273.15	1.94×10^{3}	1.94×10^{3}	1.94×10^{3}	2.02×10^{3}
275.00	2.27×10^{3}	2.27×10^{3}	2.27×10^{3}	2.36×10^{3}
298.15	1.38×10^{4}	1.38×10^{4}	1.36×10^{4}	1.40×10^{4}
300.00	1.58×10^{4}	1.57×10^{4}	1.55×10^{4}	1.60×10^{4}
325.00	8.14×10^{4}	8.14×10^{4}	7.90×10^{4}	8.11×10^{4}
350.00	3.33×10^{5}	3.33×10^{5}	3.21×10^{5}	3.28×10^{5}
373.15	1.04×10^{6}	1.04×10^{6}	9.96×10^{5}	1.01×10^{6}
375.00	1.13×10^{6}	1.13×10^{6}	1.08×10^{6}	1.10×10^{6}
400.00	3.30×10^{6}	3.30×10^{6}	3.15×10^{6}	3.20×10^{6}

Table 23. Computed rate constants in s^{-1} of the reaction **1c**-CO_2 → **1t**-CO_2 at the B3LYP/6-311+G(d,p) level of theory.

T / K	TST	CVT	CVT/ZCT	CVT/SCT
4.00	0.00	0.00	NaN	NaN
5.00	0.00	0.00	NaN	NaN
6.00	0.00	0.00	NaN	NaN
8.00	0.00	0.00	NaN	NaN
10.00	2.91×10^{-250}	2.89×10^{-250}	8.02×10^{-22}	4.03×10^{-19}
20.00	2.25×10^{-119}	2.25×10^{-119}	1.03×10^{-21}	4.85×10^{-19}
30.00	1.15×10^{-75}	1.15×10^{-75}	1.79×10^{-21}	7.37×10^{-19}
40.00	9.00×10^{-54}	8.99×10^{-54}	3.72×10^{-21}	1.31×10^{-18}
50.00	1.30×10^{-40}	1.30×10^{-40}	9.81×10^{-21}	2.76×10^{-18}
75.00	5.16×10^{-23}	5.16×10^{-23}	2.13×10^{-18}	1.39×10^{-16}
77.36	6.13×10^{-22}	6.13×10^{-22}	5.17×10^{-18}	2.58×10^{-16}
100.00	3.56×10^{-14}	3.56×10^{-14}	4.23×10^{-13}	1.23×10^{-12}
125.00	7.52×10^{-9}	7.52×10^{-9}	2.60×10^{-8}	3.65×10^{-8}
150.00	2.75×10^{-5}	2.75×10^{-5}	6.14×10^{-5}	7.36×10^{-5}
175.00	9.86×10^{-3}	9.86×10^{-3}	1.75×10^{-2}	1.97×10^{-2}
194.70	3.54×10^{-1}	3.54×10^{-1}	5.62×10^{-1}	6.15×10^{-1}
200.00	8.24×10^{-1}	8.23×10^{-1}	1.28×10^{0}	1.39×10^{0}
225.00	2.60×10^{1}	2.60×10^{1}	3.68×10^{1}	3.92×10^{1}
250.00	4.13×10^{2}	4.13×10^{2}	5.49×10^{2}	5.77×10^{2}
273.15	3.43×10^{3}	3.42×10^{3}	4.36×10^{3}	4.54×10^{3}
275.00	3.99×10^{3}	3.99×10^{3}	5.07×10^{3}	5.28×10^{3}
298.15	2.33×10^{4}	2.33×10^{4}	2.86×10^{4}	2.96×10^{4}
300.00	2.66×10^{4}	2.66×10^{4}	3.25×10^{4}	3.36×10^{4}
325.00	1.32×10^{5}	1.32×10^{5}	1.58×10^{5}	1.62×10^{5}
350.00	5.25×10^{5}	5.25×10^{5}	6.12×10^{5}	6.27×10^{5}
373.15	1.60×10^{6}	1.60×10^{6}	1.83×10^{6}	1.87×10^{6}
375.00	1.73×10^{6}	1.73×10^{6}	1.99×10^{6}	2.03×10^{6}
400.00	4.95×10^{6}	4.95×10^{6}	5.58×10^{6}	5.68×10^{6}

Table 24. Computed rate constants in s^{-1} of the reaction **1c** → **thiol_6** at the B3LYP/6-311+G(d,p) level of theory.

T / K	TST	CVT	CVT/ZCT	CVT/SCT
0.10	NaN	NaN	NaN	NaN
8.00	0.00×10^{0}	0.00×10^{0}	NaN	NaN
10.00	0.00×10^{0}	0.00×10^{0}	NaN	NaN
15.00	0.00×10^{0}	0.00×10^{0}	NaN	NaN
20.00	0.00×10^{0}	0.00×10^{0}	NaN	NaN
25.00	0.00×10^{0}	0.00×10^{0}	NaN	NaN
30.00	0.00×10^{0}	0.00×10^{0}	NaN	NaN
35.00	2.11×10^{-276}	2.07×10^{-276}	4.04×10^{-21}	2.19×10^{-18}
40.00	2.32×10^{-240}	2.27×10^{-240}	4.04×10^{-21}	2.19×10^{-18}
45.00	2.52×10^{-212}	2.48×10^{-212}	4.04×10^{-21}	2.19×10^{-18}
50.00	6.86×10^{-190}	6.75×10^{-190}	4.04×10^{-21}	2.19×10^{-18}
200.00	3.78×10^{-38}	3.77×10^{-38}	1.86×10^{-20}	4.38×10^{-18}
250.00	5.75×10^{-28}	5.72×10^{-28}	1.11×10^{-18}	2.71×10^{-17}
300.00	3.66×10^{-21}	3.65×10^{-21}	2.19×10^{-16}	1.30×10^{-15}
350.00	2.72×10^{-16}	2.71×10^{-16}	7.84×10^{-14}	2.08×10^{-13}

Table 25. Computed rate constants in s^{-1} of the reaction **1t** → **thiol_5** at the B3LYP/6-311+G(d,p) level of theory.

T / K	TST	CVT	CVT/ZCT	CVT/SCT
0.10	NaN	NaN	NaN	NaN
8.00	0.00×10^{0}	0.00×10^{0}	NaN	NaN
10.00	0.00×10^{0}	0.00×10^{0}	NaN	NaN
15.00	0.00×10^{0}	0.00×10^{0}	NaN	NaN
20.00	0.00×10^{0}	0.00×10^{0}	NaN	NaN
25.00	0.00×10^{0}	0.00×10^{0}	NaN	NaN
30.00	0.00×10^{0}	0.00×10^{0}	NaN	NaN
35.00	2.96×10^{-274}	2.96×10^{-274}	3.56×10^{-21}	2.43×10^{-18}
40.00	1.75×10^{-238}	1.75×10^{-238}	3.56×10^{-21}	2.43×10^{-18}
45.00	1.18×10^{-210}	1.18×10^{-210}	3.56×10^{-21}	2.43×10^{-18}

50.00	2.18×10^{-188}	2.18×10^{-188}	3.56×10^{-21}	2.43×10^{-18}
200.00	9.03×10^{-38}	9.03×10^{-38}	2.05×10^{-20}	5.32×10^{-18}
250.00	1.15×10^{-27}	1.15×10^{-27}	1.59×10^{-18}	4.02×10^{-17}
300.00	6.54×10^{-21}	6.54×10^{-21}	3.56×10^{-16}	2.16×10^{-15}
350.00	4.47×10^{-16}	4.47×10^{-16}	1.28×10^{-13}	3.47×10^{-13}

Table 26. Computed rate constants in s^{-1} of the reaction **1t** → **thione** at the B3LYP/6-311+G(d,p) level of theory.

T / K	TST	CVT	CVT/ZCT	CVT/SCT
0.10	NaN	NaN	NaN	NaN
8.00	0.00×10^{0}	0.00×10^{0}	NaN	NaN
10.00	0.00×10^{0}	0.00×10^{0}	NaN	NaN
15.00	0.00×10^{0}	0.00×10^{0}	NaN	NaN
20.00	0.00×10^{0}	0.00×10^{0}	NaN	NaN
25.00	4.15×10^{-243}	3.07×10^{-243}	6.81×10^{-10}	8.37×10^{-9}
30.00	1.12×10^{-200}	8.68×10^{-201}	6.81×10^{-10}	8.38×10^{-9}
35.00	2.33×10^{-170}	1.87×10^{-170}	6.83×10^{-10}	8.40×10^{-9}
40.00	1.31×10^{-147}	1.07×10^{-147}	6.86×10^{-10}	8.43×10^{-9}
45.00	6.60×10^{-130}	5.48×10^{-130}	6.90×10^{-10}	8.48×10^{-9}
50.00	9.72×10^{-116}	8.16×10^{-116}	6.95×10^{-10}	8.55×10^{-9}
200.00	1.28×10^{-19}	1.01×10^{-19}	3.00×10^{-9}	2.73×10^{-8}
250.00	4.01×10^{-13}	3.10×10^{-13}	3.33×10^{-8}	1.60×10^{-7}
300.00	9.00×10^{-9}	6.78×10^{-9}	1.60×10^{-6}	3.95×10^{-6}
350.00	1.18×10^{-5}	8.72×10^{-6}	1.59×10^{-4}	2.42×10^{-4}

Cartesian Coordinates of Computed Structures

In this section, electronic and zero-point vibrational energies (ZPVEs) are provided for each structure. For transition states, the imaginary frequency is given additionally. For the full cartesian coordinates of the computed geometries at the CCSD(T)/cc-pVTZ, the B3LYP/6-311++G(3df,3pd), and the MP2/def2-QZVPP levels of theory please see the published supporting information: https://www.rsc.org/suppdata/d2/sc/d2sc05388h/d2sc05388h1.pdf.

For CCSD(T)/cc-pVTZ and B3LYP/6-311++G(3df,3pd) geometries of thioformamide and its thiolimine tautomers see:

https://pubs.rsc.org/en/content/articlelanding/2023/SC/D2SC05388H

Table 27. Electronic and zero-point vibrational energies (ZPVEs) at the CCSD(T)/cc-pVTZ level of theory.

Structure	**E / au**	**ZPVE / kcal mol^{-1}**	ν_i **/*i* cm^{-1}**
1c	−492.177533201648714	25.2367	
1t	−492.177819346771571	25.5404	
TS: 1t → 1c	−492.159698956876639	24.7388	391.3
1c-CO_2	−680.512402831025042	33.2153	
1t-CO_2	−680.512969882841276	33.5207	
TS: 1t-CO_2 → **1c**-CO_2	−680.494478242239893	32.7021	394.9
TS: 1t-CO_2 → **2c**	−680.506474541059561	33.6575	214.4
CO_2	−188.327217847799375	7.2380	
2t	−680.552608465715139	37.2399	
2c	−680.559917124698927	37.5291	
3a	−680.536555058892645	35.1017	
3b	−680.529285495559293	34.8678	
TS: 3a → 2t	−680.486257311029703	33.1731	1834.7
TS: 3b → 2c	−680.484444459190854	33.0679	1809.3
TS: 2t → 2c	−680.535066092372745	36.1632	630.8243
TS_tf1	−492.098393717232113	21.1683	1947.7
TS_tf2	−492.098890642865570	21.3554	1962.7
TS_tf3 (C_1)	−492.125707736241168	22.8172	1675.3
Dihydroxymethylene-CO_2 **complex**	−377.770921524285484	29.3267	

Structure	**E / au**	**ZPVE / kcal mol^{-1}**	ν_i **/*i* cm^{-1}**
Aminomethylene-CO_2 **complex**	−282.751367779795260	33.3169	
Aminohydroxymethylene-CO_2 **complex**	−357.918469840371245	36.8402	

Table 28. Electronic and zero-point vibrational energies (ZPVEs) at the B3LYP/6-311++G(3df,3pd) level of theory.

Structure	**E / au**	**ZPVE / kcal mol^{-1}**	ν_i **/*i* cm^{-1}**
1c	−492.8651962	0.0398879	
1t	−492.8646319	0.0404994	
TS: 1t → 1c	−492.8436498	0.0391178	430.8
1c-CO_2	−681.5306927	0.0527453	
1t-CO_2	−681.5305073	0.0533081	
TS: 1t-CO_2 **→ 1c-**CO_2	−681.5091572	0.0519173	434.0
TS: 1t-CO_2 **→ 2c**	−681.5270882	0.0534466	151.3
CO_2	−188.6604007	0.0117227	
2t	−681.5663854	0.0591648	
2c	−681.5738753	0.0594046	
3a	−681.5469988	0.0556568	
3b	−681.5397071	0.0552246	
2t'	−681.5618741	0.0587476	
2* (Zwitterion)	−681.475634	0.0551773	
3c	−681.537135	0.0552831	
3d	−681.5374791	0.0554331	
3e	−681.5463785	0.0556955	
3f	−681.5466142	0.0557245	
3g	−681.5453992	0.055652	
3h	−681.536557	0.0552241	
3i	−681.5403508	0.0553023	
3j	−681.5533085	0.0560519	
3k	-	-	
3l	−681.5435001	0.055639	

Structure	**E / au**	**ZPVE / kcal mol^{-1}**	**ν_i /*i* cm^{-1}**
3m	−681.5330168	0.0549181	
3n	−681.5457088	0.0555533	
3o	−681.5408091	0.0552121	
3p	−681.5496327	0.0560287	
TS: 3a → 2t	−681.4982053	0.0525787	1781.7
TS: 3b → 2c	−681.4960935	0.052377	1753.9
TS: 2t → 2c	−681.5489329	0.0573238	645.4
TS_tf1	−492.7850248	0.0334823	1905.6
TS_tf2	−492.7853887	0.0338407	1912.7
TS_tf3	−492.8132748	0.0359615	1661.1
Dimer_A	−13623.15587	0.1200014	
Dimer_B	−1363.156321	0.1199167	
Dimer_C	−1363.146604	0.1198165	
12	−757.722007	0.0703586	
13	−757.695887	0.0678521	
14	−569.042598	0.055214	
15	−569.088892	0.0550984	
TS13	−569.042598	0.048762	0.0661858
TS14	−568.974921	0.0486441	1712.2614
TS15	−681.481012	0.0518805	1261.9511
TS16	−757.687524	0.0681282	179.4305

Table 29. Electronic and zero-point vibrational energies (ZPVEs) at the MP2/def2-QZVPP level of theory.

Structure	**E / au**	**ZPVE / kcal mol^{-1}**	**ν_i /*i* cm^{-1}**
1c	−492.1747052	0.0407957	
1t	−492.1749769	0.0413122	
TS: 1t → 1c	−492.1543923	0.0399709	421.3
1c-CO_2	−680.5512359	0.053554	
1t-CO_2	−680.5518426	0.0540646	
TS: 1t-CO_2 → **1c**-CO_2	−680.5309307	0.0527052	423.5
TS: 1t-CO_2 → **2c**	−680.547686	0.0540389	194.9
CO_2	−188.3685783	0.0115804	

Structure	**E / au**	**ZPVE / kcal mol^{-1}**	**ν_i /i cm^{-1}**
2t	−680.5963501	0.0594597	
2c	−680.6040706	0.0597681	
2t'	−680.5921744	0.0589776	
2 (Zwitterion)	−680.5003580	0.0558367	
3a	−680.5763523	0.0560141	
3b	−680.5690439	0.0556249	
3c	−680.5662319	0.055744	
3d	−680.566686	0.0558894	
3e	−680.5758308	0.0560373	
3f	−680.5760157	0.0560828	
3g	−680.5746694	0.0560113	
3h	−680.5656139	0.0556612	
3i	−680.5693267	0.0556582	
3j	−680.5831062	0.0564362	
3k	−680.5625698	0.0553733	
3l	−680.5724038	0.0559701	
3m	−680.5617232	0.0553483	
3n	−680.5747306	0.055905	
3o	−680.569837	0.055613	
3p	−680.5791465	0.0564207	
TS: 3a → 2t	−680.5308174	0.0527743	1677.6
TS: 3b → 2c	−680.5292074	0.0525923	1642.9
TS: 2t → 2c	−680.5781340	0.057676	645.7
TS_tf1	−492.0981027	0.0340052	1960.2
TS_tf2	−492.0984322	0.034361	1986.8
TS_tf3	−492.1275722	0.0365519	1620.3
Thione	−492.238718	0.0440399	
Thiol_3	−492.2195021	0.0406766	
Thiol_4	−492.2175519	0.0405699	
Thiol_5	−492.2184924	0.040527	
Thiol_6	−492.2185178	0.0407071	
TSCS_1	−492.2074113	0.0397467	340.2
TSCS_2	−492.2109126	0.0399207	278.6

Structure	**E / au**	**ZPVE / kcal mol^{-1}**	**ν_i /*i* cm^{-1}**
TSCN_1	−492.1792425	0.0377611	1095.5
TSCN_2	−492.1790216	0.0376988	1087.5
TSCA	−492.1769829	0.0377055	1635.3

Table 30. Electronic and zero-point vibrational energies (ZPVEs) at the B3LYP/6-311+G(d,p) level of theory.

Structure	**E / au**	**ZPVE / kcal mol^{-1}**	**ν_i /*i* cm^{-1}**
1c-CO_2	−681.449215	0.052679403	
1t-CO_2	−681.449729	0.053256863	
TS_1t-CO_2 → **2c**	−681.446691	0.053348622	143.3086
2t	−681.480888	0.059087391	
2c	−681.546313514	0.059254514	
3a	−681.463710	0.055528355	
3b	−681.455813	0.055071577	
TS_3a to 2t	−681.418568	0.052475973	1778.4355
TS_3b to 2c	−681.415591	0.052186925	1751.2527
TS_2t to 2c	−681.465050	0.057230692	648.4266
TS_1c-CO_2 → **1t**-CO2	−681.430170	0.051853034	420.8355

2.4. References

[1] M. Aresta, (Ed.), Carbon Dioxide as Chemical Feedstock, Wiley-VCH, Weinheim, **2010**.

[2] A. Gulzar, A. Gulzar, M. B. Ansari, F. He, S. Gai, P. Yang, *Chem. Eng. J.* **2020**, 100013.

[3] C. M. Momming, E. Otten, G. Kehr, R. Frohlich, S. Grimme, D. W. Stephan, G. Erker, *Angew. Chem. Int. Ed.* **2009**, *48*, 6643.

[4] C. Wang, H. Luo, D. E. Jiang, H. Li, S. Dai, *Angew. Chem. Int. Ed.* **2010**, *49*, 5978.

[5] C. Villiers, J. P. Dognon, R. Pollet, P. Thuery, M. Ephritikhine, *Angew. Chem. Int. Ed.* **2010**, *49*, 3465.

[6] M.-Y. Wang, Q.-W. Song, R. Ma, J.-N. Xie, L.-N. He, *Green Chem.* **2016**, *18*, 282.

[7] H. Zhou, G.-X. Wang, W.-Z. Zhang, X.-B. Lu, *ACS Catal.* **2015**, *5*, 6773.

[8] L. Yang, H. Wang, *ChemSusChem* **2014**, ***7***, 962.

[9] A. Tudose, A. Demonceau, L. Delaude, *J. Organomet. Chem.* **2006**, *691*, 5356.

[10] M. Hans, L. Delaude, J. Rodriguez, Y. Coquerel, *J. Org. Chem.* **2014**, *79*, 2758.

[11] L. Gu, Y. Zhang, *J. Am. Chem. Soc.* **2010**, *132*, 914.

[12] J. D. Holbrey, W. M. Reichert, I. Tkatchenko, E. Bouajila, O. Walter, I. Tommasi, R. D. Rogers, *Chem. Commun.* **2003**, *28*.

[13] H. A. Duong, T. N. Tekavec, A. M. Arif, J. Louie, *Chem. Commun.* **2004**, *40*, 112.

[14] I. Tommasi, F. Sorrentino, *Tetrahedron Lett.* **2006**, *47*, 6453.

[15] I. Tommasi, F. Sorrentino, *Tetrahedron Lett.* **2005**, *46*, 2141.

[16] H. Zhou, W.-Z. Zhang, C.-H. Liu, J.-P. Qu, X.-B. Lu, *J. Org. Chem*, **2008**, *73*, 8039.

[17] Y. Kayaki, M. Yamamoto, T. Ikariya, *Angew. Chem. Int. Ed.* **2009**, *121*, 4258.

[18] D. M. Denning, D. E. Falvey, *J. Org. Chem.* **2014**, *79*, 4293.

[19] L. Delaude, *Adv. Synth. Catal.* **2020**, *362*, 3259.

[20] L. Farkas, O. H. Wansbrough-Jones, *Z. Phys. Chem B 18* **1932**, *124*.

[21] M. K. R. Noyori, M Kawanisi, H. Nozaki, *Tetrahedro* **1969**, *25*, 1125.

[22] G. Maier, J. Endres, *Eur. J. Org. Chem.* **1998**, *1998*, 1517.

[23] G. Maier, J. Endres, H. P. Reisenauer, *Angew. Chem. Int. Ed.* **1997**, *36*, 1709.

[24] P. J. M. D. Kong, E. K. J. Lui, O. Bsharat, R. J. Lundgren, *Science* **2020**, *369*, 557.

[25] R. Breslow, *J. Am. Chem. Soc.* **1958**, *80*, 3719.

[26] M. Schauermann, P. R. Schreiner, *J. Phys. Chem. Lett.* **2022**, *13*, 3138.

[27] E. E. Gard, M. J. Kleeman, D. S. Gross, L. S. Hughes, J. O. Allen, B. D. Morrical, D. P. Fergenson, T. Dienes, M. E. Gälli, R. J. Johnson, *Science* **1998**, *279*, 1184.

[28] S. Doddipatla, C. He, R. I. Kaiser, Y. Luo, R. Sun, G. R. Galimova, A. M. Mebel, T. J. Millar, *PNAS* **2020**, *117*, 22712.

[29] P. R. Schreiner, *J. Am. Chem. Soc.* **2017**, *139*, 15276.

[30] P. R. Schreiner, *Trends Chem.* **2020**, *2*, 980.

[31] P. R. Schreiner, H. P. Reisenauer, D. Ley, D. Gerbig, C.-H. Wu, W. D. Allen, *Science* **2011**, *322*, 1300.

[32] W. T. Borden, *WIREs Comput. Mol. Sci.* **2016**, *6*, 20.

[33] R. S. Sheridan, In *Review Reactive Intermediate Chemistry* **2007**, 415.

[34] C. Castro, W. L. Karney, *Angew. Chem. Int. Ed.* **2020**, *59*, 8355.

[35] C. M. Nunes, A. K. Eckhardt, I. Reva, R. Fausto, P. R. Schreiner, *J. Am. Chem. Soc.* **2019**, *141*, 14340.

[36] Z. Wu, R. Feng, H. Li, J. Xu, G. Deng, M. Abe, D. Bégué, K. Liu, X. Zeng, *Angew. Chem. Int. Ed.* **2017**, *129*, 15878.

[37] P. R. Schreiner, H. P. Reisenauer, F. C. Pickard IV, A. C. Simmonett, W. D. Allen, E. Mátyus, A. G. Császár, *Nature* **2008**, *453*, 906.

[38] P. R. Schreiner, H. P. Reisenauer, *Angew. Chem. Int. Ed*, **2008**, *47*, 7071.

[39] D. Ley, D. Gerbig, J. P. Wagner, H. P. Reisenauer, P. R. Schreiner, *J. Am. Chem. Soc.* **2011**, *133*, 13614.

[40] D. Ley, D. Gerbig, P. R. Schreiner, *Chem. Sci.* **2013**, *4*, 677.

[41] A. Mardyukov, H. Quanz, P. R. Schreiner, *Nat. Chem.* **2017**, *9*, 71.

[42] A. K. Eckhardt, F. R. Erb, P. R. Schreiner, *Chem. Sci.* **2019**, *10*, 802.

[43] D. Gerbig, H. P. Reisenauer, C.-H. Wu, D. Ley, W. D. Allen, P. R. Schreiner, *J. Am. Chem. Soc.* **2010**, *132*, 7273.

[44] A. K. Eckhardt, M. M. Linden, R. C. Wende, B. Bernhardt, P. R. Schreiner, *Nat. Chem.* **2018**, *10*, 1141.

[45] B. Bernhardt, F. Dressler, A. K. Eckhardt, J. Becker, P. R. Schreiner, *Chem. Eur. J.* ***2021***, *27*, 6732.

[46] M. Pettersson, E. M. S. Maçôas, L. Khriachtchev, J. Lundell, R. Fausto, M. Räsänen, *J. Chem. Phys. A* **2002**, *117*, 9095.

[47] G. Maier, J. Endres, H. P. Reisenauer, *J. Mol. Struct.* **2012**, *1025*, 2.

[48] D. Gerbig, P. R. Schreiner, *J. Chem. Phys. B* **2015**, *119*, 693.

[49] M. Tsuge, L. Khriachtchev, *J. Phys. Chem. A* **2015**, *119*, 2628.

[50] P. R. Schreiner, J. P. Wagner, H. P. Reisenauer, D. Gerbig, D. Ley, J. Sarka, A. G. Császár, A. Vaughn, W. D. Allen, *J. Am. Chem. Soc.* **2015**, *137*, 7828.

[51] H. Rostkowska, L. Lapinski, M. J. Nowak, *Phys. Chem. Chem. Phys.* **2018**, *20*, 13994.

[52] H. Rostkowska, L. Lapinski, M. J. Nowak, *J. Phys. Chem. A* **2017**, *121*, 6932.

[53] S. Góbi, I. Reva, I. P. Csonka, M. N. C, G. Tarczay, R. Fausto, *Phys. Chem. Chem. Phys.* **2019**, *21*, 24935.

[54] S. Góbi, C. M. Nunes, I. Reva, G. Tarczay, R. Fausto, *Phys. Chem. Chem. Phys.* **2019**, *21*, 17063.

[55] E. M. Brás, R. Fausto, *J. Photoch. Photobio. A* **2018**, *357*, 185.

[56] E. M. Brás, R. Fausto, *J. Mol. Struct.* **2018**, *1172*, 42.

[57] D. Prusinowska, L. Lapinski, M. J. Nowak, L. Adamowicz, *Spectrochim. Acta A* **1995**, *51*, 1809.

[58] M. J. Nowak, L. Lapinski, H. Rostkowska, A. Les, L. Adamowicz, *J. Phys. Chem.* **1990**, *94*, 7406.

[59] M. J. Nowak, L. Lapinski, J. Fulara, A. Les, L. Adamowicz, *J. Phys. Chem.* **1991**, *95*, 2404.

[60] L. Lapinski, H. Rostkowska, A. Khvorostov, M. Yaman, R. Fausto, M. J. Nowak, *J. Chem. Phys. A* **2004**, *108*, 5551.

[61] L. Lapinski, H. Rostkowska, A. Khvorostov, M. J. Nowak, *Phys. Chem. Chem. Phys.* **2003**, *5*, 1524.

[62] H. Rostkowska, L. Lapinski, A. Khvorostov, M. J. Novak, *J. Phys. Chem. A* **2003**, *107*, 6373.

[63] T. Schleif, J. Tatchen, J. F. Rowen, F. Beyer, E. Sanchez-Garcia, W. Sander, *Chem. Eur. J.* **2020**, *26*, 10452.

[64] A. K. Eckhardt, P. R. Schreiner, *Angew. Chem. Int. Ed.* **2018**, *57*, 5248.

[65] B. Bernhardt, M. Ruth, H. P. Reisenauer, P. R. Schreiner, *J. Phys. Chem. A* **2021**, *125*, 7023.

[66] A. D. Becke, *J. Chem. Phys.* **1988**, *88*, 1053.

[67] C. Lee, W. Yang, R. G. Parr, *Phys. Rev. B* **1988**, *37*, 785.

[68] A. D. McLean, G. S. Chandler, *J. Chem. Phys.* **1980**, *72*, 5639.

[69] R. Krishnan, J. S. Binkley, R. Seeger, J. A. Pople, *J. Chem. Phys.* **1980**, *72*, 650.

[70] C. Møller, M. S. Plesset, *Phys. Rev.* **1934**, *46*, 618.

[71] M. Head-Gordon, J. A. Pople, M. J. Frisch, *Phys. Lett.* **1988**, *153*, 503.

[72] F. Weigend, R. Ahlrichs, *Phys. Chem. Chem. Phys.* **2005**, *7*, 3297.

[73] F. Weigend, *Phys. Chem. Chem. Phys.* **2006**, *8*, 1057.

[74] G. D. Purvis III, R. J. Bartlett, *J. Chem. Phys.* **1982**, *76*, 1910.

[75] K. Raghavachari, G. W. Trucks, J. A. Pople, M. Head-Gordon, *Chem. Phys. Lett.* **1989**, *157*, 479

[76] Thom H. Dunning Jr., *J. Chem. Phys.* **1989**, *90*, 1007.

[77] K. A. Peterson, D. E. Woon, Thom H. Dunning Jr., *J. Chem. Phys.* **1994**, *100*, 7410.

[78] D. E. Woon, Thom H. Dunning Jr., *J. Chem. Phys.* **1995**, *103*, 4572.

[79] Rick A. Kendall, Thom H. Dunning Jr., Robert J. Harrison, *J. Chem. Phys.* **1992**, *96*, 6796.

[80] T. A. Keith, AIMAll. (TK Gristmill Software, USA, **2019**).

[81] R. F. Bader, *Acc. Chem. Res.* **1985**, *18*, 9.

[82] B. Liu, A. McLean, *J. Chem. Phys.* **1973**, *59*, 4557.

[83] J. Vogt, S. Alvarez, *Inorg. Chem.* **2014**, *53*, 9260.

[84] Y. Mo, *J. Phys. Chem. A* **2012**, *116*, 5240.

[85] P. R. Schreiner, H. P. Reisenauer, *Angew. Chem. Int. Ed.* **2008**, *120*, 7179.

Gaussian 16

Gaussian 16, Revision A.03; Frisch, M. J.; Trucks, G. W.; Schlegel, H. B.; Scuseria, G. E.; Robb, M. A.; Cheeseman, J. R.; Scalmani, G.; Barone, V.; Petersson, G. A.; Nakatsuji, H.; Li, X.; Caricato, M.; Marenich, A. V.; Bloino, J.; Janesko, B. G.; Gomperts, R.; Mennucci, B.; Hratchian, H. P.; Ortiz, J. V.; Izmaylov, A. F.; Sonnenberg, J. L.; Williams-Young, D.; Ding, F.; Lipparini, F.; Egidi, F.; Goings, J.; Peng, B.; Petrone, A.; Henderson, T.; Ranasinghe, D.; Zakrzewski, V. G.; Gao, J.; Rega, N.; Zheng, G.; Liang, W.; Hada, M.; Ehara, M.; Toyota, K.; Fukuda, R.; Hasegawa, J.; Ishida, M.; Nakajima, T.; Honda, Y.; Kitao, O.; Nakai, H.; Vreven, T.; Throssell, K.; Montgomery, J. A., Jr.; Peralta, J. E.; Ogliaro, F.; Bearpark, M. J.; Heyd, J. J.; Brothers, E. N.; Kudin, K. N.; Staroverov, V. N.; Keith, T. A.; Kobayashi, R.; Normand, J.; Raghavachari, K.; Rendell, A. P.; Burant, J. C.; Iyengar, S. S.; Tomasi, J.; Cossi, M.; Millam, J. M.; Klene, M.; Adamo, C.; Cammi, R.; Ochterski, J. W.; Martin, R. L.; Morokuma, K.; Farkas, O.; Foresman, J. B.; Fox, D. J., Gaussian Inc., Wallingford CT **2016**.

Full Citations for Electronic Structure Codes

Cfour

Coupled-Cluster techniques for Computational Chemistry, a quantum-chemical program package by Stanton, J.F.; Gauss, J.; Harding, M.E.; Szalay, P.G. with contributions from Auer, A.A.; Bartlett, R.J.; Benedikt, U.; Berger, C.; Bernholdt, D.E.; Bomble, Y.J.; Christiansen, O.; Heckert, M.; Heun, O.; Huber, C.; Jagau, T.-C.; Jonsson, D.; Jusélius, J.; Klein, K.; Lauderdale,

W.J.; Matthews, D.A.; Metzroth, T.; O'Neill, D.P.; Price, D.R.; Prochnow, E.; Ruud, K.; Schiffmann, F.; Stopkowicz, S.; Tajti, A.; Vázquez, J.; Wang, F.; Watts, J.D. and the integral packages MOLECULE (Almlöf, J. and Taylor, P.R.), PROPS (Taylor, P.R.), ABACUS (Helgaker, T.; Jensen, H.J. Aa.; Jørgensen, P. and Olsen, J.), and ECP routines by Mitin, A. V. and van Wüllen, C. For the current version, see http://www.cfour.de.

Polyrate 2017-C

POLYRATE 2017-C; Zheng, J.; Bao, J. L.; Meana-Pañeda, R.; Zhang, S.; Lynch, B. J.; Corchado, J. C.; Chuang, Y.-Y.; Fast, P. L.; Hu, W.-P.; Liu, Y.-P.; Lynch, G. C.; Nguyen, K. A.; Jackels, C. F.; Ramos, A. F.; Ellingson, B. A.; Melissas, V. S.; Vill, J.; Rossi, I.; Coitio, E. L.; Pu, J.; Albu, T. V.; Steckler, R.; Garrett, B. C.; Isaacson, A. D.; Truhlar, D. G., **2017**.

CYLview

CYLview, 1.0b; Legault, C. Y., Université de Sherbrooke, **2009** (http://www.cylview.org).

NBO7

E. D. Glendening, J, K. Badenhoop, A. E. Reed, J. E. Carpenter, J. A. Bohmann, C. M. Morales, P. Karafiloglou, C. R. Landis, F. Weinhold, NBO 7.0, **2018**, Theoretical Chemistry Institute, University of Wisconsin, Madison.

Chapter 3: Trifluoromethylmercaptomethylene

3.1. Abstract

Schreiner and coworkers reported the formation of trifluoromethylhydroxycarbene *via* HVFP of 3,3,3-trifluoro-2-oxopropanoic acid.[1] Theoretical investigations showed the *cis*- and the *trans*-conformers **1c** and **1t** to be in close energetic proximity (0.8 kcal mol^{-1}, CCSD(T)/cc-pVTZ, Fig. 1).

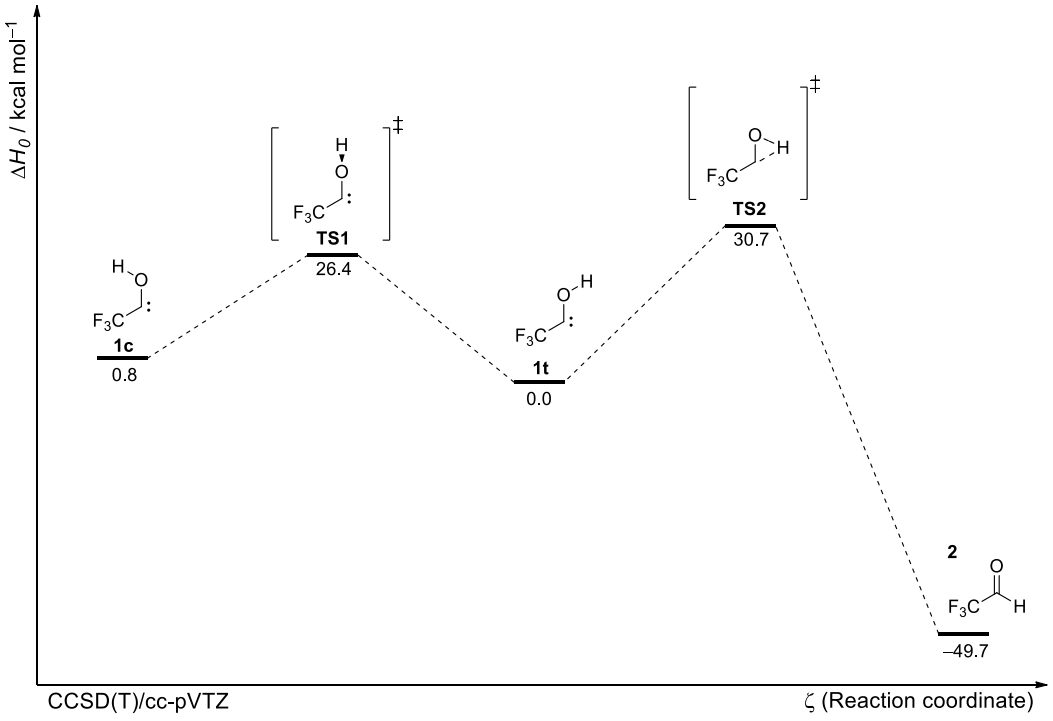

Fig. 1. PES of trifluoromethylhydroxycarbene **1**. **1t** and **1c** interconvert *via* rotation along the CO-bond over **TS2**. A 1,2[H]-shift along the CO-bond leads to trifluoroacetaldehyde **2**. This reaction is only feasible through QMT.[1]

TS1 represents the rotamerization of the two conformers and **TS2** leads to trifluoroacetaldehyde. According to the Curtin-Hammett principle, an interconversion of the two conformers seems more conclusive than a reaction of **1t** to **2**.[2-4] However, the experimental results show that **1t** preferentially rearranges to **2** through conformer-specific hydrogen tunneling due to the high barrier between **1t** and **1c**. The barrier is much narrower for this path which facilitates this reaction by QMT. Therefore, the Curtin-Hammett principle is not applicable in this case. Difluoromethylene was detected as a side product upon pyrolysis.

After we successfully generated hydroxymercapto- and aminomercaptomethylene we planned to investigate trifluoromethylmercaptomethylene and compare this species to its congener trifluoromethylhydroxymethylene, expecting a lower reactivity due to the elongated XH bond (X = O, S).

3.2. Results and Discussion

To compare trifluoromethylmercaptomethylene **3** with its congener trifluoromethylhydroxymethylene **1**, we computed the PES of **3** for a first theoretical comparison. The computed PES on the CCSD(T)/cc-pVDZ level of theory is comparable to the PES of **1** (Figures 1 and 2). Trying to compute the PES of **3** turned out to be too time and resource consuming due to the large number of electrons to be considered in this system.

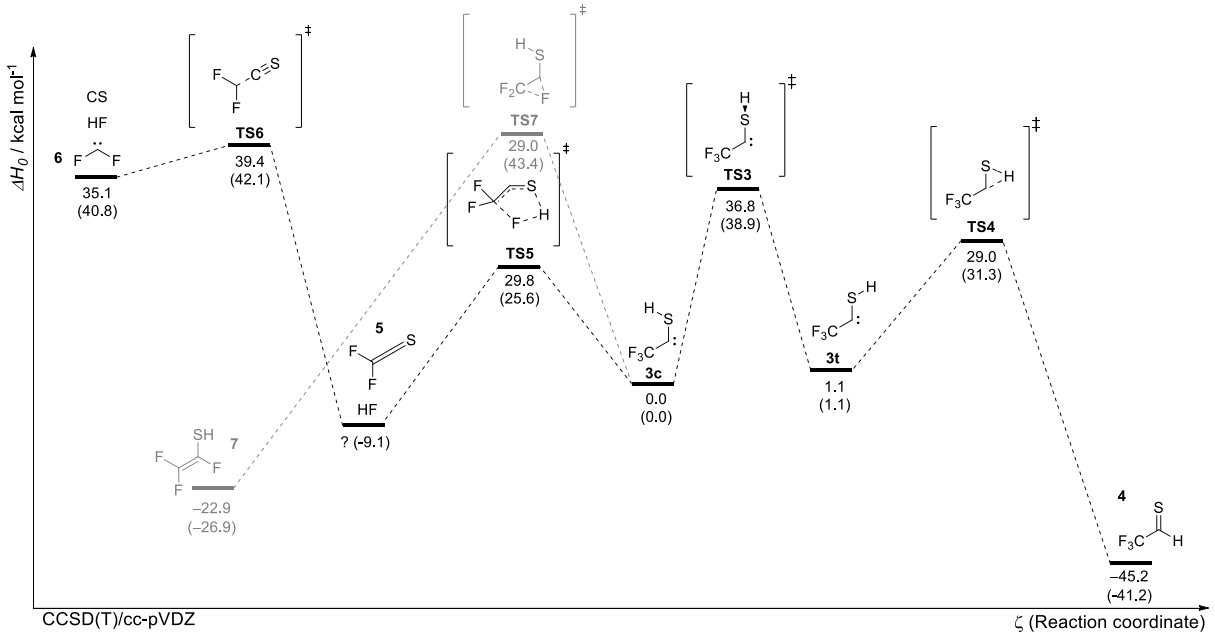

Fig 2. PES of **3**. **3c** and **3t** interconvert *via* rotation along the CS axis (**TS3**). A 1,2[H]-shift in **3t** gives **4** with a lower barrier compared to **TS3**. Starting from **3c** two possible fragmentation pathways are plausible: a) A 1,2[F]- shift along the C−C bond giving **7**, b) HF extrusion to give **5**, that further decomposes to difluoromethylene and CS. We could not locate **5** as a minimum structure at the given level of theory (B3LYP/6-311++G(3df,3pd) values in parentheses).

The barrier for the 1,2[H]-shift is lower compared to the rotamerization of **1t** and **1c** which is the opposite of what was found for trifluorohydroxymethylene which should make the tunneling reaction to **4** faster compared to the reaction of **1t** to **2** in trifluoromercaptomethylene. Rotamerization between **3c** and **3t** might be possible under irradiation as for its congener trifluorohydroxymethylene.[1] This reaction has a high activation energy of 36.8 kcal mol^{-1} (CCSD(T)/cc-pVDZ), whereas in trifluoromethylhydroxymethylene the barrier is 26.4 kcal mol^{-1} high due to shorter SH and CS bonds (CCSD(T)/cc-pVTZ).[1]

Precursor Synthesis

In analogy to the generation of trifluoromethylhydroxymethylene[1] we planned the synthesis of dithiotrifluoromethylethylpyruvate **10**. Since thionation of free carboxylic acids leads to very

unstable compounds we choose the corresponding ethyl ester that are commercially available and showed to form hydroxycarbenes after extrusion of ethylene and CO_2.[5]

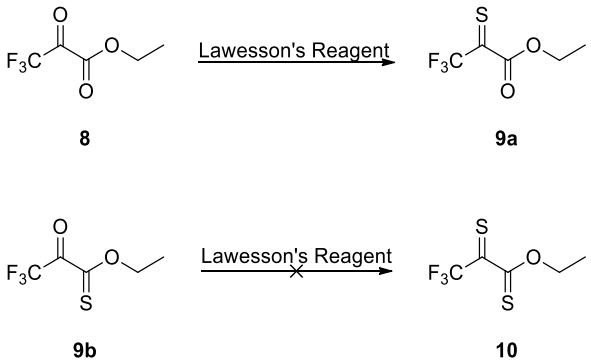

Fig. 3. Compound **10** should be prepared in a pressure tube starting from commercially available **8** in toluene at 130 °C.

GC-MS reaction control showed the formation of two products that we assigned to the formation of the monothionated starting material **9a** and **9b** after 24 h. Adding more Lawesson's reagent and after additional 72 h reaction time did not result in higher conversion, so the two products were isolated by column flash chromatography. Both products showed the same *m/z*-signals and the $^{1}H/^{13}C$-NMR spectra were nearly identical. Since one quaternary carbon was missing in ^{13}C-NMR we concluded that two types of dimers formed (Fig. 4).

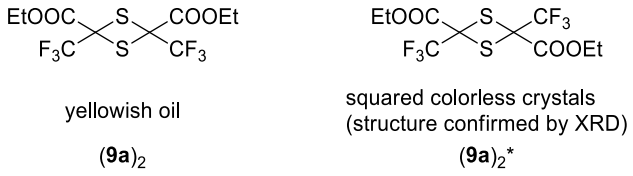

Fig. 4. Dimers of the desired precursor compound **9a.**

The formation of trimers is known for example for thioacetone that can be cracked to its monomers at 500-600 °C so the dimer should represent an acceptable storage form for our system.[6-8]

Matrix isolation experiments

(9a)2 and **(9a) 2*** showed the same behavior under HVFP conditions. It is quite difficult to differentiate between monomer and the dimers *via* IR spectra but it seems like the computed spectra of the monomeric form gives the best fit with the experimental spectrum (Fig. 5).

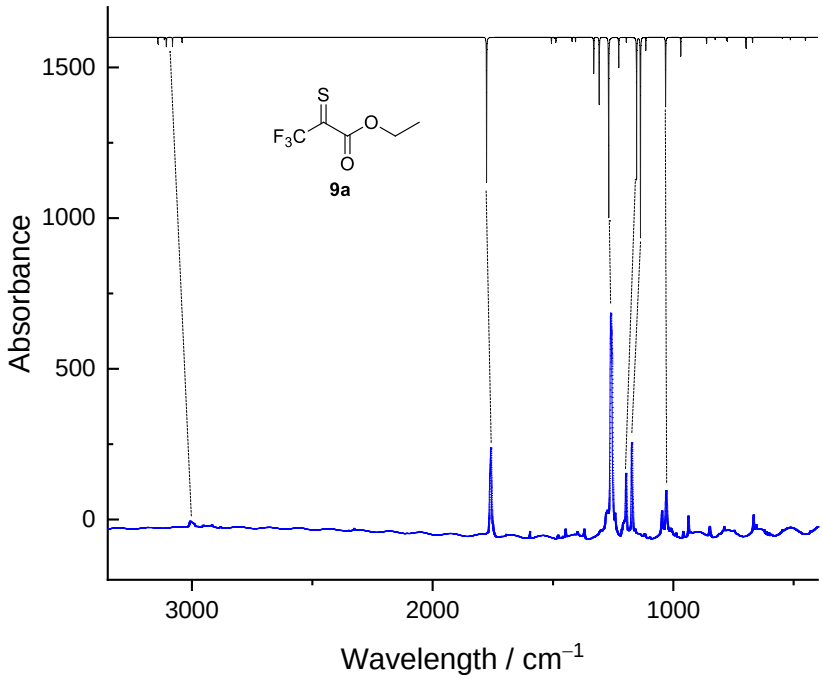

Fig. 5. Experimental spectrum of **9a** isolated in Ar at 3 K (blue) compared to computed spectra of **9a** (black) at the B3LYP/6-311++G(3df,3pd) level of theory.

Therefore, we assume that the compound evaporates in monomeric form that is then pyrolyzed in the HVFP zone of the apparatus. Upon pyrolysis at 890 °C little ethylene was detected (Fig. 23). We expected no reactivity when irradiating the matrix since all plausible fragments and the precursor itself do not absorb above 220 nm according to computations, what met our observations. We detected strong bands that we assigned to thioaldehyde **2**. Additional new bands of difluoromethylene show a good fit with the computed spectrum of **1t** and **1c**. (B3LYP/6-311++G(3df,3pd).

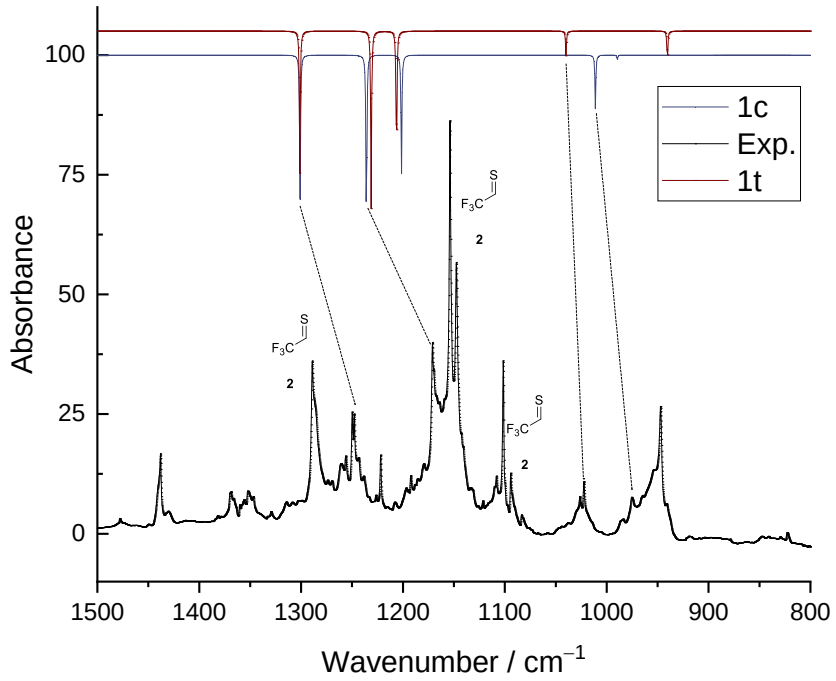

Fig. 6. Experimental **s**pectrum upon HVFP (black) compared to computed spectra of **1t** and **1c** at the CCSD(T)/cc-pVTZ level of theory (red and blue).

The detection of difluoromethylene **5** further ensures that the pyrolysis temperature is high enough to achieve decomposition (Fig. 7). The IR bands of **5** are very weak but the carbene has a characteristic UV/Vis spectrum.

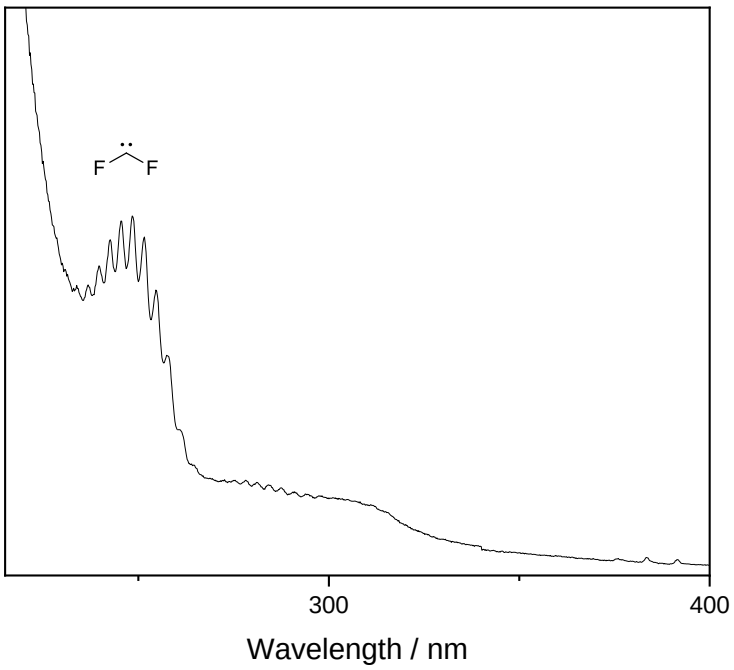

Fig. 7. UV/Vis spectrum after pyrolysis at 890 °C indicating the formation of difluoromethylene.

Theoretical considerations

Although the *cis*-conformer of trifluoromethylhydroxymethylene is less stable compared to the *trans*-conformer, QTAIM analysis indicates an O−H−F-hydrogen bond.[1] In contrast to trifluorohydroxymethylene bond critical point (BCP) analysis shows no interaction between F and the proton of the SH group in trifluoromethylmercaptomethylene (Fig. 8).

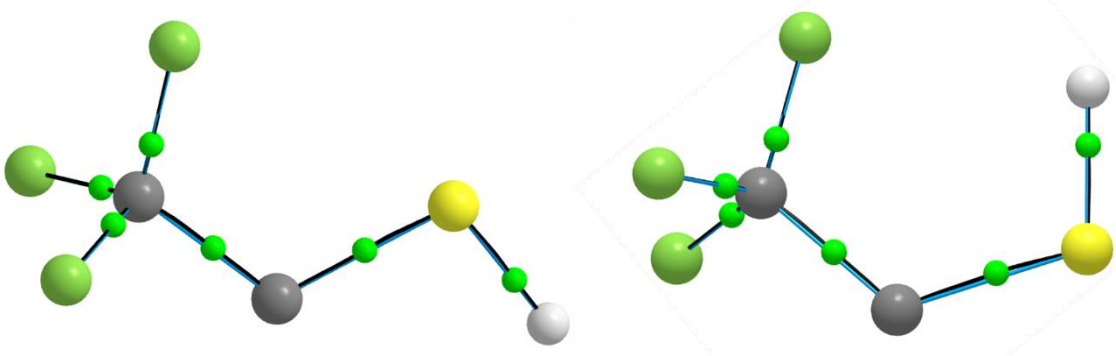

Fig. 8. BCPs of **1t** and **1c** showing no bonding interaction of the SH and the CF_3 group.

The isolated fragments upon pyrolysis showed no reactivity up to 35 K and irradiation with 254 nm. This makes it quite difficult to assign bands to a possible structure. Therefore, we planned to synthesize the perdeuterated precursor compound since the specific shift of the IR bands should give more insight to the identity of the fragments. Computations using Polyrate support our experimental results that we do not observe any tunneling reactions (Tab. 3).

Synthesis of the deuterated precursor

The significant wavelength-shift of X-D bonds compared to X-H-bonds typically gives additional information about the system. We tried to synthesize the perdeuterated starting material **5**-d_5. Starting from the commercially available carboxylic acid **11** (Fig. 9) various conditions have not led to the formation of the desired ester.

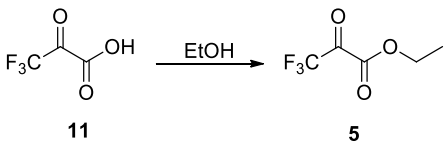

11 **5**

Fig. 9. Synthesis of **5.**

Therefore, we tried various synthetic approaches for the ester formation, but we always reisolated starting material **9**. No product formed probably due to the strongly deactivating −I-effect of the CF_3-group. Additionally, we tried synthetic strategies as shown in Fig. 10 starting from diester **12**.[9]

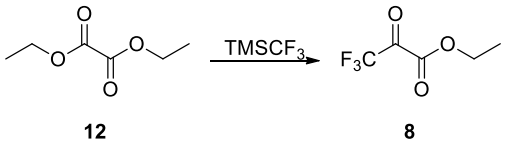

Fig. 10. Synthetic alternative.

A further method starts from trifluoro pyruvic acid monohydrate **8**. Under basic conditions, esterification was successful using ethyl iodide with TEA (Fig. 11).

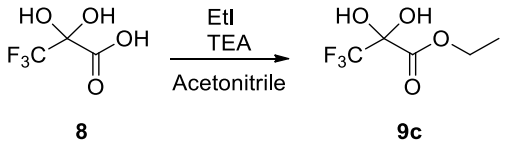

Fig. 11. Esterification of trifluoro pyruvic acid monohydrate.

Drying and dehydration of the monohydrated product **9** and starting material **8** has not been successful wherefore we discarded this approach. Trifluoromethyl pyruvic acid sublimes as its monohydrate. Therefore, we envisaged a new synthesis according to Fig. 12.

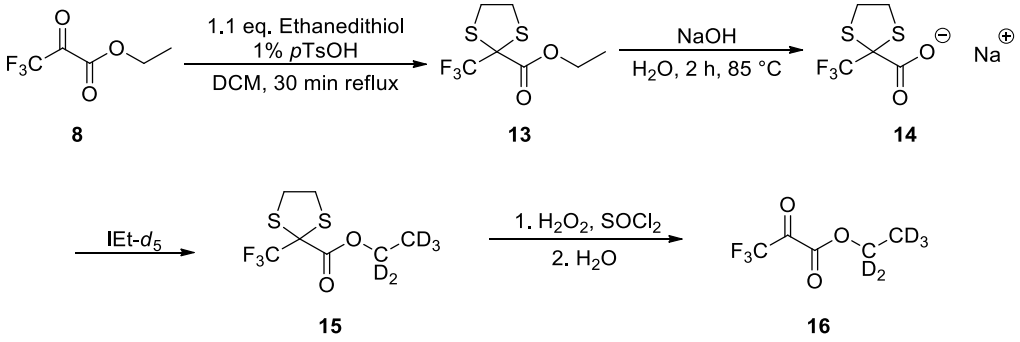

Fig. 12. New approach for the deuterated precursor **16**.

Generation of dithiolane **13** follows a procedure by Pihlaja *et al.*[10] Saponification of the ethyl ester with subsequent esterification with IEt-d_5 yields the dithiolane protected **15** that can be deprotected with a method by Bahrami *et al.*[11] Starting from **16** another strategy can be considered: Oxidized dithiolanes like **17** form thioaldehydes upon high vacuum flash pyrolysis (Fig. 13).[8]

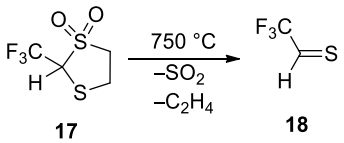

Fig. 13. Generation of a thioaldehyde under HVFP conditions.[8]

Oxidation of **15** yields **19**, that itself is a possible precursor system for trifluoromethylmercaptomethylene (Fig. 14).

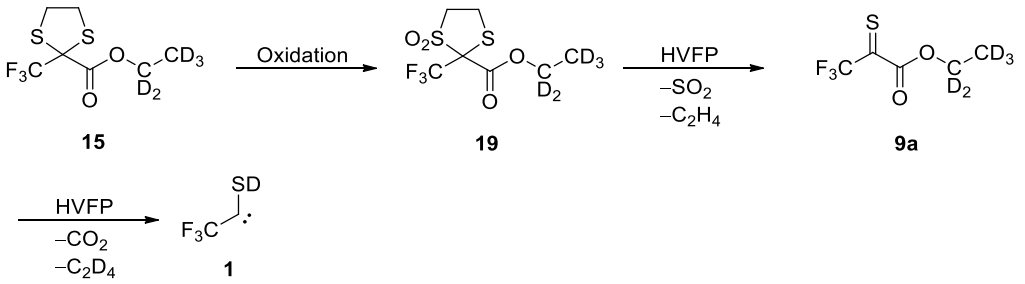

Fig. 14. Oxidized dithiolane **15** as potential precursor system.

The initial reaction for the formation of **15** with ethanedithiol was fast and exothermic but instead of **15** we isolated the open-ring product **17** after additional 20 h at r.t. (Fig. 15).

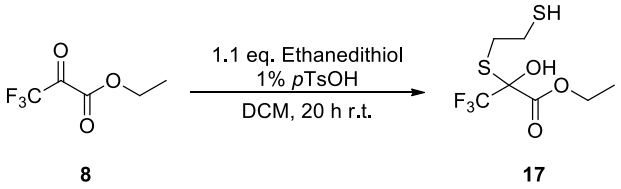

Fig. 15. Reaction of **8** with ethanedithiol yields **17** at r.t.

To achieve ring closing, isolated **17** was further reacted in DCM in the presence of *p*TsOH for 20 h under reflux but we did not obtain **15**. This reaction is challenging and we could not get rid of the impurities in **15**. For the usage in matrix isolation experiments a higher purity is needed. We changed our synthetic approach to the procedure shown in Fig. 16.

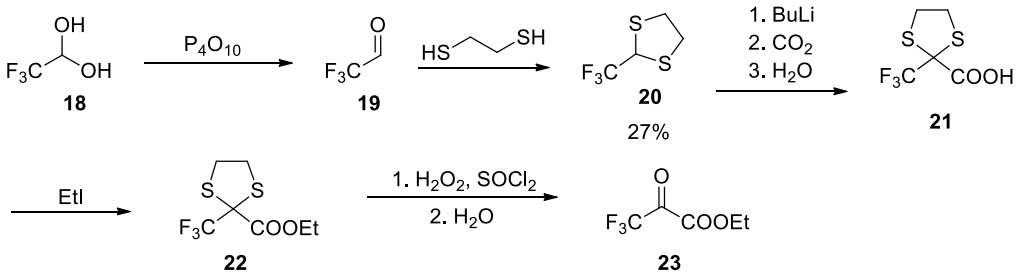

Fig. 16. Alternative synthetic approach for the perdeuterated precursor.

The reaction of **20** to **21** failed and no product formed. Although first results seemed quite promising, deuteration of the precursor failed. This is the only way of further identifying the pyrolysis products, since these seem to be very unreactive in terms of tunneling reactions and photochemistry. With a suitable method to synthesize a deuterated precursor for **3**, the significant band shift due to deuterium helps to identify the pyrolysis products more clearly.

3.3. Experimental

Methods

Matrix isolation studies

The matrix isolation experiments were performed with a Sumitomo cryostat system consisting of an F-70 compressor unit and an RDK 408D2 closed-cycle refrigerator cold head. For the infrared (IR) measurements polished KBr windows in the vacuum shroud and a CsI window on the sample holder was used. Silicon diodes attached to the sample holder measured the temperature (deposition at 15 K, measurements at 3 K). During the experiments pure 2-amino-2-thioxoacetic acid (**2**) was kept in a storage bulb in the dark and at room temperature (r.t.). The matrix host gas (Ar, gas purity of 99.999%) was stored in a 2 L glass balloon that was refilled and flushed three times with Ar before the experiments. The typical deposition time of our experiments was 1 h in which a total amount of ca. 60 mbar of Ar together with **2** were deposed on both sides of the matrix window. For irradiation a high-pressure mercury lamp (SP200) in conjunction with an MSH 150 monochromator system from LOT-QuantumDesign GmbH was used. The IR spectra were recorded with a Bruker Vertex 70 FTIR spectrometer equipped with a standard KBr or wide-range beam-splitter in a range from 7000 cm^{-1} to 350 cm^{-1} (resolution: 0.7 cm^{-1}). For every measurement 50 scans were recorded. For ultra-violet/visible (UV/Vis) measurements a Jasco V-760 spectrophotometer was used in the range from 190 nm to 800 nm (resolution: 1 nm). Prior to deposition a background spectrum of the cold matrix window was recorded. During deposition the matrix was kept in the dark to avoid unwanted photochemistry.

Computations

All computations at the B3LYP/6-311++G(3df,3pd) and the MP2/def2-QZVPP levels of theory using an ultrafine grid and very tight conversion criteria were performed with Gaussian16 Revision B.01 (full citations of electronic structure codes are given at the end of this document). The anharmonic frequencies at the B3LYP/6-311++G(3df,3pd) level of theory were computed using the Freq=Anharmonic keyword. The computed minima on the PES feature no imaginary frequencies while all transition states possess one such frequency. UV/Vis spectra were simulated at the TD-B3LYP/6-311++G(3df,3pd) level of theory.

CVT/SCT rate constants were computed with POLYRATE 2017 at the B3LYP/6-311++G(3df,3pd) level of theory.

For coupled-cluster computations (CCSD(T)/cc-pVDZ) CFOUR 1.0 was used with the following keywords: ABCDTYPE=AOBASIS, CC_PROG=ECC, SCF_CONV=8, and

CC_CONV=10; CONVERGENCE=8 in addition for geometry optimizations; VIB=EXACT for analytical computations of harmonic frequencies; METHOD=TS for transition states.

High resolution mass spectrometry was performed with a Bruker MicrOTOF (negative mode ESI-MS).

Synthesis of the Starting Materials

Ethyl-3,3,3-trifluoro-2-thiopropanoate (Dimers, Monomer: **9a**)

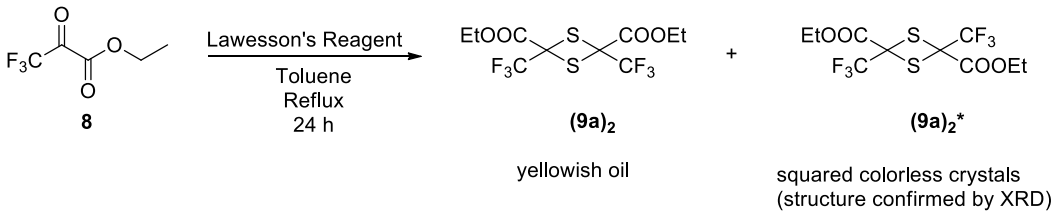

Fig. 17. Synthesis of Ethyl-3,3,3-trifluoro-2-thiopropanoate (**9a**).

Ethyl-3,3,3-trifluoro-2-oxopropanoate was obtained from Sigma-Aldrich Chemie GmbH in > 97% purity and was used without further purification. 0.7 mL Ethyl-3,3,3-trifluoro-2-oxopropanoate (0.93 g, 5.5 mmol) and 1.5 g Lawesson's reagent (LR) (3.7 mmol) were dissolved in 20 mL of dry toluene in a flame dried pressure tube and stirred for 24 h at 130 °C. The solution was cooled to r.t. and filtered over a silica plug to remove side products formed of LR (diethylether : pentane 7:1). The solvents were removed and the residue was purified *via* column chromatography (diethylether : pentane 7:1). Two products were obtained as a yellow oil and colorless squared crystals (X (R_f = 0.4) and X' R_f = 0.2)).

(9a)$_2$

Yield: 316 mg (0.85 mmol, 32%).

^{1}H-NMR (400 MHz, $CDCl_3$): δ = 4.40 (q, J = 7.1 Hz, 4H), 1.36 (t, J = 7.1 Hz, 6H) ppm.

^{13}C-NMR (101 MHz, $CDCl_3$): δ = 165.0, 127.9, 125.1, 122.3, 119.5, 64.7, 41.5, 41.2, 40.8, 40.5, 13.9 ppm.

^{19}F-NMR (400 MHz, $CDCl_3$): δ = 75.2 ppm.

IR (ATR): ν = 2988.6, 1749.2, 1448.6, 1370.2, 1239.8, 1163.1, 1096.6, 1022.4, 934.0, 843.8, 771.4, 742.7, 667.0, 547.6 cm^{-1}.

HRMS (ESI): m/z = 394.9818 $[M+Na]^+$ (calcd. m/z = 394.9817).

(9a)$_2$*

Yield: 250 mg (0.67 mmol, 25%).

^{1}H-NMR (400 MHz, $CDCl_3$): δ = 4.38 (q, J = 7.1 Hz, 4H), 1.34 (t, J = 7.1 Hz, 6H) ppm.

^{13}C-NMR (101 MHz, $CDCl_3$): δ = 165.5, 127.8, 125.0, 122.2, 119.4, 64.7, 40.3 (m) 13.9 ppm.

^{19}F-NMR (400 MHz, $CDCl_3$): δ = 73.5 ppm.

IR (ATR): ν = 2989.3, 1746.9, 1469.9, 1449.7, 1395.9, 1370.8, 1227.5, 1186.0, 1158.7, 1015.8, 933.2, 840.9, 773.6, 740.7, 658.5, 544.0, 437.7 cm^{-1}.

HRMS (ESI): m/z = 394.9819 $[M+Na]^+$ (calcd. m/z = 394.9817).

Synthesis of **15**.

0.6 g of **20** (3.4 mmol) was dissolved in 20 mL of dry THF at −78 °C. Over 5 min, 1.6 mL of n-BuLi (2.5 M, 4 mmol 1.2 equiv.) was added by a syringe. From another round-bottom flask containing dry ice, CO_2 was channeled into the yellow solution and thereby the solution was allowed to reach r.t. After 45 min 10 mL of dry THF was added because the mixture became viscous. 0.3 mL EtI (0.58 g, 3.7 mmol, 2.6 equiv.) was added and the solution was stirred overnight. GCMS control showed the acid still to be present so additional 0.3 mL of EtI was added and the mixture was stirred over the weekend. 25 mL H_2O was added together with 25 mL diethyl ether. The phases were separated and acidified with aqueous HCl (6%). The aqueous phase was extracted with 75 mL of diethylether. The combined organic phases were dried over Na_2SO_4 and the solvent was removed. The crude product (1.3 g, slightly yellow liquid) was purified by column chromatography (diethylether 3:1 pentane). Three fractions were separated:

R_f = 0.57: **15** with impurities (70 mg)

R_f = 0.33: Mixed fraction, mainly **20** (249 mg)

R_f = 0.33 – 0.10: **20** (70 mg)

Synthesis of **20**

2 mL of aqueous **18** (75%, 1.5g **6**, 1.3 mmol) was dropped to P_4O_{10}. The evolving gas (**19**) was channeled in a solution of 3.4 mL ethane dithiol (4 mmol, 3.1 equiv.) in 40 mL of DCM. When the gas evolution stopped, the solvent was removed and ethane dithiol was removed by column chromatography (diethyl ether 1:5 pentane). 0.6 g of dithiane **20** was obtained as a colorless liquid (27%, R_f = 0.25).

Yield: 600 mg (0.35 mmol, 27%).

^{1}H-NMR (400 MHz, $CDCl_3$): δ = 5.14 – 4.98 (m, 1H), 3.21 – 2.92 (m, 2H), 2.87 – 2.69 (m, 2H) ppm.

^{13}C-NMR (101 MHz, $CDCl_3$): δ = 123.6 (qd, J = 281.5, 4.4 Hz), 75.9 (qd, J = 34.6, 2.8 Hz), 34.0 ppm.

NMR Spectra

All NMR spectra were recorded with a Bruker AV400 spectrometer at 298 K. The Chemical shifts (δ) are given in ppm relative to the respective solvent residual peak of $CDCl_3$ (δ = 7.26 and 77.16 ppm). ATR-IR spectra were recorded on a Bruker Alpha spectrometer (4000 – 400 cm^{-1}).

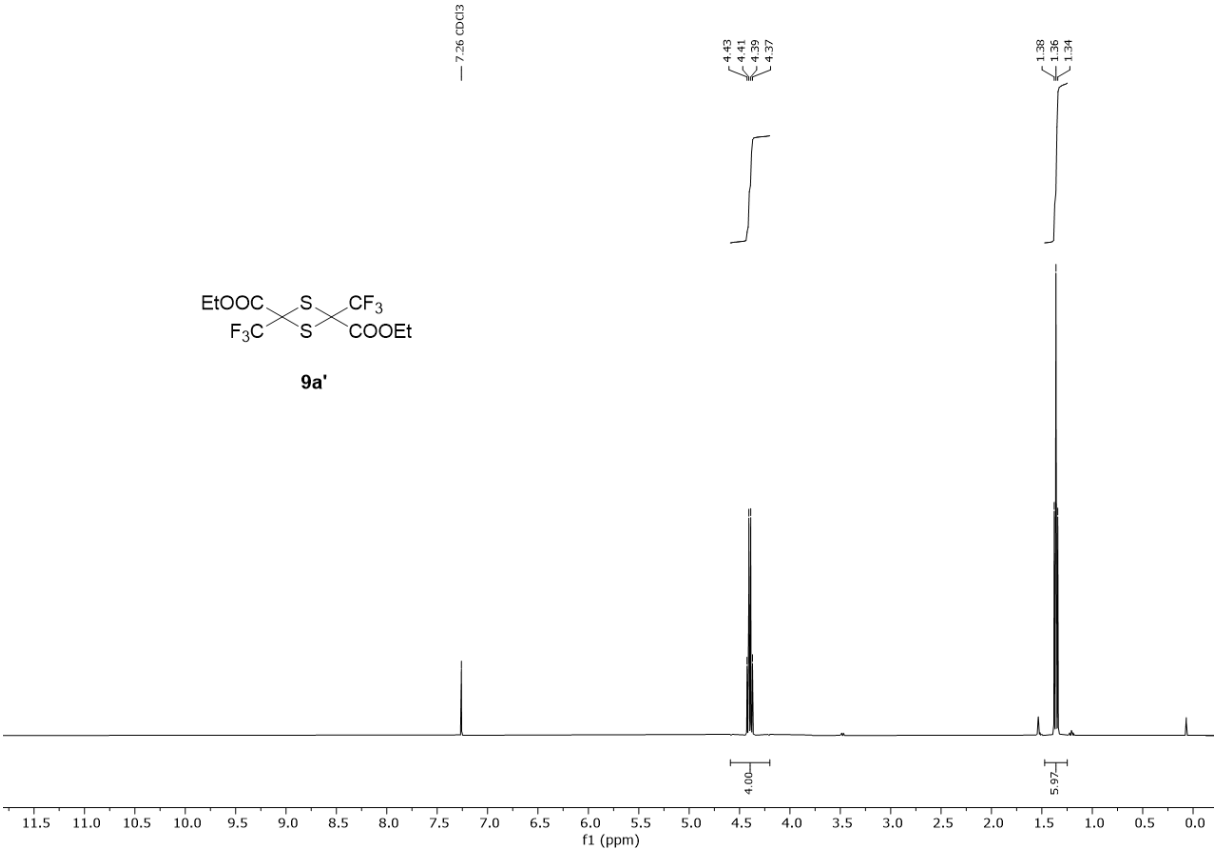

Fig. 18. ^{1}H NMR (400 MHz, $CDCl_3$) of **(9a)$_2$***.

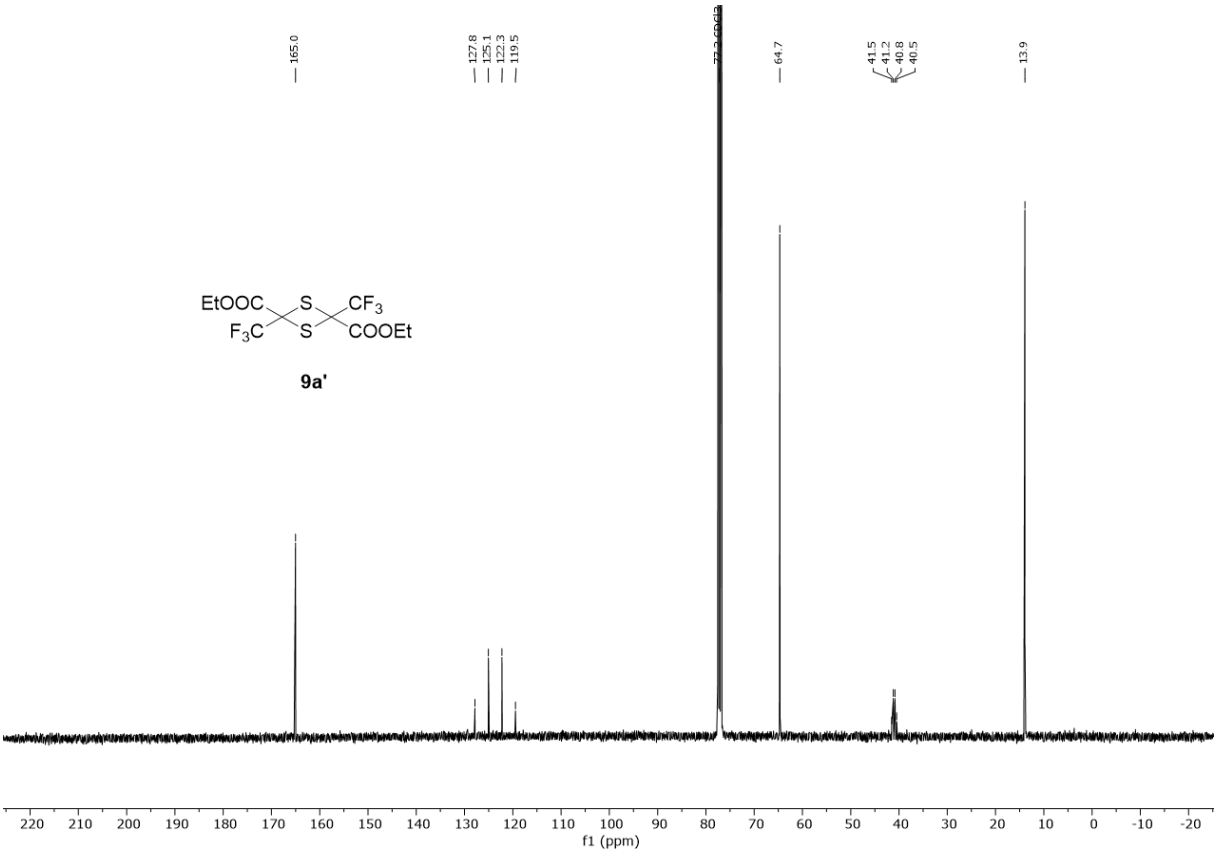

Fig. 19. $^{13}C\{^{1}H\}$ NMR (101 MHz, $CDCl_3$) of **(9a)$_2$***.

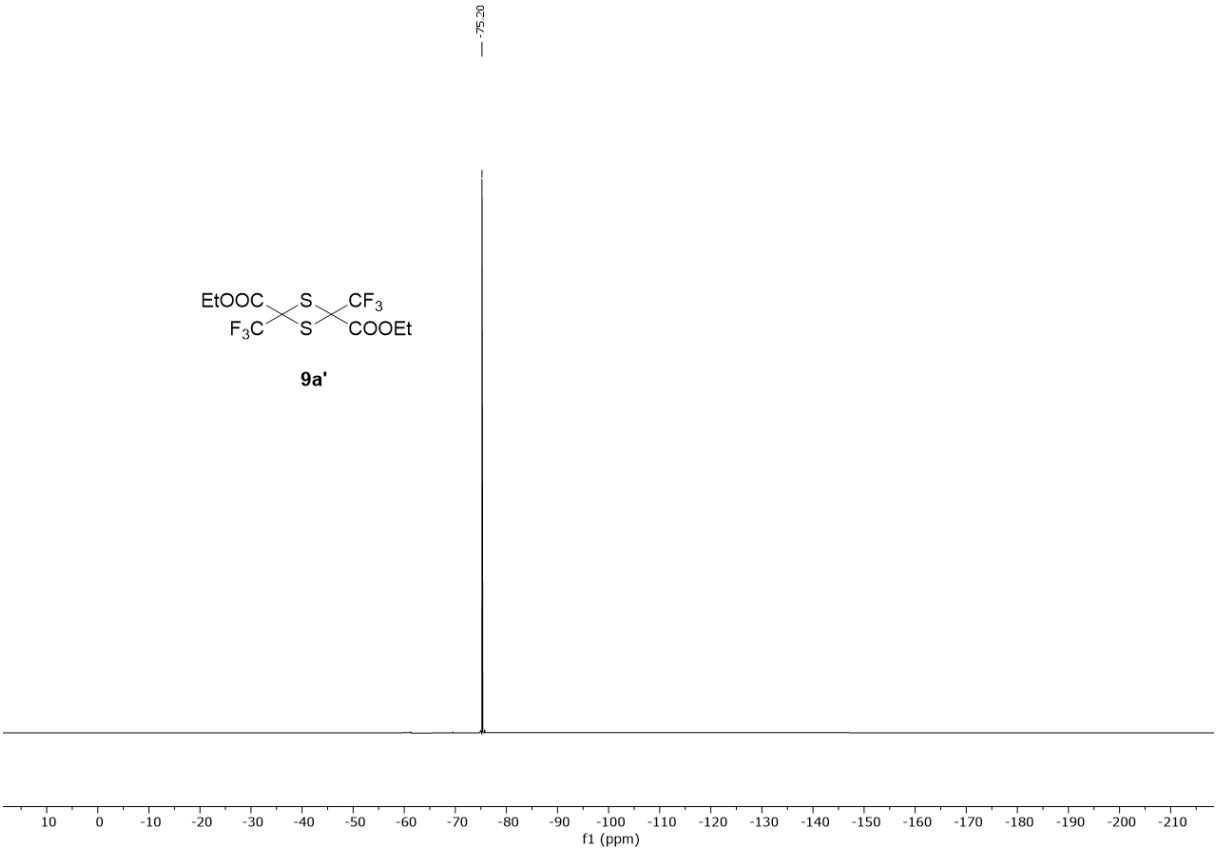

Fig. 20. ^{19}F NMR (400 MHz, $CDCl_3$) of **(9a)$_2$***.

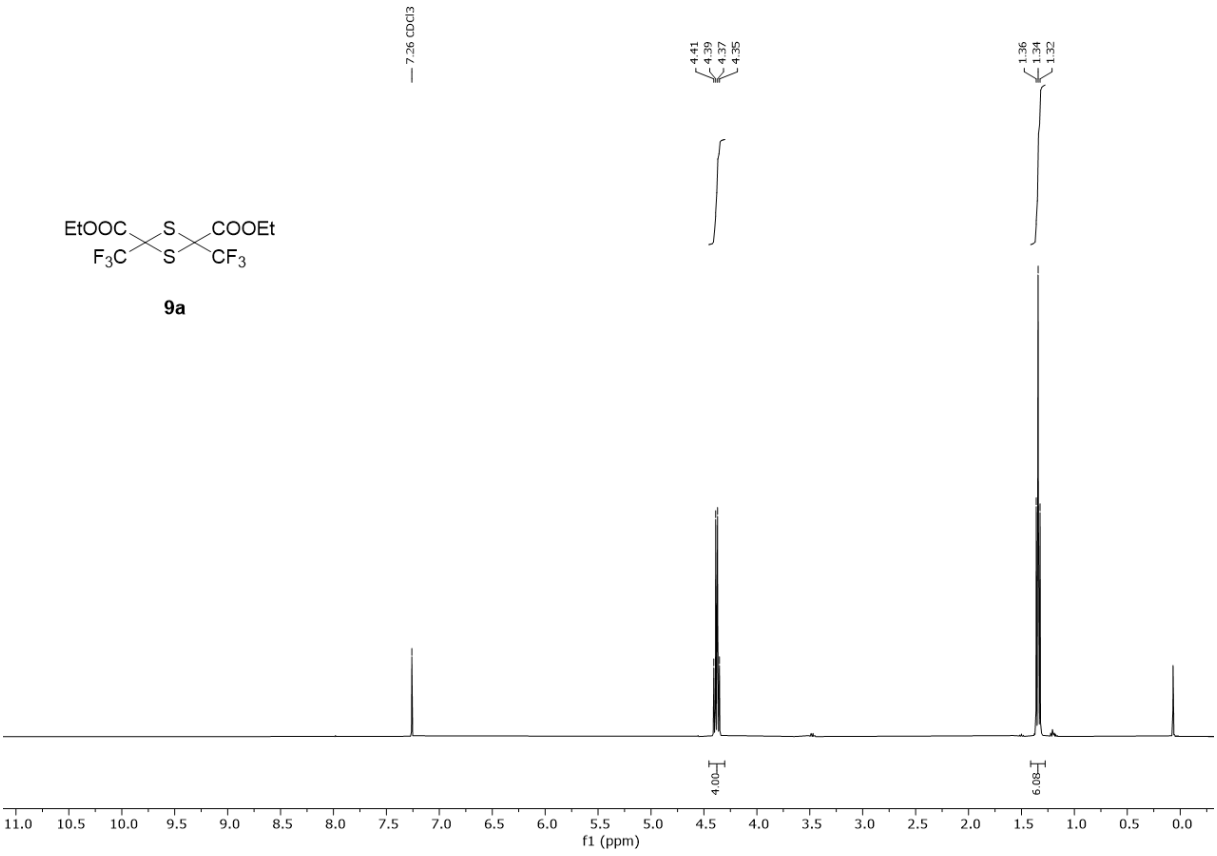

Fig. 21. ^{1}H NMR (400 MHz, $CDCl_3$) of **(9a)$_2$**.

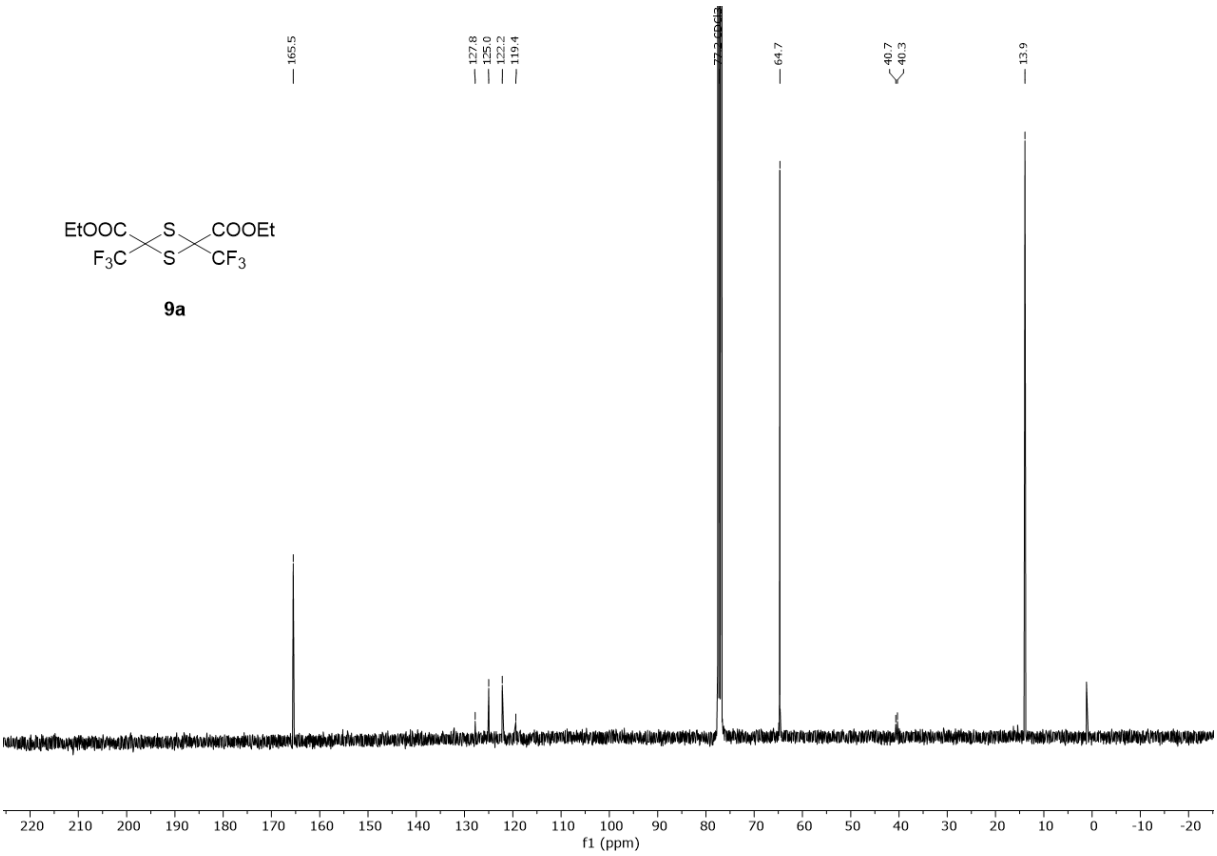

Fig. 22. $^{13}C\{^{1}H\}$ NMR (101 MHz, $CDCl_3$) of **(9a)$_2$**.

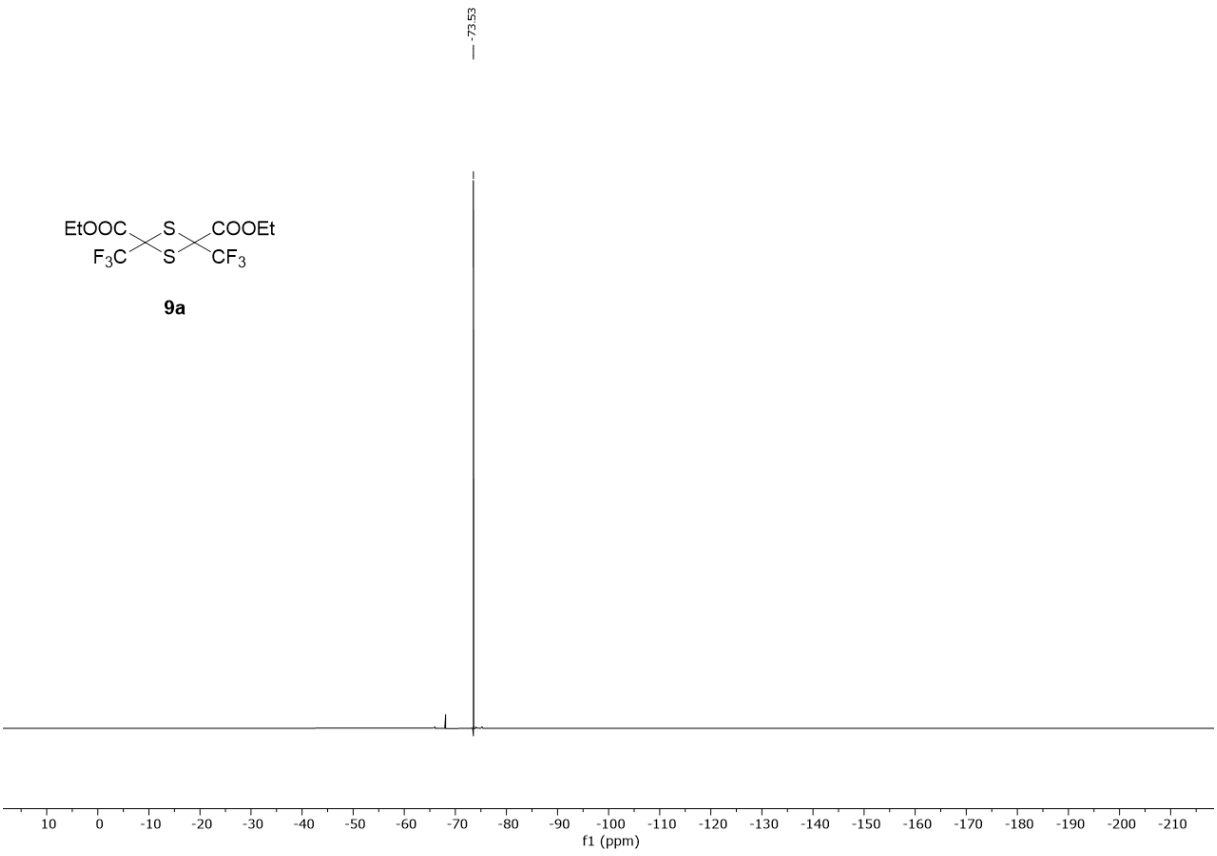

Fig. 23. ^{19}F NMR (400 MHz, $CDCl_3$) of **(9a)**$_2$.

Matrix Isolated Spectra

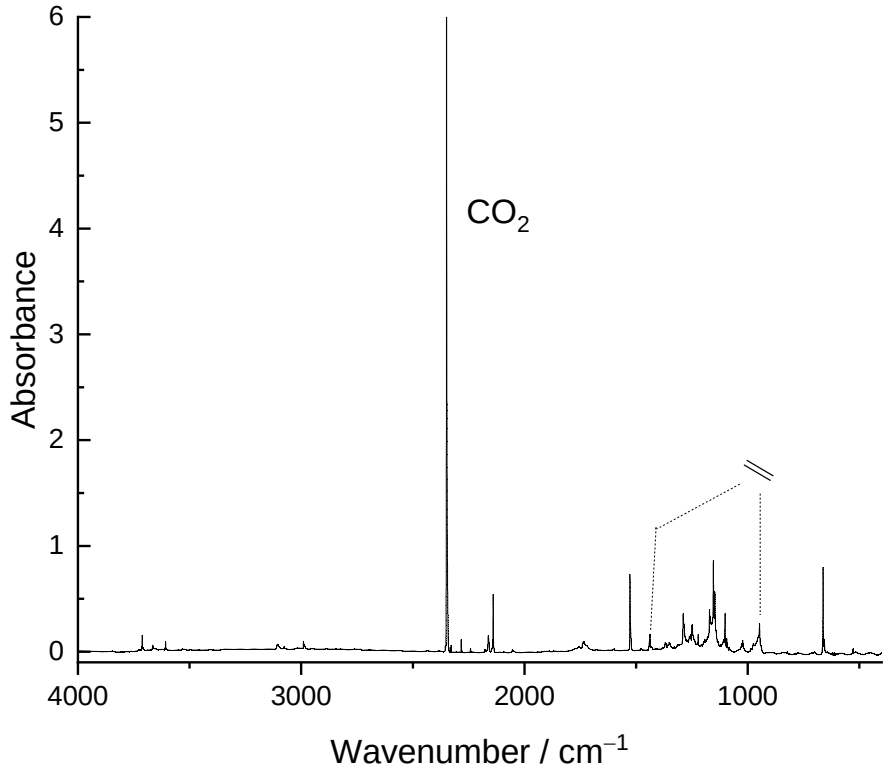

Fig. 24. Spectrum of **5** upon pyrolysis at 850 °C and isolation in solid Ar at 3 K.

IR Spectroscopic Data

Table 1. Comparison of experimental vibrational frequencies of **1t** isolated in an argon matrix at 15 K and computed vibrational frequencies at the CCSD(T)/cc-pVTZ level of theory (unscaled).

Assignment	Sym.	$\tilde{\nu}_{harm.}$ / cm^{-1}	$I_{rel.}$ / km mol^{-1}	$\tilde{\nu}_{exp.}$ / cm^{-1}	$I_{rel.}$
ω(CF_2)	*a''*	38.0	1.6	n.o.	
δ	*a'*	219.7	3.4	n.o.	
	a'	360.2	0.3	n.o.	
	a''	387.2	1.0.	n.o.	
	a''	527.3	0.8	n.o.	
	a'	551.3	1.2	528.3	w
	a'	623.4	17.0	612.2	w
	a''	686.6	5.9	n.o.	
	a'	792.2	4.3	n.o.	
υ(CS)	*a'*	948.5	42.2	946.9	s
δ(CSH)	*a'*	1051.5	45.4	1022.5	w
υ (CF)	*a'*	1195.0	218.5	1101.7	s
$\upsilon_{asym.}$(CF_2)	*a''*	1222.8	275.1	1147.8	s
δ(CC)	*a'*	1299.8	237.8	1248.0	m
δ(SH)	*a'*	2635.0	1.1	2844.1	vw

rel. experimental intensities (vw = very weak, w = weak, m = middle, s = strong, vs = very strong); n.o. = not observed; o.o.r. = out of range.

Table 2. Comparison of experimental vibrational frequencies of **1c** isolated in an argon matrix at 15 K and computed vibrational frequencies at the CCSD(T)/cc-pVTZ level of theory (unscaled).

Assignment	Sym.	$\tilde{\nu}_{harm.}$ / cm^{-1}	$I_{rel.}$ / km mol^{-1}	$\tilde{\nu}_{exp.}$ / cm^{-1}	$I_{rel.}$
ω(CF_2)	*a''*	36.1741	5.2484	n.o.	
δ	*a'*	251.1463	6.2749	n.o.	
	a'	363.1469	0.7713	n.o.	
	a''	384.2164	22.076	n.o.	
	a''	529.6455	14.3464	516.0	w
	a'	545.8611	1.1401	n.o.	
	a'	608.0655	5.0428	n.o.	
	a''	692.1594	4.4608	n.o.	

	a'	770.8899	8.7531	n.o.	
υ(CS)	*a'*	992.1388	3.0337	n.o.	
δ(CSH)	*a'*	1022.3809	89.8124	975.4	w
υ (CF)	*a'*	1189.8914	205.3037	1094.0	w
$\upsilon_{asym.}(CF_2)$	*a''*	1226.1938	272.6541	1153.8	s
δ(CC)	*a'*	1300.1382	243.1767	1249.6	m
δ(SH)	*a'*	2471.7084	31.3738	2734.6	w

rel. experimental intensities (vw = very weak, w = weak, m = middle, s = strong, vs = very strong); n.o. = not observed; o.o.r. = out of range.

Tunneling Computations

Table 3. Computed rate constants in s^{-1} of the reaction **1t → 2** at the B3LYP/6-311+G(d,p) level of theory.

T / K	TST	CVT	CVT/ZCT	CVT/SCT
4.0	0.00×10^{00}	0.00×10^{00}	NaN	NaN
5.0	0.00×10^{00}	0.00×10^{00}	NaN	NaN
6.0	0.00×10^{00}	0.00×10^{00}	NaN	NaN
8.0	0.00×10^{00}	0.00×10^{00}	NaN	NaN
10.0	0.00×10^{00}	0.00×10^{00}	NaN	NaN
20.0	0.00×10^{00}	0.00×10^{00}	NaN	NaN
28.0	1.47×10^{-219}	3.69×10^{-227}	9.91×10^{-17}	3.22×10^{-13}
40.0	3.22×10^{-150}	8.80×10^{-159}	1.10×10^{-16}	3.57×10^{-13}
50.0	7.76×10^{-118}	7.94×10^{-127}	1.23×10^{-16}	4.00×10^{-13}
75.0	1.30×10^{-74}	3.99×10^{-84}	1.64×10^{-16}	5.32×10^{-13}
77.4	5.62×10^{-72}	1.61×10^{-81}	1.68×10^{-16}	5.46×10^{-13}
100.0	5.83×10^{-53}	1.07×10^{-62}	2.12×10^{-16}	6.86×10^{-13}
125.0	6.05×10^{-40}	8.66×10^{-50}	2.69×10^{-16}	8.66×10^{-13}
150.0	2.99×10^{-31}	3.77×10^{-41}	3.41×10^{-16}	1.08×10^{-12}
175.0	5.00×10^{-25}	5.93×10^{-35}	4.40×10^{-16}	1.36×10^{-12}
194.7	3.05×10^{-21}	3.54×10^{-31}	5.46×10^{-16}	1.64×10^{-12}
200.0	2.38×10^{-20}	2.75×10^{-30}	5.81×10^{-16}	1.72×10^{-12}
225.0	1.05×10^{-16}	1.34×10^{-26}	8.76×10^{-16}	2.43×10^{-12}
250.0	8.76×10^{-14}	1.13×10^{-23}	1.26×10^{-15}	3.15×10^{-12}
273.2	1.50×10^{-11}	1.97×10^{-21}	1.91×10^{-15}	4.07×10^{-12}

275.0	2.17×10^{-11}	2.86×10^{-21}	1.98×10^{-15}	4.16×10^{-12}
298.2	1.58×10^{-9}	2.14×10^{-19}	3.41×10^{-15}	5.51×10^{-12}
300.0	2.17×10^{-9}	2.94×10^{-19}	3.59×10^{-15}	5.64×10^{-12}
325.0	1.07×10^{-7}	1.50×10^{-17}	8.26×10^{-15}	8.03×10^{-12}
350.0	3.06×10^{-6}	4.43×10^{-16}	2.79×10^{-14}	1.24×10^{-11}
373.2	4.58×10^{-5}	6.85×10^{-15}	1.24×10^{-13}	2.10×10^{-11}
375.0	5.60×10^{-5}	8.41×10^{-15}	1.41×10^{-13}	2.20×10^{-11}
400.0	7.16×10^{-4}	1.11×10^{-13}	8.82×10^{-13}	4.77×10^{-11}

Cartesian Coordinates of Computed Structures

In this section the Cartesian coordinates of the computed geometries are given in Angstrom at the CCSD(T)/cc-pVTZ and CCSD(T)/cc-pVDZ level of theory. Electronic and zero-point vibrational energies (ZPVEs) are provided for each structure. For transition states, the imaginary frequency is given additionally.

CCSD(T)/cc-pVTZ.

1c

6	0.586180619	0.863445214	0.000000000
6	-0.694875071	0.050450880	0.000000000
16	1.996429087	0.029654839	0.000000000
9	-0.580163101	-1.296989624	0.000000000
9	-1.399820644	0.369423289	-1.088398452
9	-1.399820644	0.369423289	1.088398452
1	1.672163218	-1.300873706	0.000000000

E = −773.520097623622746 au

ZPVE = 17.7034 kcal mol^{-1}

1t

6	0.571926055	0.919858588	0.000000000
6	-0.682817338	0.052961329	0.000000000
16	1.925514716	-0.044826319	0.000000000
9	-0.522899471	-1.290512183	0.000000000
9	-1.399147118	0.350705205	-1.088004998
9	-1.399147118	0.350705205	1.088004998
1	2.843132318	0.943957659	0.000000000

E = −773.519175227555252 au

ZPVE = 17.9250 kcal mol^{-1}

2

16	-2.065142139	0.014716022	-0.000000016
6	-0.628336112	-0.720882413	0.000000598

6	0.714225040	-0.013302833	-0.000000011
1	-0.519152155	-1.803529713	0.000001376
9	0.622641122	1.308343768	-0.000001021
9	1.413019557	-0.386851287	-1.081922386
9	1.413019568	-0.386849466	1.081922984

E = −773.594518055585468 au

ZPVE = 19.7523kcal mol^{-1}

CCSD(T)/cc-pVDZ

1c

6	0.584227013	0.878212259	0.000000000
6	-0.699673317	0.049989777	0.000000000
16	2.009693640	0.029255358	0.000000000
9	-0.580413598	-1.305644556	0.000000000
9	-1.408816636	0.369860172	-1.095211947
9	-1.408816636	0.369860172	1.095211947
1	1.675641013	-1.311857028	0.000000000

E = −773.081866999266708 au

ZPVE = 17.7098 kcal mol^{-1}

1t

6	0.568314897	0.932495367	0.000000000
6	-0.688933834	0.052078614	0.000000000
16	1.940909546	-0.044826324	0.000000000
9	-0.521682856	-1.298678748	0.000000000
9	-1.410075199	0.350638608	-1.094768407
9	-1.410075199	0.350638608	1.094768407
1	2.859648808	0.960462163	0.000000000

E = −773.080490234126387 au

ZPVE = 17.9061 kcal mol^{-1}

2

16	-2.077204999	0.013716655	-0.000000005
6	-0.627111352	-0.728535745	0.000000370
6	0.718492172	-0.013730663	0.000000000
1	-0.511829274	-1.826314990	0.000000926
9	0.620164694	1.316034142	-0.000000635
9	1.422479294	-0.386698709	-1.088276646
9	1.422479315	-0.386697571	1.088277005

E = −773.157120128167321 au

ZPVE = 19.7109 kcal mol^{-1}

4

1	-2.195727018	-0.222539237	1.227356799
16	-1.833412104	-0.472748036	-0.056175091
6	-0.297852759	0.397820263	0.017582703
6	0.906294278	-0.206779857	0.008127046
9	1.086541373	-1.515767311	0.028733483
9	-0.323907129	1.753103857	0.013024126
9	2.054949481	0.449380611	-0.028569343

E = −773.118802952140300 au

ZPVE = 17.9819 kcal mol^{-1}

5

9	0.000000000	-1.040242465	0.192981550
6	0.000000000	0.000000000	-0.611056882
9	0.000000000	1.040242465	0.192981550

E = −237.183565994247346 au

ZPVE = 4.3720 kcal mol^{-1}

CS

16	0.000000000	0.000000000	0.427664193
6	0.000000000	0.000000000	-1.139442492

E = −435.605316975626465 au

ZPVE = 1.8026 kcal mol^{-1}

HF

9	0.000000000	0.000000000	0.046339369
1	0.000000000	0.000000000	-0.873538529

E = −435.605316975626465 au

ZPVE = 1.8026 kcal mol^{-1}

TS1: 1t → 1c

6	0.492219621	-0.479354983	-0.840964658
6	-0.725198885	-0.001276053	-0.053349544
16	2.011679028	0.001657272	-0.009361950
9	-0.656317301	1.189640585	0.556006022
9	-0.869200551	-0.966139123	0.884118883
9	-1.819829563	0.018803128	-0.817282532
1	2.018669968	1.102558245	-0.795692962

E = − 773.020697318359908 au

ZPVE = 16.0880 kcal mol^{-1}

ν_i = 1052.7265*i* cm^{-1}

TS2: 1t → 2

6	0.583843809	0.826006553	0.000000000
6	-0.716777961	0.044992438	0.000000000
16	2.023191739	-0.034479173	0.000000000
9	-0.564122633	-1.295065494	0.000000000
9	-1.427964047	0.363701851	-1.089853816
9	-1.427964047	0.363701851	1.089853816
1	1.870446801	1.423908252	0.000000000

E = − 773.030973591474662 au

ZPVE = 15.7659 kcal mol^{-1}

ν_i = 1757.9558*i* cm^{-1}

TS3: 1c → 4

1	-1.705648094	0.332392174	-1.440638482
16	-1.943333320	0.351723511	-0.095237448
6	-0.458192624	0.045995076	0.599665183
6	0.801481918	0.203380740	0.024896837
9	1.747838205	0.855577152	0.615396548
9	0.176479104	-1.509193263	0.396255729
9	1.219731852	-0.113439510	-1.169449446

E = −772.994173508536846 au

ZPVE = 16.3987 kcal mol^{-1}

ν_i = 486.4412*i* cm^{-1}

TS4: 1c → 3 + HF

6	0.532381036	0.992843805	0.000000000
6	-0.701072922	0.291399453	0.000000000
16	1.882369021	0.095426470	0.000000000
9	-1.423383970	0.298238307	-1.075568020
9	-1.423383970	0.298238307	1.075568020
1	0.962788865	-1.144280157	0.000000000
9	-0.265559697	-1.507535641	0.000000000

E = − 773.028232735253027 au

ZPVE = 15.9853 kcal mol^{-1}

ν_i = 1286.0031*i* cm^{-1}

TS5: 3 → 5 + CS + HF

16	0.111789033	-2.318293285	0.000000000
6	-0.544852993	-0.934477533	0.000000000
6	0.473372285	1.265844659	0.000000000
9	-0.071489121	1.846055968	-1.035921791
9	-0.071489121	1.846055968	1.035921791

E = − 672.785705030838926 au

ZPVE = 7.0369 kcal mol^{-1}

v_i = 186.6720*i* cm^{-1}

Full Citations for Electronic Structure Codes

Gaussian 16.

Gaussian 16, Revision A.03; Frisch, M. J.; Trucks, G. W.; Schlegel, H. B.; Scuseria, G. E.; Robb, M. A.; Cheeseman, J. R.; Scalmani, G.; Barone, V.; Petersson, G. A.; Nakatsuji, H.; Li, X.; Caricato, M.; Marenich, A. V.; Bloino, J.; Janesko, B. G.; Gomperts, R.; Mennucci, B.; Hratchian, H. P.; Ortiz, J. V.; Izmaylov, A. F.; Sonnenberg, J. L.; Williams-Young, D.; Ding, F.; Lipparini, F.; Egidi, F.; Goings, J.; Peng, B.; Petrone, A.; Henderson, T.; Ranasinghe, D.; Zakrzewski, V. G.; Gao, J.; Rega, N.; Zheng, G.; Liang, W.; Hada, M.; Ehara, M.; Toyota, K.; Fukuda, R.; Hasegawa, J.; Ishida, M.; Nakajima, T.; Honda, Y.; Kitao, O.; Nakai, H.; Vreven, T.; Throssell, K.; Montgomery, J. A., Jr.; Peralta, J. E.; Ogliaro, F.; Bearpark, M. J.; Heyd, J. J.; Brothers, E. N.; Kudin, K. N.; Staroverov, V. N.; Keith, T. A.; Kobayashi, R.; Normand, J.; Raghavachari, K.; Rendell, A. P.; Burant, J. C.; Iyengar, S. S.; Tomasi, J.; Cossi, M.; Millam, J. M.; Klene, M.; Adamo, C.; Cammi, R.; Ochterski, J. W.; Martin, R. L.; Morokuma, K.; Farkas, O.; Foresman, J. B.; Fox, D. J., Gaussian Inc., Wallingford CT **2016**.

Cfour.

Coupled-Cluster techniques for Computational Chemistry, a quantum-chemical program package by Stanton, J.F.; Gauss, J.; Harding, M.E.; Szalay, P.G. with contributions from Auer, A.A.; Bartlett, R.J.; Benedikt, U.; Berger, C.; Bernholdt, D.E.; Bomble, Y.J.; Christiansen, O.; Heckert, M.; Heun, O.; Huber, C.; Jagau, T.-C.; Jonsson, D.; Jusélius, J.; Klein, K.; Lauderdale, W.J.; Matthews, D.A.; Metzroth, T.; O'Neill, D.P.; Price, D.R.; Prochnow, E.; Ruud, K.; Schiffmann, F.; Stopkowicz, S.; Tajti, A.; Vázquez, J.; Wang, F.; Watts, J.D. and the integral packages MOLECULE (Almlöf, J. and Taylor, P.R.), PROPS (Taylor, P.R.), ABACUS (Helgaker, T.; Jensen, H.J. Aa.; Jørgensen, P. and Olsen, J.), and ECP routines by Mitin, A. V. and van Wüllen, C. For the current version, see; CFOUR, **2010**.

Polyrate 2017-C.

POLYRATE 2017-C; Zheng, J.; Bao, J. L.; Meana-Pañeda, R.; Zhang, S.; Lynch, B. J.; Corchado, J. C.; Chuang, Y.-Y.; Fast, P. L.; Hu, W.-P.; Liu, Y.-P.; Lynch, G. C.; Nguyen, K. A.; Jackels, C. F.; Ramos, A. F.; Ellingson, B. A.; Melissas, V. S.; Vill, J.; Rossi, I.; Coitio, E. L.; Pu, J.; Albu, T. V.; Steckler, R.; Garrett, B. C.; Isaacson, A. D.; Truhlar, D. G., **2017**.

CYLview.

CYLview, 1.0b; Legault, C. Y., Université de Sherbrooke, **2009** (http://www.cylview.org).

XRD Analysis

Crystal data and structure refinement for D21112 (**9a**)$_2$*.

Identification code	D21112	
Empirical formula	C10 H10 F6 O4 S2	
Formula weight	372.30	
Temperature	100(2) K	
Wavelength	0.71073 Å	
Crystal system	Monoclinic	
Space group	$P2_1$	
Unit cell dimensions	a = 7.1463(4) Å	a= 90°.
	b = 11.4086(5) Å	b= 111.260(2)°.
	c = 9.5022(4) Å	g = 90°.
Volume	721.98(6) Å^3	
Z	2	
Density (calculated)	1.713 Mg/m^3	
Absorption coefficient	0.450 mm^{-1}	
F(000)	376	
Crystal size	0.441 x 0.261 x 0.062 mm^3	
Theta range for data collection	2.300 to 30.997°.	
Index ranges	-10<=h<=10, -16<=k<=16, -13<=l<=13	
Reflections collected	25860	
Independent reflections	4617 [R(int) = 0.0437]	
Completeness to theta = 25.242°	100.0 %	
Absorption correction	Semi-empirical from equivalents	
Refinement method	Full-matrix least-squares on F^2	
Data / restraints / parameters	4617 / 191 / 210	
Goodness-of-fit on F^2	1.061	
Final R indices [I>2sigma(I)]	R1 = 0.0282, wR2 = 0.0652	
R indices (all data)	R1 = 0.0322, wR2 = 0.0673	
Absolute structure parameter	0.47(6)	

Extinction coefficient	n/a
Largest diff. peak and hole	0.388 and -0.311 e.Å^{-3}

Table 4. Atomic coordinates ($\cdot 10^4$) and equivalent isotropic displacement parameters ($Å^2 \cdot 10^3$) for D21112. U(eq) is defined as one third of the trace of the orthogonalized U^{ij} tensor.

	x	y	z	U(eq)
S(1)	4823(1)	4312(1)	1146(1)	20(1)
S(2)	5600(1)	5410(1)	3818(1)	17(1)
F(1)	8580(2)	5728(1)	2143(2)	29(1)
F(2)	7453(2)	7387(1)	2539(2)	25(1)
F(3)	6566(2)	6714(1)	268(2)	26(1)
C(1)	6962(3)	6414(2)	1708(2)	19(1)
C(2)	5132(3)	5811(2)	1857(2)	15(1)
O(1)	1828(3)	6212(2)	59(2)	32(1)
O(2)	3393(2)	7576(1)	1780(2)	23(1)
C(3)	3228(3)	6547(2)	1112(2)	17(1)
C(4)	1691(3)	8381(2)	1137(3)	27(1)
C(5)	2365(3)	9566(2)	1785(3)	24(1)
F(11)	1760(2)	3952(1)	2638(2)	28(1)
F(12)	3705(2)	3189(1)	4727(2)	24(1)
F(13)	3120(2)	2271(1)	2623(2)	27(1)
C(11)	3429(3)	3333(2)	3264(2)	17(1)
C(12)	5270(3)	3913(2)	3099(2)	15(1)
O(11)	8170(30)	3270(20)	5230(14)	25(3)
O(12)	7430(40)	2427(19)	2943(16)	23(1)
C(13)	7122(14)	3147(8)	3931(8)	15(1)
C(14)	9044(3)	1553(2)	3514(3)	25(1)
C(15)	8292(6)	491(4)	4020(8)	25(1)
O(11A)	7930(50)	3140(30)	5128(19)	23(3)
O(12A)	7380(60)	2380(30)	2820(20)	23(1)
C(13A)	7100(20)	3116(12)	3791(11)	15(1)
C(14A)	9044(3)	1553(2)	3514(3)	25(1)
C(15A)	8122(9)	344(6)	3513(11)	25(1)

Table 5. Bond lengths [Å] and angles [°] for D21112.

S(1)-C(2)	1.8233(19)
S(1)-C(12)	1.8235(19)
S(2)-C(12)	1.822(2)
S(2)-C(2)	1.8281(19)
F(1)-C(1)	1.332(2)
F(2)-C(1)	1.334(2)
F(3)-C(1)	1.337(2)
C(1)-C(2)	1.529(3)
C(2)-C(3)	1.536(3)
O(1)-C(3)	1.192(3)
O(2)-C(3)	1.319(2)
O(2)-C(4)	1.469(2)
C(4)-C(5)	1.492(3)
C(4)-H(4A)	0.9900

C(4)-H(4B)	0.9900
C(5)-H(5A)	0.9800
C(5)-H(5B)	0.9800
C(5)-H(5C)	0.9800
F(11)-C(11)	1.327(2)
F(12)-C(11)	1.341(2)
F(13)-C(11)	1.338(2)
C(11)-C(12)	1.530(3)
C(12)-C(13A)	1.530(11)
C(12)-C(13)	1.543(8)
O(11)-C(13)	1.198(10)
O(12)-C(13)	1.324(10)
O(12)-C(14)	1.472(11)
C(14)-C(15)	1.475(5)
C(14)-H(14A)	0.9900
C(14)-H(14B)	0.9900
C(15)-H(15A)	0.9800
C(15)-H(15B)	0.9800
C(15)-H(15C)	0.9800
O(11A)-C(13A)	1.192(15)
O(12A)-C(13A)	1.314(15)
O(12A)-C(14A)	1.472(16)
C(14A)-C(15A)	1.528(7)
C(14A)-H(14C)	0.9900
C(14A)-H(14D)	0.9900
C(15A)-H(15D)	0.9800
C(15A)-H(15E)	0.9800
C(15A)-H(15F)	0.9800

S(1)-C(2)	1.8233(19)
S(1)-C(12)	1.8235(19)
S(2)-C(12)	1.822(2)
C(2)-S(1)-C(12)	84.48(8)
C(12)-S(2)-C(2)	84.37(8)
F(1)-C(1)-F(2)	107.02(16)
F(1)-C(1)-F(3)	107.81(17)
F(2)-C(1)-F(3)	107.77(17)
F(1)-C(1)-C(2)	112.50(17)
F(2)-C(1)-C(2)	111.67(16)
F(3)-C(1)-C(2)	109.85(16)
C(1)-C(2)-C(3)	110.88(15)
C(1)-C(2)-S(1)	112.33(14)
C(3)-C(2)-S(1)	111.95(13)
C(1)-C(2)-S(2)	111.16(13)
C(3)-C(2)-S(2)	114.25(13)
S(1)-C(2)-S(2)	95.48(9)
C(3)-O(2)-C(4)	116.12(16)

O(1)-C(3)-O(2)	126.2(2)
O(1)-C(3)-C(2)	123.02(19)
O(2)-C(3)-C(2)	110.77(16)
O(2)-C(4)-C(5)	107.50(17)
O(2)-C(4)-H(4A)	110.2
C(5)-C(4)-H(4A)	110.2
O(2)-C(4)-H(4B)	110.2
C(5)-C(4)-H(4B)	110.2
H(4A)-C(4)-H(4B)	108.5
C(4)-C(5)-H(5A)	109.5
C(4)-C(5)-H(5B)	109.5
H(5A)-C(5)-H(5B)	109.5
C(4)-C(5)-H(5C)	109.5
H(5A)-C(5)-H(5C)	109.5
H(5B)-C(5)-H(5C)	109.5
F(11)-C(11)-F(13)	107.76(16)
F(11)-C(11)-F(12)	107.44(16)
F(13)-C(11)-F(12)	107.37(16)
F(11)-C(11)-C(12)	112.97(16)
F(13)-C(11)-C(12)	110.58(16)
F(12)-C(11)-C(12)	110.50(15)
C(11)-C(12)-C(13A)	109.3(6)
C(11)-C(12)-C(13)	108.2(4)
C(11)-C(12)-S(2)	111.49(13)
C(13A)-C(12)-S(2)	114.9(5)
C(13)-C(12)-S(2)	111.6(4)
C(11)-C(12)-S(1)	111.84(13)
C(13A)-C(12)-S(1)	113.1(4)
C(13)-C(12)-S(1)	117.6(3)
S(2)-C(12)-S(1)	95.67(9)
C(13)-O(12)-C(14)	118.0(10)
O(11)-C(13)-O(12)	126.6(13)
O(11)-C(13)-C(12)	124.4(11)
O(12)-C(13)-C(12)	108.7(7)
O(12)-C(14)-C(15)	110.3(14)
O(12)-C(14)-H(14A)	109.6
C(15)-C(14)-H(14A)	109.6
O(12)-C(14)-H(14B)	109.6
C(15)-C(14)-H(14B)	109.6
H(14A)-C(14)-H(14B)	108.1
C(14)-C(15)-H(15A)	109.5
C(14)-C(15)-H(15B)	109.5
H(15A)-C(15)-H(15B)	109.5
C(14)-C(15)-H(15C)	109.5
H(15A)-C(15)-H(15C)	109.5
H(15B)-C(15)-H(15C)	109.5
C(13A)-O(12A)-C(14A)	113.8(15)

O(11A)-C(13A)-O(12A)	128.0(17)
O(11A)-C(13A)-C(12)	117.6(15)
O(12A)-C(13A)-C(12)	113.8(11)
O(12A)-C(14A)-C(15A)	107.5(19)
O(12A)-C(14A)-H(14C)	110.2
C(15A)-C(14A)-H(14C)	110.2
O(12A)-C(14A)-H(14D)	110.2
C(15A)-C(14A)-H(14D)	110.2
H(14C)-C(14A)-H(14D)	108.5
C(14A)-C(15A)-H(15D)	109.5
C(14A)-C(15A)-H(15E)	109.5
H(15D)-C(15A)-H(15E)	109.5
C(14A)-C(15A)-H(15F)	109.5
H(15D)-C(15A)-H(15F)	109.5
H(15E)-C(15A)-H(15F)	109.5

Symmetry transformations used to generate equivalent atoms.

Table 6. Anisotropic displacement parameters ($Å^2 \cdot 10^3$) for D21112. The anisotropic displacement factor exponent takes the form: $-2\pi^2[\ h^2\ a^{*2}U^{11} + ...\ + 2\ h\ k\ a^*b^*U^{12}]$.

	U^{11}	U^{22}	U^{33}	U^{23}	U^{13}	U^{12}
S(1)	34(1)	13(1)	13(1)	-1(1)	8(1)	-1(1)
S(2)	25(1)	11(1)	12(1)	-1(1)	6(1)	-1(1)
F(1)	23(1)	26(1)	40(1)	6(1)	12(1)	7(1)
F(2)	24(1)	20(1)	30(1)	-6(1)	10(1)	-6(1)
F(3)	35(1)	27(1)	22(1)	6(1)	16(1)	0(1)
C(1)	21(1)	16(1)	20(1)	1(1)	8(1)	2(1)
C(2)	21(1)	11(1)	13(1)	1(1)	5(1)	0(1)
O(1)	26(1)	28(1)	30(1)	-7(1)	-5(1)	-1(1)
O(2)	22(1)	17(1)	23(1)	-4(1)	-2(1)	5(1)
C(3)	19(1)	15(1)	16(1)	1(1)	5(1)	-2(1)
C(4)	18(1)	21(1)	35(1)	2(1)	0(1)	6(1)
C(5)	28(1)	19(1)	25(1)	5(1)	11(1)	7(1)
F(11)	18(1)	28(1)	34(1)	1(1)	5(1)	5(1)
F(12)	28(1)	28(1)	21(1)	3(1)	13(1)	-3(1)
F(13)	29(1)	17(1)	38(1)	-11(1)	17(1)	-9(1)
C(11)	19(1)	14(1)	19(1)	-1(1)	6(1)	0(1)
C(12)	18(1)	12(1)	14(1)	-1(1)	6(1)	-1(1)
O(11)	24(4)	28(5)	13(2)	-7(2)	-5(2)	0(3)
O(12)	25(1)	23(2)	17(2)	-5(2)	3(2)	8(1)
C(13)	18(1)	12(1)	14(1)	-1(1)	6(1)	-1(1)
C(14)	22(1)	24(1)	28(1)	-1(1)	8(1)	6(1)
C(15)	22(1)	24(1)	28(1)	-1(1)	8(1)	6(1)
O(11A)	23(7)	20(5)	20(4)	-2(4)	2(4)	7(6)
O(12A)	25(1)	23(2)	17(2)	-5(2)	3(2)	8(1)
C(13A)	18(1)	12(1)	14(1)	-1(1)	6(1)	-1(1)
C(14A)	22(1)	24(1)	28(1)	-1(1)	8(1)	6(1)
C(15A)	22(1)	24(1)	28(1)	-1(1)	8(1)	6(1)

Table 7. Hydrogen coordinates ($\cdot 10^4$) and isotropic displacement parameters ($Å^2 \cdot 10^3$) for D21112.

	x	y	z	U(eq)
H(4A)	537	8118	1397	33
H(4B)	1271	8404	23	33
H(5A)	3512	9816	1525	36
H(5B)	2764	9535	2886	36
H(5C)	1262	10127	1370	36
H(14A)	10172	1889	4368	30
H(14B)	9551	1344	2705	30
H(15A)	7166	165	3177	38
H(15B)	7838	694	4847	38
H(15C)	9370	-91	4374	38
H(14C)	9844	1796	4560	30
H(14D)	9939	1533	2926	30
H(15D)	7255	138	2481	38
H(15E)	7326	358	4163	38
H(15F)	9195	-240	3895	38

3.4. References

[1] A. Mardyukov, H. Quanz, P. R. Schreiner, *Nat. Chem.* **2017**, *9(1)*, 71.

[2] D. Y. Curtin-Hammett, *Rec. Chem. Prog.* **1954**, *15*, 111-128.

[3] J. I. Seeman, *Chem. Rev.* **1983**, *83*, 84-134.

[4] J. I. Seeman, *J. Chem. Educ.* **1986**, *63*, 42-48.

[5] M. Schauermann, P. R. Schreiner, *J. Phys. Chem. Lett.* **2022**, *13*, 3138.

[6] O.G. von Ettinghausen, E. Kendrick, *Polymer* **1966**, *7(9)*, 469.

[7] V. C. E. Burnop, K. G. Latham, *Polymer* **1967**, *8*, 589.

[8] H. W. Kroto, B. M. Landsberg, R. J. Suffolk, A. Vodden A., *Chem. Phys. Lett.* **1974**, *29(2)*, 265.

[9] R. P. Singh, G. Cao, R. L. Kirchmeier, J. M. Shreeve, *J. Org. Chem.* **1999**, *64(8)*, 2873.

[10] K. Pihlaja, J. Sinkkonen, G. Stájer, A. Koch, E. Kleinpeter, *Magn. Reson. Chem.* **2011**, *49(7)*, 433.

[11] K. Bahrami, M. M. Khodaei, M. Tajik, V. Shakibaian, *Chin. Chem. Lett.* **2012**, *23(1)*, 81.

Chapter 4: Miscellaneous Mercaptocarbene Precursor Systems

4.1. Abstract

During my studies I worked on different approaches for various unknown substituted mercaptocarbenes in parallel. In this chapter I describe projects that were not successful although the information presented in this chapter is helpful for further studies on these systems. I do not present analytical data in all its depth here since most synthetic approaches have not resulted in clearly identifiable products. Some of this work had been abandoned due to more promising projects but, nevertheless, might be useful as a basis for further investigations.

4.2. Methylmercaptomethylene

Since parent mercaptomethylene and methylmercaptomethylene were already investigated computationally and identified as hitherto unreported but viable reactive intermediates, we planned to identify suitable precursors for these elusive carbenes as well.[1,2] Furthermore, we planned to study the tunneling behavior of these fascinating new species. In analogy to the strategy for hydroxymercaptomethylene (Chapter 1), thionated pyruvic acid ester **1** could give access to methylmercaptomethylene (Fig. 1).

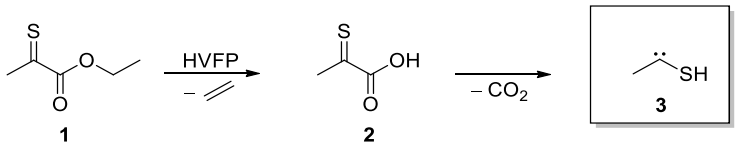

Fig. 1. A Possible new precursor for methylmercaptomethylene **3**.

In methylhydroxycarbene the barrier for a proton shift to the carbene center from the methyl group to form vinyl alcohol is lower but broader than for the shift from the OH-group to form acetaldehyde. Therefore, at low temperatures, tunneling control for the formation of acetaldehyde is observed.[3] Figure 2 shows the PES and the tunneling paths for the formation of acetaldehyde and vinyl alcohol.[2]

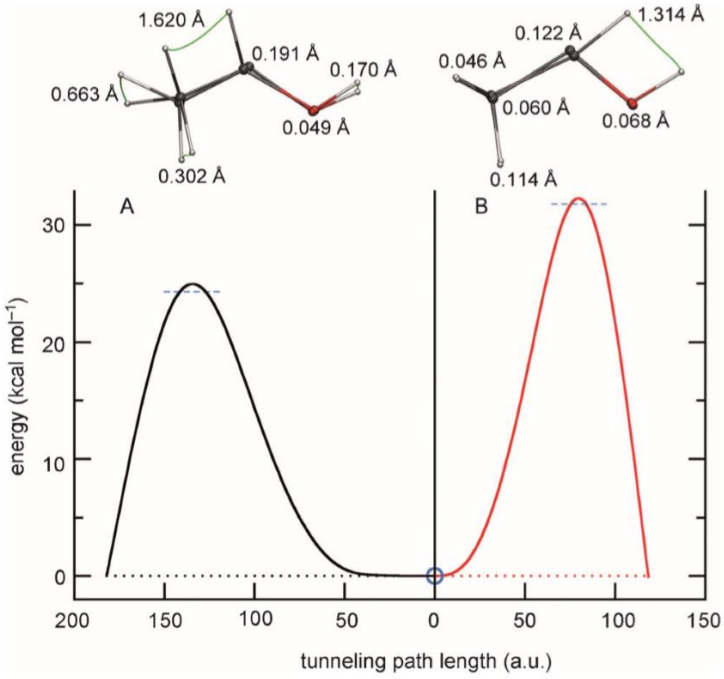

Fig. 2. Due to the narrow barrier for path B, acetaldehyde forms in a tunneling controlled reaction at cryogenic temperatures (instanton paths depicted in green). *This image is directly taken from* J. Kästner, *Chem. Eur. J.* **2013**, *19*, 8207.[2]

Full-dimensional machine learning can reproduce these high-level computations that are in accordance with the experimental findings.[4] When O is substituted with S, computations show a significant change of the 1,2[H]-shift behavior. The influence of this substitution has negligible influence on the barrier heights but the tunneling path length increases due to the longer CS-bond. This makes tunneling to the vinyl thiol more efficient (Tab. 1).[2] This tautomer has already been identified by microwave spectroscopy in ethanedithiol pyrolysis.[5]

Table 1: Kinetic and energetic data for the tunneling paths A and B calculated at the CCSD(T)-F12/cc-pVTZ level of theory (rates: B3LYP/cc-pVTZ).[2] For methyl hydroxymethylene experimental and theoretical data are in good agreement.[3]

	Route A			**Route B**		
	$\Delta^{\ddagger}H$ [kcal mol^{-1}]	τ	L [a.u.]	$\Delta^{\ddagger}H$ [kcal mol^{-1}]	τ	L [a.u.]
H_3C-C-OH (exp.)	22.8	-	-	28.0	1 h	-
H_3C-C-OH	25.0	139 d	182	32.1	2.9 h	121
H_3C-C-SH	21.5	9.4 h	172	30.6	221 d	141

These theoretical assumptions should be examined experimentally. Synthesis of the thionated pyruvic acid ester failed with Lawesson's reagent. We performed the reaction with P_4O_{10} instead of Lawesson's reagent and in THF for a better solubility at lower temperatures. The control of the reaction with a gas chromatograph indicates to the formation of a trimer which is known for thioacetone (Fig. 3).[6]

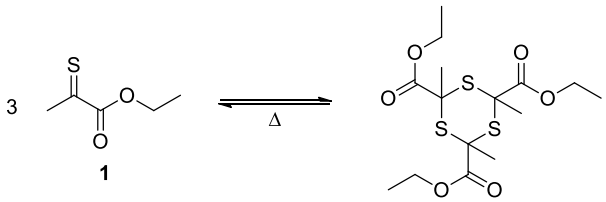

Fig. 3. Trimer-formation is favored under standard conditions.

In the case of thioacetone the trimer cracks at 500–600 °C.[6] The trimer is possibly less sensitive towards oxidation and could turn out to be a stable storage form. Unfortunately, we have not succeeded in the isolation of **1** or its dimer to test it in matrix isolation experiments. We changed our synthetic strategy for a synthetic idea related to the deuterated precursor synthesis in chapter 3. After 20 h we observed the desired product that could be isolated after column chromatography in high purity. We also observed **5** as a side product (Fig. 4). A longer reaction time might help to convert **5** to **6** completely. We oxidized **6** with $KMnO_4$ after a protocol by Gokel *et al*. to use the **7** as an alternative precursor.[7] However, **7** was not obtained upon extensive synthetic effort.

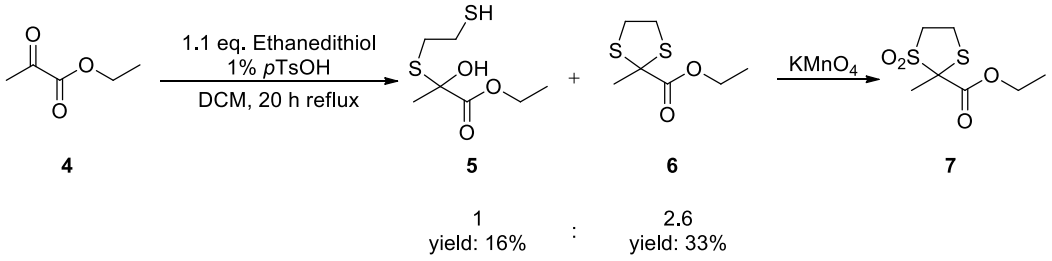

Fig. 4. Ethyl pyruvate reacts to the desired compound **6** and **5** as a side product in a 1:2.6 ratio.

4.3. Mercaptomethylene

Mercaptomethylene, the simplest mercaptocarbene, is expected to isomerize thermally or by tunneling to thioformaldehyde. Thioformaldehyde has first been characterized by Johnson and Powell in 1970 by microwave spectroscopy.[8] Only three years later Godfrey *et al*. could identify H_2CS in Sagittarius B2 by MHz spectroscopy.[9] Marcelino *et al*. investigated D_2CS and HDCS

in the dark cloud Barnard 1 and found a similar isotopic enhancement for D as it is found for D_2CO and HDCO.[10]

Since thioformaldehyde was detected on Comet Hale-Bopp and investigated with GHz spectroscopy at the National Radio Astronomy Observatory (NRAO) in 1998, H_2CS has been extensively studied in the ground state as well as in excited states.[11-13] Despite the good understanding of this system, the high energy isomer HS-C-H has never been observed. The only evidence comes from crossed molecular beam experiments of atomic carbon ($C(^3P_J)$) and H_2S followed by TOF-MS analysis by Kaiser, Lee and co-workers in 1998.[14] Matrix isolation spectroscopy together with precursors as **8** or **10** (Fig. 5) could enable access to investigate this system. Schreiner *et al.* suggested a system which is better represented as ylide structure in which the carbon atom is partially negatively charged and the sulfur positive.[1]

According to theoretical investigations, no tunneling should occur in mercaptomethylene according to computational studies (Tab. 2).

Table 2. Kinetic and energetic data for the tunneling reaction computed at the B3LYP/Def2QZVPP level of theory in mercaptomethylene.

	$\Delta^{\ddagger}H$	$\tau_{1/2}$
	[kcal mol^{-1}]	
H-C-SH	32.0	17149 d
D-C-SD	34.0	$2.4 \cdot 10^{14}$ d

To investigate mercaptomethylene experimentally, we want to use **8** and/or **10** as precursor systems (Fig. 5)

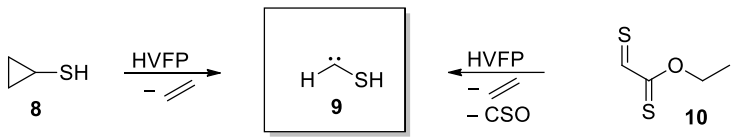

Fig. 5. Possible new precursor molecules for mercaptomethylene.

Structure **8** is available by reacting a cyclopropyl Grignard reagent with sulfur. Species **10** might be accessible through thionation of glyoxylic acid. Trimer formation might take place here as well. With the pyrolysis of cyclopropyl amine, Schreiner's group was able to prepare the simplest aminocarbene.[4] The glyoxylic acid ethyl ester has already been prepared by ozonolysis of malonic acid diethylester during my master thesis. The unreported trimer of precursor **10** is available by reacting glyoxylic ethyl ester with Lawesson's reagent. Analysis after 20 h at 100 °C showed 28% starting material, 43% mono thionated- and 29% dithionated

glyoxylic ethyl ester (GC-MS). After another 20 h GC-MS showed no peaks which could be assigned to the desired products. After column chromatography one of the compounds isolated seems to be the trimer of **10** (NMR-spectroscopy). However, further analytics did not support this finding.

Our second synthetic approach started from commercially available cyclopropylbromide **11**. A Grignard reagent was prepared and S_8 was added (Fig. 6). After several attempts to optimize the reaction, we always ended up with disulfide **13**, an intensively smelly liquid we only obtained in very small amounts. We therefore stopped this approach.

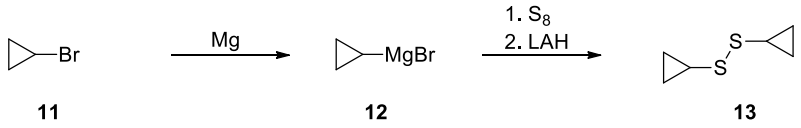

Fig. 6. Synthetic approach for cyclopropyl thiol **8**, only yielding disulfide **13**.

The precursors **8** and **10** (Fig. 5) turned out to be very difficult to synthesize and isolate. We stopped this project.

4.4. Dimercaptomethylene

Tetrathiooxalic acid could act as a possible precursor for dimercaptomethylene. Since tetrathiooxalic acid itself is still an elusive compound, we had to think about good alternatives. Figure 7 depicts the synthesis of a possible precursor **12** starting from commercially available zinc complex **11**.[15,16] Extrusion of ethylene CS and CS_2 could give dimercaptomethylene under HVFP conditions (Fig. 7).

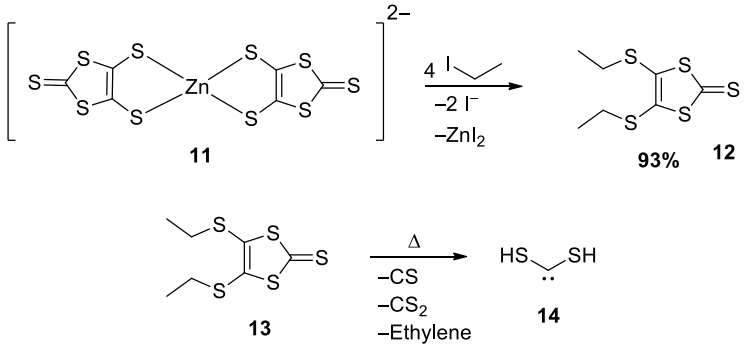

Fig. 7. Zink complex **11** reacts with ethyl iodide to form **12** in high yield.[16]

With **12** in hand, there is a known route to tetrathiodiethyloxalate **14** by exchange of the thione sulfur atom for oxygen and subsequent irradiation to extrude CO (Fig. 8).[17]

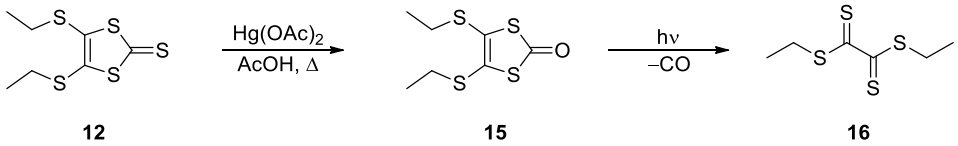

Fig. 8. When the thione sulfur atom is exchanged for oxygen, irradiation gives **16** upon extrusion of CO.[17]

Another route to **16** is depicted in Figure 9. When oxalyl chloride is reacted with ethyl mercaptan, **18** forms as yellow crystals in 94% yield. Compound **16** is already an alternative precursor for hydroxymercaptomethylene but matrix isolation resulted in no carbene bands with pyrolysis temperatures of 800 and 1000 °C. At 800 °C there is still a lot of starting material, so we did not try lower temperatures.

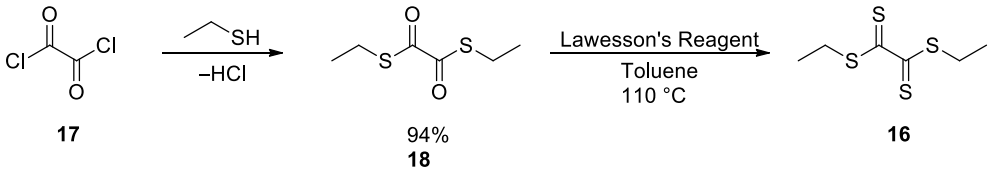

Fig. 9. Alternative precursor synthesis for **16** gives **18** in the first step that was obtained in good yield as yellow crystals. Subsequent reaction with Lawesson's reagent did not result in the formation of **16**.

Upon HVFP of **18** we could not assign bands of the carbene isomers **14ct** and **14tt** (Fig. 10).

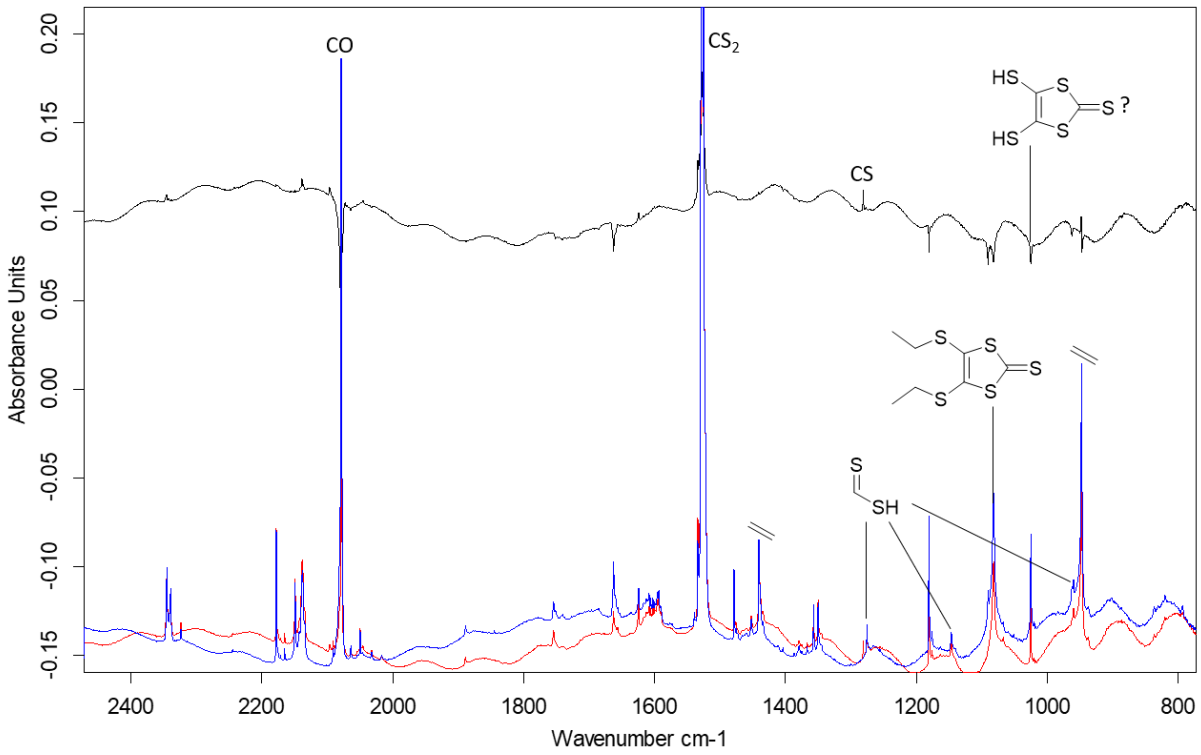

Fig. 10. Pyrolysis of **12** gives CO, CS_2, dithioformicacid, and ethylene. The difference spectrum (black) shows formation of CS when the matrix is irradiated with UV light (254 nm). No bands could be assigned to reactive species like dimercaptomethylene.

Another approach, synthesis of **19**, by reacting oxalyl chloride with hydrogen sulfide failed, probably due to its low stability (Fig. 11).

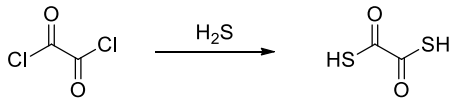

17 **19**

Fig. 11. Quenching of oxalyl chloride with hydrogen sulfide should give **19**. The work up and isolation was not successful due to the low stability of **19**.

Another precursor system is **20** that was used by Vivekananda *et al*. to generate dimercaptomethylene by neutralization-reionization mass spectrometry (Fig. 13).[18] In these experiments 70 eV were necessary to cleave **20** to Nitrogen, HCN and dimercaptomethylene as a radical cation. Thermally, we will have to work with very high temperatures. Further

fragmentation gave carbon and HS radical which led the authors to conclude the dimercaptocarbene isomer for the peak with *m/z* = 78.

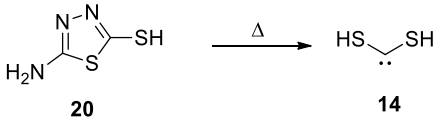

20 **14**

Fig. 12. Precursor **20** was used from Vivekananda *et al*.[18]

Compound **20** turned out to be unsuitable for our matrix isolation setup due to a very low vapor pressure.

Theoretical considerations

In contrast to dihydroxymethylene, here the cc-conformer is the most stable one (Fig. 13).

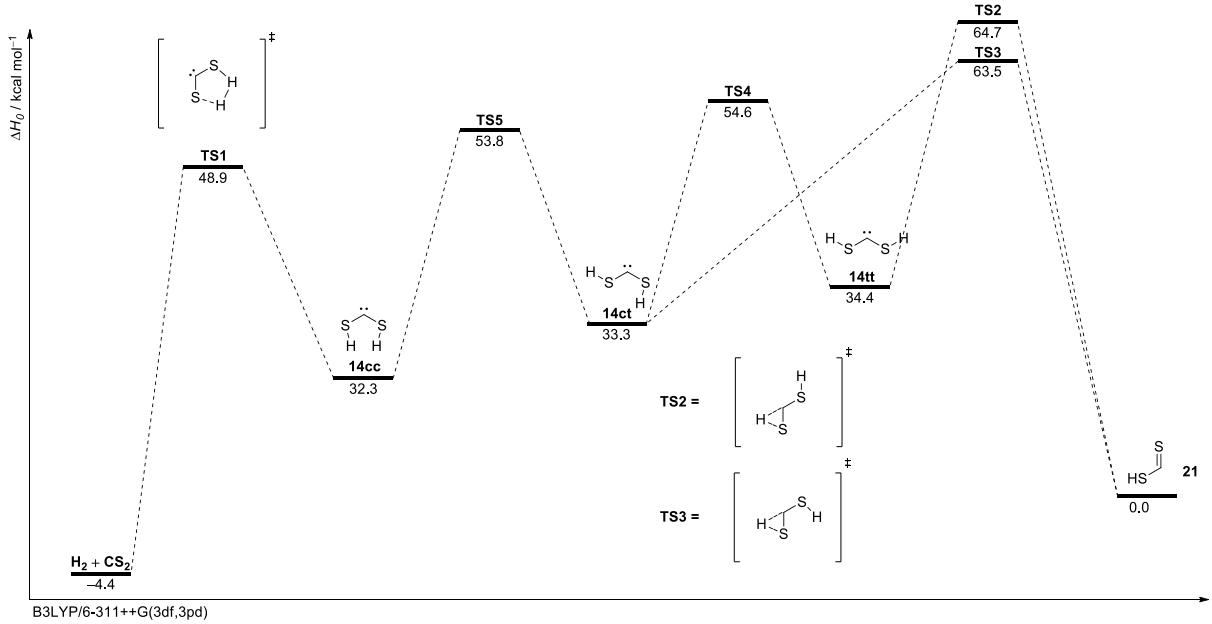

Fig. 13. PES of **14** computed at the B3LYP/6-311++G(3df,3pd) level of theory.

This is probably because the CS and SH bonds are elongated compared to CO and OH bonds. Therefore, the two hydrogen atoms are 24 nm distant from each other. In dihydroxymethylene the distance is 19 nm which brings the two hydrogen atoms in close proximity. The ct conformer has the lowest dipole moment although it is not the most stable one (Fig. 14).

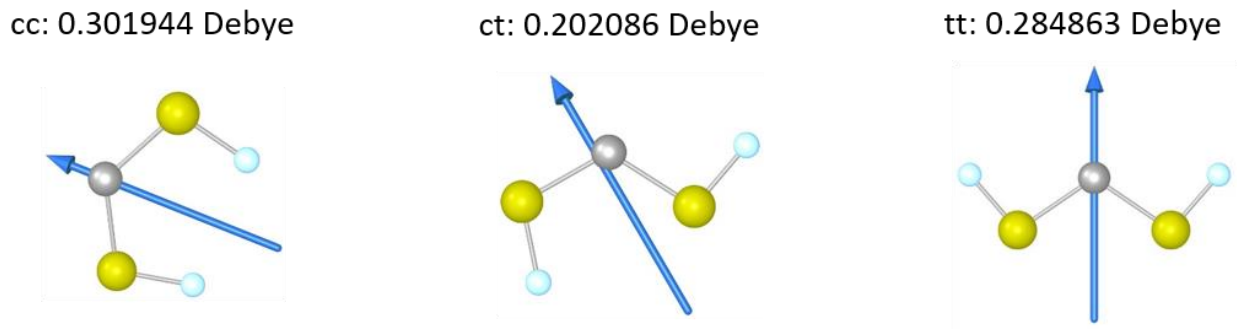

Fig. 14. Dipole moments of the conformations of dimercaptomethylene. Despite having the highest dipole moment, the cc conformation is most stable.

HF level of theory shows the tt-conformer being the most stable one. This basis-set was chosen to investigate the influence of Coulomb correlation of electrons being neglegted in this method. When we compute the three conformers with a DFT method and a larger basis set, the cc-conformer is the most stable one. This hints to a correlation effect being responsible for this trend. When incorporating the D3 correction, this trend is even more clear (Tab. 3).

Table 3: On HF level of theory, the tt-conformer is most stable. When using larger basis sets and methods considering exchange correlation the trend is inverted.

	HF/6-311++G(d,p) /kcal mol^{-1}	B3LYP/6-311++G(3df,3dp) /kcal mol^{-1}	B3LYP-D3/6-311++G(3df,3dp) /kcal mol^{-1}
cc	0.0	0.0	0.0
ct	−1.0	1.0	1.3
tt	−1.5	2.1	2.6

Pyrolysis of **11** at 750 °C gives CO, CS_2, bisthioformic acid, and ethylene (Fig. 10). Upon irradiation with UV-light (254 nm) CS forms. The decreasing bands could not be assigned certainly. We could not assign bands to dimercaptomethylene.

This chapter summarizes attempts to synthesize new compounds as precursor systems for mercaptocarbenes. The synthetic approaches in this chapter are not straight-forward and need more time and intensive optimization. Our precursor systems for hydroxymercaptomethylene and aminomercaptomethylene worked wherefore we focused on these projects.

4.5. References

[1] J. Sarka, A. G. Császár, P. R. Schreiner, *Collect. Czech. Chem. Commun.* **2011**, *76(6)*, 645.

[2] J. Kästner, *Chem. Eur. J.* **2013**, *19*, 8207.

[3] P. R. Schreiner, H. P. Reisenauer, D. Ley, D. Gerbig, C.-H. Wu, W. D. Allen, *Science* **2011**, *332(6035)*, 1300.

[4] H.-D. Wang, Y.-L. Fu, B. Fu, W. Fang, D. H. Zhang, *Phys. Chem. Chem. Phys.* **2023**, *25(11)*, 8117.

[5] M. Tanimoto, S. Saito, *Chem. Lett.* **1977**, *6(6)*, 637-630.

[6] H. W. Kroto, B. M. Landsberg, R. J. Suffolk, A. Vodden, *Chem. Phys. Lett.* **1974**, *29(2)*, 265.

[7] G. W. Gokel, H. M. Gerdes, D. M. Dishong, *J. Org. Chem.* **1980**, *45(18)*, 3634.

[8] D. R. Johnson, F. X. Powell, *Science* **1970**, *169(3946)*, 679.

[9] M. W. Sinclair, N. Fourikis, J. C. Ribes, B. J. Robinson, R. D. Brown, P. D Godfrey, *Aust. J. Phys.* **1973**, *26*, 85.

[10] N. Marcelino, J. Cernicharo, E. Roueff, N. Gerin, R. Mauersberger, *Astrophys. J.* **2005**, *620*, 308.

[11] D. J. Clouthier, D. A. Ramsay, *Ann. Rev. Phys. Chem.* **1983**, *34*, 31.

[12] L. M. Woodney, M. F. A'Hearn, *Earth, Moon and Planets* **1997**, *78*, 69.

[13] D. Despois, Earth, *Moon and Planets* **1997**, *79*, 103.

[14] R. I. Kaiser, C. Ochsenfeld, M. Head-Gordon, Y. T. Lee, *Science* **1998**, *279*, 1181.

[15] P. Jeroschewski, P. Hansen, *Sulfur Reports* **1986**, *7(1)*, 1.

[16] E. A. Ignatenko, A. A. Gorbunov, E. V. Shklyaeva, G. G. Abashev, *Chem. Heterocycl. Compd.* **2014**, *50(5)*, 691.

[17] W. Kusters, P. de Mayo, *J. Am. Chem. Soc.* **1974**, *96(11)*, 3502.

[18] S. Vivekananda, R. Srinivas, *J. Phys. Chem. A* **1999**, *103*, 5123.

Chapter 5: A Synthetic Pathway to *α*-Ether Substituted Thiophenes

5.1. Abstract

New synthetic pathways for the formation of complex organic compounds are of particular interest in industry concerning atom economy, energy consumption and simplicity. Since substituted thiophenes are widely used in electronics, a new synthetic pathway to thiophenes is desirable.

5.2. Results and Discussion

To generate mercaptocarbenes we planned to synthesize the thionated analogues of *α*-keto carboxylic acid precursors used before to generate a variety of hydroxycarbenes.[1] Small substituents like H or Me did not facilitate the formation of the desired compound but we succeeded to synthesize thionated diethyl oxalate to generate hydroxylmercaptomethylene.[2] To generate phenyl mercapto methylene we planned to thionate **2** with Lawesson's reagent (Figure 1).

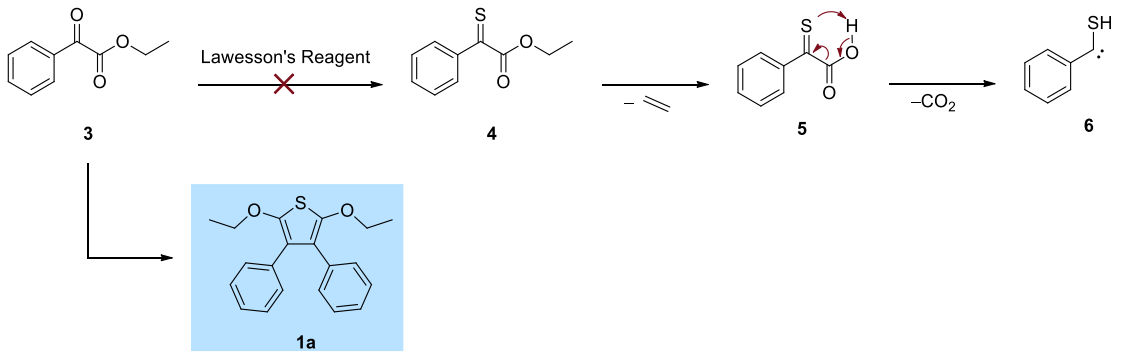

Fig. 1. Thionation of **3** yields thiophene **1a** instead of the desired monothiolethylbenzoylformate **4**.

To test if the reaction is applicable to similar systems, *p*-methyl-**2** and *p*-Br-**2** were reacted with Lawesson's reagent under the same conditions and we isolated the corresponding thiophene. The thiophenes were analyzed with X-ray diffraction (XRD) (Fig. 2).

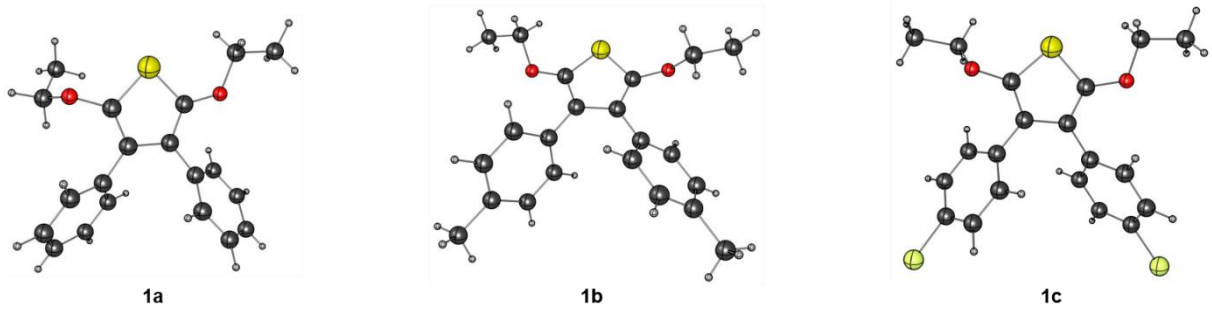

Fig. 2. XRD derived structures of thiophenes **1a-c**.

We examined the scope of the thiophene synthesis with the substrates **2a**-**2k** (Tab. 1).

Table 1. Substrate scope for the reaction of **2** to **1**.

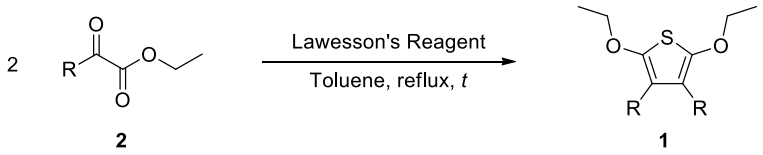

2 **1**

Product	R	yield[a] (%)	Reaction time *t* (d)
1a	Ph	99	4
1b	*p*-Me-Ph	48	5
1c	*p*-Br-Ph	62	3
1d	*p*-TMS-Ph	8	2
1f	*m,m*-TMS-Ph	12	2
1g	*p*-HO-Ph	0	5
1h	*o,p*-CF_3-Ph	0	2
1i	*p*-CF_3-Ph	0	2
1j	*m,m*-Br-Ph	0	1
1k	Pyridyl	0	3
1l	*m,m*-OMe-Ph	0	1

[a]Yield after column chromatography.

The parent system **1a** was isolated in excellent yields after column chromatography whereas **1b** and **1c** were only isolated in moderate yields. The workup procedure should be further optimized. Starting from **1g** we were not able to detect traces of the desired product and reisolated the starting material. For these systems other solvents or thionating reactants such as P_4S_{10} might facilitate product formation. The mechanism of the formation of the heterocycle is not clear yet. In Figure 3 we present a possible reaction mechanism. In a first step, Lawesson's reagent thionated starting material **3** to **4** and **5**. In a formal [2+2]-cycloaddition **4** and **5** yield **6**. Since this reaction type is thermally forbidden, the formation of **6** and reaction to **7** might involve asynchronous elemental reactions. Ring closure to **8** yield an epoxide. The oxygen atom is than cleaved by evolving SO, a mechanism that is known for CO, and **1a** forms.[3]

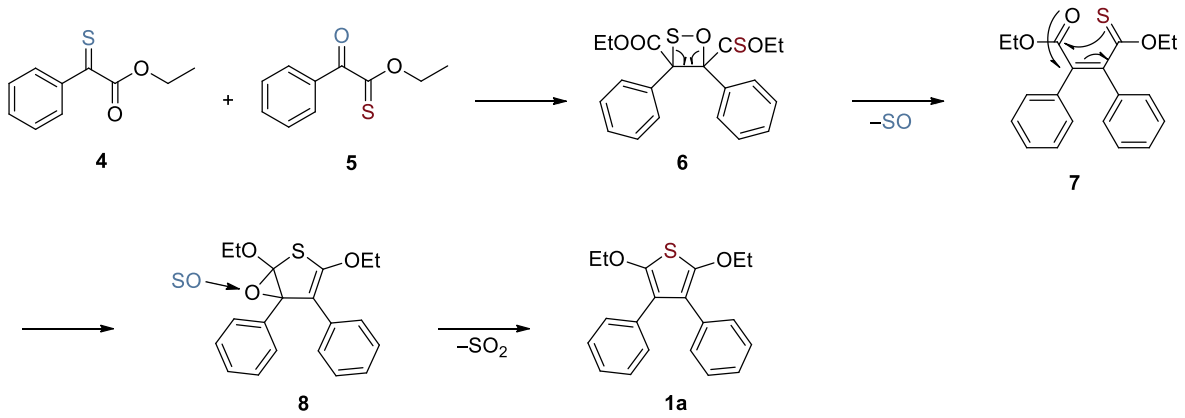

Fig. 3. Possible reaction mechanism for the formation of the substituted thiophene **1a**.

Since these systems might be useful for organic electronics, we computed the molecular orbitals of **1a-c** for a first glance on their electronic properties. Figure 4 shows the highest occupied molecular orbital (HOMO) and the lowest unoccupied molecular orbital (LUMO) with electronic energy gap for selected thiophenes.

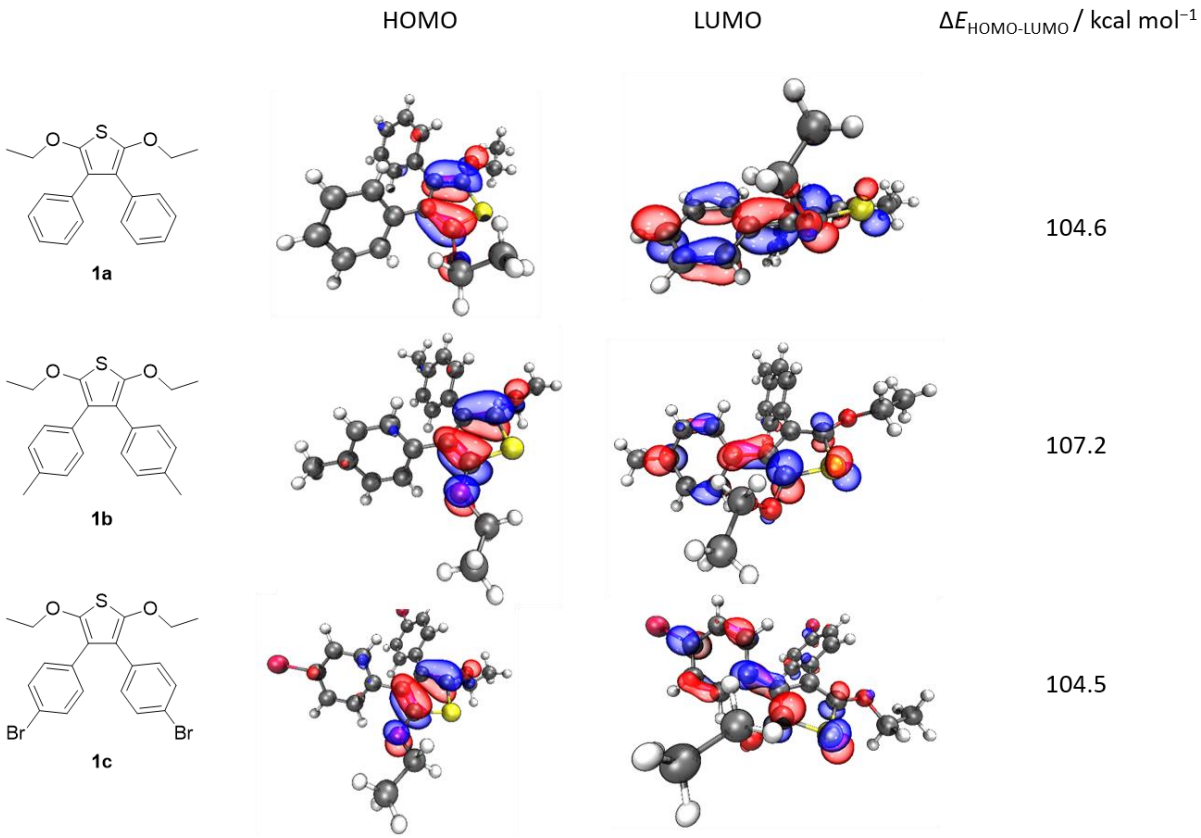

Fig. 4. HOMO and LUMO of **1a-c** at the B3LYP/6-311++G(3df,3pd) level of theory with HOMO/LUMO-gap (visualized with VMD software).

The HOMO and the LUMO are mostly located at the thiophene core. We found little influence of the substituents towards the electronic energy gap because the twisted substituted phenyl

moieties hinder a good orbital overlap of the π-orbitals located at the thiophene core. The computed energy gap values are in good agreement with literature values of other small substituted thiophene derivatives.[4]

In this chapter I report a novel synthetic route to substituted thiophenes bearing ether- and substituted aromatic moieties from *α*-keto carboxylic acids. Since the starting materials are in most cases commercially available, our method provides highly functionalized building blocks in an easy and efficient way. The scope must be extended to other functionalized starting materials and the method turned out to be not equally good yielding for all tested substrates. A mechanistic insight might provide an explanation for this and could help to make this reaction applicable for a broader scope.

5.3. Experimental

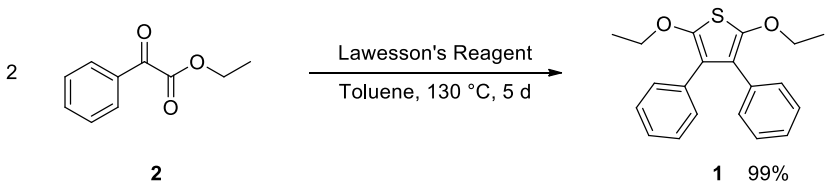

Fig. 5. Typical procedure for the thiophene synthesis.

0.4 mL of **1'** (0.45 g, 2.5 mmol) were dissolved in 20 dry toluene in a flame dried round-bottom flask. 1.5 g Lawesson's reagent (3.7 mmol, 1.5 equiv.) were added and the mixture was refluxed for 5 days. The mixture was filtered over a silica plug at r.t. (diethyl ether 1:10 *n*-pentane). The solvent was removed resulting in a mixture of orange crystals and an orange oil. The crude product was purified by column flash chromatography (diethyl ether 1:10 *n*-pentane, R_f = 0.3).

1a

Yield: 403 mg (1.24 mmol, 99%).

^{1}H NMR (600 MHz, $CDCl_3$): δ = 7.23 – 7.09 (m, 10H), 3.96 (q, J = 7.0 Hz, 4H), 1.27 (t, J = 7.0 Hz, 6H) ppm.

^{13}C{^{1}H} NMR (151 MHz, $CDCl_3$): 149.0, 134.3, 130.4, 127.8, 126.3, 122.4, 77.4, 77.2, 77.0, 71.8, 15.1 ppm.

IR (ATR): ν = 2981.5, 2925.2, 2868.9, 1600.2, 1580.1, 1556.5, 1518.9, 1493.5, 1439.2, 1385.0, 1378.0, 1354.3, 1292.2, 1188.0, 1149.5, 1125.9, 1071.7, 1019.1, 929.9, 909.8, 887.9, 867.7, 800.4, 764.5, 733.0, 693.6, 642.0, 557.9, 537.8, 502.0, 467.8 cm^{-1}.

HRMS (ESI): *m/z* = 347.1073 $[M+Na]^+$ (calcd. *m/z* = 347.1076).

1b

Yield: 48%

^{1}H NMR (400 MHz, $CDCl_3$): 7.02 (s, 8H), 3.95 (q, *J* = 7.0 Hz, 4H), 2.30 (s, 6H), 1.28 (t, *J* = 7.0 Hz, 6H).

^{13}C NMR{^{1}H} (101 MHz, $CDCl_3$): δ = 148.6, 135.8, 131.4, 130.2, 128.5, 122.4, 71.7, 21.4, 15.1 ppm.

IR (ATR): *v* = 3023.9, 2980.6, 2919.6, 2894.2, 2866.2, 1732.0, 1691.3, 1580.0, 1533.9, 1508.5, 1473.6, 1447.3, 1387.2, 1353.1, 1291.9, 1278.0, 1213.7, 1179.8, 1148.7, 1125.2, 1108.2, 1099.0, 1017.3, 967.9, 948.1, 917.1, 886.9, 871.9, 843.6, 831.4, 815.4, 783.3, 764.5, 711.8, 646.8, 629.8, 593.1, 579.0, 547.9, 510.2, 480.1, 438.7 cm^{-1}.

HRMS (ESI): *m/z* = 375.1391 $[M+Na]^+$ (calcd. *m/z* = 375.1389).

1c

Yield: 62%

^{1}H NMR (400 MHz, $CDCl_3$): 7.39 – 7.31 (m, 4H), 7.02 – 6.93 (m, 4H), 3.96 (q, J = 7.0 Hz, 4H), 1.27 (t, J = 7.0 Hz, 6H).

^{13}C NMR{^{1}H} (101 MHz, $CDCl_3$): δ = 149.4, 132.9, 131.9, 131.2, 120.5, 71.9, 15.1 ppm.
IR (ATR): *v* = 2982.4, 2935.2, 1896.8, 1732.2, 1589.5, 1574.2, 1520.4, 1484.4, 1389.9, 1366.6, 1293.1, 1262.2, 1560.0, 1140.8, 1094.6, 1069.3, 1009.1, 920.2, 870.6, 833.0, 773.4, 704.7, 617.0, 585.7, 552.0, 505.0, 484.2 cm^{-1}.

HRMS (ESI): *m/z* 480.9466 $[M+H]^+$ (calcd. *m/z* = 480.9467).

1d

Yield: 8%

^{1}H NMR (600 MHz, $CDCl_3$): 7.34 (d, *J* = 8.0 Hz, 3H), 7.10 (d, *J* = 8.0 Hz, 3H), 3.97 (q, *J* = 7.0 Hz, 4H), 1.29 (t, *J* = 7.0 Hz, 5H), 0.23 (s, 13H).

^{13}C NMR{^{1}H} (151 MHz, $CDCl_3$): δ = 149.0, 137.9, 133.7, 132.8, 129.5, 122.2, 71.7, 15.1, -0.9 ppm.
IR (ATR): *v* = 2955.0, 2895.9, 1599.9, 1571.6, 1523.7, 1496.0, 1443.2, 1387.6, 1296.0, 1247.6, 1138.4, 1108.3, 1088.5, 1025.5, 833.3, 752.1, 697.1, 623.1, 517.3, 443.4 cm^{-1}.

HRMS (ESI): *m/z* = 491.1864 $[M+Na]^+$ (calcd. *m/z* = 491.1867).

NMR-Spectra

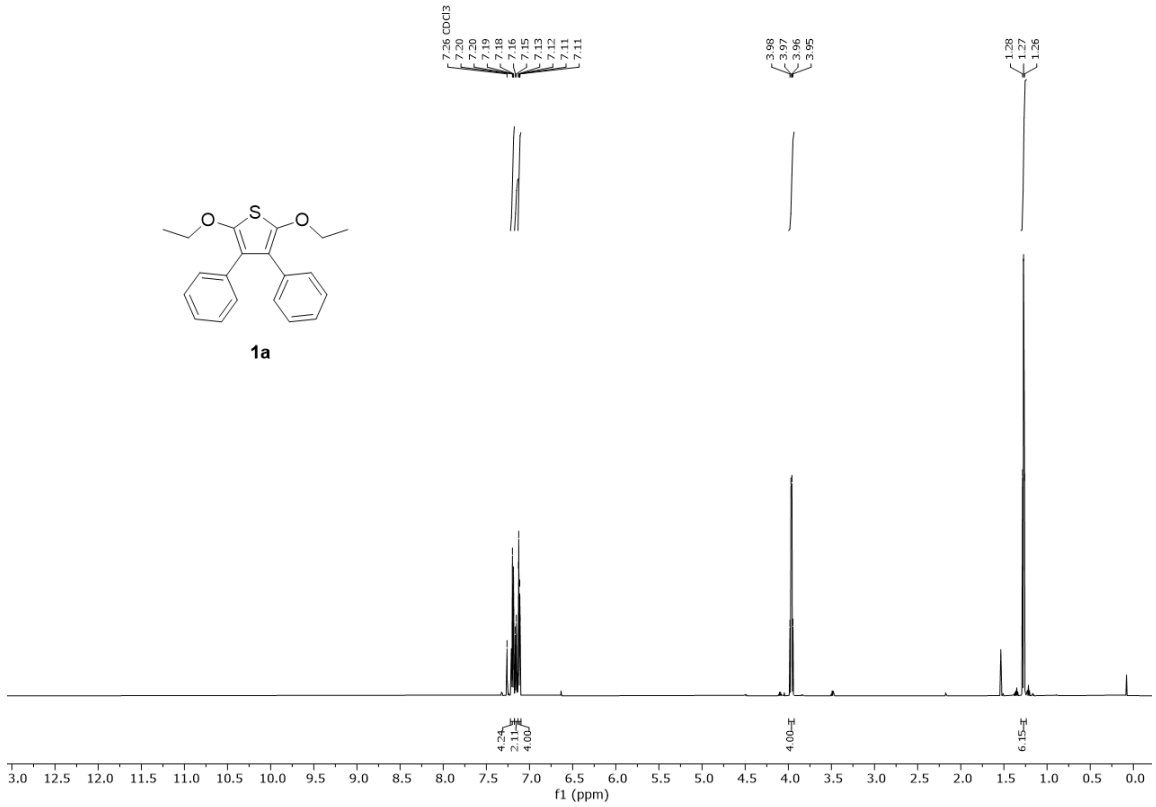

Fig. 6. ^{1}H NMR (600 MHz, $CDCl_3$) of **1a**.

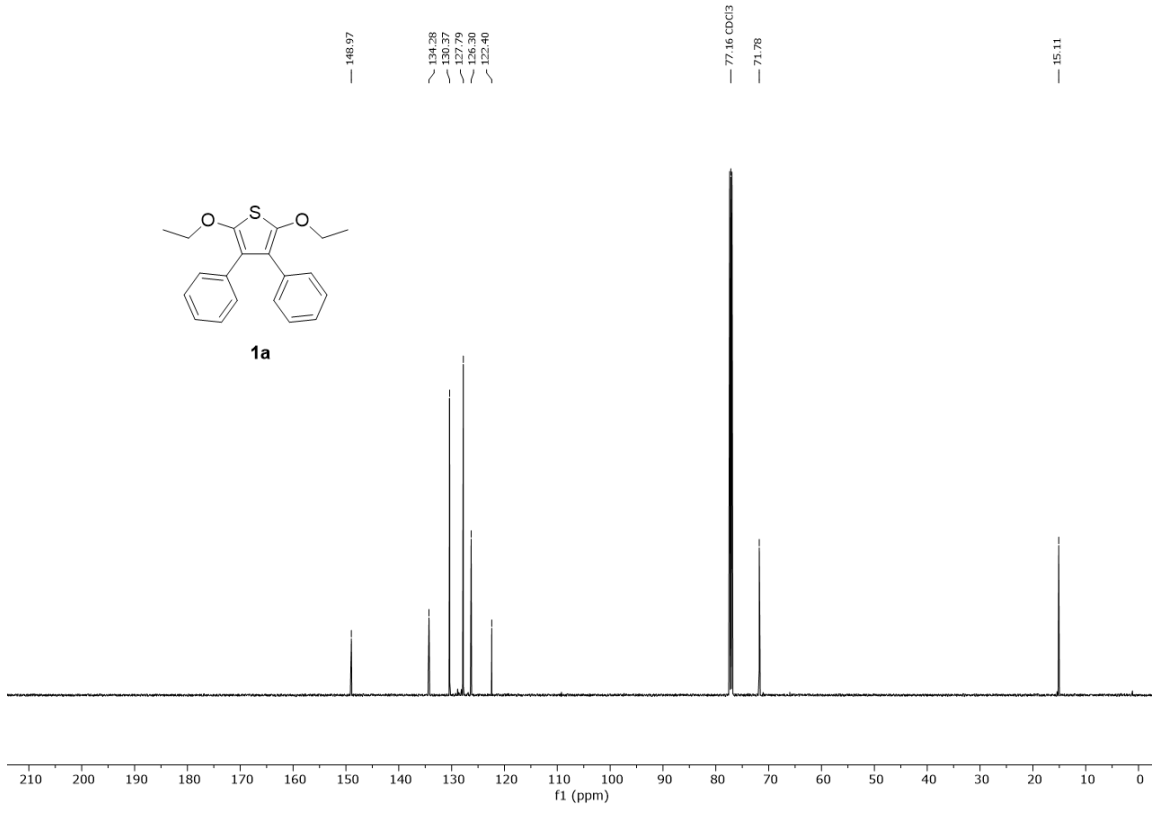

Fig. 7. $^{13}C\{^{1}H\}$ NMR (151 MHz, $CDCl_3$) of **1a**.

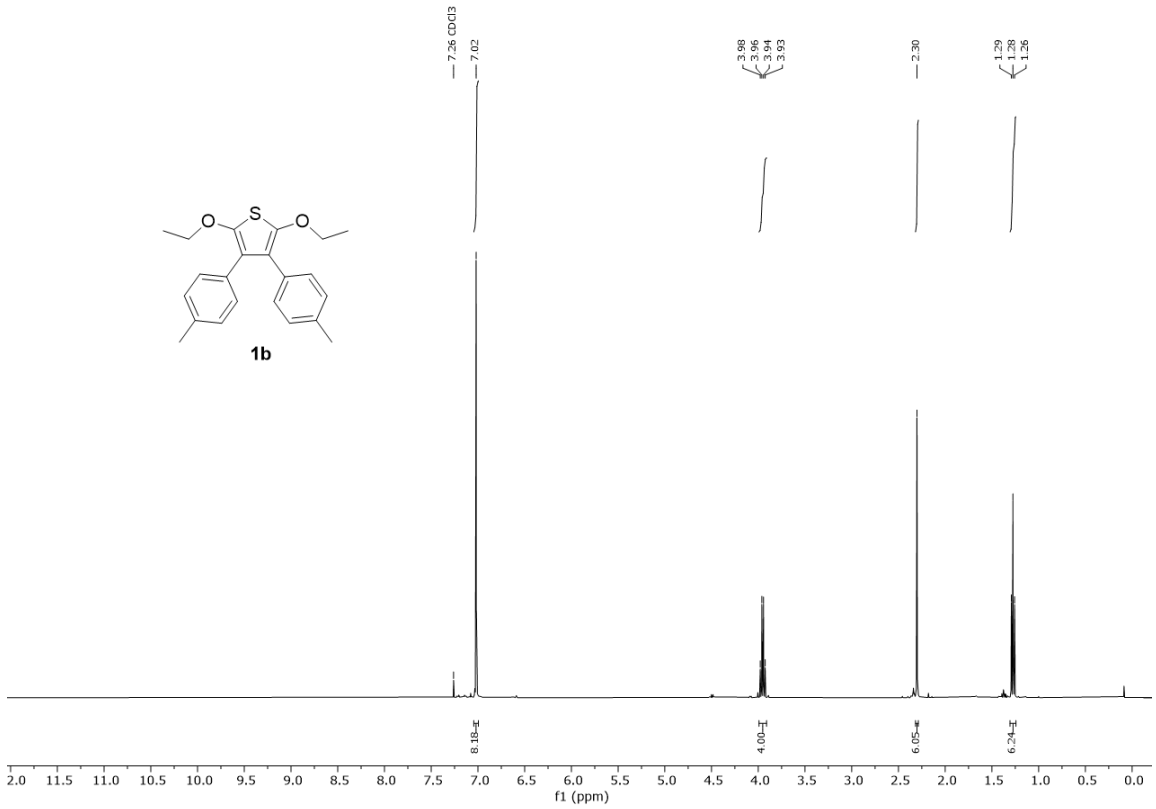

Fig. 8. ^{1}H NMR (400 MHz, $CDCl_3$) of **1b**.

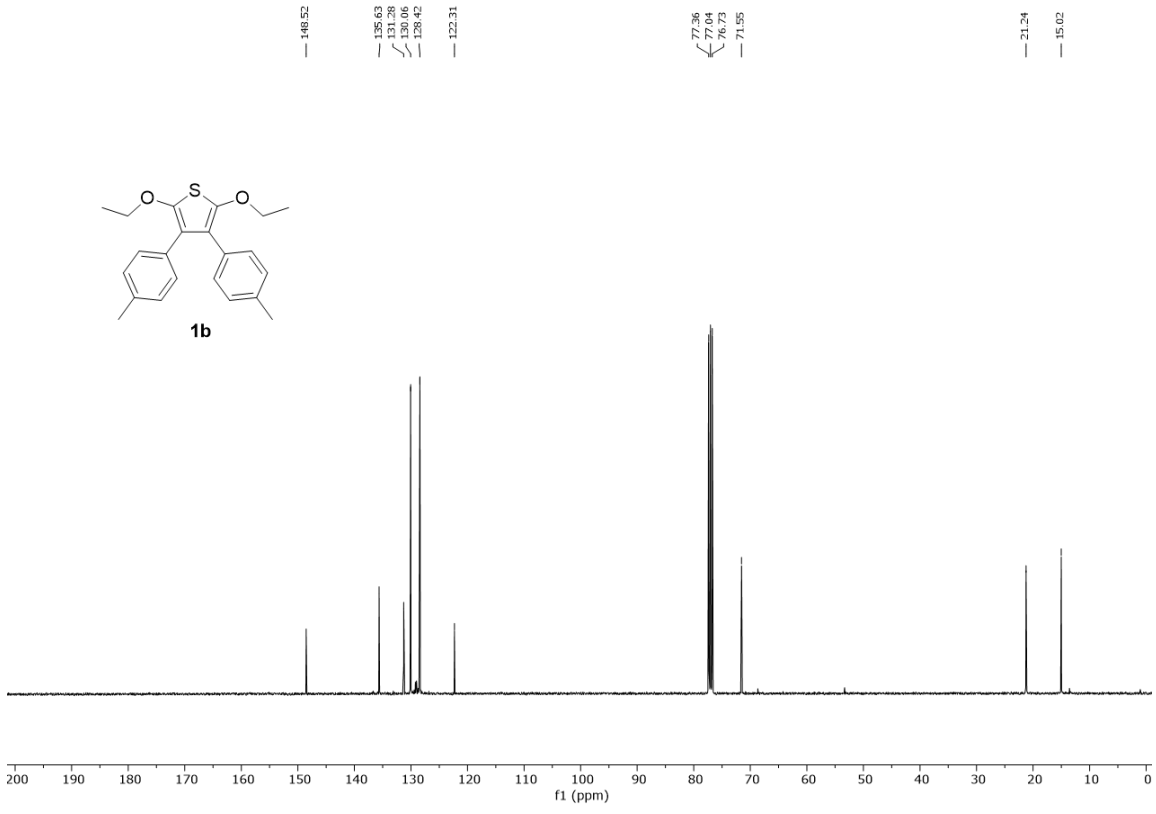

Fig. 9. $^{13}C\{^{1}H\}$ NMR (101 MHz, $CDCl_3$) of **1b**.

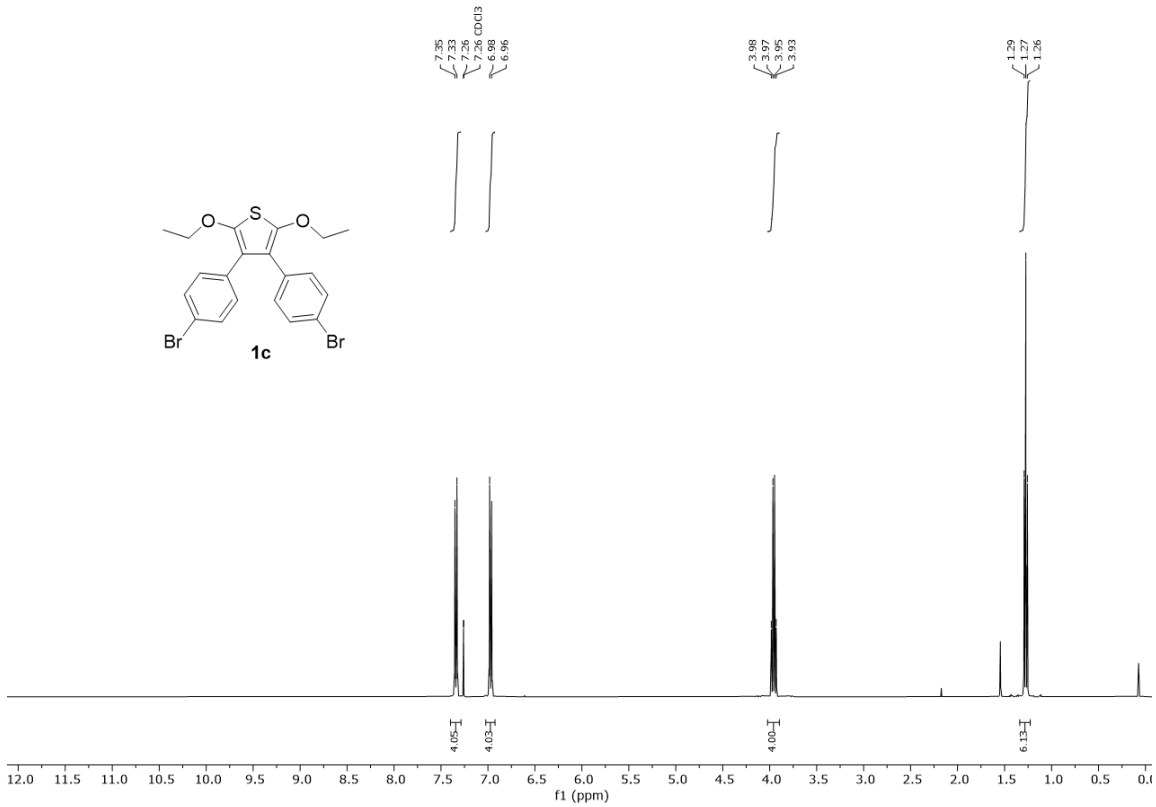

Fig. 10. ^{1}H NMR (400 MHz, $CDCl_3$) of **1c**.

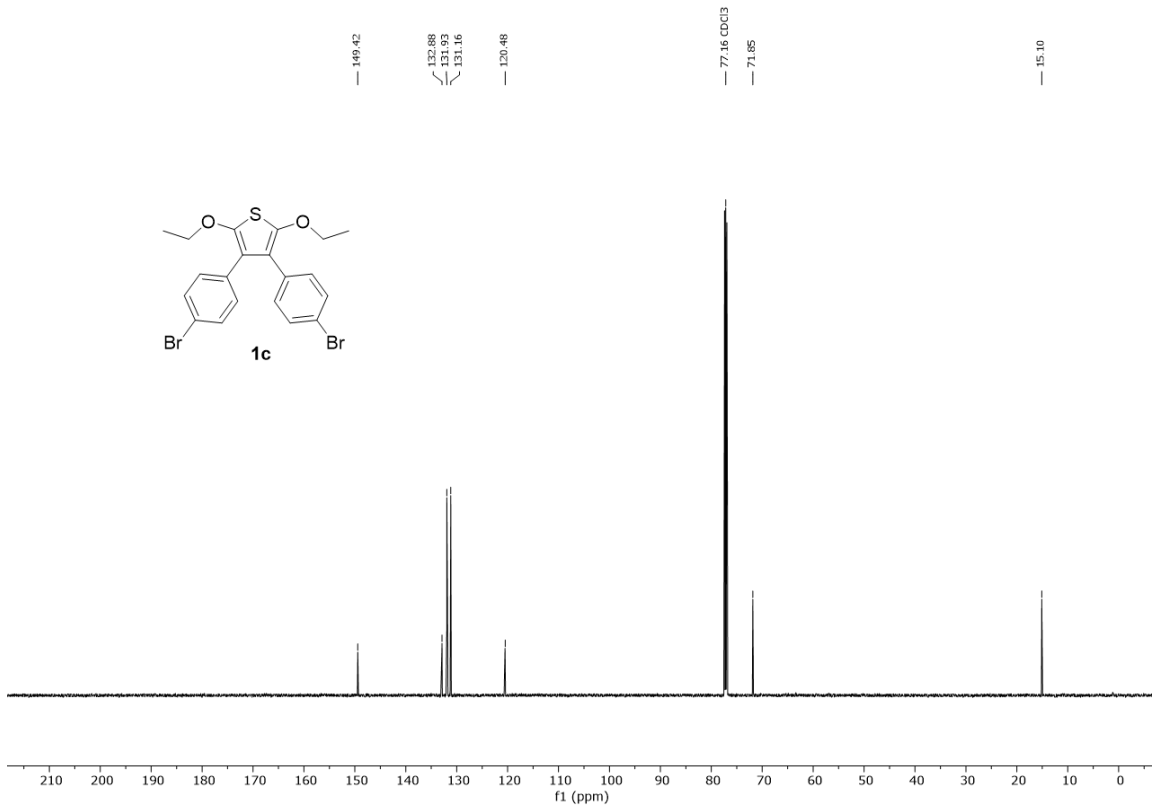

Fig. 11. $^{13}C\{^{1}H\}$ NMR (101 MHz, $CDCl_3$) of **1c**.

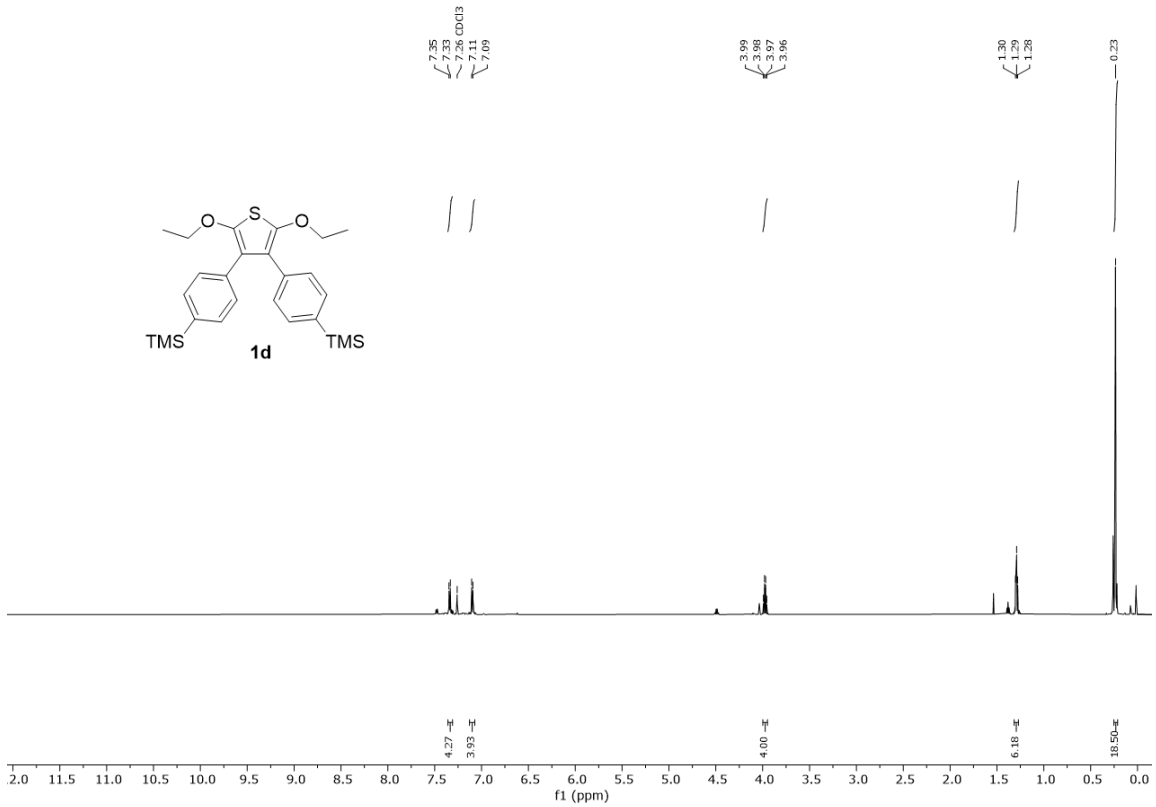

Fig. 12. ^{1}H NMR (400 MHz, $CDCl_3$) of **1d**.

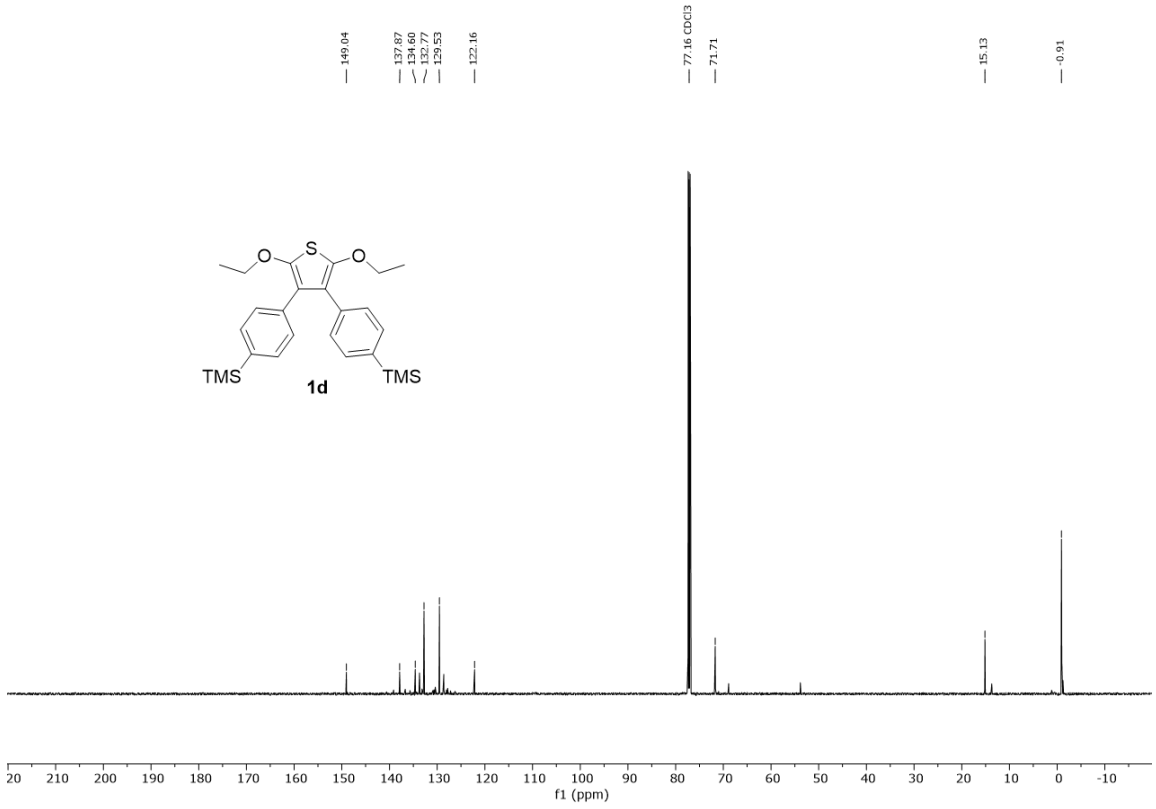

Fig. 13. $^{13}C\{^{1}H\}$ NMR (101 MHz, $CDCl_3$) of **1c**.

XRD Analysis

3a

Crystal data and structure refinement for D19096 (**3a**).

Identification code	D19096	
Empirical formula	C20 H20 O2 S	
Formula weight	324.42	
Temperature	100(2) K	
Wavelength	0.71073 Å	
Crystal system	Monoclinic	
Space group	$P2_1/n$	
Unit cell dimensions	a = 11.0887(5) Å	α = 90°.
	b = 8.6689(4) Å	β = 101.5049(12)°.
	c = 17.9301(8) Å	γ = 90°.
Volume	1688.93(13) $Å^3$	
Z	4	
Density (calculated)	1.276 Mg/m^3	
Absorption coefficient	0.199 mm^{-1}	
F(000)	688	
Crystal size	0.939 · 0.503 · 0.301 mm^3	
Theta range for data collection	2.318 to 37.036°.	
Index ranges	-18<=h<=18, -14<=k<=14, -30<=l<=30	
Reflections collected	77544	
Independent reflections	8624 [R(int) = 0.0484]	
Completeness to theta = 25.242°	100.0%	
Absorption correction	Semi-empirical from equivalents	
Refinement method	Full-matrix least-squares on F^2	
Data / restraints / parameters	8624 / 0 / 210	
Goodness-of-fit on F^2	1.065	
Final R indices [I>2sigma(I)]	R1 = 0.0379, wR2 = 0.0953	
R indices (all data)	R1 = 0.0501, wR2 = 0.1007	
Extinction coefficient	n/a	
Largest diff. peak and hole	0.547 and -0.343 $e.Å^{-3}$	

Table 2. Atomic coordinates ($\cdot 10^4$) and equivalent isotropic displacement parameters ($Å^2 \cdot 10^3$) for D19096. U(eq) is defined as one third of the trace of the orthogonalized U^{ij} tensor.

	x	y	z	U(eq)
S(1)	6081(1)	4221(1)	7089(1)	12(1)
O(1)	5675(1)	2217(1)	5942(1)	14(1)
O(2)	5089(1)	6732(1)	7649(1)	16(1)
C(1)	4040(1)	5590(1)	6475(1)	10(1)
C(2)	4166(1)	4298(1)	5983(1)	10(1)
C(3)	5228(1)	3489(1)	6241(1)	11(1)
C(4)	4994(1)	5658(1)	7092(1)	11(1)
C(5)	5032(1)	788(1)	6042(1)	18(1)
C(6)	5187(1)	322(1)	6865(1)	25(1)
C(7)	6242(1)	6863(1)	8171(1)	17(1)
C(8)	6123(1)	8175(1)	8702(1)	19(1)
C(11)	3100(1)	6825(1)	6324(1)	11(1)
C(12)	2878(1)	7609(1)	5629(1)	14(1)
C(13)	2081(1)	8870(1)	5512(1)	19(1)
C(14)	1496(1)	9360(1)	6087(1)	23(1)
C(15)	1697(1)	8571(1)	6775(1)	23(1)
C(16)	2488(1)	7311(1)	6894(1)	17(1)
C(21)	3229(1)	3814(1)	5315(1)	10(1)
C(22)	3576(1)	3296(1)	4649(1)	12(1)
C(23)	2696(1)	2753(1)	4040(1)	15(1)
C(24)	1458(1)	2732(1)	4085(1)	16(1)
C(25)	1100(1)	3265(1)	4741(1)	16(1)
C(26)	1978(1)	3798(1)	5352(1)	13(1)

Table 3. Bond lengths [Å] and angles [°] for D19096.

S(1)-C(4)	1.7340(7)
S(1)-C(3)	1.7424(7)
O(1)-C(3)	1.3617(9)
O(1)-C(5)	1.4579(10)
O(2)-C(4)	1.3539(9)
O(2)-C(7)	1.4310(10)
C(1)-C(4)	1.3707(10)
C(1)-C(2)	1.4497(10)
C(1)-C(11)	1.4811(10)
C(2)-C(3)	1.3702(10)
C(2)-C(21)	1.4807(10)

C(5)-C(6)	1.5075(13)
C(5)-H(5A)	0.9900
C(5)-H(5AB)	0.9900
C(6)-H(6A)	0.9800
C(6)-H(6B)	0.9800
C(6)-H(6C)	0.9800
C(7)-C(8)	1.5063(12)
C(7)-H(7A)	0.9900
C(7)-H(7AB)	0.9900
C(8)-H(8A)	0.9800
C(8)-H(8B)	0.9800
C(8)-H(8C)	0.9800
C(11)-C(12)	1.3985(10)
C(11)-C(16)	1.3996(10)
C(12)-C(13)	1.3953(11)
C(12)-H(12)	0.9500
C(13)-C(14)	1.3910(14)
C(13)-H(13)	0.9500
C(14)-C(15)	1.3887(15)
C(14)-H(14)	0.9500
C(15)-C(16)	1.3909(13)
C(15)-H(15)	0.9500
C(16)-H(16)	0.9500
C(21)-C(22)	1.4005(10)
C(21)-C(26)	1.4027(10)
C(22)-C(23)	1.3930(10)
C(22)-H(22)	0.9500
C(23)-C(24)	1.3907(12)
C(23)-H(23)	0.9500
C(24)-C(25)	1.3928(11)
C(24)-H(24)	0.9500
C(25)-C(26)	1.3917(11)
C(25)-H(25)	0.9500
C(26)-H(26)	0.9500

C(4)-S(1)-C(3)	90.43(3)
C(3)-O(1)-C(5)	114.52(6)
C(4)-O(2)-C(7)	117.68(6)
C(4)-C(1)-C(2)	111.82(6)

C(4)-C(1)-C(11)	121.22(6)
C(2)-C(1)-C(11)	126.65(6)
C(3)-C(2)-C(1)	111.76(6)
C(3)-C(2)-C(21)	123.03(6)
C(1)-C(2)-C(21)	125.06(6)
O(1)-C(3)-C(2)	129.62(7)
O(1)-C(3)-S(1)	117.49(5)
C(2)-C(3)-S(1)	112.87(5)
O(2)-C(4)-C(1)	123.95(7)
O(2)-C(4)-S(1)	122.96(5)
C(1)-C(4)-S(1)	113.09(5)
O(1)-C(5)-C(6)	112.61(7)
O(1)-C(5)-H(5A)	109.1
C(6)-C(5)-H(5A)	109.1
O(1)-C(5)-H(5AB)	109.1
C(6)-C(5)-H(5AB)	109.1
H(5A)-C(5)-H(5AB)	107.8
C(5)-C(6)-H(6A)	109.5
C(5)-C(6)-H(6B)	109.5
H(6A)-C(6)-H(6B)	109.5
C(5)-C(6)-H(6C)	109.5
H(6A)-C(6)-H(6C)	109.5
H(6B)-C(6)-H(6C)	109.5
O(2)-C(7)-C(8)	107.09(7)
O(2)-C(7)-H(7A)	110.3
C(8)-C(7)-H(7A)	110.3
O(2)-C(7)-H(7AB)	110.3
C(8)-C(7)-H(7AB)	110.3
H(7A)-C(7)-H(7AB)	108.6
C(7)-C(8)-H(8A)	109.5
C(7)-C(8)-H(8B)	109.5
H(8A)-C(8)-H(8B)	109.5
C(7)-C(8)-H(8C)	109.5
H(8A)-C(8)-H(8C)	109.5
H(8B)-C(8)-H(8C)	109.5
C(12)-C(11)-C(16)	118.77(7)
C(12)-C(11)-C(1)	120.38(6)
C(16)-C(11)-C(1)	120.66(7)
C(13)-C(12)-C(11)	120.52(7)

C(13)-C(12)-H(12)	119.7
C(11)-C(12)-H(12)	119.7
C(14)-C(13)-C(12)	120.19(8)
C(14)-C(13)-H(13)	119.9
C(12)-C(13)-H(13)	119.9
C(15)-C(14)-C(13)	119.54(8)
C(15)-C(14)-H(14)	120.2
C(13)-C(14)-H(14)	120.2
C(14)-C(15)-C(16)	120.53(8)
C(14)-C(15)-H(15)	119.7
C(16)-C(15)-H(15)	119.7
C(15)-C(16)-C(11)	120.43(8)
C(15)-C(16)-H(16)	119.8
C(11)-C(16)-H(16)	119.8
C(22)-C(21)-C(26)	118.67(6)
C(22)-C(21)-C(2)	120.92(6)
C(26)-C(21)-C(2)	120.34(6)
C(23)-C(22)-C(21)	120.55(7)
C(23)-C(22)-H(22)	119.7
C(21)-C(22)-H(22)	119.7
C(24)-C(23)-C(22)	120.30(7)
C(24)-C(23)-H(23)	119.9
C(22)-C(23)-H(23)	119.9
C(23)-C(24)-C(25)	119.67(7)
C(23)-C(24)-H(24)	120.2
C(25)-C(24)-H(24)	120.2
C(26)-C(25)-C(24)	120.23(7)
C(26)-C(25)-H(25)	119.9
C(24)-C(25)-H(25)	119.9
C(25)-C(26)-C(21)	120.58(7)
C(25)-C(26)-H(26)	119.7
C(21)-C(26)-H(26)	119.7

Symmetry transformations used to generate equivalent atoms.

Table 4. Anisotropic displacement parameters ($Å^2 \cdot 10^3$) for D19096. The anisotropic displacement factor exponent takes the form: $-2\pi^2[h^2 a^{*2}U^{11} + ... + 2 h k a^* b^* U^{12}]$.

	U^{11}	U^{22}	U^{33}	U^{23}	U^{13}	U^{12}
S(1)	11(1)	11(1)	12(1)	0(1)	0(1)	0(1)
O(1)	16(1)	10(1)	16(1)	-1(1)	5(1)	2(1)
O(2)	15(1)	16(1)	15(1)	-7(1)	-3(1)	1(1)
C(1)	9(1)	10(1)	10(1)	-1(1)	2(1)	-1(1)
C(2)	10(1)	10(1)	10(1)	0(1)	2(1)	-1(1)
C(3)	11(1)	9(1)	11(1)	-1(1)	2(1)	0(1)
C(4)	11(1)	10(1)	11(1)	-1(1)	1(1)	-1(1)
C(5)	24(1)	9(1)	19(1)	-1(1)	-1(1)	-1(1)
C(6)	34(1)	17(1)	21(1)	4(1)	2(1)	-7(1)
C(7)	14(1)	20(1)	14(1)	-4(1)	-2(1)	-1(1)
C(8)	23(1)	20(1)	12(1)	-5(1)	0(1)	-3(1)
C(11)	9(1)	11(1)	12(1)	-2(1)	2(1)	0(1)
C(12)	12(1)	14(1)	14(1)	0(1)	1(1)	1(1)
C(13)	16(1)	15(1)	24(1)	1(1)	-2(1)	3(1)
C(14)	16(1)	17(1)	35(1)	-7(1)	0(1)	5(1)
C(15)	16(1)	24(1)	29(1)	-11(1)	7(1)	3(1)
C(16)	14(1)	21(1)	16(1)	-5(1)	6(1)	1(1)
C(21)	10(1)	10(1)	10(1)	-1(1)	2(1)	-1(1)
C(22)	13(1)	13(1)	11(1)	-1(1)	4(1)	-1(1)
C(23)	19(1)	15(1)	10(1)	-1(1)	3(1)	-1(1)
C(24)	17(1)	16(1)	13(1)	-2(1)	-1(1)	-2(1)
C(25)	12(1)	19(1)	16(1)	-3(1)	1(1)	-3(1)
C(26)	11(1)	16(1)	13(1)	-3(1)	3(1)	-2(1)

3b

Crystal data and structure refinement for D21437 (**3b**).

Identification code	D21437	
Empirical formula	C22 H24 O2 S	
Formula weight	352.47	
Temperature	100(2) K	
Wavelength	0.71073 Å	
Crystal system	Monoclinic	
Space group	$P2_1/n$	
Unit cell dimensions	a = 9.8237(6) Å	α = 90°.
	b = 10.3889(7) Å	β = 103.3814(19)°.
	c = 19.3330(12) Å	γ = 90°.

Volume	1919.5(2) $Å^3$
Z	4
Density (calculated)	1.220 Mg/m^3
Absorption coefficient	0.180 mm^{-1}
F(000)	752
Crystal size	0.790 x 0.645 x 0.592 mm^3
Theta range for data collection	2.155 to 35.630°.
Index ranges	-16<=h<=15, -17<=k<=17, -31<=l<=31
Reflections collected	65049
Independent reflections	8842 [R(int) = 0.0380]
Completeness to theta = 25.242°	100.0%
Absorption correction	Semi-empirical from equivalents
Refinement method	Full-matrix least-squares on F^2
Data / restraints / parameters	8842 / 0 / 231
Goodness-of-fit on F^2	1.030
Final R indices [I>2sigma(I)]	R1 = 0.0406, wR2 = 0.1059
R indices (all data)	R1 = 0.0521, wR2 = 0.1136
Extinction coefficient	0.0320(17)
Largest diff. peak and hole	0.470 and -0.355 $e.Å^{-3}$

Table 5. Atomic coordinates ($\cdot 10^4$) and equivalent isotropic displacement parameters ($Å^2 \cdot 10^3$) for D21437. U(eq) is defined as one third of the trace of the orthogonalized U^{ij} tensor.

	x	y	z	U(eq)
S(1)	5165(1)	5173(1)	9075(1)	20(1)
O(1)	4238(1)	7224(1)	8288(1)	19(1)
O(2)	5767(1)	2634(1)	8970(1)	25(1)
C(1)	4606(1)	5968(1)	8265(1)	17(1)
C(2)	4665(1)	5212(1)	7693(1)	15(1)
C(3)	5178(1)	3932(1)	7910(1)	15(1)
C(4)	5478(1)	3782(1)	8631(1)	18(1)
C(5)	5229(1)	8138(1)	8120(1)	22(1)
C(6)	4626(1)	9456(1)	8166(1)	34(1)
C(7)	6618(1)	2652(1)	9675(1)	30(1)
C(8)	6632(1)	1334(1)	9987(1)	32(1)
C(11)	4331(1)	5694(1)	6953(1)	15(1)
C(12)	3144(1)	6454(1)	6693(1)	19(1)
C(13)	2854(1)	6923(1)	5999(1)	23(1)
C(14)	3737(1)	6665(1)	5547(1)	23(1)
C(15)	4924(1)	5919(1)	5808(1)	21(1)
C(16)	5218(1)	5434(1)	6498(1)	17(1)
C(17)	3428(2)	7168(1)	4796(1)	36(1)
C(21)	5280(1)	2854(1)	7423(1)	15(1)
C(22)	6536(1)	2193(1)	7474(1)	17(1)
C(23)	6614(1)	1165(1)	7023(1)	19(1)
C(24)	5438(1)	755(1)	6519(1)	19(1)
C(25)	4186(1)	1420(1)	6469(1)	20(1)
C(26)	4106(1)	2463(1)	6910(1)	18(1)
C(27)	5523(1)	-379(1)	6048(1)	29(1)

Table 6. Bond lengths [Å] and angles [°] for D21437.

S(1)-C(1)	1.7421(8)
S(1)-C(4)	1.7436(8)
O(1)-C(1)	1.3578(10)
O(1)-C(5)	1.4498(11)
O(2)-C(4)	1.3589(10)
O(2)-C(7)	1.4253(12)
C(1)-C(2)	1.3672(11)
C(2)-C(3)	1.4500(11)
C(2)-C(11)	1.4797(11)
C(3)-C(4)	1.3654(11)
C(3)-C(21)	1.4810(11)
C(5)-C(6)	1.5027(14)
C(5)-H(5A)	0.9900
C(5)-H(5AB)	0.9900
C(6)-H(6A)	0.9800
C(6)-H(6B)	0.9800
C(6)-H(6C)	0.9800
C(7)-C(8)	1.4942(14)
C(7)-H(7A)	0.9900
C(7)-H(7AB)	0.9900
C(8)-H(8A)	0.9800
C(8)-H(8B)	0.9800
C(8)-H(8C)	0.9800
C(11)-C(16)	1.4010(11)
C(11)-C(12)	1.4017(11)
C(12)-C(13)	1.3923(12)
C(12)-H(12)	0.9500
C(13)-C(14)	1.3928(14)
C(13)-H(13)	0.9500
C(14)-C(15)	1.3948(13)
C(14)-C(17)	1.5066(13)
C(15)-C(16)	1.3916(11)
C(15)-H(15)	0.9500
C(16)-H(16)	0.9500
C(17)-H(17A)	0.9800
C(17)-H(17B)	0.9800
C(17)-H(17C)	0.9800
C(21)-C(26)	1.3960(11)

C(21)-C(22)	1.3962(11)
C(22)-C(23)	1.3913(11)
C(22)-H(22)	0.9500
C(23)-C(24)	1.3946(12)
C(23)-H(23)	0.9500
C(24)-C(25)	1.3946(12)
C(24)-C(27)	1.5032(12)
C(25)-C(26)	1.3918(12)
C(25)-H(25)	0.9500
C(26)-H(26)	0.9500
C(27)-H(27A)	0.9800
C(27)-H(27B)	0.9800
C(27)-H(27C)	0.9800

C(1)-S(1)-C(4)	90.33(4)
C(1)-O(1)-C(5)	115.15(7)
C(4)-O(2)-C(7)	117.38(7)
O(1)-C(1)-C(2)	129.73(7)
O(1)-C(1)-S(1)	117.20(6)
C(2)-C(1)-S(1)	113.01(6)
C(1)-C(2)-C(3)	111.70(7)
C(1)-C(2)-C(11)	123.09(7)
C(3)-C(2)-C(11)	125.09(7)
C(4)-C(3)-C(2)	112.21(7)
C(4)-C(3)-C(21)	122.23(7)
C(2)-C(3)-C(21)	125.41(7)
O(2)-C(4)-C(3)	124.27(7)
O(2)-C(4)-S(1)	122.15(6)
C(3)-C(4)-S(1)	112.74(6)
O(1)-C(5)-C(6)	106.82(8)
O(1)-C(5)-H(5A)	110.4
C(6)-C(5)-H(5A)	110.4
O(1)-C(5)-H(5AB)	110.4
C(6)-C(5)-H(5AB)	110.4
H(5A)-C(5)-H(5AB)	108.6
C(5)-C(6)-H(6A)	109.5
C(5)-C(6)-H(6B)	109.5
H(6A)-C(6)-H(6B)	109.5
C(5)-C(6)-H(6C)	109.5

H(6A)-C(6)-H(6C)	109.5
H(6B)-C(6)-H(6C)	109.5
O(2)-C(7)-C(8)	108.80(9)
O(2)-C(7)-H(7A)	109.9
C(8)-C(7)-H(7A)	109.9
O(2)-C(7)-H(7AB)	109.9
C(8)-C(7)-H(7AB)	109.9
H(7A)-C(7)-H(7AB)	108.3
C(7)-C(8)-H(8A)	109.5
C(7)-C(8)-H(8B)	109.5
H(8A)-C(8)-H(8B)	109.5
C(7)-C(8)-H(8C)	109.5
H(8A)-C(8)-H(8C)	109.5
H(8B)-C(8)-H(8C)	109.5
C(16)-C(11)-C(12)	118.00(7)
C(16)-C(11)-C(2)	120.77(7)
C(12)-C(11)-C(2)	121.21(7)
C(13)-C(12)-C(11)	120.73(8)
C(13)-C(12)-H(12)	119.6
C(11)-C(12)-H(12)	119.6
C(12)-C(13)-C(14)	121.24(8)
C(12)-C(13)-H(13)	119.4
C(14)-C(13)-H(13)	119.4
C(13)-C(14)-C(15)	118.05(8)
C(13)-C(14)-C(17)	121.52(9)
C(15)-C(14)-C(17)	120.43(9)
C(16)-C(15)-C(14)	121.21(8)
C(16)-C(15)-H(15)	119.4
C(14)-C(15)-H(15)	119.4
C(15)-C(16)-C(11)	120.76(8)
C(15)-C(16)-H(16)	119.6
C(11)-C(16)-H(16)	119.6
C(14)-C(17)-H(17A)	109.5
C(14)-C(17)-H(17B)	109.5
H(17A)-C(17)-H(17B)	109.5
C(14)-C(17)-H(17C)	109.5
H(17A)-C(17)-H(17C)	109.5
H(17B)-C(17)-H(17C)	109.5
C(26)-C(21)-C(22)	118.54(7)

C(26)-C(21)-C(3)	120.39(7)
C(22)-C(21)-C(3)	121.06(7)
C(23)-C(22)-C(21)	120.63(7)
C(23)-C(22)-H(22)	119.7
C(21)-C(22)-H(22)	119.7
C(22)-C(23)-C(24)	121.02(7)
C(22)-C(23)-H(23)	119.5
C(24)-C(23)-H(23)	119.5
C(23)-C(24)-C(25)	118.14(7)
C(23)-C(24)-C(27)	120.63(8)
C(25)-C(24)-C(27)	121.23(8)
C(26)-C(25)-C(24)	121.14(8)
C(26)-C(25)-H(25)	119.4
C(24)-C(25)-H(25)	119.4
C(25)-C(26)-C(21)	120.50(7)
C(25)-C(26)-H(26)	119.7
C(21)-C(26)-H(26)	119.7
C(24)-C(27)-H(27A)	109.5
C(24)-C(27)-H(27B)	109.5
H(27A)-C(27)-H(27B)	109.5
C(24)-C(27)-H(27C)	109.5
H(27A)-C(27)-H(27C)	109.5
H(27B)-C(27)-H(27C)	109.5

Symmetry transformations used to generate equivalent atoms.

Table 7. Anisotropic displacement parameters ($Å^2 \cdot 10^3$) for D21437. The anisotropic displacement factor exponent takes the form: $-2\pi^2[h^2 a \cdot {}^2U^{11} + ... + 2 h k a \cdot b \cdot U^{12}]$

	U^{11}	U^{22}	U^{33}	U^{23}	U^{13}	U^{12}
S(1)	30(1)	17(1)	15(1)	0(1)	7(1)	1(1)
O(1)	21(1)	14(1)	25(1)	0(1)	10(1)	2(1)
O(2)	40(1)	16(1)	17(1)	3(1)	2(1)	2(1)
C(1)	20(1)	15(1)	18(1)	1(1)	7(1)	2(1)
C(2)	16(1)	14(1)	15(1)	1(1)	4(1)	1(1)
C(3)	17(1)	14(1)	15(1)	1(1)	4(1)	1(1)
C(4)	24(1)	14(1)	16(1)	2(1)	5(1)	1(1)
C(5)	22(1)	18(1)	27(1)	0(1)	7(1)	-1(1)
C(6)	50(1)	16(1)	43(1)	1(1)	27(1)	1(1)
C(7)	42(1)	22(1)	21(1)	5(1)	-3(1)	-1(1)
C(8)	38(1)	29(1)	27(1)	14(1)	5(1)	2(1)
C(11)	17(1)	14(1)	15(1)	0(1)	3(1)	0(1)
C(12)	18(1)	17(1)	22(1)	2(1)	2(1)	2(1)
C(13)	24(1)	18(1)	23(1)	3(1)	-3(1)	2(1)
C(14)	32(1)	16(1)	16(1)	1(1)	-1(1)	-1(1)
C(15)	28(1)	18(1)	15(1)	0(1)	4(1)	-2(1)
C(16)	20(1)	17(1)	15(1)	1(1)	4(1)	1(1)
C(17)	58(1)	27(1)	17(1)	5(1)	-1(1)	4(1)
C(21)	15(1)	13(1)	15(1)	1(1)	4(1)	0(1)
C(22)	14(1)	17(1)	19(1)	-2(1)	2(1)	0(1)
C(23)	18(1)	18(1)	22(1)	-1(1)	5(1)	2(1)
C(24)	24(1)	15(1)	17(1)	-1(1)	6(1)	-1(1)
C(25)	20(1)	20(1)	19(1)	-2(1)	0(1)	-2(1)
C(26)	15(1)	19(1)	19(1)	0(1)	1(1)	1(1)
C(27)	39(1)	22(1)	26(1)	-8(1)	7(1)	1(1)
S(1)	30(1)	17(1)	15(1)	0(1)	7(1)	1(1)
O(1)	21(1)	14(1)	25(1)	0(1)	10(1)	2(1)
O(2)	40(1)	16(1)	17(1)	3(1)	2(1)	2(1)

Table 8. Hydrogen coordinates ($\cdot 10^4$) and isotropic displacement parameters ($Å^2 \cdot 10^3$) for D21437.

	x	y	z	U(eq)
H(5A)	5365	7981	7636	26
H(5AB)	6145	8057	8463	26
H(6A)	5299	10109	8093	51
H(6B)	4427	9573	8636	51
H(6C)	3758	9546	7799	51
H(7A)	6238	3278	9968	37
H(7AB)	7582	2916	9668	37
H(8A)	5683	1102	10022	48
H(8B)	7258	1324	10462	48
H(8C)	6963	713	9682	48
H(12)	2531	6652	6993	23
H(13)	2038	7429	5832	28
H(15)	5545	5738	5509	25
H(16)	6029	4921	6661	21
H(17A)	3016	6480	4467	54
H(17B)	4298	7464	4682	54
H(17C)	2769	7889	4750	54
H(22)	7346	2448	7819	20
H(23)	7481	735	7060	23
H(25)	3373	1156	6129	24
H(26)	3246	2911	6862	22
H(27A)	4702	-387	5648	44
H(27B)	5550	-1176	6321	44
H(27C)	6374	-313	5867	44

Table 9. Hydrogen coordinates ($\cdot 10^4$) and isotropic displacement parameters ($Å^2 \cdot 10^3$) for D19096.

	x	y	z	U(eq)
H(5A)	5349	-48	5757	22
H(5AB)	4145	918	5824	22
H(6A)	4785	-675	6900	37
H(6B)	4810	1103	7142	37
H(6C)	6065	236	7090	37
H(7A)	6911	7076	7893	20
H(7AB)	6435	5892	8461	20
H(8A)	5885	9115	8406	29
H(8B)	6914	8340	9050	29
H(8C)	5493	7922	8996	29
H(12)	3274	7280	5233	16
H(13)	1938	9396	5037	23
H(14)	962	10227	6010	28
H(15)	1290	8895	7167	27
H(16)	2614	6776	7366	20
H(22)	4418	3314	4611	15
H(23)	2942	2396	3592	18
H(24)	860	2355	3670	19
H(25)	255	3265	4770	19
H(26)	1727	4154	5799	16

3c

Crystal data and structure refinement for D22024_a (**3c**).

Identification code	D22024_a	
Empirical formula	C20 H18 Br2 O2 S	
Formula weight	482.22	
Temperature	100(2) K	
Wavelength	0.71073 Å	
Crystal system	Orthorhombic	
Space group	Pbca	
Unit cell dimensions	a = 19.894(2) Å	α = 90°.
	b = 9.5013(10) Å	β = 90°.
	c = 20.803(2) Å	γ = 90°.
Volume	3932.3(7) $Å^3$	
Z	8	
Density (calculated)	1.629 Mg/m^3	

Absorption coefficient	4.239 mm^{-1}
F(000)	1920
Crystal size	0.417 x 0.234 x 0.064 mm^3
Theta range for data collection	1.958 to 26.732°.
Index ranges	-25<=h<=25, -12<=k<=12, -26<=l<=26
Reflections collected	92040
Independent reflections	4169 [R(int) = 0.0654]
Completeness to theta = 25.242°	100.0%
Absorption correction	Semi-empirical from equivalents
Refinement method	Full-matrix least-squares on F^2
Data / restraints / parameters	4169 / 0 / 228
Goodness-of-fit on F^2	1.026
Final R indices [I>2sigma(I)]	R1 = 0.0294, wR2 = 0.0629
R indices (all data)	R1 = 0.0422, wR2 = 0.0680
Extinction coefficient	n/a
Largest diff. peak and hole	0.361 and -0.561 $e.Å^{-3}$

Table 10. Atomic coordinates ($\cdot 10^4$) and equivalent isotropic displacement parameters ($Å^2 \cdot 10^3$) for D22024_a. U(eq) is defined as one third of the trace of the orthogonalized U^{ij} tensor.

	x	y	z	U(eq)
Br(1)	5686(1)	8798(1)	6547(1)	33(1)
Br(2)	4039(1)	5877(1)	2972(1)	38(1)
S(1)	8347(1)	5761(1)	3565(1)	23(1)
O(1)	8390(1)	6985(2)	4741(1)	26(1)
O(2)	7462(1)	5043(2)	2642(1)	23(1)
C(1)	6914(1)	7084(2)	4793(1)	18(1)
C(2)	6390(1)	6294(2)	5055(1)	21(1)
C(3)	6020(1)	6795(3)	5575(1)	23(1)
C(4)	6174(1)	8100(3)	5825(1)	23(1)
C(5)	6689(1)	8912(2)	5576(1)	23(1)
C(6)	7058(1)	8396(2)	5061(1)	22(1)
C(7)	7316(1)	6547(2)	4244(1)	20(1)
C(8)	8002(1)	6537(2)	4246(1)	21(1)
C(9)	7539(1)	5435(2)	3267(1)	21(1)
C(10)	7047(1)	5902(2)	3668(1)	19(1)
C(11)	9102(1)	6777(3)	4677(1)	34(1)
C(12)	9426(1)	7265(3)	5286(1)	40(1)
C(13)	7627(1)	3590(2)	2501(1)	25(1)
C(14)	7460(1)	3334(3)	1808(1)	29(1)
C(15)	6326(1)	5881(2)	3493(1)	19(1)
C(16)	5944(1)	7105(2)	3536(1)	21(1)
C(17)	5270(1)	7118(3)	3368(1)	23(1)
C(18)	4977(1)	5880(3)	3159(1)	25(1)
C(19)	5339(1)	4649(3)	3101(1)	26(1)
C(20)	6017(1)	4662(3)	3264(1)	23(1)

Table 11. Bond lengths [Å] and angles [°] for D22024_a.

Br(1)-C(4)	1.908(2)
Br(2)-C(18)	1.908(2)
S(1)-C(8)	1.738(2)
S(1)-C(9)	1.751(3)
O(1)-C(8)	1.355(3)
O(1)-C(11)	1.436(3)
O(2)-C(9)	1.363(3)
O(2)-C(13)	1.449(3)
C(1)-C(2)	1.395(3)
C(1)-C(6)	1.395(3)
C(1)-C(7)	1.484(3)
C(2)-C(3)	1.393(3)
C(2)-H(2)	0.9500
C(3)-C(4)	1.378(3)
C(3)-H(3)	0.9500
C(4)-C(5)	1.384(3)
C(5)-C(6)	1.390(3)
C(5)-H(5)	0.9500
C(6)-H(6)	0.9500
C(7)-C(8)	1.365(3)
C(7)-C(10)	1.448(3)
C(9)-C(10)	1.360(3)
C(10)-C(15)	1.481(3)
C(11)-C(12)	1.495(4)
C(11)-H(11A)	0.9900
C(11)-H(11B)	0.9900
C(12)-H(12A)	0.9800
C(12)-H(12B)	0.9800
C(12)-H(12C)	0.9800
C(13)-C(14)	1.498(3)
C(13)-H(13A)	0.9900
C(13)-H(13B)	0.9900
C(14)-H(14A)	0.9800
C(14)-H(14B)	0.9800
C(14)-H(14C)	0.9800
C(15)-C(16)	1.392(3)
C(15)-C(20)	1.395(3)
C(16)-C(17)	1.386(3)

C(16)-H(16)	0.9500
C(17)-C(18)	1.382(3)
C(17)-H(17)	0.9500
C(18)-C(19)	1.379(4)
C(19)-C(20)	1.390(4)
C(19)-H(19)	0.9500
C(20)-H(20)	0.9500

C(8)-S(1)-C(9)	90.09(11)
C(8)-O(1)-C(11)	116.65(19)
C(9)-O(2)-C(13)	115.34(17)
C(2)-C(1)-C(6)	118.6(2)
C(2)-C(1)-C(7)	121.2(2)
C(6)-C(1)-C(7)	120.2(2)
C(3)-C(2)-C(1)	121.0(2)
C(3)-C(2)-H(2)	119.5
C(1)-C(2)-H(2)	119.5
C(4)-C(3)-C(2)	118.9(2)
C(4)-C(3)-H(3)	120.5
C(2)-C(3)-H(3)	120.5
C(3)-C(4)-C(5)	121.7(2)
C(3)-C(4)-Br(1)	119.81(18)
C(5)-C(4)-Br(1)	118.50(18)
C(4)-C(5)-C(6)	118.9(2)
C(4)-C(5)-H(5)	120.6
C(6)-C(5)-H(5)	120.6
C(5)-C(6)-C(1)	121.0(2)
C(5)-C(6)-H(6)	119.5
C(1)-C(6)-H(6)	119.5
C(8)-C(7)-C(10)	111.6(2)
C(8)-C(7)-C(1)	122.6(2)
C(10)-C(7)-C(1)	125.7(2)
O(1)-C(8)-C(7)	124.7(2)
O(1)-C(8)-S(1)	121.84(17)
C(7)-C(8)-S(1)	113.26(18)
C(10)-C(9)-O(2)	126.5(2)
C(10)-C(9)-S(1)	112.66(18)
O(2)-C(9)-S(1)	119.34(17)
C(9)-C(10)-C(7)	112.4(2)

C(9)-C(10)-C(15)	122.8(2)
C(7)-C(10)-C(15)	124.5(2)
O(1)-C(11)-C(12)	107.7(2)
O(1)-C(11)-H(11A)	110.2
C(12)-C(11)-H(11A)	110.2
O(1)-C(11)-H(11B)	110.2
C(12)-C(11)-H(11B)	110.2
H(11A)-C(11)-H(11B)	108.5
C(11)-C(12)-H(12A)	109.5
C(11)-C(12)-H(12B)	109.5
H(12A)-C(12)-H(12B)	109.5
C(11)-C(12)-H(12C)	109.5
H(12A)-C(12)-H(12C)	109.5
H(12B)-C(12)-H(12C)	109.5
O(2)-C(13)-C(14)	107.36(19)
O(2)-C(13)-H(13A)	110.2
C(14)-C(13)-H(13A)	110.2
O(2)-C(13)-H(13B)	110.2
C(14)-C(13)-H(13B)	110.2
H(13A)-C(13)-H(13B)	108.5
C(13)-C(14)-H(14A)	109.5
C(13)-C(14)-H(14B)	109.5
H(14A)-C(14)-H(14B)	109.5
C(13)-C(14)-H(14C)	109.5
H(14A)-C(14)-H(14C)	109.5
H(14B)-C(14)-H(14C)	109.5
C(16)-C(15)-C(20)	118.4(2)
C(16)-C(15)-C(10)	120.2(2)
C(20)-C(15)-C(10)	121.4(2)
C(17)-C(16)-C(15)	121.3(2)
C(17)-C(16)-H(16)	119.3
C(15)-C(16)-H(16)	119.3
C(18)-C(17)-C(16)	118.6(2)
C(18)-C(17)-H(17)	120.7
C(16)-C(17)-H(17)	120.7
C(19)-C(18)-C(17)	122.0(2)
C(19)-C(18)-Br(2)	119.48(19)
C(17)-C(18)-Br(2)	118.52(19)
C(18)-C(19)-C(20)	118.5(2)

C(18)-C(19)-H(19)	120.7
C(20)-C(19)-H(19)	120.7
C(19)-C(20)-C(15)	121.2(2)
C(19)-C(20)-H(20)	119.4
C(15)-C(20)-H(20)	119.4

Symmetry transformations used to generate equivalent atoms.

Table 12. Anisotropic displacement parameters ($Å^2 \cdot 10^3$) for D22024_a. The anisotropic displacement factor exponent takes the form: $-2\pi^2[h^2 a^{*2}U^{11} + ... + 2 h k a^* b^* U^{12}]$.

	U^{11}	U^{22}	U^{33}	U^{23}
Br(1)	40(1)	32(1)	27(1)	-5(1)
Br(2)	26(1)	50(1)	37(1)	1(1)
S(1)	21(1)	21(1)	26(1)	2(1)
O(1)	18(1)	32(1)	30(1)	-3(1)
O(2)	32(1)	16(1)	20(1)	1(1)
C(1)	20(1)	19(1)	16(1)	3(1)
C(2)	23(1)	21(1)	20(1)	-1(1)
C(3)	22(1)	25(1)	24(1)	3(1)
C(4)	24(1)	26(1)	19(1)	2(1)
C(5)	28(1)	19(1)	22(1)	-1(1)
C(6)	22(1)	18(1)	24(1)	4(1)
C(7)	22(1)	15(1)	22(1)	4(1)
C(8)	25(1)	16(1)	21(1)	2(1)
C(9)	25(1)	16(1)	23(1)	3(1)
C(10)	21(1)	13(1)	22(1)	2(1)
C(11)	20(1)	52(2)	32(1)	5(1)
C(12)	28(2)	52(2)	41(2)	4(1)
C(13)	27(1)	17(1)	30(1)	1(1)
C(14)	32(1)	26(1)	29(1)	-4(1)
C(15)	22(1)	19(1)	15(1)	5(1)
C(16)	25(1)	16(1)	23(1)	2(1)
C(17)	25(1)	24(1)	22(1)	3(1)
C(18)	21(1)	36(1)	18(1)	2(1)
C(19)	32(1)	24(1)	22(1)	-1(1)
C(20)	29(1)	18(1)	23(1)	2(1)

Table 13. Hydrogen coordinates ($\cdot 10^4$) and isotropic displacement parameters ($Å^2 \cdot 10^3$) for D22024_a.

	x	y	z	U(eq)
H(2)	6285	5402	4876	26
H(3)	5668	6246	5755	28
H(5)	6789	9808	5755	27
H(6)	7414	8945	4887	26
H(11A)	9276	7322	4308	41
H(11B)	9201	5768	4604	41
H(12A)	9913	7121	5259	60
H(12B)	9245	6728	5649	60
H(12C)	9331	8268	5350	60
H(13A)	7364	2950	2779	29
H(13B)	8111	3417	2578	29
H(14A)	7733	3953	1537	43
H(14B)	6982	3531	1735	43
H(14C)	7554	2350	1700	43
H(16)	6149	7947	3684	26
H(17)	5014	7960	3395	28
H(19)	5130	3810	2954	31
H(20)	6274	3826	3219	28

5.4. References

[1] P. R. Schreiner, *Trends Chem.* **2020**, *2(11)*, 980.

[2] M. Schauermann, P. R. Schreiner, *J. Phys. Chem. Lett.* **2022**, *13(13)*, 3138.

[3] T. Maulbetsch, E. Jürgens, D. Kunz, *Chem. Eur. J.* **2020**, *26(46)*, 10634.

[4] H. W. Tsai, K. L. Hsueh, M. H. Chen, C. W. Hong, *Crystals* **2021**, 11(11), 1292.

Chapter 6: NMR-Investigations towards the Breslow-Intermediate

6.1. Abstract

This project started during my Master thesis.

Since Breslow postulated his mechanism for the "Umpolung"-reaction of thiamine pyrophosphate in 1958,[1] the characterization of the henceforth named "Breslow-Intermediate" failed due to its extremely low stability. Several attempts to characterize this intermediate spectroscopically by reacting thiamine derivatives under basic conditions with aldehydes failed. While carrying out the following investigations vast progress was made by Berkessel's group (see Chapter Introduction for more detail).[2-3] In our approach we focused on an alternative route starting from silyl-protected precursor salts.[5] We were able to identify the TMS-protected enaminol and the free enaminol *via* low temperature NMR spectroscopy. Understanding the mechanism of benzoin-type reactions is of great interest not only for catalytic applications in industry but also in the field of biochemical catalysis.

6.2. Results and Discussion

Thiamine-based Breslow intermediates are too unstable to be characterized with established analytical techniques. We therefore used the corresponding silyl-protected precursor salts (Fig. 1), that were employed for fluorine induced benzoin-type reactions by Scheidt *et al*.[5]

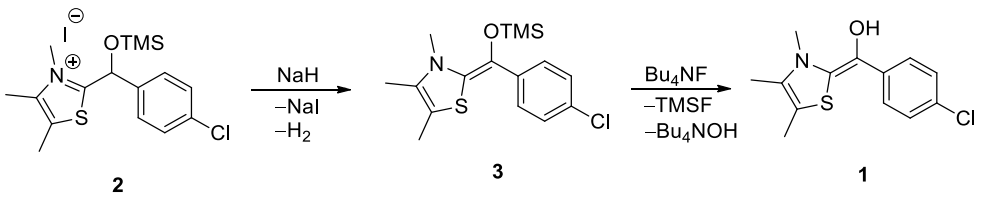

Fig. 1. Strategy for the generation of a thiamine-based Breslow intermediate **1**.

In the first step we planned to deprotonate **2** with NaH in THF-d_8 (NaI precipitates in the chosen solvent) and hydrogen is released (Scheme 1). This step was be carried out in a glove box (N_2 atmosphere) to avoid possible oxidation reactions of the starting material or intermediates. In a second step **3**, TMS protected Breslow intermediate, will be deprotonated with TBAF. The deprotonation works well under inert conditions at r.t.; ^{1}H- and ^{13}C-spectra are shown in Figures 1 and 2. To confirm the NMR spectroscopy assignments, the starting compound was synthesized with a ^{13}C label at the initial carbonyl carbon of the aldehyde. The resulting spectra are shown in Figures 2 and 3.

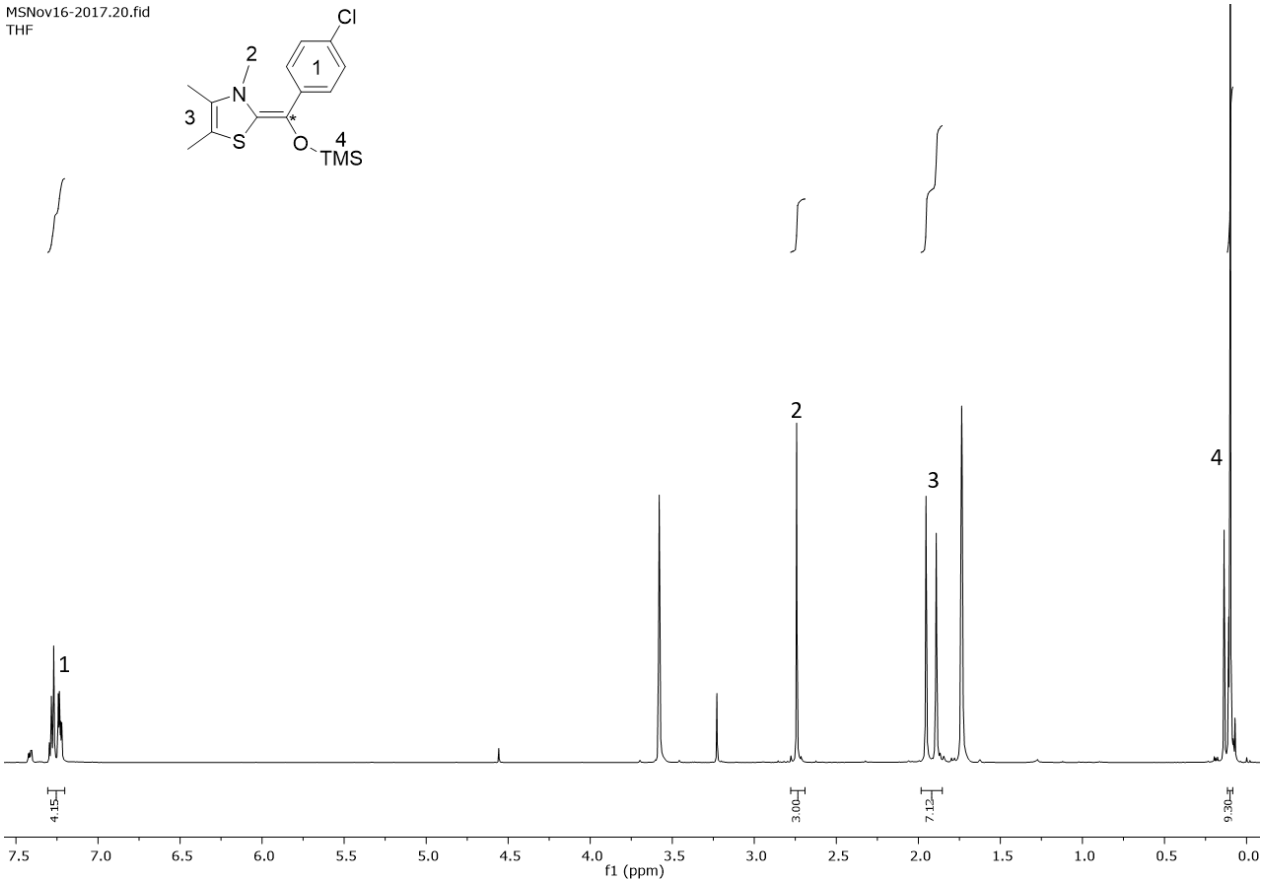

Fig. 2. ^{1}H-NMR spectra of the silyl-protected Breslow-Intermediate recorded at r.t. after hydrogen formation stopped.

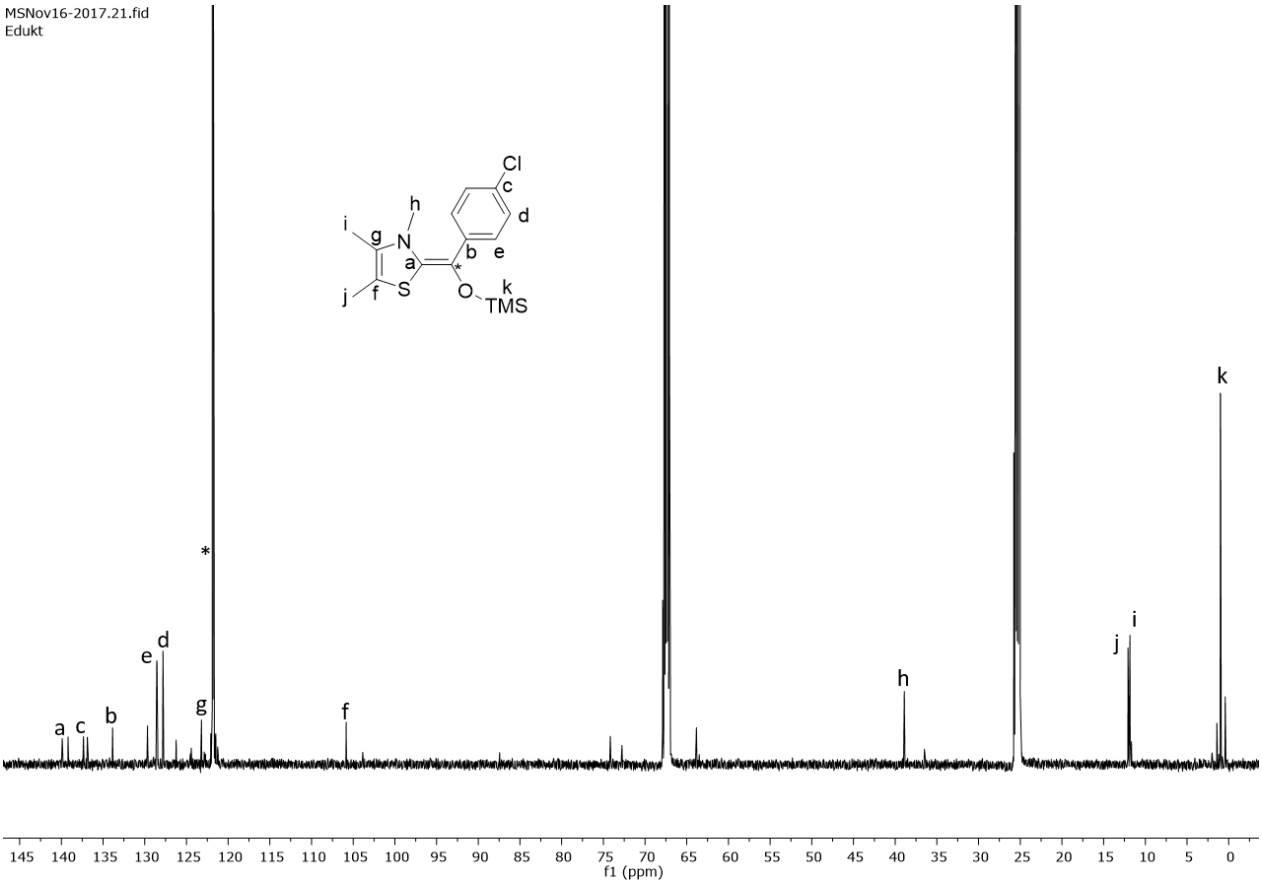

Fig. 3. ^{13}C-NMR spectra of the silyl-protected, ^{13}C-labelled Breslow-Intermediate.

Figure 4 shows two new labelled species that were assigned to the *E*- the *Z*-conformation of the silyl protected enaminol.

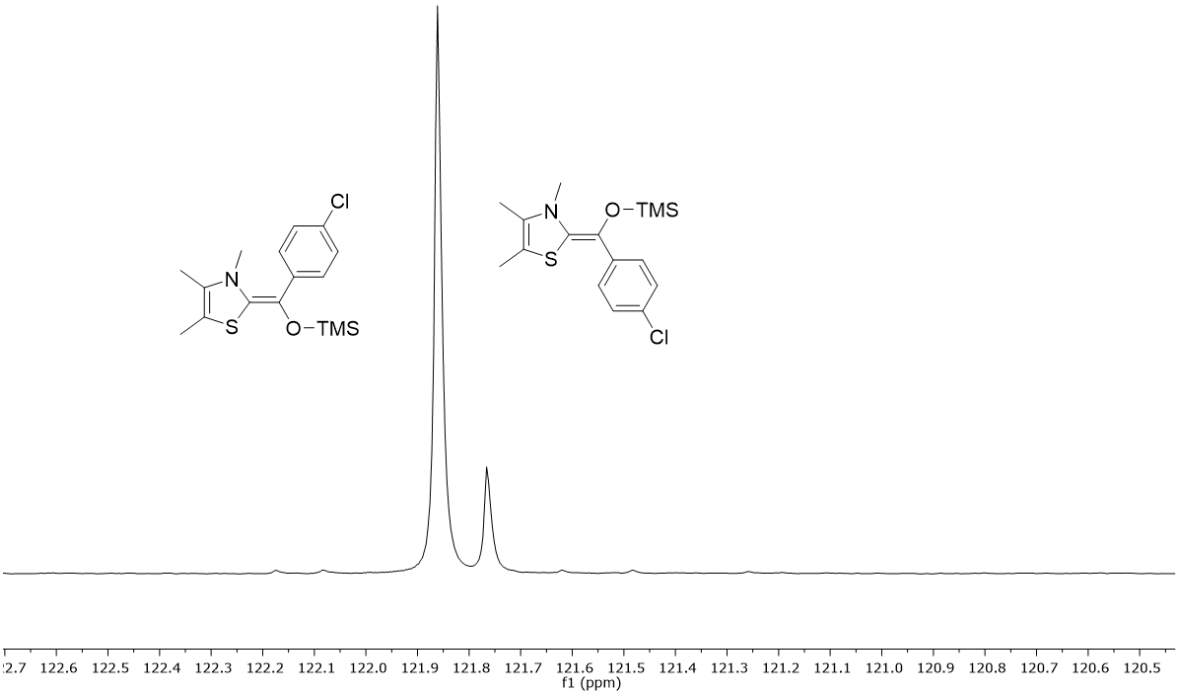

Fig. 4. ^{13}C-spectra of the *E*- and *Z*-conformer of the silyl-protected enaminol.

NOESY experiments show that the main conformer is *Z* (Figure 5). The correlation between the methyl group attached to the nitrogen atom and the aromatic protons could be measured.

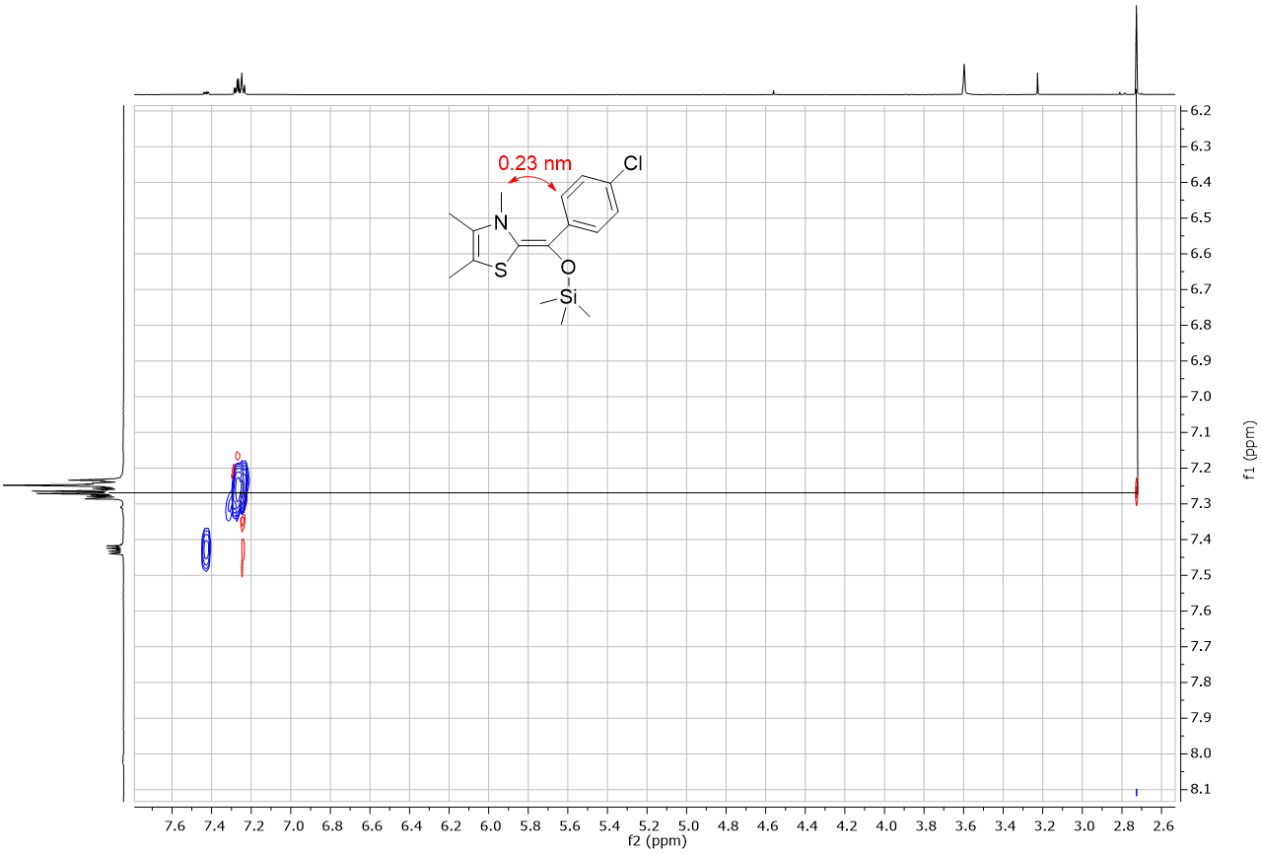

Fig. 5. NOESY-NMR of the silyl-protected enaminol (labelled in red: proton-proton distance computed at the B3LYP-D3(BJ)/6-31++G(d,p) level of theory.

The synthesis for the precursor salt should give a 1:1 mixture of *E* and *Z*. Currently it is not sure why the deprotonation should not give an *E* to *Z* ratio of 1. With an energy difference for the two conformers of the silyl-protected enaminol of 0.8 kcal mol^{-1} we expected an *E* to *Z* ratio of approximately 1 (B3LYP-D3(BJ)/6-311++G(d,p)).

As suitable fluoride source we expected *tert*-butylammonium fluoride trihydrate (TBAF) in THF-d_8 to avoid a biphasic system. The hydrate of TBAF was chosen to protonate the deprotected enolate by water. Additionally, Bu_4NOH as a strong base avoids protonation of the enaminol. Following the measurements of the silyl-protected enaminol, the sample was removed from the spectrometer and the TBAF · 3 H_2O solution was added at −50 to −60 °C with stoichiometric amounts of TBAF. When transferring the sample to the spinner the solution turned from yellow to green and a gas evolved (Fig. 6).

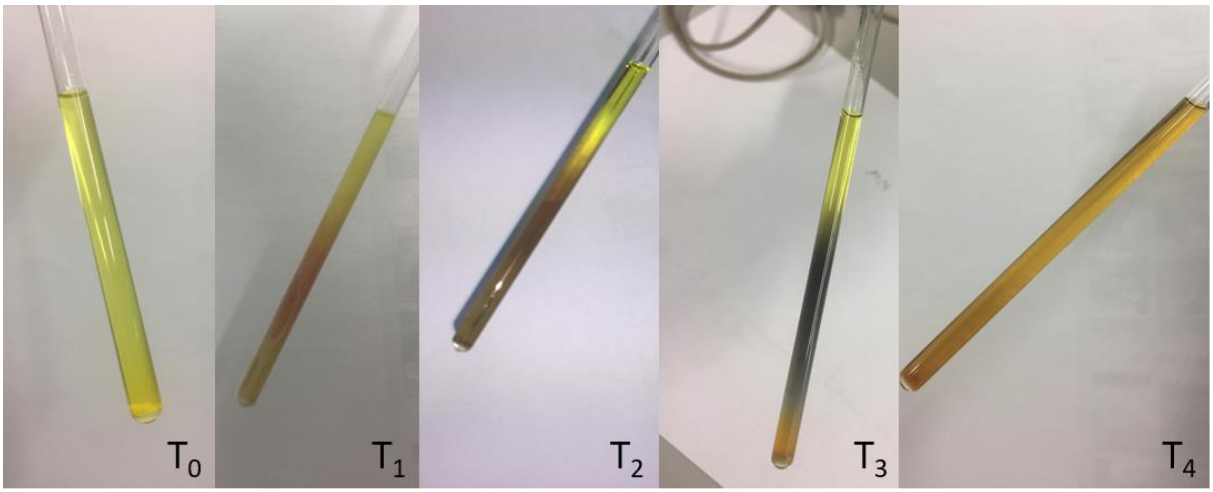

Fig. 6. T_0: Silyl-protected enamiol with precipitated NaI. T_1-T_3 color evolution at ca. –80 °C. T_4: Mixture after measurements at r.t.

Further measurements were carried out at −50 °C. Figure 7 shows the resulting ^{1}H-NMR spectrum. In first experiments we unambiguously identified the keto-form of the desired enaminol forming through keto-enol tautomerism (Fig. 7).

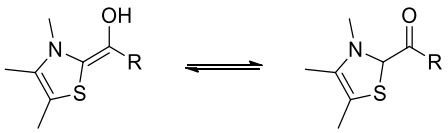

Fig. 7. Keto-enol tautomerism of a thiamine-based enaminol.

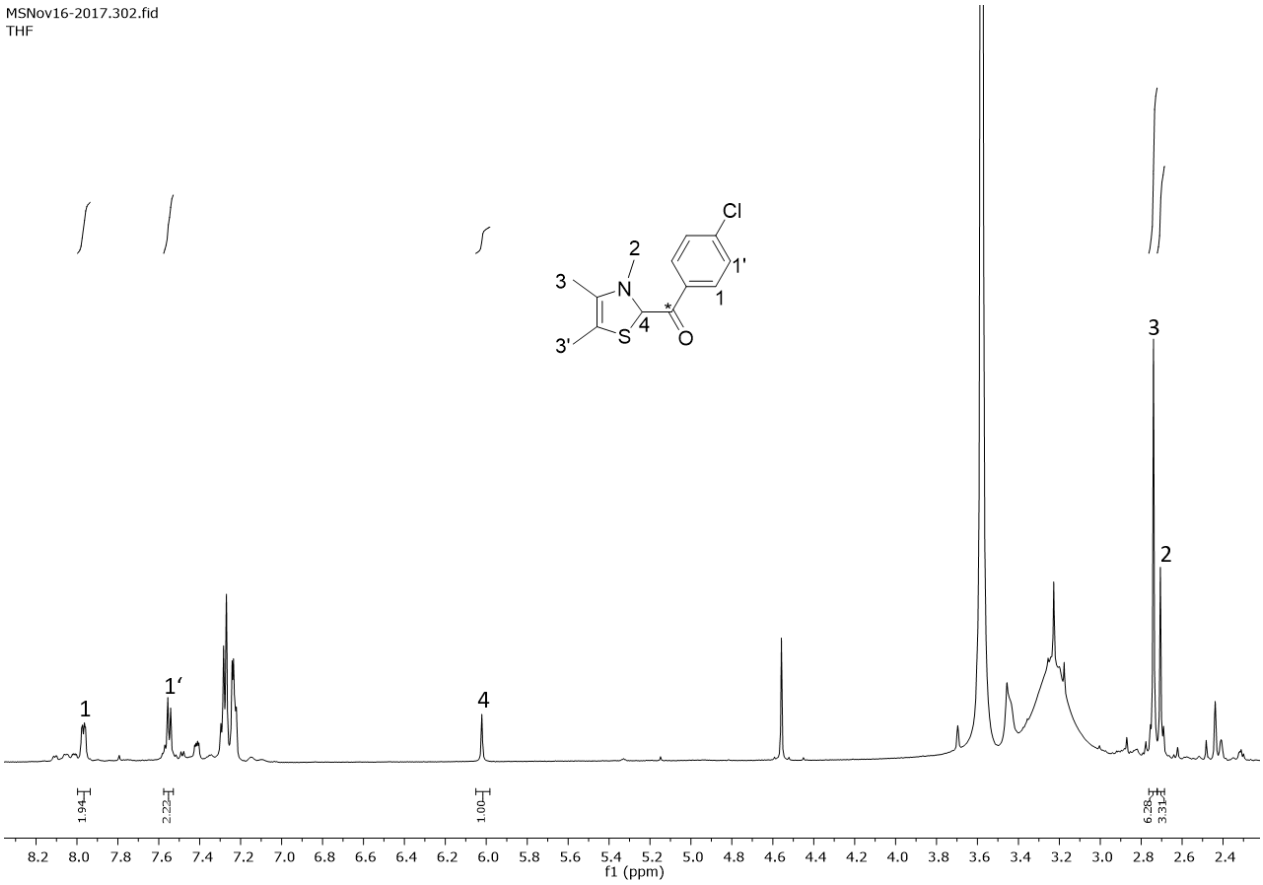

Fig. 8. ^{1}H-NMR spectra of the ketone.

No aldehyde signals could be detected and the acid should not form under the reductive conditions. The proton signal arising from proton **4** shows a weak coupling to a carbon directly attached (green) to it and it couples with the labelled quarternary carbon through a ^{2}J-coupling (Figures 9 and 10).

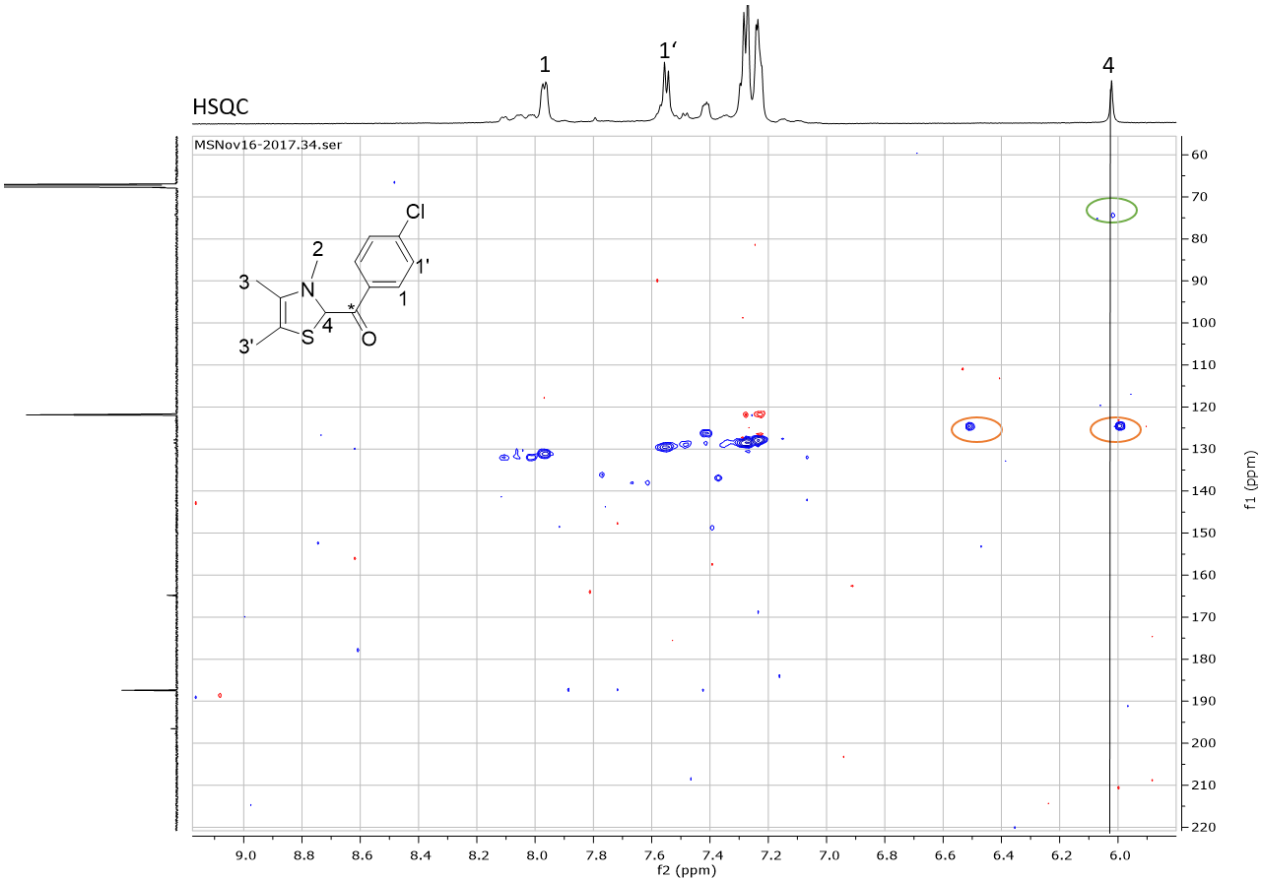

Fig. 9. HSQC spectrum recorded at −50 °C. Proton 4 shows coupling to a carbon. In Berkessel's systems the shifts of the tertiary carbon which would be attached to a methine proton in the ketone are in the range of 70 to 80 ppm.[2,6] The signals encircled in orange are ^{1}J coupling signals of the proton attached to the labelled carbon in the precursor salt.

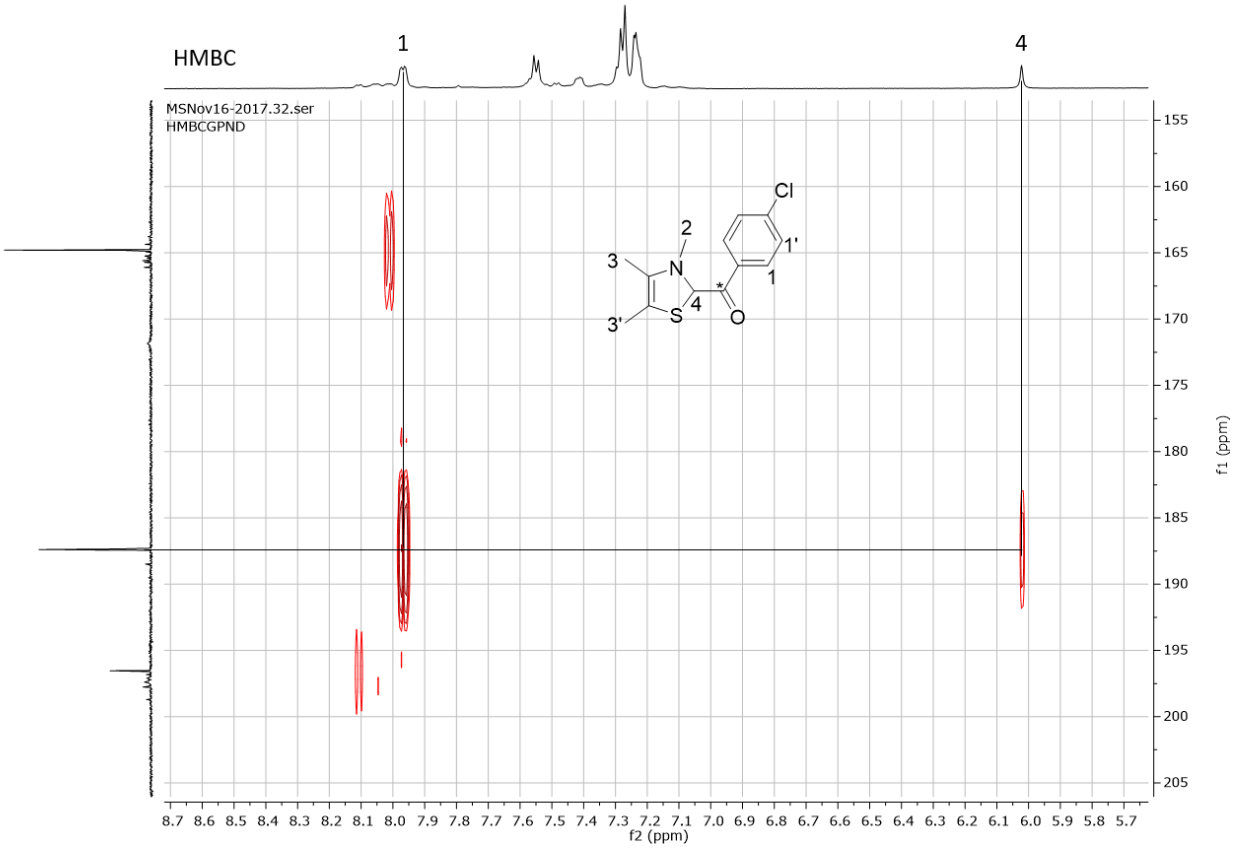

Fig. 10. HMBC spectrum recorded at −50 °C. Proton 4 couples to the quaternary carbon at about 187 ppm.

Figure 11 shows further coupling signals of the ketone.

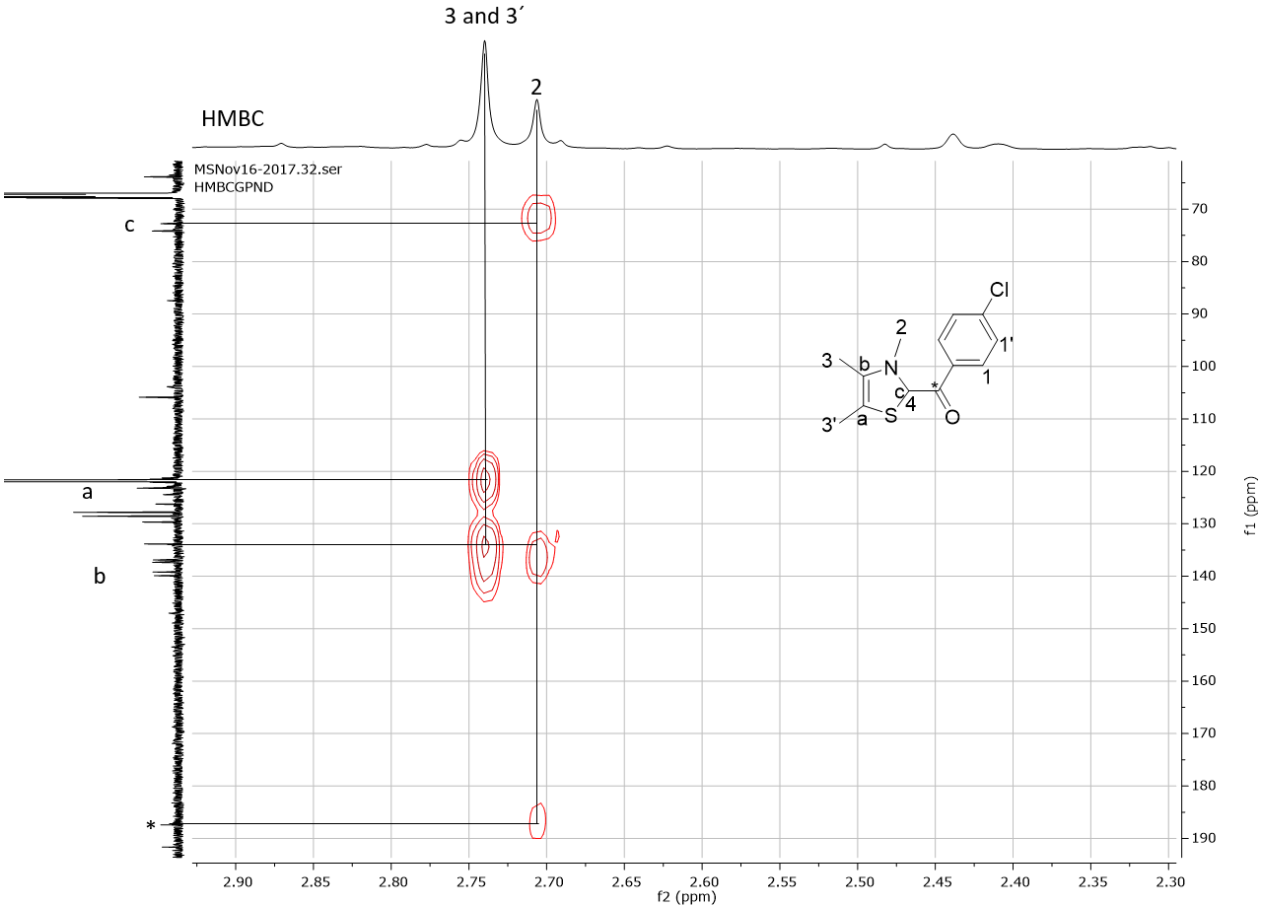

Fig. 11. HMBC spectrum recorded at −50 °C. The coupling signals shown here ensure that the thiazole moiety is still connected to the labelled carbon.

The ketone has only one configuration but there are two signals in nearly the same ratio (5:1) as the protected enaminol (Fig. 12). A possible explanation is the rotation barrier of about 7.8 kcal mol^{-1} (B3LYP/6-311++G(d,p)). At −50 °C two conformers could be visible.[7] The enaminol shows only one signal at about 164 ppm. Here we would expect two signals for the *E* and the *Z* configuration.

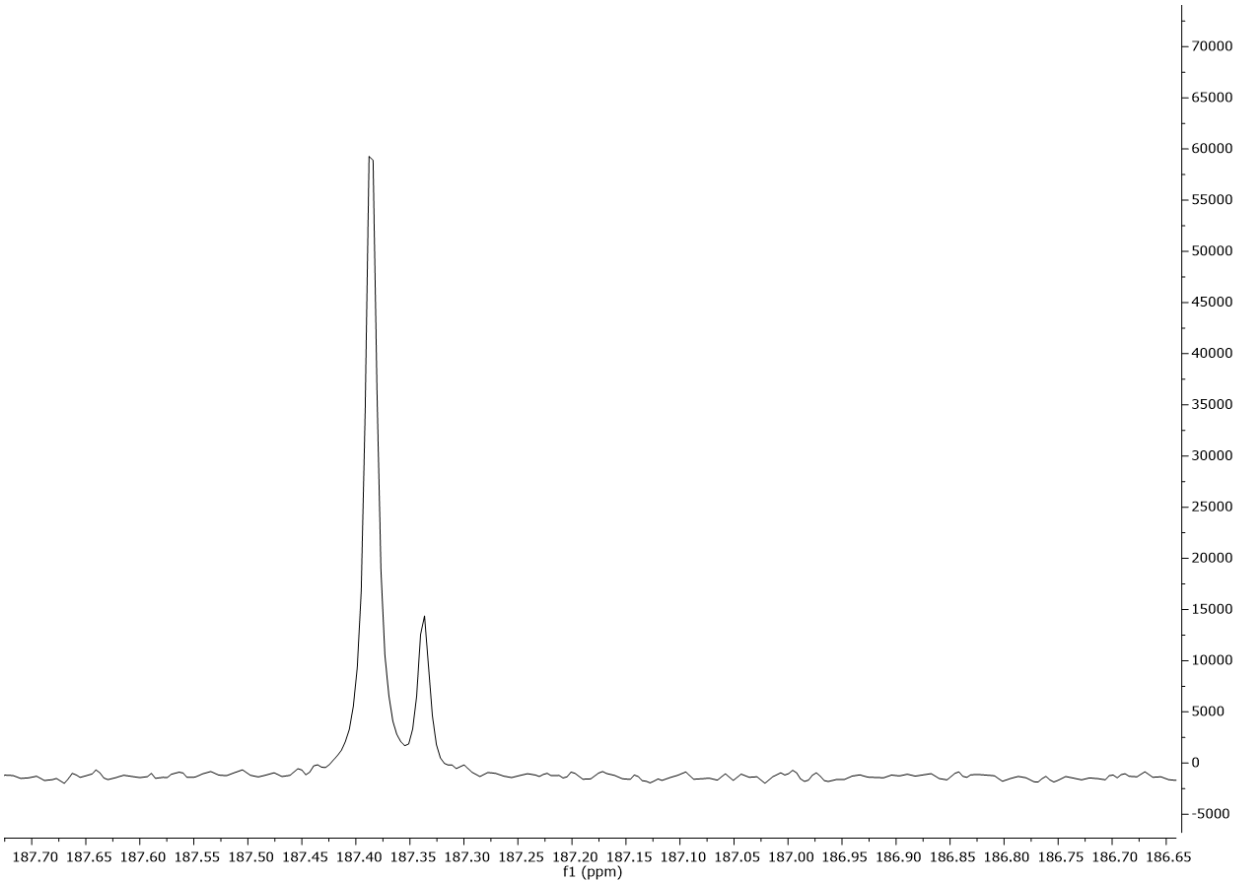

Fig. 12. ^{13}C-spectra of the isotope labelled quaternary ketone carbon. Two signals imply two rotamers whose isomerization is hindered at −50 °C.

Besides the ketone we managed to observe two other species evolving that we assigned to an enaminolate, which slowly hydrolyzes to the free enaminol under given conditions. The hydrolysis of the enolate could be slow due to the following reasons:

- The low temperature strengthens hydrogen bindings so that water could be inactivated. Furthermore, the solubility is lower in THF at lower temperatures. With TBAF · 3 H_2O about three equivalents of water were added but the solution was dried due to an excess of NaH. The concentration of water could be just right to make these observations.
- The negative charge of the enolate is stabilized due to the thiazole- and the *p*-chlorobenzylic substituents. Additionally, the solution is very basic because of the NaH and the OH^- in solution.
- The deprotection seems to be a very fast reaction because the protected structure could not be seen even at the first measurement. When the starting material is deprotected, the counter ion of the enolate is the bulky *tert*-butylammonium cation which could sterically hinder water to hydrolyze the enolate.

When the sample was brought to room temperature the signals corresponding to the enaminol disappeared (Fig. 13).

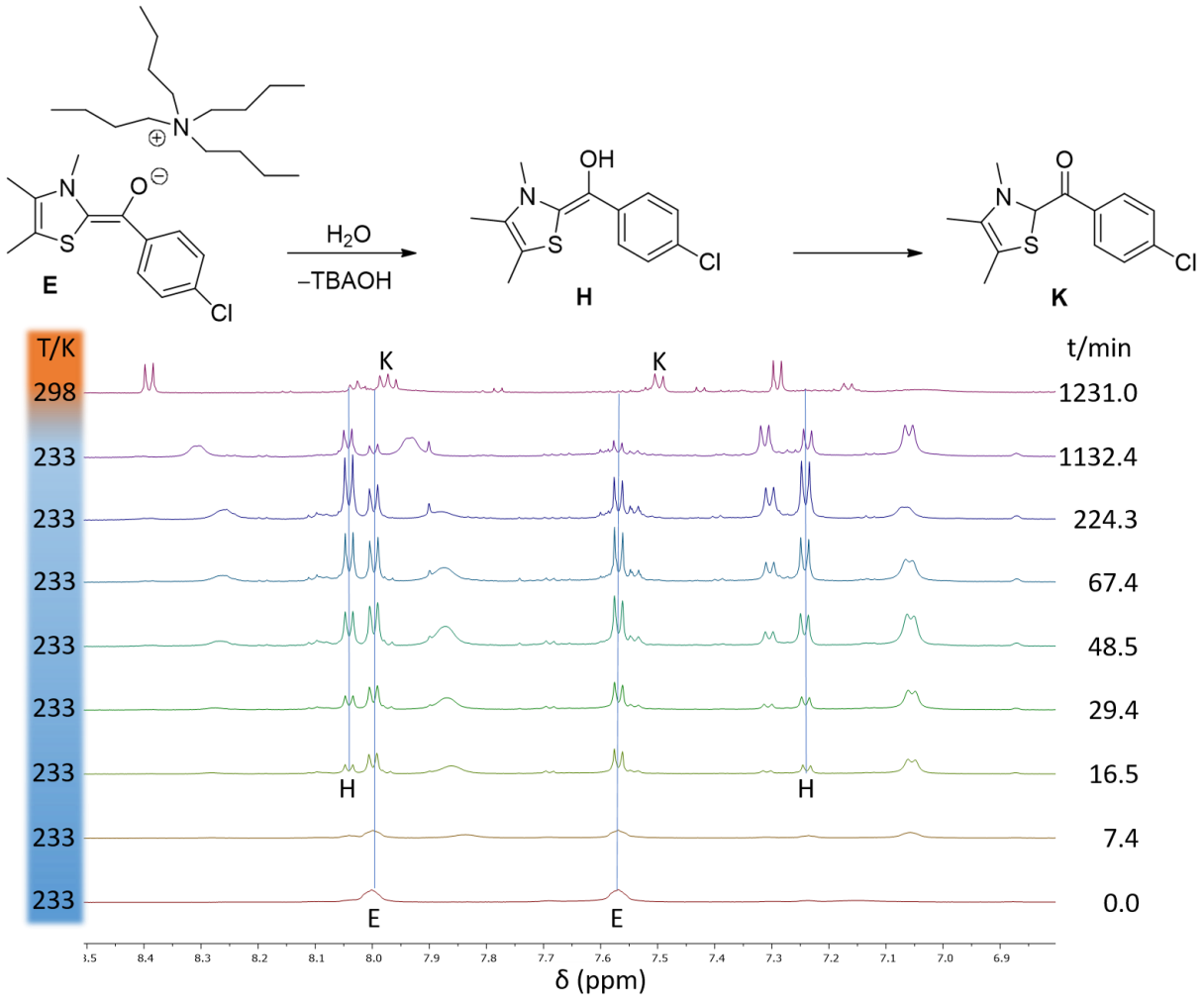

Fig. 13. At 233 K enaminolate E evolves through deprotection of the silyl-protected enaminol by TBAF. Over time the salt slowly gets hydrolyzed to form enaminol H. When the mixture was allowed to reach r.t. ketone K forms through keto-enol tautomerism.

To ensure these assignments HSQC spectra were recorded (Fig. 14).

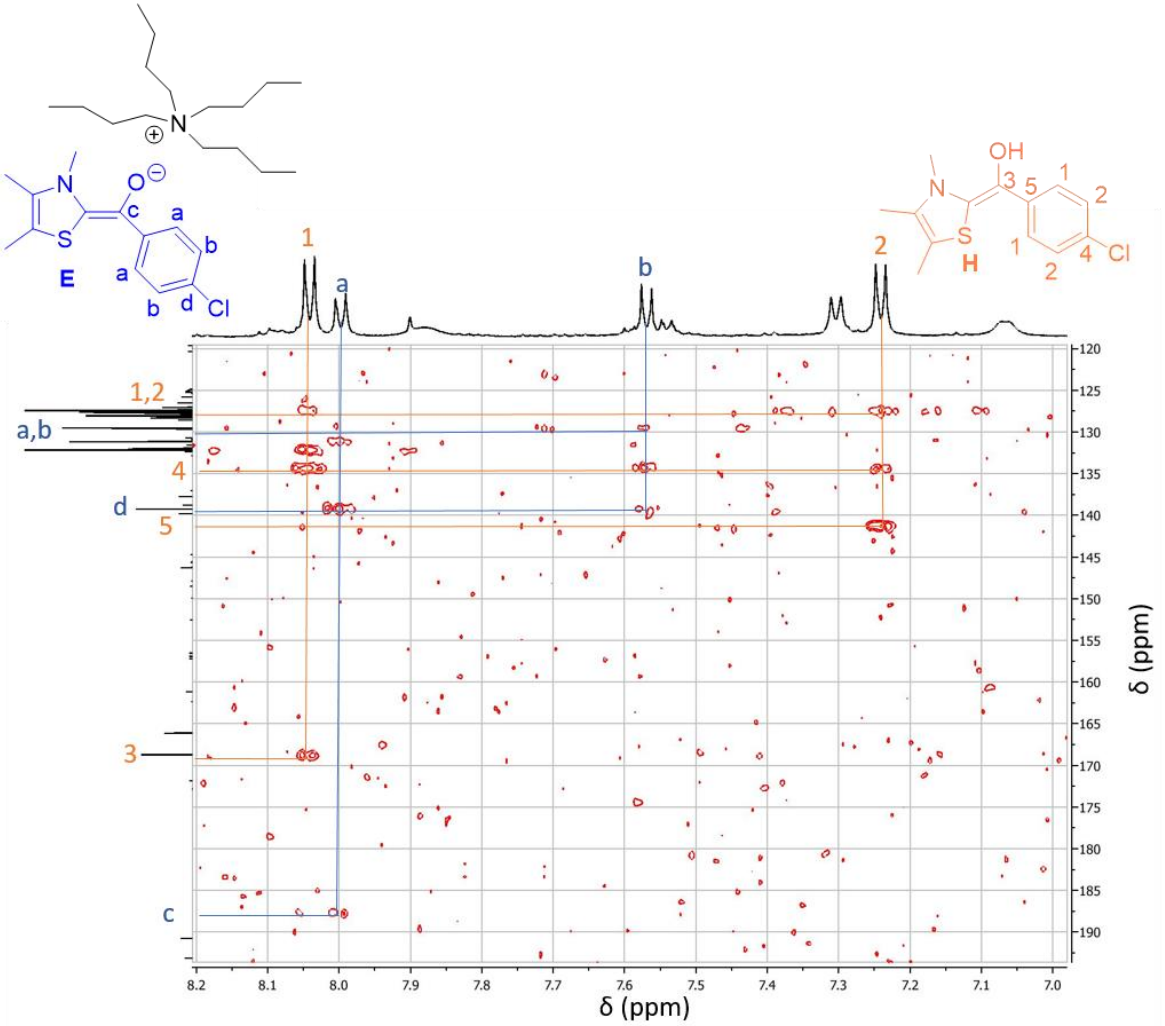

Fig. 14. HSQC spectrum recorded at −50 °C. The shift region for protons and carbons of aromatic systems is shown.

Discussion of reaction parameters

Solvent

For the experiments THF was used as a solvent. The thiazolium salt and NaH do not dissolve in THF. The reaction should be more efficient, if all the reactants would dissolve. DMSO dissolves the thiazolium salt but solidifies at 18 °C. Chloroform dissolves the salt, too but it could form the dichlorocarbene under basic conditions. $CDCl_3$ should be tested to see if it forms the carbene or if the reaction with the salt takes place first.

Base

NaH was used for the experiments. An organic base could help to make the reaction complete.

Fluoride source

TBAF · 3 H_2O was used because the water should act as a proton source to protonate the enaminolate. Since we are not quite sure which species evolves, we should change to strictly aprotic conditions and investigate the enaminolate first. A suitable fluoride source is TASF since it is known to be a rare anhydrous fluoride source.

Time

The time from the addition of the fluoride source until the first measurement must be decreased. In the best case we should be measuring exactly when it is added to the NMR tube.

Based on the assumptions made above we tried to react the enaminol with another aldehyde to see if the system shows the expected reactivity, namely an “Umpolung” reaction.

Reactivity of the thiazole-based Breslow-intermediate

The experiment was repeated and *p*-nitrobenzaldehyde was added together with TBAF at – 90 °C. The solutions did not mix instantly because of the temperature difference. Blue streaks from the lower phase rose up to the upper clear phase. When warmed the solution turned purple. The solution was filtered and measured at r.t. The resulting spectra are shown in Figures 15 and 16.

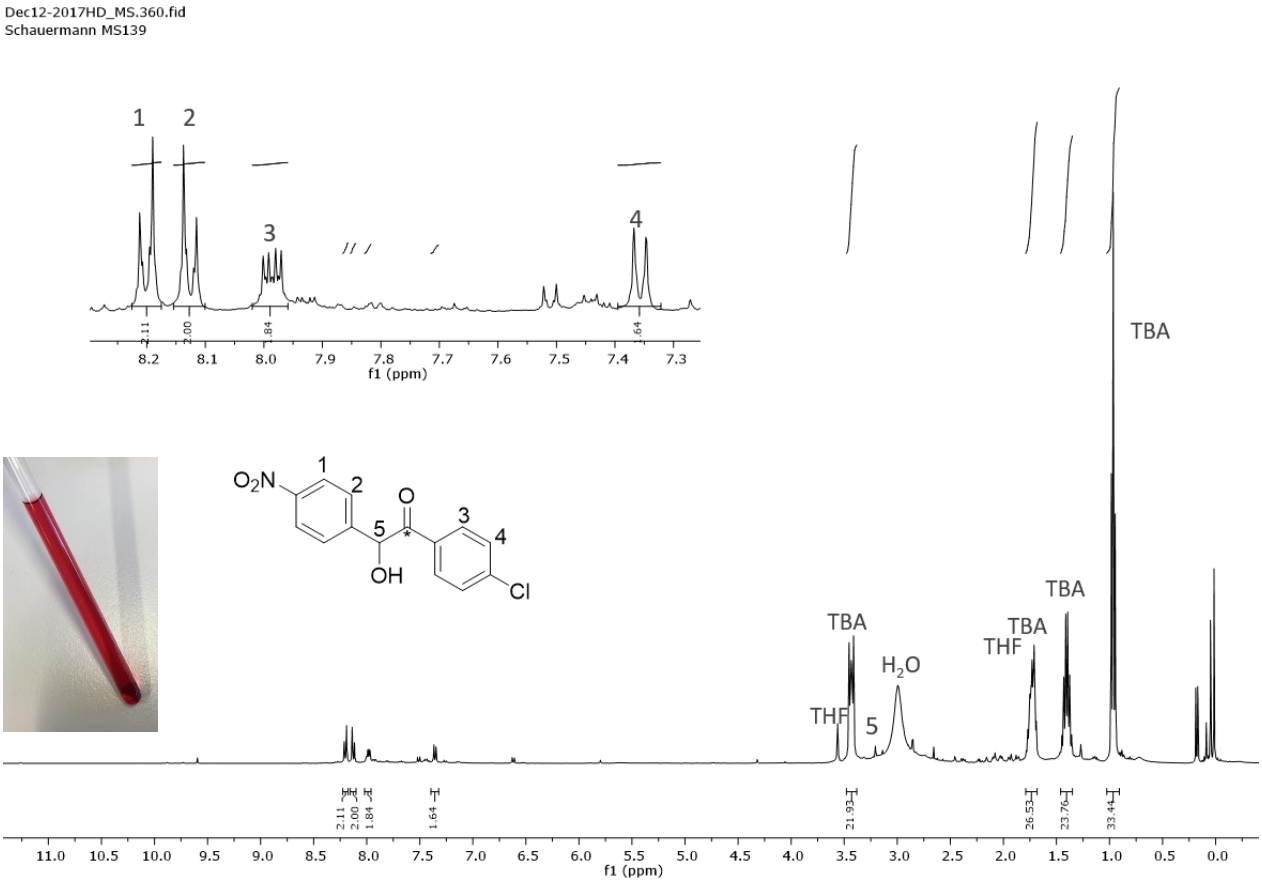

Fig. 15. ^{1}H-NMR spectra of the benzoin product. The filtered solution contains no side products but water, THF and some kind of *tert*-butyl ammonium salt (TBA). Inlet: the splitting of the proton signals 3 and 4 show incorporation of the labelled carbon originating from the enaminol.

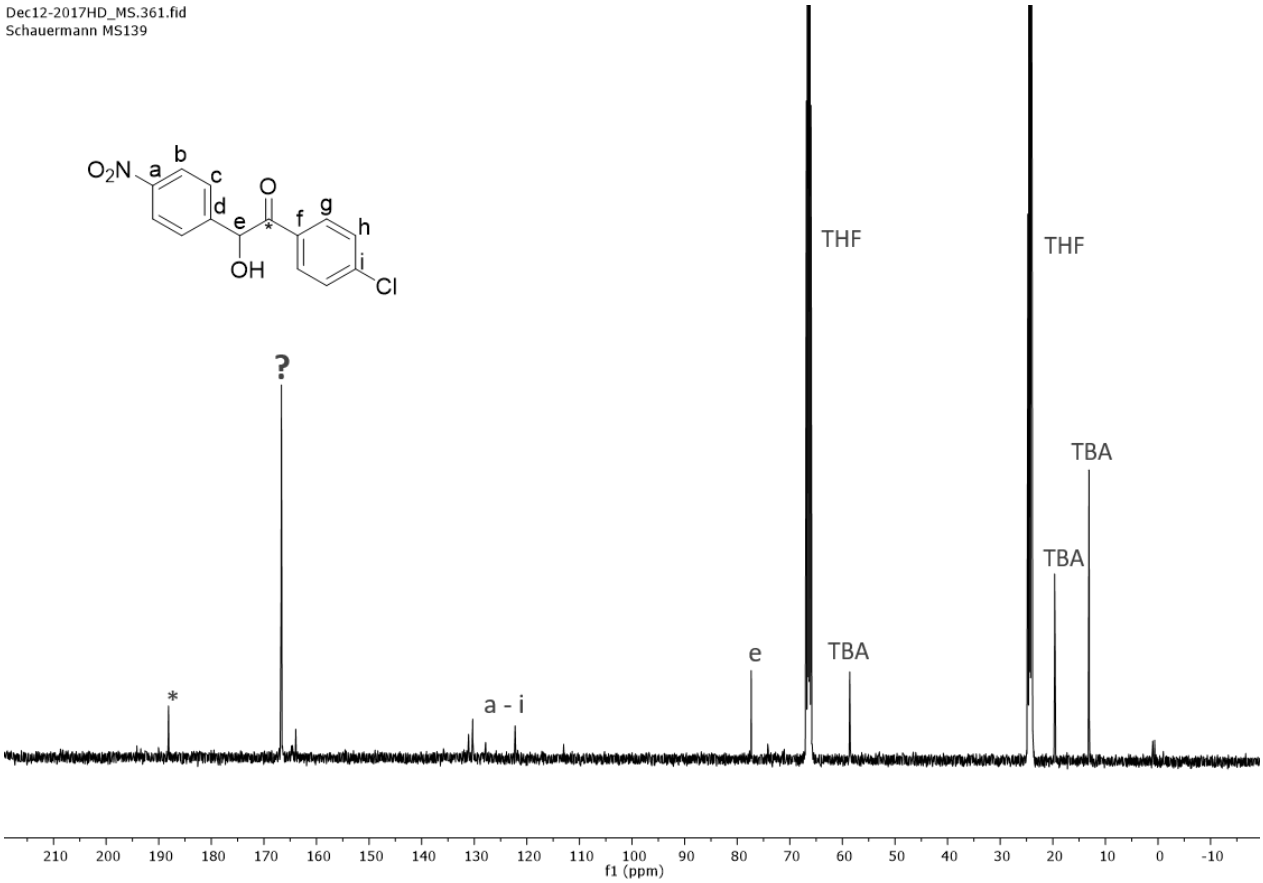

Fig. 16. ^{13}C-NMR spectra of the benzoin product. The intensity of the labeled carbon is high compared to the aromatic carbons. One large signal labeled with „?“ could not be identified.

One has to keep in mind that the benzoin condensation takes place when fluorine is added to the precursor salt. When the silyl-protected enaminol was generated with about 5 equivalents of NaH, no precursor salt could be detected what makes this route unlikely.

The results presented herein provide spectroscopic evidence for a thiamine-derived Breslow-Intermediate in its active enaminol-form. The verification of this structure supports the mechanism Breslow postulated decades ago.[1]

6.3. Experimental

Synthesis of the Thiazolium-precursor salts

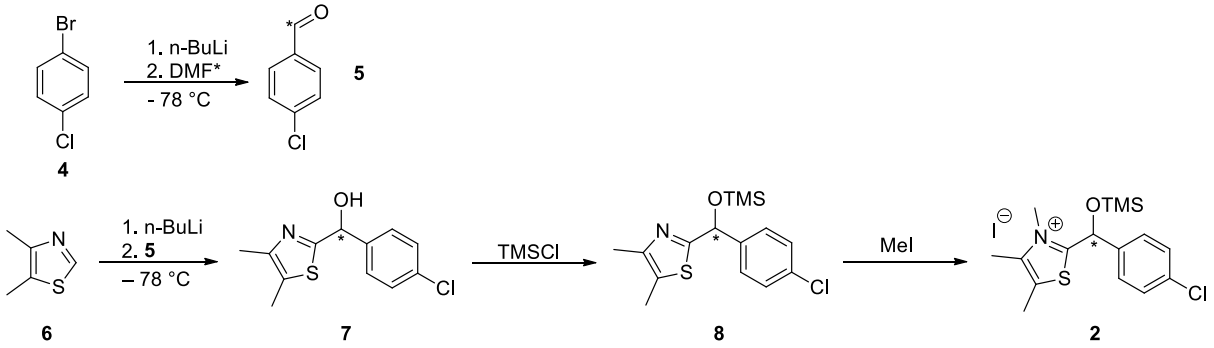

Fig. 17. Route for the synthesis of the isotope labelled precursor salt.

Isotope-labelled *p*-Chlorobenzaldehyde

1.15 g *p*-chlorobromobenzene (6.1 mmol, 1.04 eq.) was dissolved in 20 mL try THF under Argon. 3.8 mL n-BuLi (1.6 M in hexane, 6.1 mmol, 5.8 eq.) was added whereby the solution did not get warmer than −85 °C. The reaction was stirred 2 hours at −90 °C. 0.47 mL carbonyl-^{13}C labelled DMF was added dropwise and the solution was stirred over night at r.t. The yellow solution was then quenched with 25 mL H_2O and stirred for 20 min. The mixture was extracted with DCM and EtOAc and the combined organic layers were dried over Na_2SO_4. The crude product was purified *via* column flash chromatography (*n*-hexane 10:1 EtOAc).

R_f (*p*-chlorobenzaldehyde) = 0.25

The product was obtained as yellow needles (373 mg, 45%).

^{1}H-NMR (400 MHz; $CDCl_3$): δ = 9.99 (s, 1H), 7.83 (m, 2H), 7.52 (m; 2H) ppm.

^{13}C{^{1}H} NMR (101 MHz, $CDCl_3$): δ = 191.1, 141.1,134.6, 131.1, 129.6 ppm.

Isotope-labelled 7

The following synthesis for the precursor salt was carried out according to a protocol of Scheidt *et al.*[8]

0.28 mL dimethyl thiazol (2.6 mmol) was dissolved in 20 mL try THF. The solution was cooled to −80 °C. 2.8 mL n-BuLi (1.6 M in hexane, 4.5 mmol, 1.7 eq.) was added. After 1 h 370 mg *p*-chlorobenzaldehyde (2.6 mmol, 1 eq.) in 10 ml dry THF was added over 30 min. The solution turned yellow, then green and brown. The solution was brought to r.t. overnight and was quenched with 25 mL dest. H_2O. The solution was stirred for 10 min and was then extracted

with EtOAc and the organic phases were tried over Na_2SO_4. The crude product was purified *via* column flash chromatography (*n*-pentan 1:2 Et_2O).

R_f(**7**) = 0.27

The product was obtained as a yellow oil (341 mg, 51%).

^{1}H-NMR (400 MHz; $CDCl_3$): δ = 7.42 (m, 2H), 7.34 (m, 2H), 5.99 (s, 1H), 3.80 (bs, 1H), 2.30 (m, 6H) ppm.

^{13}C{^{1}H} NMR (101 MHz, $CDCl_3$): δ = 169.6, 147.1, 140.2, 134.4, 129.0, 128.1, 127.9, 72.8, 14.5, 11.5 ppm.

Isotope-labelled 8

First 340 mg **7** (1.3 mmol, 1 eq.) was dissolved in 15 mL try DCM. 0.1 g imidazole (1.5 mmol, 1.2 eq.) was added before 0.5 mL TMSCl (433 mg, 3 eq.) was added dropwise. The solution clouded. The mixture was stirred overnight and then diluted with 20 mL DCM. The reaction mixture was extracted with DCM and the combined organic phases were washed with brine. The organic phase was dried over Na_2SO_4. The solvent was removed and the product was obtained as a yellow oil (**8**, 388 mg, 89%). The crude product **8** was dissolved in 2.5 mL MeI and refluxed at 80 °C overnight. The excess MeI was destilled and the residue was stirred in 10 mL Et_2O for 1 h. After filtering the product **2** was obtained as a pale green solid (420 mg, 67%). No further purification was necessary.

^{1}H-NMR (400 MHz; DMSO): δ = 7.54 (m, 4H), 6.68 (s, 3H), 3.73 (s, 3H), 2.49 (s, 3H), 2.35 (s, 3H), 0.12 (s, 9H) ppm.

^{13}C{^{1}H} NMR (400 MHz; DMSO): δ = 173.3, 144.1, 136.4, 134.3, 130.1, 129.7, 129.3, 70.5, 38.1, 11.8, 11.7, −0.1 ppm.

NMR-experiments

The NMR-experiments for the detection of a Breslow-Intermediate were carried out with an Avance III HD 600 MHz, BJ 2007 with tempering unit, 5 mm-ATM-BBO-sample unit with z-gradient coil; Software: TopSpin 3.5.

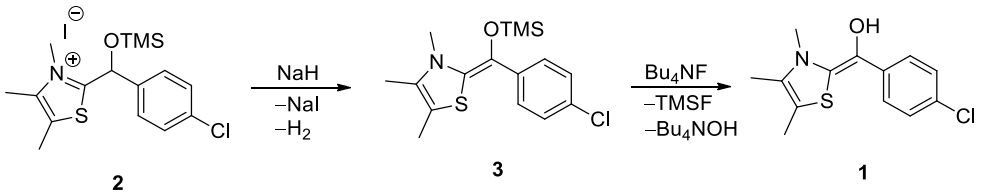

5 mg (0.011 mmol) **2** were suspended in 0.4 mL THF-d_8 (N_2-glovebox). After addition of 1.2 mg (0.05 mmol) NaH the solution turned yellow and a gas evolved (Hydrogen). After 60 min 3,4 mg (0.011 mmol) TBAF · 3 H_2O in 0.3 mL THF-d_8 were added at −50 °C. First the solution turns from yellow to red and then to green/blue. This happens in the short period of time it takes to transfer the sample to the spectrometer. The measurements were started at −50 °C.

NMR Spectra

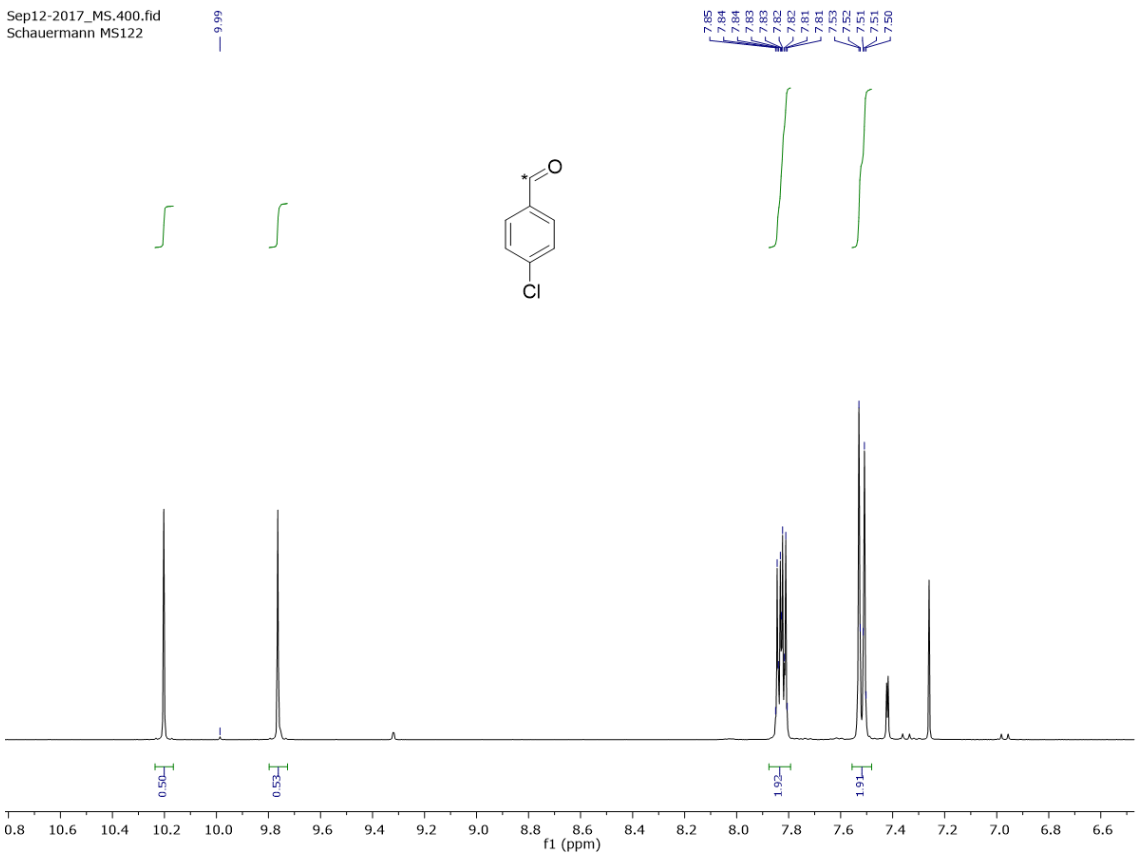

Fig. 18. ^{1}H NMR (400 MHz, $CDCl_3$) of the isotope labelled *p*-chlorobenzaldehyde.

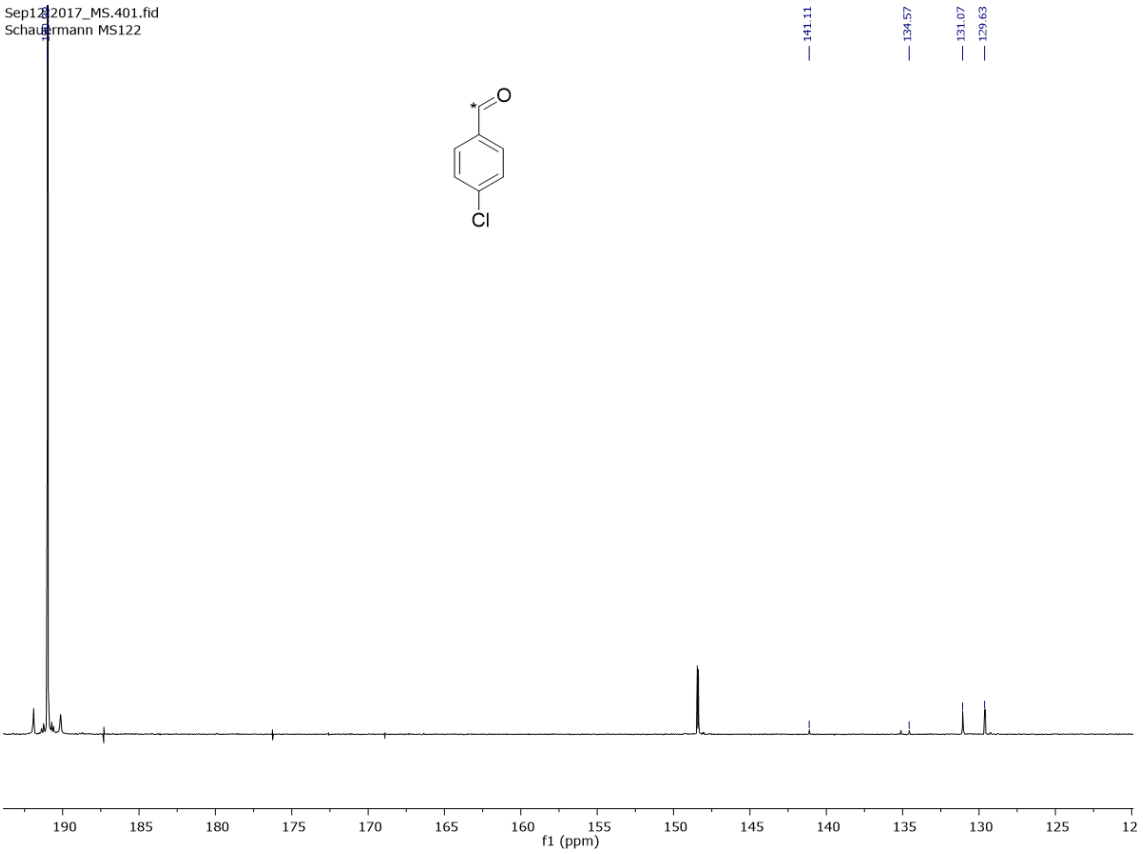

Fig. 19. $^{13}C\{^{1}H\}$ NMR (101 MHz, $CDCl_3$) of the isotope labelled *p*-chlorobenzaldehyde.

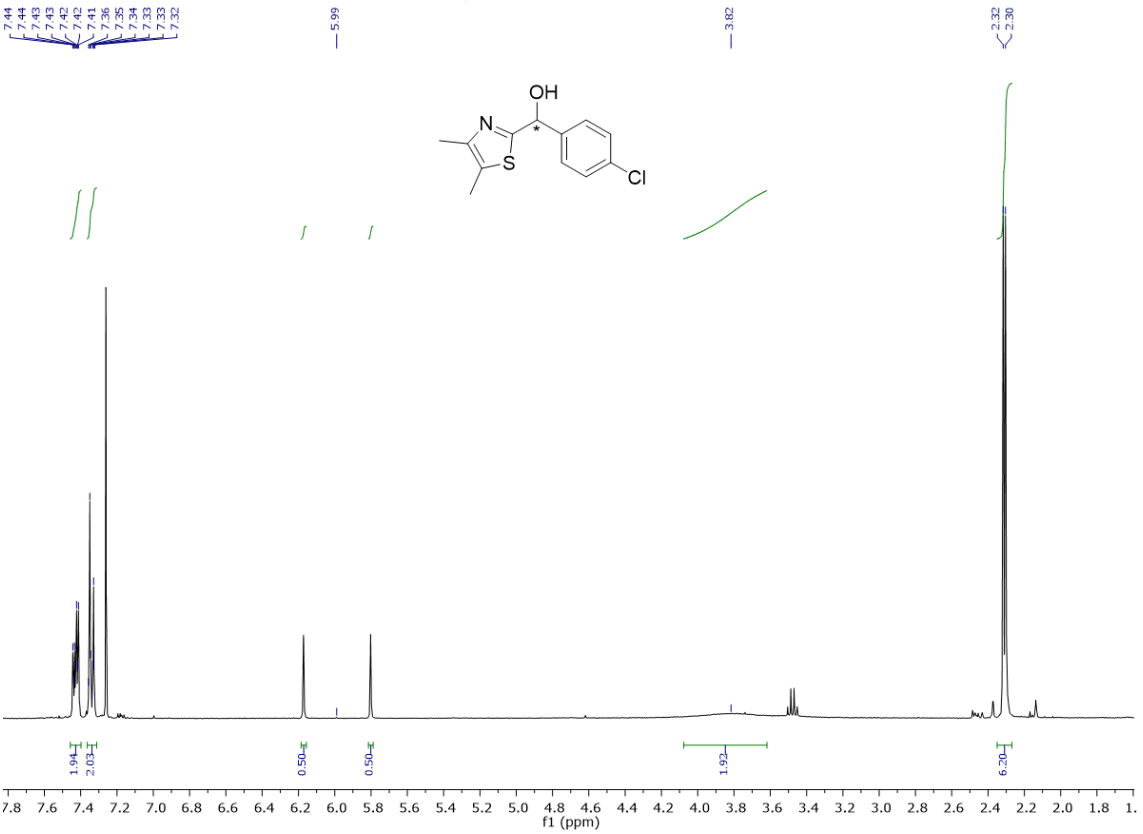

Fig. 20. ^{1}H NMR (400 MHz, $CDCl_3$) of isotope labelled **7**.

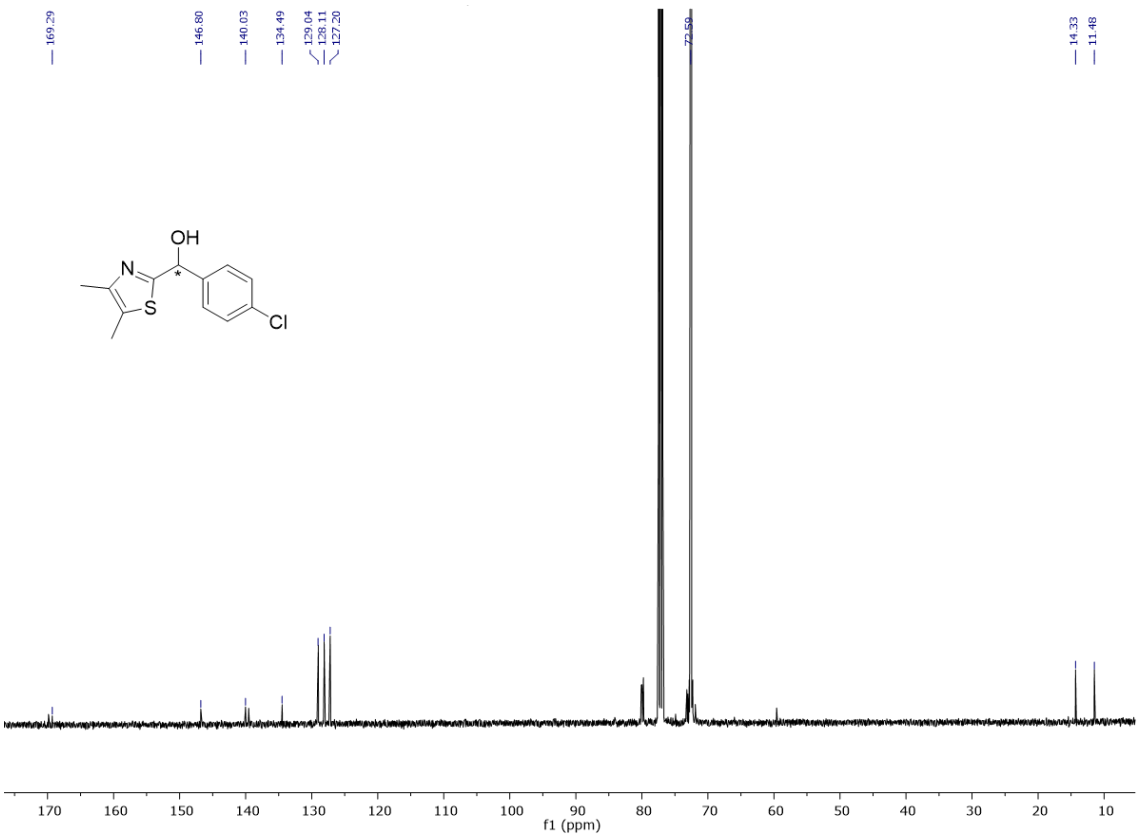

Fig. 21. $^{13}C\{^{1}H\}$ NMR (101 MHz, $CDCl_3$) of isotope labelled **7**.

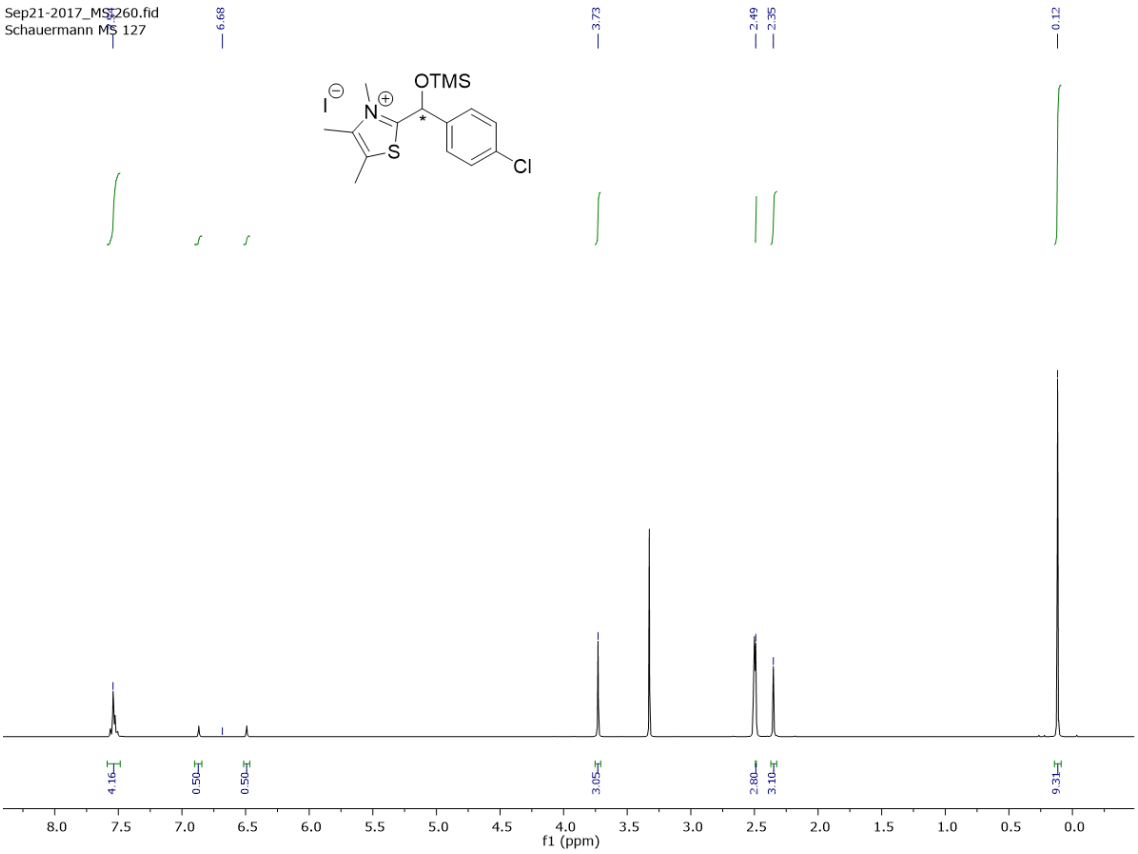

Fig. 22. ^{1}H NMR (400 MHz, $CDCl_3$) of precursor salt **2**. One methyl group has nearly the same shift as DMSO.

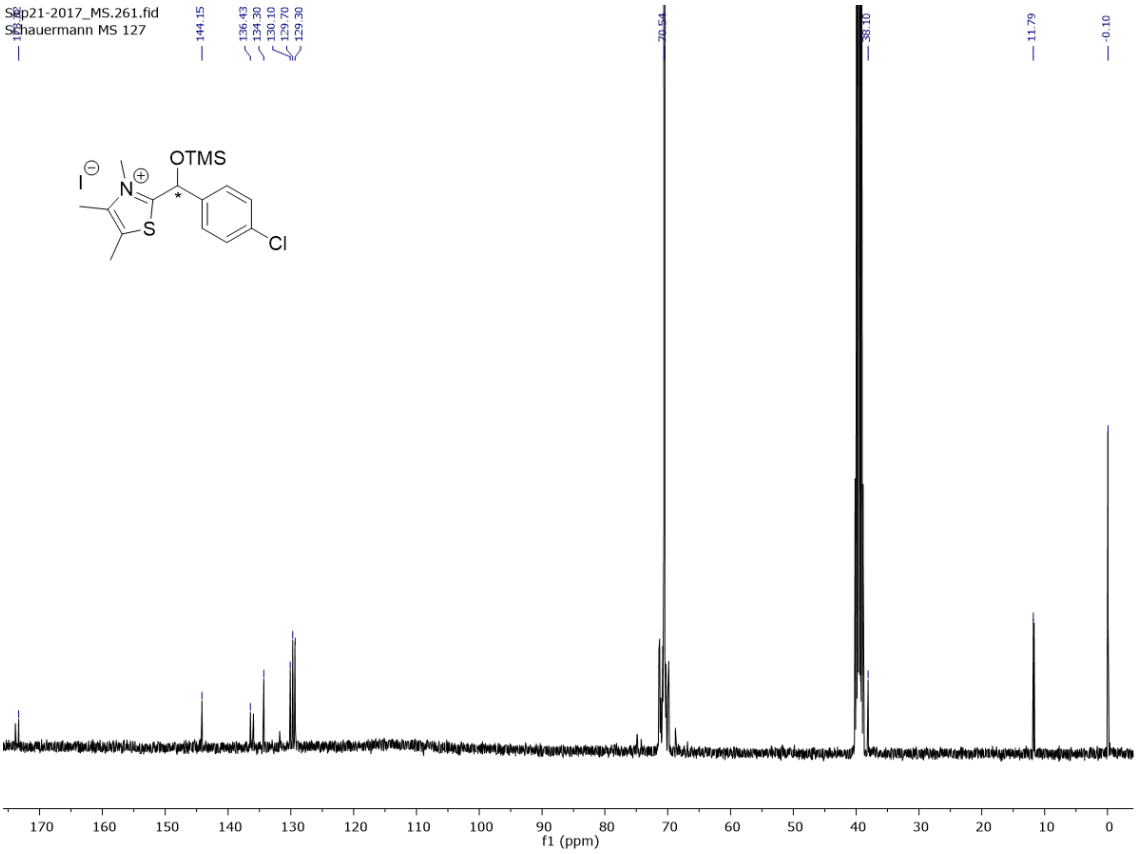

Fig. 23. $^{13}C\{^{1}H\}$ NMR (101 MHz, $CDCl_3$) of the precursor salt.

6.4. References

[1] R. Breslow, *J. Am. Chem. Soc.* **1958**, *80(14)*, 3719.

[2] M. Paul, P. Sudkaow, A. Wessels, N. E. Schlörer, J. Neudörfl, A. Berkessel, *Angew. Chem. Int. Ed.* **2018**, *57(27)*, 8310.

[3] M. Paul, M. Breugst, J. M. Neudörfl, R. B. Sunoj, A. Berkessel, *J. Am. Chem. Soc.* **2016**, *138(15)*, 5044.

[4] M. Paul, J. M. Neudörfl, A. Berkessel, *Angew. Chem. Int. Ed.* **2019**, *58(31)*, 10596.

[5] A. K. Mathies, A. E. Mattson, K. A. Scheidt, *Synlett* **2009**, *3*, 377.

[6] M. Paul, M. Breugst, J.-M. Neudörfl, R. B. Sunoj, A. Berkessel, *J. Am. Chem. Soc.* **2016**, *138*, 5044.

[7] F. A. Bovey, E. W. Anderson, F. P. Hood, R. L. Kornegay, *J. Am. Chem. Soc.* **1964**, 40, 3099.

[8] A. E. Mattson, A. M. Zuhl, T. E. Reynolds, K. A. Scheidt, *J. Am. Chem. Soc.* **2006**, *128*, 4932.

Conclusion and Outlook

During the work presented herein I combined synthesis, computational chemistry and special analytical tools such as matrix isolation spectroscopy or low temperature NMR spectroscopy to investigate new and highly reactive species.

We reported the generation and characterization of hydroxymercaptomethylen (HO–C̈–SH) and aminomercaptomethylen (H_2N–C̈–SH), the first two members of the mercaptocarbene family that were spectroscopically identified. These projects were published in highly acknowledged journals and expand the knowledge of carbenes and tunneling processes that even led to CO_2 activation under cryogenic conditions. These fundamental results open the door to the investigation of other mercaptocarbenes, a new family of carbenes as fascinating as their oxygen analogues, hydroxy carbenes. Chapter 4 describes various approaches for other mercaptocarbenes that have not given fruitful results but might help for further studies on these systems.

Furthermore, we found a route to generate and investigate an enaminol with low temperature NMR spectroscopy. The system could in future allow to study the influence of dispersion energy donors attached to the NHC moiety and of electronic properties of the aldehyde regarding NHC catalyzed Umpolung-reactions.

In a synthetic project I established a new one-pot- procedure for substituted thiophenes that might be useful to generate compounds featuring electronic properties for electronic applications. At the moment the scope is quite limited and future work might help to improve the scope as well as the yields of this reaction.

Abbreviations

Attenuated total reflection	ATR
Basis set superposition error	BSSE
Bond critical point	BCP
Canonical variational transition state theory	CVT
confer	cf.
Deoxyribonucleic acid	DANN
Dichloromethane	DCM
Dimethylformamide	DMF
Dimethyl sulfoxide	DMSO
Electron donating group	EDG
Electron withdrawing group	EWG
Electrospray ionization	ESI
Flash vacuum pyrolysis	FVP
Frustrated Lewis pair	FLP
Heteronuclear multiple-bond correlation spectroscopy	HMBC
Heteronuclear single-quantum correlation spectroscopy	HSQC
High vacuum flash pyrolysis	HVFP
Highest occupied molecular orbital	HOMO
High resolution mass spectrometry	HRMS
Infrared	IR
Kinetic isotope effect	KIE
Lowest unoccupied molecular orbital	LUMO
Mass spectrometry	MS
Natural bond orbitals	NBO
Natural resonance theory	NRT
N-heterocyclic Carbene	NHC
Nuclear magnetic resonance	NMR
Nuclear Overhauser effect spectroscopy	NOESY
Potential energy surface	PES
Quantum mechanical Tunneling	QMT
quantum theory of atoms in molecules	QTAIM
Room temperature	r.t.
Ring critical point	RCP
Small curvature tunneling	SCT
tert-butyl ammonium salt	TBA
tert-Butylammoniumfluorid	TBAF
Tetrahydrofuran	THF
thiamine pyrophosphate	TPP
Transition state	TS
Transition state theory	TST
Trimethylsilyl	TMS
Tris(dimethylamino)sulfonium difluorotrimethylsilicate	TSAF
Ultraviolett	UV
Visible	Vis
X-ray diffraction	XRD

Zero-point vibrational energy	ZPVE

Acknowledgement − Danksagung

Ich bedanke mich bei meinem Betreuer und Doktorvater Prof. Dr. Peter R. Schreiner, Ph.D., für seine Unterstützung und die Freiheit in der Forschung. Ich bedanke mich für die exzellente Ausbildung in seiner Arbeitsgruppe und die Möglichkeit der Teilnahme an internationalen Konferenzen, um mein Wissen zu vertiefen und mich mit vielen interessanten Forschern der ganzen Welt auszutauschen.

Ich bedanke mich bei Prof. Dr. Hermann A. Wegner, dem Zweitgutachter dieser Arbeit.

Ich bedanke mich bei Michael Linden, der mich in der Master-Arbeit betreut und mich auf das selbstständige Forschen vorbereitet hat.

Ich bedanke mich bei Dr. Dominik Niedek, Dr. Jan Philipp Berndt, Dr. Frederik R. Erb, Lukas Ochmann, Alexander Seitz, Finn M. Wilming für zahlreiche schmackhafte Mittagspausen mit unserer Subgroup „Kochen“.

Ich bedanke mich bei Dr. Frederik R. Erb, Lukas Ochmann, Alexander Seitz und Simon Hofmann für eine schöne Zeit in B204, für zahlreiche Diskussionen und Gespräche wissenschaftlicher und privater Natur.

Mein Dank gilt Michaela Richter und allen Mitarbeiterinnen und Mitarbeitern des Instituts für Organische Chemie, ohne die das Arbeiten nicht möglich gewesen wäre.

Allen Mitarbeiterinnen und Mitarbeitern des Instituts für Organische Chemie für eine schöne Zeit im Labor und im privaten Umfeld.

Ich bedanke mich bei Dr. Raffael C. Wende, Dr. Christian Eschmann, Dr. Dominik Niedek, Jean M. Pohl, Rainer Schauermann und Tomas Schauermann für das Korrekturlesen dieser Arbeit.

Ich bedanke mich bei meiner Familie für die ständige Unterstützung und aufbauenden Worte in dieser, nicht immer einfachen Zeit.

Ich bedanke mich bei meinen Freunden, insbesondere Moritz Großkopf, Tomas Schauermann, Anke Budde, Adrian Lehnhardt, Christoph Hofmann, Carolin Mogk, Jan M. Schümann, Alexander Seitz, Dr. Dominik Niedek, Jean M. Pohl, Dr. Christian Eschmann, Jochen und Sonja Röder, und für eine gute Zeit zwischen den Laborstunden und ihre Unterstützung.

Ich bedanke mich bei meiner Frau Svenia V. Schauermann, für ihre Liebe, ihre bedingungslose Unterstützung und aufbauende Worte in oft anstrengenden Zeiten.